Faculty of Mathematics and Physics
CHARLES UNIVERSITY in PRAGUE

Oscillations and lightcurve patterns of accreting black holes

Thesis submitted for the degree of Doctor Philosophiae

Jiří Horák

Supervisor: doc. RNDr. Vladimír Karas, DrSc.

Prague, August 2005

Contents

Preface

This thesis concentrates on two phenomena connected with the accretion process onto the black holes and neutron stars. The first Part deals with the twin peak high-frequency quasiperiodic oscillations – the phenomenon observed in the last decade in low mass X-ray binaries with neutron stars and, recently, also in four systems with acreting black holes. In the second Part we concentrate on the interaction of fast moving matter with an ambient dense radiation field. This process likely occurs at the initial stages of relativistic jets in strong gravity of a central black hole. Several results have already been published: in Horák et al. (2004) our results are discussed in the context of the observation data of the source Sco X-1; the general approach to multiple scales was presented in Horák (2004). Some other papers are in preparation: the epicyclic modes of the accretion torus are derived in Abramowicz et al. (2005a), phase-plane topologies of the epicyclic resonances are explored in Horák & Karas (2005a) and the possibility of the X-ray modulation through the modulation of the accretion rate in the boundary layer of accreting neutron stars is examined in Horák (2005a) and Abramowicz et al. (2005b). Several results of the second Part are presented in Horák & Karas (2005b).

I would like to thank my supervisor, Vladimír Karas, for all of his helpful advice, useful ideas and pertinent comments on this work and my research. I wish to thank Marek Abramowicz and Wlodek Kluźniak for many discussions about the resonance model of QPOs. A lot of calculations were motivated by our discussions in Prague, Opava, Leicester, Copenhagen and Wojnowice.

Many thanks go to my colleagues, Paola Rebusco, Michal Bursa, Michal Dovčiak and Ladislav Šubr for many comments improving the text. I thank everyone whom I worked with at the Astronomical Institute of the Academy of Sciences for their friendship. I gratefully acknowledge the support from the Czech Science Foundation grants 205/03/H144 and 205/03/0902 and from the GAAV grant IAA 300030510. Finally, I would like to thank the Department of the English Language for letting me successfully pass the Examination.

Part I

The epicyclic resonance mechanism for twin-peak oscillations: an axially symmetric scheme

Introduction

The quasi-periodic oscillations (QPOs) have been reported in the light curves of more than 20 bright low-mass X ray-binaries (LMXBs). Most of them contain accreting neutron stars, there are also several sources with accreting black holes (van der Klis 2000; McClintock & Remillard 2003). It appears that that these oscillations originate in accretion disks, however, the mechanism of signal modulation has not been discovered yet. Much attention is attracted to the kilohertz QPOs because their frequencies are comparable with orbital frequencies in the innermost parts of the accretion disks. The orbital frequency of a particle orbiting the neutron star of mass M at the innermost stable circular orbit (ISCO) is $\nu_{\rm ISCO} = 1580(1 + 0.75j)$ Hz $\times\, 1.4M_{\odot}/M$ (Kluźniak et al. 1990).

Many models have been proposed to explain the excitation mechanism of QPOs and subsequent modulation of the X-ray signal. Among suggested mechanisms are the model of relativistic precession (Stella & Vietri 1999), the orbiting spot model (Schnittman & Bertschinger 2004), the models, where QPOs are produced by the magnetically driven resonance in a diamagnetic accretion disk (Lai 1999), the transition layer model (Titarchuk 2002) or an interesting idea of p-mode oscillations of a small accretion torus (Rezzolla et al. 2003). Also in this context, Kato (2004) discussed the resonant interaction between waves propagating in a warped disk, including their rigorous mathematical description. Comprehensive reviews of possible models and a their detailed discussions in comparison to observations are given by van der Klis (2000) and McClintock & Remillard (2003). Recently, it has been suggested that the high frequency QPOs arise from a resonance between two oscillation modes of the innermost part of the accretion disk (Kluźniak & Abramowicz 2001; Abramowicz & Kluźniak 2001). Among the reasons to believe that high frequency QPOs reflect a non-linear resonance between two oscillation modes of a disk, probably occurring only in strong-field gravity, are the $3:2$ ratio of the frequencies of the twin QPOs in black holes (Abramowicz & Kluźniak 2001; McClintock & Remillard 2003), and the sub-harmonic frequency difference between the two QPOs observed in the accreting 2.5 ms pulsar (Wijnands et al. 2003; Kluźniak et al. 2004; Lee et al. 2004). The oscillations of the fluid in an accretion disk can be easily modeled by epicyclic oscillations of a test particle on a circular orbit in equatorial plane.

In the first part of this work we study properties of nonlinear epicyclic oscillations in the vicinity of a resonance. We show that the coupling of the two modes arises naturally if we consider non-spherical but still axisymmetric gravitational field. In Chapter 1 we introduce epicyclic approach according to Chandrasekhar (1960) and Binney & Tremaine (1950). In addition, we calculate epicyclic frequencies for the gravitational field of a Newtonian or pseudo-Newtonian star surrounded by a massive ring. Finally, based on rather heuristic arguments we suggests that the periodic exchange of energy between the radial and vertical oscillation modes is a general property of epicyclic resonance. Then, in Chapter 2 we introduce the method of multiple scales according to Nayfeh & Mook

(1979). Particularly, one can easily find so called solvability conditions that determine slow behavior of amplitudes and phases of oscillations. That is why it seems to be very useful in study of a weakly nonlinear system. Next, we point to its algorithmic nature that allows us to find explicit form of the solvability conditions characteristic for all conservative two-degree-of-freedom systems. In Chapter 3 the method of multiple time scales is applied to epicyclic oscillations and properties of three epicyclic resonances, 1:2, 1:1 and 3:2 are discussed. We also show different topologies of the phase-space in the way that closely resembles the method of disturbing function familiar from the studies of the mean orbital elements in celestial mechanics (Kozai 1962). This analogy is very illuminating because it provides a systematic way of distinguishing topologically different systems. Finally, in Chapter 4 we come back to our original motivation and apply the above-given theory in the frame of the quasiperiodic oscillations.

Chapter 1

Epicyclic motion

The idea of epicyclic motion has a long-lasting history in astronomy. Indeed, elliptic trajectories of planets around the Sun were modelled in this way by Appolonius at the end of the third century B.C., as well as by Copernicus in the middle of the 16th century. Interestingly enough, this simple concept meets useful applications also in the present-day astrophysics, where it can be employed in order to grasp certain aspects of fluid oscillations near an accreting body. In the next section we will summarize basic equations describing the particle motion in terms of the epicyclic approximation. Then we embark on more advanced and perhaps even suprising approach to epicyclic resonances via multiple-scales formalism. Finally, we will discuss a general scheme of quasi-periodic oscillations, which is build on the epicyclic approximation and prides itself as being independent of any particular mechanism modulating the observed light signal – still to be discovered.

1.1 Linear epicyclic oscillations

Let us consider a motion of a test particle in an axially symmetric gravitational field of a massive body. The gravitational field is described by the potential $\Phi(r,\theta)$. We employ spherical coordinates $\{r,\phi,\theta\}$. Furthermore, we suppose that the gravitational field is symmetric with respect to the equatorial plane $\theta=\pi/2$. These assumptions are sufficient for the existence of circular orbits in the equatorial plane.

The Lagrangian of a test particle of unit mass orbiting the body reads

$$\mathcal{L}=\tfrac{1}{2}\left(\dot{r}^2+r^2\dot{\theta}^2+r^2\dot{\phi}^2\sin^2\theta\right)-\Phi(r,\theta), \tag{1.1}$$

where dots denote the derivatives with respect to time. The Lagrangian does not depend on time and the azimuthal angle, therefore two quantities, energy and angular momentum, are conserved along the particle trajectory,

$$E = \tfrac{1}{2}\left(\dot{r}^2+r^2\dot{\theta}^2+r^2\dot{\phi}^2\sin^2\theta\right)+\Phi(r,\theta), \tag{1.2}$$

$$\ell = r^2\dot{\phi}\sin^2\theta. \tag{1.3}$$

The Euler-Lagrange equations for the system are

$$\ddot{r}-r\,\dot{\theta}+\frac{\partial\Phi}{\partial r}-\frac{\ell^2}{r^3\sin^2\theta} = 0, \tag{1.4}$$

$$r^2\ddot{\theta}+2r\,\dot{r}\,\dot{\theta}+\frac{\partial\Phi}{\partial\theta}-\frac{\ell^2\cos\theta}{r^2\sin^3\theta} = 0. \tag{1.5}$$

Introducing the *effective potential*

$$\mathcal{U}(r,\theta) \equiv \Phi(r,\theta) + \frac{\ell^2}{2r^2\sin^2\theta}, \tag{1.6}$$

the governing equations take the form

$$\ddot{r} - r\dot{\theta}^2 + \frac{\partial \mathcal{U}}{\partial r} = 0, \tag{1.7}$$

$$\ddot{\theta} + 2\,\frac{\dot{r}\,\dot{\theta}}{r} + \frac{1}{r^2}\,\frac{\partial \mathcal{U}}{\partial \theta} = 0, \tag{1.8}$$

where partial derivatives are calculated keeping the angular momentum constant. With the aid of definition (1.6) equation (1.2) becomes

$$E = \tfrac{1}{2}\left(\dot{r}^2 + r^2\dot{\theta}^2\right) + \mathcal{U}(r,\theta). \tag{1.9}$$

The simplest solution of equations (1.7) and (1.8) is an equatorial circular orbit given by conditions $r = r_0 = \text{const}$ and $\theta = \pi/2$. After substitution into governing equations (1.7) and (1.8), we find

$$\left(\frac{\partial \mathcal{U}}{\partial r}\right)_0 = 0 \quad \text{and} \quad \left(\frac{\partial \mathcal{U}}{\partial \theta}\right)_0 = 0, \tag{1.10}$$

where subscript "0" refers to the point $[r_0, \pi/2]$. Hence, for a given angular momentum ℓ, the radius of the circular orbit correspond to an extreme of the effective potential. The stable and unstable orbits correspond to a maxima and minima of the effective potential. The second condition is satisfied automatically by assumed reflection symmetry with respect to the equatorial plane and the first one relates the angular momentum ℓ and the angular velocity Ω of the particle with the radius r_0,

$$\ell^2 = r_0^4\Omega^2 = r_0^3\left(\frac{\partial \Phi}{\partial r}\right)_0. \tag{1.11}$$

The energy of the particle is given by $E_0 = \mathcal{U}(r_0, \pi/2) = \mathcal{U}_0$.

An observer moving along a circular orbit measures radial, vertical and azimuthal epicyclic oscillations of particles having the same angular momentum and slightly higher energy. Suppose that the particle instantaneous position is at coordinates $[r(t), \theta(t), \phi(t)]$ and its angular momentum is ℓ. We assume that $r(t)$ and $\theta(t)$ are given by small deviations from the circular orbit that corresponds to the same angular momentum,

$$r = r_0(1 + \delta\rho), \quad \theta = \pi/2 + \delta\theta. \tag{1.12}$$

By substitution into equations (1.7) and (1.8) and expanding all terms up to the linear order in deviations $\delta\rho$ and $\delta\theta$, we arrive at governing equations of two independent harmonic oscillators

$$\delta\ddot{\rho} + \omega_r^2\delta\rho = 0 \quad \text{and} \quad \delta\ddot{\theta} + \omega_\theta^2\delta\theta = 0, \tag{1.13}$$

where the *radial* and *vertical epicyclic frequencies* are given as

$$\omega_r^2 = \left(\frac{\partial^2 \mathcal{U}}{\partial r^2}\right)_0, \quad \omega_\theta^2 = \frac{1}{r_0^2}\left(\frac{\partial^2 \mathcal{U}}{\partial \theta^2}\right)_0, \tag{1.14}$$

or in terms of the gravitational potential $\Phi(r,z)$,

$$\omega_r^2 = \left(\frac{\partial^2\Phi}{\partial r^2}\right)_0 + \frac{3}{r_0}\left(\frac{\partial\Phi}{\partial r}\right)_0, \quad \omega_\theta^2 = \frac{1}{r_0^2}\left(\frac{\partial^2\Phi}{\partial\theta^2}\right)_0 + \frac{\ell^2}{2r_0^2}. \tag{1.15}$$

The solution of equations (1.13) are sinusoidal oscillations $\delta\rho(t)$ and $\delta\theta(t)$ in the radial and vertical direction, respectively. Without loss of generality we can assume that $\delta\rho = 0$ at the time $t = 0$. Denoting the phase difference between the two oscillations as ψ, the solutions can be written as

$$\delta\rho(t) = a_\rho \cos(\omega_r t), \quad \delta\theta(t) = a_\theta \cos(\omega_\theta t + \psi). \tag{1.16}$$

By substituting the expression for radial oscillations into equation (1.3) and expanding all terms up to the linear order, we find that the particle oscillates also in the azimuthal direction,

$$\phi(t) = \phi(0) + \Omega_0 t - \frac{2\Omega_0 a_\rho}{\omega_r}\sin\omega_r t. \tag{1.17}$$

The frequency of the azimuthal epicyclic oscillations is always equal to the radial epicyclic frequency. Hence, in the linear approximation, motion of the particles following nearly circular orbits can be viewed as the motion along strictly circular orbits plus addition motion on small epicycles in the equatorial plane and independent oscillations in the vertical direction.

Equations (1.13) imply that the two epicyclic oscillators independently conserve energy. Denote δE_r and δE_θ the energy of the radial and vertical oscillations, respectively. They are given by

$$\delta E_r = \tfrac{1}{2}r_0^2\left(\delta\dot\rho^2 + \omega_r^2\delta\rho^2\right), \quad \delta E_\theta = \tfrac{1}{2}r_0^2\left(\delta\dot\theta^2 + \omega_\theta^2\delta\theta^2\right). \tag{1.18}$$

Expanding equation (1.9) up to the quadratic order in deviations $\delta\rho$ and $\delta\theta$, we find the total energy of orbiting particle as

$$E = E_0 + \delta E = E_0 + \delta E_r + \delta E_\theta, \tag{1.19}$$

where E_0 is the particle energy on the circular orbit of the same angular momentum and δE is the total energy in the epicyclic oscillations of the particle. By inserting the solutions (1.16) into equation (1.18) we find the epicyclic energy in the form

$$\delta E = r_0^2\omega_r^2\left(a_\rho^2 + \frac{\omega_\theta^2}{\omega_r^2}a_\theta^2\right). \tag{1.20}$$

1.2 Epicyclic oscillations in selected systems

1.2.1 Keplerian ellipse

Consider the well-known case of nearly circular Keplerian orbits. The source of the gravitational field is Newtonian spherically-symmetric star. The gravitational potential dependends only on the radial coordinate and it follows from the Newton gravitational law

$$\Phi(r) = -\frac{GM}{r^2}, \tag{1.21}$$

where M is the mass of the star and G is the gravitational constant.

The orbits corresponding to negative particle energy are ellipses, focuses of which coincide with the center of the star. The orbital ellipse and its orientation in the space are described by six parameters – *orbital elements*. The orbit itself is characterized by its semi-major axis a and the eccentricity e. Its position with respect to the equatorial plane is determined by two other parameters: the inclination i of the orbital plane with respect to the equatorial plane and by the argument of pericenter w (sometimes denoted as ω) that is an angle between the pericenter, where the closest approach of the particle to the star occurs, and the ascending node, where the orbit crosses the equatorial plane. The angle is measured in the orbital plane in the direction of orbital motion. The remaining two orbital parameters, the longitude of ascending node and the time of pericenter passage are not important for present discussion.

Let us consider particular orbit. Suppose that it has low eccentricity and inclination with respect to the equatorial plane, i.e. $e \ll 1$ and $i \ll 1$. We introduce a cartesian system $\{x, y, z\}$ as follows: the origin coincides with the center of the star, the z-axis is perpendicular to the equatorial plane, and the x-axis coincides with a nodal line (the intersection of the orbital and the equatorial plane). Finally, the y-axis is chosen with an appropriate orientation. Let us also introduce two azimuthal angles ϕ and φ that are measured from the x-axis to the plane that contains orbiting particle and the z-axis. The angle ϕ is measured in the equatorial plane and the angle φ is measured in the orbital plane. For small inclinations the difference $\phi - \varphi$ is of order of i^2 and up to the linear order in i we can interchange them.

Simple geometrical arguments lead to the expression for the deviation $\delta\theta(\phi)$ of the orbit from the equatorial plane,

$$\delta\theta(\phi) \approx \frac{z(\phi)}{r(\phi)} = \sin\varphi \sin i \approx i \sin\phi. \tag{1.22}$$

The ellipse polar equation gives the dependence $r(\phi)$,

$$r(\phi) = \frac{p}{1 + e\cos(\varphi + w)} \approx p\left[1 - e\cos(\phi + w)\right], \tag{1.23}$$

where $p \equiv a(1 - e^2)$ is the parameter of the ellipse.

On the other hand, using equations (1.11) and (1.14), we find that all three frequencies Ω, ω_r and ω_θ are equal,

$$\omega_r = \omega_\theta = \Omega = \sqrt{\frac{GM}{r^3}}. \tag{1.24}$$

Then, with the aid of equation (1.16)–(1.17) the expressions for the particle instantaneous position reads

$$\begin{aligned} \phi(t) &= \tilde{\phi} + \Omega t - 2a_\rho \sin(\Omega_0 t), & (1.25)\\ r(t) &= r_0\left[1 + a_\rho \cos(\Omega t)\right], & (1.26)\\ \delta\theta(t) &= a_\theta \cos(\Omega t + \psi), & (1.27) \end{aligned}$$

where $\tilde{\phi} \equiv \phi(0)$ is the azimuthal angle at the time $t = 0$.

Neglecting the oscillating term, we express Ωt from equation (1.25) and substitute it into equations (1.26) and (1.27). Then, changing the independent variable from t to ϕ we obtain expressions

$$\begin{aligned} r(\phi) &= r_0\left[1 + a_\rho \cos(\phi - \tilde{\phi})\right], & (1.28)\\ \delta\theta(\phi) &= a_\theta \cos(\phi - \tilde{\phi} + \psi) & (1.29) \end{aligned}$$

that are correct up to the linear order in amplitudes a_ρ and a_θ.

Comparing equation (1.23) with (1.28) and equation (1.22) with (1.29) we find

$$a_\rho = e, \quad a_\theta = i, \quad \psi = \pi/2 - w, \quad r_0 = a(1-e^2). \tag{1.30}$$

Expressions (1.30) gives a physical meaning of quantities characterizing epicyclic oscillations: the relative amplitude of radial oscillations a_ρ and the amplitude of the vertical oscillations a_θ equal the eccentricity and the inclination of the elliptical orbit. The phase difference is connected to the argument of pericenter.

1.2.2 Strong gravity

The strong gravitational fields close to black holes and very compact stars call for use of general relativity. However, if we are interested only in qualitative properties of relativistic orbits, the effects of strong gravity can be modelled using the pseudo-Newtonian gravitational potential firstly introduced by Paczyński & Wiita (1980),

$$\Phi(r) = -\frac{GM}{r - R_\mathrm{S}}, \tag{1.31}$$

where $R_\mathrm{S} \equiv 2GM/c^2$ is Schwarzschild gravitational radius of the source of gravity. In general relativity mass of the central body itself provides natural length scale.

Substituting this potential into equations (1.11) and (1.14), we calculate the orbital frequency and the radial and vertical epicyclic frequencies as (see Figure 1.1)

$$\omega_r^2 = \frac{GM(r-3R_\mathrm{S})}{r(r-R_\mathrm{S})^3}, \quad \omega_\theta^2 = \Omega_0^2 = \frac{GM}{r(r-R_\mathrm{S})^2}. \tag{1.32}$$

The fact that vertical epicyclic frequency equals the orbital frequency is connected to the spherical symmetry of the gravitational field: the orbits are planar because any of them can be equally considered as equatorial. The radial epicyclic frequency is always smaller than the latter two and it vanishes at radius $r = 3R_\mathrm{S}$. Bellow this radius we have $\omega_r^2 < 0$ – the radial epicyclic oscillations are not possible anymore and circular orbits are unstable. We note that this radius agrees with the location of the marginally stable circular orbit above Schwarzschild black hole.

1.2.3 Epicyclic frequencies close to a massive ring

As an example of a nonspherical gravitational field we consider a system that constitutes of a star and a massive equatorial ring. Let the mass of the star be M and that of the ring m. We assume that the ring radius is a. The axial and reflection symmetries of the system assure the existence of equatorial circular orbits. The total gravitational field acting on orbiting particles is given by a superposition of the spherically-symmetric potential of the star $\Phi_\mathrm{s}(r)$ and the axisymmetric potential $\Phi_\mathrm{r}(r,\theta)$ of the ring,

$$\Phi(r,\theta) = \Phi_\mathrm{s}(r) + \Phi_\mathrm{r}(r,\theta). \tag{1.33}$$

We employ the standard spherical coordinates $\{r,\theta,\phi\}$ origin of which coincides with the center of the star. The potential of the ring is given by

$$\Phi_\mathrm{r}(r,\theta) = -\int_0^{2\pi} \frac{G\lambda a \mathrm{d}\phi}{R(\phi)} = -\frac{Gm}{\pi}\int_0^{\pi} \frac{\mathrm{d}\phi}{\sqrt{r^2+a^2-2ar\sin\theta\cos\phi}}, \tag{1.34}$$

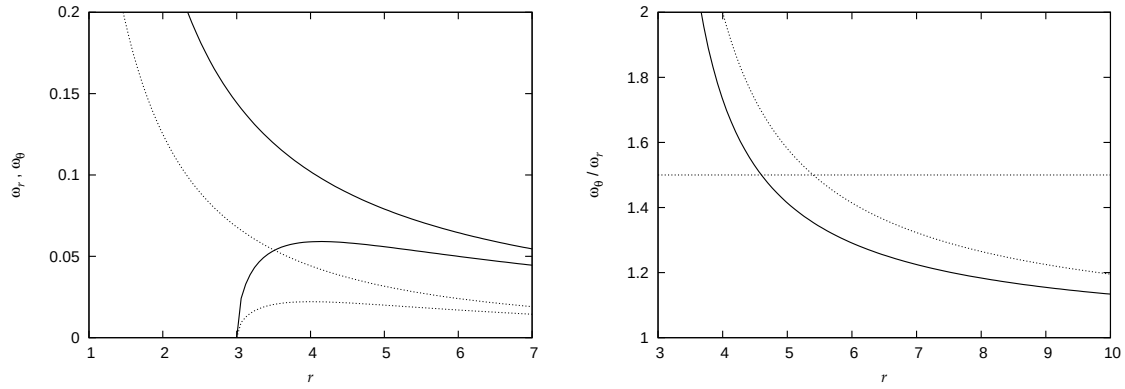

Figure 1.1: Left: The radial and vertical epicyclic frequencies in the vicinity of a compact relativistic object calculated using pseudo-Newtonian potential (solid lines). For reference, a result of general relativistic calculations for Schwarzschild black hole of same mass is also shown (dotted line). Right: The ratio of vertical and radial epicyclic frequencies. The radius is in units of $R_{\rm S}$ and frequencies are in units of c^3/GM.

where $\lambda = m/2\pi a$ is the length density of the ring mass and $R(\phi)$ is a distance between the point, where the potential is calculated, and a point on the ring at azimuthal angle ϕ. This integral can be expressed in terms of complete elliptical integral of the first kind K. We obtain

$$\Phi_{\rm r}(r,\theta) = -\frac{2Gm}{\pi}\frac{K(k)}{B^{1/2}}, \tag{1.35}$$

where $B(r,\theta) \equiv r^2 + a^2 + 2ar\sin\theta$ and $k(r,\theta) \equiv 4ar\sin\theta/B(r)$.

The total gravitational potential can be expressed in an uniform way as

$$\Phi(r,z) = -\frac{GM}{\tilde{r}} - \frac{2Gm}{\pi}\frac{K(k)}{B^{1/2}}, \tag{1.36}$$

where we substitute $\tilde{r} = r$ or $\tilde{r} = r - R_{\rm S}$ in the case of a Newtonian or of a pseudo-Newtonian star, respectively. The angular momentum of test particles orbiting the central star along equatorial circular orbits can be calculated using equation (1.11). Substituting the potential (1.36), we obtain

$$\ell(r) = GMr\left[\frac{r^2}{\tilde{r}^2} + \mu r\frac{(r+a)E(k_0) + (r-a)K(k_0)}{\pi(r^2-a^2)}\right], \tag{1.37}$$

where E is the complete elliptical integral of the second kind and $k_0 \equiv k(r,\pi/2)$. Finally, we introduced the ratio of masses $\mu \equiv m/M$. Figure 1.2 captures typical behavior of angular momenta in both, the Newtonian and the pseudo-Newtonian case. According to Rayleigh criteria the equatorial circular orbits are unstable in regions, where angular momentum decreases. This occurs close to the ring, where the ring gravity causes radial epicyclic oscillations unstable.

The orbital frequency follows from equation (1.11),

$$\Omega^2(r) = \frac{GM}{r^3}\left[\frac{r^2}{\tilde{r}^2} + \mu r\frac{(r+a)E(k_0) + (r-a)K(k_0)}{\pi(r^2-a^2)}\right], \tag{1.38}$$

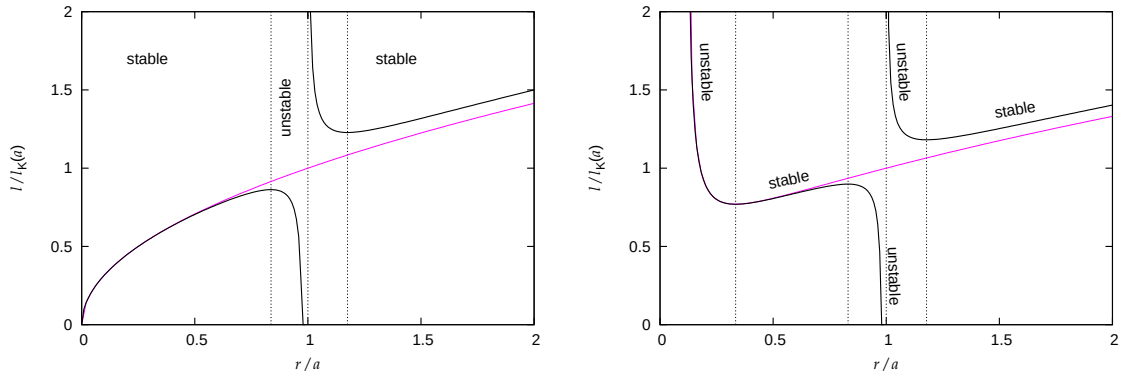

Figure 1.2: The angular momentum (thick line) of the test particle moving in the combined gravitational field of the star and ring along the circular orbit. The left and right panel correspond to the case of a Newtonian and pseudo-Newtonian central star, respectively. The ratio of masses is $\mu = 0.1$. The radial coordinate is rescalled by the radius a of the ring. In the latter case we choose $a = 9R_S$. The Keplerian angular momentum ℓ_K for solely star gravitational field is also shown (thin line) for reference. Angular momentum is rescaled by $\ell_K(a)$ in both cases. The circular orbits are unstable in regions where angular momentum decreases according to Rayleigh criteria. The epicyclic approximation of a particle motion is possible only in regions of stable circular orbits.

and the radial and vertical epicyclic frequencies can be calculated using equation (1.14). We obtain

$$\omega_r^2(r) = \frac{GM}{r^3}\left[\frac{r^2(3\tilde{r}-2r)}{\tilde{r}^3} + \frac{2\mu}{\pi}\frac{(r-a)^2K(k_0)-a^2E(k_0)}{r^2(r-a)^2(r+a)}\right], \tag{1.39}$$

$$\omega_\theta^2(r) = \frac{GM}{r^3}\left[\frac{r^2}{\tilde{r}^2} + \frac{2\mu}{\pi}\frac{E(k_0)}{(r-a)^2(r+a)}\right]. \tag{1.40}$$

The epicyclic frequencies as functions of radius are plotted in Figure 1.3. The radial epicyclic frequency is defined only in regions of stable circular orbit and it is smaller between the ring and the central object than in absence of the ring because the radial components of gravitational force of the ring and of the star act against. On the other hand, the vertical epicyclic frequency greater than in the case without the ring because the vertical components of the gravitational force acts together.

In close vicinity of the ring and the central object the vertical epicyclic frequency diverges: circular orbits are stable when perturbed vertically, however they are unstable with respect to radial perturbations.

The approach of epicyclic oscillations is also usefull for qualitative discussion of properties of orbit. The difference of a radial epicyclic frequency and the orbital frequency gives us the angular velocity of pericenter shift and the difference of vertical epicyclic and orbital frequency gives the frequency of nodal precession. The expressions (1.38), (1.39) and (1.40) illustrate that the nodal precession is connected to a nonsphericity of the gravitational field (the lowest-order term in the difference $\Omega - \omega_\theta$ is proportional to μ).

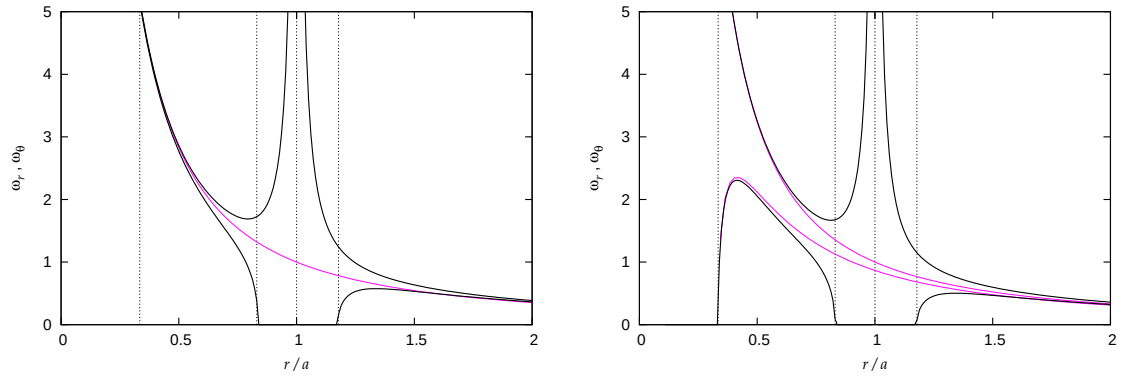

Figure 1.3: The radial and vertical epicyclic frequencies (thick line) of a test particle moving in the gravitational field of a star and ring. The left and right panel show the case of a Newtonian and pseudo-Newtonian central star, respectively. The parameters are chosen in the same way as in Figure 1.2. Epicyclic frequencies in absence of the ring are also shown (thin line).

1.3 Nonlinear effects

The linear theory of epicyclic oscillations captures many essential features characteristic for orbits that are not too different from circular, like pericenter advance and nodal precession. It is valid as long as the deviations δr and $\delta\theta$ from the circular orbits are small and the nonlinear terms in equations of motion can be neglected. However in some, rather specific cases the nonlinear dynamics should not be ignored at all. In those cases, the epicyclic oscillations are strongly influenced by nonlinear terms.

The equations governing orbital motion, (1.7) and (1.8), can be expressed in the particular form with the linear terms on the left-hand side and the nonlinear on the other one,

$$\delta\ddot{\rho} + \omega_r^2\delta\rho = (1+\delta\rho)\delta\dot{\theta} - \left[\frac{1}{1+\delta\rho}\frac{\partial\mathcal{U}}{\partial r} - \omega_r^2\delta\rho\right], \tag{1.41}$$

$$\delta\ddot{\theta} + \omega_\theta^2\delta\theta = 2\frac{\delta\dot{\rho}\delta\dot{\theta}}{1+\delta\rho} - \left[\frac{1}{(1+\delta\rho)^2}\frac{\partial\mathcal{U}}{\partial\theta} - \omega_\theta^2\delta\theta\right]. \tag{1.42}$$

A suggestive example of nonlinear behavior of orbiting particles has been given by Kluźniak & Abramowicz (2002). Let us take the nonlinear equations of motion and start with purely radial epicyclic oscillations. If the amplitude a_ρ is small, the oscillations have the sinusoidal form $\delta\rho(t) = a_\rho\cos(\omega_r t)$ in accordance with the linear theory. In the equation for vertical oscillations we keep also the nonlinear term proportional to $\delta\rho\delta\theta$ that appears in the Taylor expansion of the right hand side. Then the equation governing vertical oscillations becomes

$$\delta\ddot{\theta} + \omega_\theta^2\left[1 + \kappa a_\rho\cos(\omega_r t)\right]\delta\theta = 0, \tag{1.43}$$

where κ arises as a coefficient of the Taylor expansion. Equation (1.43) is the famous Mathieu equation for which it is known that the solution $\delta\theta = 0$ is unstable if the frequencies ω_r and ω_θ satisfy $\omega_r/\omega_\theta \approx n/2$ with $n = 1, 2, 3...$ (Landau & Lifshitz 1969; Nayfeh & Mook 1979). In that case, referred to as the *parameteric resonance*, the amplitude of vertical oscillations exponentially grows on the time scale proportional to $(\kappa a_\rho)^n$. Suppose that

there is a particular radius where the ratio of epicyclic frequencies equals 1:2. According to the Mathieu equation a small vertical perturbation of the orbit in vertical direction (that is always present) would lead to exponential grow of the amplitude of vertical oscillations.

However, what provides the energy for the exponential grow? In fact, the energy source are radial oscillations, the energy of which is transfered into the vertical mode by parametric resonance. In this example, we did not consider any influence of the vertical oscillations on the radial ones.

Actually, one can consider directly opposite mechanism. If, vice versa, we start with small vertical excursion from the equatorial plane, the oscillations of the particle are given as $\delta\theta = a_\theta \cos(\omega_\theta t)$. The Taylor expansion of the nonlinearities in equation (1.42) contains the term proportional to $\delta\theta^2$. Keeping this term on the right-hand side, we get

$$\delta\ddot{\rho} + \omega_\theta^2 \delta\rho = \lambda a_\theta^2 \cos^2(\omega_\theta t) = \tfrac{1}{2}\lambda a_\theta^2 \left[1 + \cos(2\omega_\theta t)\right]. \tag{1.44}$$

This equations describes a driven harmonic oscillator, natural frequency of which is ω_r and the frequency of forcing is $2\omega_\theta$. The resonant condition gives us the same resonance as Mathieu equation however in this case the radial mode of oscillations is resonantly excited by the vertical one.

Because the epicyclic oscillator described by equations (1.41) and (1.42) conserves energy, the grows of energy of one mode must be accompanied by the energy loss of the other mode. Hence, we expect that close to the radii where the two epicyclic frequencies are in a ratio of small integers the periodic exchange of energy between the two modes of oscillations occurs.

We note that this behavior is characteristic for systems with *internal* or *autoparametric resonance*. One particular example of such system is a spring pendulum whose eigenfrequencies are in rational ratio.

Regarding the results of section 1.2.1, the internal resonance in epicyclic oscillators has an interesting consequences. Since the amplitude of the radial and vertical epicyclic oscillations are connected to the eccentricity and inclination of the particle orbit. we expect that close to radii, where the epicyclic frequencies are in rational ratios, periodic exchange of energy between radial and vertical epicyclic oscillations may occur. The orbit of particles switches between highly-inclined and nearly-circular to highly-eccentric and nearly equatorial.

t has been shown by Abramowicz et al. (2003), Rebusco (2004) that, the nonlinear coupling between the radial and vertical epicyclic oscillations may lead to the epicyclic resonance occurring close to the radii where the two epicyclic frequencies are comersuable. In the two papers, the two modes were coupled by introducing additional nonlinear force acting on the particle whose form was chosen ad-hoc and whose strength was parameterized by a single parameter α. Natural consequence of nonlinear coupling is that the observed frequencies of oscillations are shifted with respect to the epicyclic frequencies. The frequency shift depends on the strength of the coupling and on the amplitudes of oscillations. By setting various initial amplitudes or the strength of the coupling, the authors were able to fit the correlation between the two kilohertz frequencies observed in Sco X-1.

In what follows, we study properties of orbital motion in general axisymmetric gravitational field in the case when internal ("epicyclic") resonance occurs. This part of work was strongly influenced by earlier results of Rebusco (2004), who considered orbital motion in Schwarzschild space-time with additional ad-hoc coupling of vertical and radial

oscillations and inferred many interesting properties of nonlinear oscillations of such system. Namely, she derived corrections of the observed frequencies to eigenfrequencies of the system and found spectrum of possible resonances. In this work the coupling appears naturally by assuming non-spherical (but still axisymmetric) gravitational field. We further generalize her approach to the case of the energy exchange that is charactiristic for internal resonance. The nonlinear dynamics of the epicyclic oscillator will be treated in framework of multiple-time scales (Nayfeh & Mook 1979) that is introduced in the next section. The theory will be immediately illustrated by examples of epicyclic resonances in the gravitational field of the both the Newtonian and pseudo-Newtonian star and the massive disk.

Chapter 2

Multiple scales

2.1 Nonlinear oscillations

Let us consider the case of small but finite oscillations of a single-degree-of-freedom system with quadratic nonlinearity governed by equation

$$\ddot{x} + \omega^2 x = \alpha\omega^2 x^2. \tag{2.1}$$

The strength of the nonlinearity is parameterized by constant α. If one neglect the right-hand side of equation (2.1) one obtains governing equation of the corresponding linear system. It plays a key role in the analysis of weakly nonlinear systems. Basically the response of the nonlinear system can be found by perturbing the response of the corresponding linear system. Hence, we seek a perturbation expansion of the form

$$x(t,\epsilon) = \epsilon x_1(t) + \epsilon^2 x_2(t) + \epsilon^3 x_3(t) + \mathcal{O}(\epsilon^4), \tag{2.2}$$

The expansion parameter ϵ expresses the order of amplitude of oscillations. The main advantage of this approach is that, although the original equation is nonlinear, we solve linear equations in each step. For a practical purpose we require this expansion to be uniformly convergent for all times of interest. In that case the higher-order terms are small compared to lower-order terms and a sufficient approximation is reached concerning a finite number of terms. The expansion (2.2) can represent a periodic solution as well as an unbounded solution with exponential grow. The uniformity of the expansion means that the higher-order terms provide only small correctins to the lower-order ones. Mathematically, this requirement is equivalent to the condition

$$\lim_{t\to\infty} \frac{x_{k+1}(t)}{x_k(t)} < \infty, \quad k \in \mathcal{N}. \tag{2.3}$$

We substitute expansion (2.2) into governing equation (2.1) and, since x_k is independent of ϵ, we equate coefficients of corresponding powers of ϵ on both sides. This leads to the following system of equations

$$\begin{aligned} \ddot{x}_1 + \omega^2 x_1 &= 0, & (2.4)\\ \ddot{x}_2 + \omega^2 x_2 &= \alpha\omega^2 x_1^2, & (2.5)\\ \ddot{x}_3 + \omega^2 x_3 &= 2\alpha\omega^2 x_1 x_2. & (2.6) \end{aligned}$$

The general solution of equation (2.4) can be written in the form $x_1(t) = Ae^{\mathrm{i}\omega t} + \mathrm{cc}$, where cc denotes complex conjugation. The complex constant A contains information about the

initial amplitude and phase of oscillations. Substituting this solution into equation (2.5) we find linear equation for the first approximation $x_2(t)$

$$\ddot{x}_2 + \omega^2 x_2 = \alpha\omega^2 \left(A^2 e^{2\mathrm{i}\omega t} + |A|^2 \right) + \mathrm{cc}. \tag{2.7}$$

A general solution consists of the solution of the homogeneous equation and a particular solution,

$$x_2(t) = A_2 e^{\mathrm{i}\omega t} - \alpha \left(\frac{1}{3} A_1^2 e^{2\mathrm{i}\omega t} - |A_1|^2 \right) + \mathrm{cc}, \tag{2.8}$$

where A_1 denotes a constant A in the solution of equation (2.4). Therefore, the solution of governing equation up to the second order is given by

$$x(t) = \left(\epsilon A_1 + \epsilon^2 A_2 \right) e^{\mathrm{i}\omega t} - \alpha \left(\frac{1}{3} A_1^2 e^{2\mathrm{i}\omega t} - |A_1|^2 \right) + \mathrm{cc}. \tag{2.9}$$

In fact, there are two possible ways to satisfying general initial conditions $x(0) = \epsilon x_0$ and $\dot{x}(0) = \epsilon \dot{x}_0$ imposed on equation (2.1). The first one is to compare them with the general solution (2.9) and find constants A_1, A_2. This procedure should be repeated in each order of approximation, which involves a tedious algebra especially in higher orders. The second, equivalent and apparently much easier way is to include only particular solutions to the higher approximations and treat the constant A as a function of ϵ with expansion $A = A_1 + \epsilon A_2 + \ldots$. Then, given initial conditions are satisfied by expanding the solution for x_1 via ϵ and choosing the coefficients A_n appropriately.

According to this discussion we express the solution of equation (2.7) as

$$x_2(t) = -\alpha \left(\frac{1}{3} A^2 e^{2\mathrm{i}\omega t} - |A|^2 \right) + \mathrm{cc}. \tag{2.10}$$

Substituting x_1 and x_2 into (2.6) we obtain

$$\ddot{x}_3 + \omega^2 x_3 = \frac{2\alpha^2\omega^2}{3} \left(5A|A|^2 e^{\mathrm{i}\omega t} - A^3 e^{3\mathrm{i}\omega t} \right) + \mathrm{cc}. \tag{2.11}$$

Since the right-hand side of this equation contains the term proportional to $e^{\mathrm{i}\omega t}$, any solution must contain a secular term proportional to $te^{\mathrm{i}\omega t}$, which becomes unbounded as $t \to \infty$. This fact has nothing to do with true physical behavior of the system for large times. The reason is purely mathematical: starting from time when $(\omega t) \sim 1/(\epsilon\alpha)$, the higher-order approximation x_3, which contains the secular term, does not provide only a small correction to x_1 and x_2, and the expansion (2.2) becomes singular. Physically, the presence of the secular term in the third order reflects very general feature of nonlinear oscillations – dependence of the observed frequency on the actual amplitude. For larger amplitudes the actual frequency of oscillations differs from the eigenfrequency ω and the higher-order terms in the expansion (2.2) – always oscillating with an integer multiples of ω – must quickly increase as time grows.

2.2 The method of multiple scales

Is it possible to find an expansion representing a solution of equation (2.1) which is uniformly valid even for larger time than $\sim \epsilon^{-1}$? The answer is positive, if one considers more general form of the expansion than equation (2.2). In the *method of multiple scales*

(Nayfeh & Mook 1979) more general dependence of coefficients x_i on the time is reached by introducing several time scales T_μ, instead of a single physical time t. The time scales are introduced as

$$T_\mu \equiv \epsilon^\mu t, \quad \mu = 0, 1, 2 \ldots \tag{2.12}$$

and they are treated as independent. It follows that instead of the single time derivative we have an expansion of partial derivatives with respect to T_μ

$$\frac{d}{dt} = D_0 + \epsilon D_1 + \epsilon^2 D_2 + \epsilon^3 D_3 + \mathcal{O}(\epsilon^4), \tag{2.13}$$

$$\frac{d^2}{dt^2} = D_0^2 + 2\epsilon D_0 D_1 + \epsilon^2(D_1^2 + 2D_0 D_2) + 2\epsilon^3(D_0 D_3 + D_1 D_2) + \mathcal{O}(\epsilon^4), \tag{2.14}$$

where $D_\mu = \partial/\partial T_\mu$.

We assume that the solution can be represented by an expansion having the form

$$x(t, \epsilon) = \epsilon x_1(T_\mu) + \epsilon^2 x_2(T_\mu) + \epsilon^3 x_3(T_\mu) + \mathcal{O}(\epsilon^4). \tag{2.15}$$

The number of time scales is always the same as the order at which the expansion is truncated. We carry out the expansion to the third order and thus first three scales T_0, T_1 and T_2 are sufficient.

Substituting equations (2.14) and (2.15) into the governing equation (2.1) and equating the coefficients of ϵ, ϵ^2 and ϵ^3 to zero we obtain

$$(D_0^2 + \omega^2)x_1 = 0, \tag{2.16}$$

$$(D_0^2 + \omega^2)x_2 = -2D_0 D_1 x_1 + \alpha\omega^2 x_1^2, \tag{2.17}$$

$$(D_0^2 + \omega^2)x_3 = -2D_0 D_1 x_2 - D_1^2 x_1 - 2D_0 D_2 x_1 + \alpha\omega^2 x_1 x_2. \tag{2.18}$$

Note that although these equations are more complicated than (2.4)–(2.6), they are still linear and can be solved successively. The solution of equation (2.16) is the same as the solution of the corresponding linear system, the only difference is that constant A now generally depends on other scales

$$x_1 = A(T_1, T_2)e^{\mathrm{i}\omega T_0} + \text{cc}. \tag{2.19}$$

Substituting x_1 into equation (2.17) we obtain

$$(D_0^2 + \omega^2)x_2 = -2\mathrm{i}\omega(D_1 A)e^{\mathrm{i}\omega T_0} + \alpha\omega^2\left(A^2 e^{2\mathrm{i}\omega T_0} + |A|^2\right) + \text{cc}. \tag{2.20}$$

The first term on the right-hand side implies the presence of a secular term in the second-order approximation which causes non-uniformity of the expansion (2.15). However, in case of the method of multiple scales these terms can be eliminated by imposing additional conditions on the function $A(T_\mu)$. These conditions are sometimes called conditions of solvability or conditions of consistency. In fact, the reason why the same number of scales as the order of approximation is needed is that one secular term gets eliminated in each order, and therefore the function $A(T_\mu)$ is specified by the same number of solvability conditions as the number of its variables.

The secular term is eliminated if we require $D_1 A = 0$. Hence, in further discussion we assume that A is a function of T_2 only. A particular solution of equation (2.20) is

$$x_2(t) = -\alpha\left(\frac{1}{3}A^2(T_2)e^{2\mathrm{i}\omega T_0} - |A(T_2)|^2\right) + \text{cc}. \tag{2.21}$$

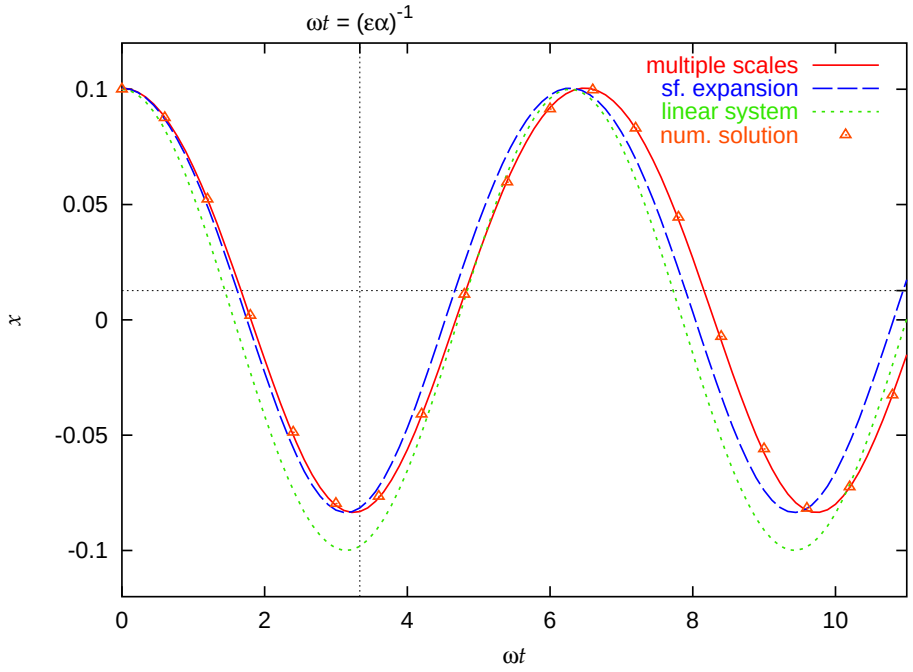

Figure 2.1: Oscillations of a system with quadratic nonlinearity are governed by equation (2.1). We compare results of the multiple scales method (solid curve), a simple straightforward expansion method (dashed curve) and the direct numerical integration of the governing equation (points). The initial condition is $x(0) = 0.1$, $\dot{x}(0) = 0$ and the strength of nonlinearity is $\alpha = 3$. The horizontal dotted line shows the shifted "equilibrium position" and the vertical one denotes the value $(\omega t) = (\epsilon\alpha)^{-1}$ at which the straightforward expansion becomes nonuniform. The solution corresponding to the linear system is also shown (dotted curve).

Using the condition $D_1 A = 0$ equation (2.18) takes much simpler form

$$(D_0^2 + \omega^2)x_3 = -\left(2\mathrm{i}\omega D_2 A + \frac{10\alpha^2\omega^2}{3}A|A|^2\right)e^{\mathrm{i}\omega T_0} - \frac{2\alpha^2\omega^2}{3}A^3 e^{3\mathrm{i}\omega T_0} + \mathrm{cc}. \tag{2.22}$$

The secular term is eliminated equating the terms in the bracket to zero

$$2\mathrm{i}\omega D_2 A + \frac{10\alpha^2\omega^2}{3}A|A|^2 = 0. \tag{2.23}$$

This additional condition fully determines (excepting initial conditions) time behavior of function $A(T_2)$. Let us write it in the polar form $A = \frac{1}{2}\tilde{a}e^{\mathrm{i}\phi}$ and then separate real and imaginary parts. We obtain

$$D_2\tilde{a} = 0 \quad \text{and} \quad D_2\phi = -\frac{5\alpha^2}{12}\omega\tilde{a}^2. \tag{2.24}$$

The solutions of these equations are

$$\tilde{a} = \tilde{a}_0 \quad \text{and} \quad \phi = -\frac{5}{12}\alpha^2\tilde{a}_0^2\omega T_2 + \phi_0, \tag{2.25}$$

where $\tilde{a}_0$ and ϕ_0 are constants which are determined from the initial conditions.

It follows from equation (2.19) that $A(T_2)$ slowly modulates the amplitude and the phase of oscillations. Since $\tilde{a}$ is constant, the amplitude is constant all the time. Since ϕ depends on $T_2 = \epsilon^2 t$ linearly, also the observed frequency of the oscillations is constant, but not equal to the eigenfrequency ω.

Substituting equations (2.25) and (2.21) into (2.15), we obtain solution of equation (2.1) up to the second order

$$x(t) = a_0 \cos(\omega^\star t + \phi_0) - \frac{\alpha}{6} a_0^2 \cos[2(\omega^\star t + \phi_0)] + \frac{\alpha}{2} a_0^2 + \mathcal{O}(a_0^3), \tag{2.26}$$

where $a_0 = \epsilon \tilde{a}_0 \ll 1$ and $\omega^\star$ is the observed frequency of oscillation given by

$$\omega^\star = \omega \left(1 - \frac{5\alpha^2}{12} a_0^2 \right). \tag{2.27}$$

The leading term of the expansion (2.26) describes oscillations with frequency close to eigenfrequency of the system. Both, the amplitude and the frequency are constant in time, but they are not independent (as in the linear approximation). The frequency correction given by equation (2.27) is proportional to the square of the amplitude. This fact is sometimes called the amplitude-frequency interaction and – as was mentioned above – it causes the non-uniformity of the expansion (2.2) (see Figure 2.1).

The second term oscillates with twice as large frequency and provides the second-order correction to the leading term. The presence of higher harmonics in the power-spectra of oscillations strongly points to the nonlinear nature of the phenomenon.

Finally, the third term describes constant shift from the equilibrium position and is related to the asymmetry of the potential energy about the point $x = 0$. In the linear analysis, this effect is not present because the potential energy depends on x^2, and therefore it is symmetric with respect to the point $x = 0$. Hence, this drift is the third characteristic feature of nonlinear oscillations.

2.3 A conservative two-degrees-of-freedom system

So far, we have studied oscillations of a one-degree-of-freedom system. However if the system contains two or more degrees of freedom additional phenomena called *internal resonances* may occur. In this section we carry out a multiple-scales expansion of a general conservative system having two degrees of freedom, the coordinate perturbations $\delta\rho$ and $\delta\theta$. The oscillations are described by two coupled differential equations of a very general form

$$\ddot{\delta\rho} + \omega_r^2 \, \delta\rho = f_\rho(\delta\rho, \delta\theta, \dot{\delta\rho}, \dot{\delta\theta}), \tag{2.28}$$

$$\ddot{\delta\theta} + \omega_\theta^2 \, \delta\theta = f_\theta(\delta\rho, \delta\theta, \dot{\delta\rho}, \dot{\delta\theta}). \tag{2.29}$$

We suppose that the functions f_ρ and f_θ are nonlinear, i.e., their Taylor expansions start with the second order. Further assumption is that these functions are invariant under reflection of time (i.e., the Taylor expansion does not contain odd powers of time derivatives of $\delta\rho$ and $\delta\theta$). Later, we show that the energy is conserved in the system that satisfies this condition. Many authors studied such systems with a particular form of functions f_ρ and f_θ (see Nayfeh & Mook 1979 and references therein), also equations (1.41) and (1.42) governing the epicyclic oscillations represents one example.

The expansion is similar to that of the one-degree-of freedom system in many respects. We seek the solutions of equations (2.28) and (2.29) in the form of the series

$$\delta\rho(t,\epsilon) = \sum_{n=1}^{4} \epsilon^n \rho_n(T_\mu), \quad \delta\theta(t,\epsilon) = \sum_{n=1}^{4} \epsilon^n \theta_n(T_\mu), \tag{2.30}$$

where $T_\mu = \epsilon^\mu t$ are independent time scales. We will finish the discussion in the fourth order, hence the first four scales ($\mu = 0, 1, 2, 3$) are sufficient, however, it is possible to proceed to higher orders in a similar way. Then, we expand the time derivatives according to equations (2.13) and (2.14) and we equate terms of the same order in ϵ on both sides of expanded equations.

2.3.1 First order

In the first order we obtain equations corresponding to the independent harmonic oscillators,

$$(D_0^2 + \omega_r^2)\rho_1 = 0, \quad (D_0^2 + \omega_\theta^2)\theta_1 = 0. \tag{2.31}$$

The solutions can be expressed in the form

$$\rho_1 = \widehat{A}_\rho + \widehat{A}_{-\rho}, \quad \theta_1 = \widehat{A}_\theta + \widehat{A}_{-\theta}, \tag{2.32}$$

where we introduce the notation $\widehat{A}_x \equiv A_x e^{\mathrm{i}\omega_x T_0}$, $\widehat{A}_{-x} = A_x^* e^{-\mathrm{i}\omega_x T_0}$, and $x = \rho$ or θ, respectively. The complex amplitudes A_x generally depend on the slower time-scales T_1, T_2, T_3.

2.3.2 Second order

In the second order, the terms proportional to ϵ^2 in the expanded left-hand side of governing equations (2.28) or (2.29) are

$$\left[\ddot{\delta x} + \omega_x^2 x\right]_2 = (D_0^2 + \omega_x^2)x_2 + 2\mathrm{i}\omega_x D_1 \widehat{A}_x - 2\mathrm{i}\omega_x D_1 \widehat{A}_{-x}, \tag{2.33}$$

On the right-hand side there are second-order terms of the Taylor expansion of the nonlinearity $f_x(\delta\rho, \delta\theta, \dot{\delta\rho}, \dot{\delta\theta})$, with ρ_1, θ_1, $D_0\rho_1$ and $D_0\theta_1$ in the place of $\delta\rho$, $\delta\theta$, $\dot{\delta\rho}$ and $\dot{\delta\theta}$, respectively. The second-order terms on the right-hand sides can be expressed as linear combinations of quadratic terms constructed from $\widehat{A}_{\pm\rho}$ and $\widehat{A}_{\pm\theta}$. This can be written as

$$\left[f_x(\delta\rho, \delta\theta, \dot{\delta\rho}, \dot{\delta\theta})\right]_2 = \sum_{|\alpha|=2} C_\alpha^{(x)} \widehat{A}_{-\rho}^{\alpha_1} \widehat{A}_\rho^{\alpha_2} \widehat{A}_{-\theta}^{\alpha_3} \widehat{A}_\theta^{\alpha_4}, \tag{2.34}$$

where $\alpha = (\alpha_1, \ldots, \alpha_4)$ and $|\alpha| = \alpha_1 + \ldots + \alpha_4$. The constants $C_\alpha^{(x)}$ are given by angular frequencies of ω_x and by coefficients of the Taylor expansion of the functions f_x. The coefficients to which terms with a time derivative contributes, are generally complex because derivating the first order solutions with respect to T_0 is equivalent to multiplying them by coefficient $\mathrm{i}\omega_x$, However, if we suppose that the Taylor expansion does not contain odd powers of time derivatives, all of the coefficients $C_\alpha^{(x)}$ must be real.

Equating right-hand sides of equations (2.33) and (2.34) we find

$$(D_0^2 + \omega_x^2)x_2 = -2\mathrm{i}\omega_x D_1 \widehat{A}_x + 2\mathrm{i}\omega_x D_1 \widehat{A}_{-x} + \sum_{|\alpha|=2} C_\alpha^{(x)} \widehat{A}_{-\rho}^{\alpha_1} \widehat{A}_\rho^{\alpha_2} \widehat{A}_{-\theta}^{\alpha_3} \widehat{A}_\theta^{\alpha_4}. \tag{2.35}$$

$\omega_\theta : \omega_r$	**Secular terms**
Outside resonance	$-2\mathrm{i}\omega_r D_1 \widehat{A}_\rho$ $-2\mathrm{i}\omega_\theta D_1 \widehat{A}_\theta$
$1:2$	$-2\mathrm{i}\omega_r D_1 \widehat{A}_\rho,\ \ \mathrm{K}_{1001}\widehat{A}_{-\rho}\widehat{A}_\theta$ $-2\mathrm{i}\omega_\theta D_1 \widehat{A}_\theta,\ \ \Lambda_{0200}\widehat{A}_\rho^2$
$2:1$	$-2\mathrm{i}\omega_r D_1 \widehat{A}_\rho,\ \ \mathrm{K}_{0002}\widehat{A}_\theta^2$ $-2\mathrm{i}\omega_\theta D_1 \widehat{A}_\theta,\ \ \Lambda_{0110}\widehat{A}_\rho\widehat{A}_{-\theta}$

Table 2.1: Possible resonances and secular terms in the second order of approximation. For a simpler notation, we introduce $\Lambda_\alpha \equiv C_\alpha^{(\rho)}$ and $\mathrm{K}_\alpha \equiv C_\alpha^{(\theta)}$. The first record is related to the case when the system is far from any listed resonance. In this case only regular secular terms are present. The first and the second row in the record of each resonance is related to the equation for the radial and vertical oscillations, respectively.

The right-hand side of equation (2.35) contains one secular term $2\mathrm{i}\omega_x D1\widehat{A}_{-x}$ independently of the eigenfrequencies ω_r and ω_θ. However, in some particular cases, additional secular terms appear. For example, when $\omega_r \approx 2\omega_\theta$ the terms proportional to $\widehat{A}_\theta^2$ in the ρ-equation ($x \to \rho$) and $\widehat{A}_\rho\widehat{A}_{-\theta}$ in the θ-equation ($x \to \theta$) become secular and they should be also included to the solvability conditions. The analogical situation happens when $\omega_r \approx \omega_\theta/2$. These cases, referred to as *internal resonances*, show qualitatively different behavior. The terms that become secular only for a particular combination of frequencies ω_r and ω_θ will be referred to as resonant terms contrary to the regular secular terms that appear always. Possible resonances in the second order of approximation and secular terms in equation (2.35) are listed in Table 2.1. At this moment, we assume that the system is far from any resonance. The regular secular terms vanishes if we set

$$D_1 A_x = 0. \tag{2.36}$$

The frequencies and the amplitudes are constant and the behavior of the system is almost the same as in the linear approximation. The only difference is the presence of the higher harmonics oscillating with the frequencies $2\omega_r$, $2\omega_\theta$ and $|\omega_r \pm \omega_\theta|$. They are given by a particular solution of equation (2.35) without the secular term and they can be expressed as a linear combination

$$x_2 = \sum_{|\alpha|=2} Q_\alpha^{(x)} \widehat{A}_{-\rho}^{\alpha_1}\widehat{A}_\rho^{\alpha_2}\widehat{A}_{-\theta}^{\alpha_3}\widehat{A}_\theta^{\alpha_4}. \tag{2.37}$$

Under the assumption of a time-reflection invariance, all constants $Q_\alpha^{(x)}$ are real and their relation to $C_\alpha^{(x)}$ becomes obvious, by substituting x_2 into equation (2.35). We find

$$Q_{klmn}^{(x)} = \frac{C_{klmn}^{(x)}}{\omega_x^2 - [(k-l)\omega_r + (m-n)\omega_\theta]^2}\,. \tag{2.38}$$

$\omega_\theta : \omega_r$	**Secular terms**
Outside	$2\mathrm{i}\omega_r D_2\widehat{A}_\rho,\ \mathrm{K}_{1200}\lvert A_\rho\rvert^2\widehat{A}_\rho,\ \mathrm{K}_{0111}\lvert A_\theta^2\rvert\widehat{A}_\rho$
resonance	$2\mathrm{i}\omega_\theta D_2\widehat{A}_\theta,\ \Lambda_{1101}\lvert A_\rho\rvert^2\widehat{A}_\theta,\ \Lambda_{0012}\lvert A_\theta^2\rvert\widehat{A}_\theta$
$1:3$	$2\mathrm{i}\omega_r D_2\widehat{A}_\rho,\ \mathrm{K}_{1200}\lvert A_\rho\rvert^2\widehat{A}_\rho,\ \mathrm{K}_{0111}\lvert A_\theta^2\rvert\widehat{A}_\rho,\ \mathrm{K}_{0030}\widehat{A}_\theta^3$
	$2\mathrm{i}\omega_\theta D_2\widehat{A}_\theta,\ \Lambda_{1101}\lvert A_\rho\rvert^2\widehat{A}_\theta,\ \Lambda_{0012}\lvert A_\theta^2\rvert\widehat{A}_\theta,\ \Lambda_{0120}\widehat{A}_\rho\widehat{A}_{-\theta}^2$
$1:1$	$2\mathrm{i}\omega_r D_2\widehat{A}_\rho,\ \mathrm{K}_{1200}\lvert A_\rho\rvert^2\widehat{A}_\rho,\ \mathrm{K}_{0111}\lvert A_\theta^2\rvert\widehat{A}_\rho,\ \mathrm{K}_{1110}\lvert A_\rho\rvert^2\widehat{A}_\theta,$ $\mathrm{K}_{0012}\lvert A_\theta\rvert^2\widehat{A}_\theta,\ \mathrm{K}_{0210}\widehat{A}_\rho^2\widehat{A}_{-\theta},\ \mathrm{K}_{1002}\widehat{A}_{-\rho}\widehat{A}_\theta^2$
	$2\mathrm{i}\omega_\theta D_2\widehat{A}_\theta,\ \Lambda_{1101}\lvert A_\rho\rvert^2\widehat{A}_\theta,\ \Lambda_{0012}\lvert A_\theta^2\rvert\widehat{A}_\theta,\ \Lambda_{2100}\lvert A_\rho\rvert^2\widehat{A}_\rho,$ $\Lambda_{0021}\lvert A_\theta\rvert^2\widehat{A}_\theta,\ \Lambda 1002\widehat{A}_{-\rho}\widehat{A}_\theta^2,\ \Lambda_{0210}\widehat{A}_\rho^2\widehat{A}_{-\theta}$
$3:1$	$2\mathrm{i}\omega_r D_2\widehat{A}_\rho,\ \mathrm{K}_{1200}\lvert A_\rho\rvert^2\widehat{A}_\rho,\ \mathrm{K}_{0111}\lvert A_\theta^2\rvert\widehat{A}_\rho,\ \mathrm{K}_{2001}\widehat{A}_{-\rho}^2\widehat{A}_\theta$
	$2\mathrm{i}\omega_\theta D_2\widehat{A}_\theta,\ \Lambda_{1101}\lvert A_\rho\rvert^2\widehat{A}_\theta,\ \Lambda_{0012}\lvert A_\theta^2\rvert\widehat{A}_\theta,\ \Lambda_{0300}\widehat{A}_\rho^3$

Table 2.2: Possible resonances in the third order of approximation.

2.3.3 Third order

When we proceed to the higher order, the discussion is analogical in many respects. The terms proportional to ϵ^3, which appear on the left-hand side of the governing equations, are given by

$$\left[\ddot{\delta x} + \omega_x^2 x\right]_3 = (D_0^2 + \omega_x^2)x_3 + 2\mathrm{i}\omega_x D_2\widehat{A}_x - 2\mathrm{i}\omega_x D_2\widehat{A}_{-x}. \tag{2.39}$$

The terms containing $D_1 x_1$ and $D_1 x_2$ vanish in consequence of the solvability condition (2.36). The right-hand side contains cubic terms of the Taylor expansion combined using first-order approximations ρ_1, θ_1 and quadratic terms combined using one first-order – ρ_1 or θ_1 – and one second-order quantity – ρ_2 or θ_2. Since the second-order terms are linear combinations of $\widehat{A}_{\pm\rho}$ and $\widehat{A}_{\pm\theta}$, the expanded equations in the third order takes the form

$$(D_0^2 + \omega_x^2)x_3 = -2\mathrm{i}\omega_x D_2\widehat{A}_x + 2\mathrm{i}\omega_x D_2\widehat{A}_{-x} + \sum_{|\alpha|=3} C_\alpha^{(x)}\widehat{A}_{-\rho}^{\alpha_1}\widehat{A}_\rho^{\alpha_2}\widehat{A}_{-\theta}^{\alpha_3}\widehat{A}_\theta^{\alpha_4}, \tag{2.40}$$

where all constants $C_\alpha^{(x)}$ are real.

The secular terms together with possible resonances are summarized in Table 2.2. Far from any resonance, we eliminate only the regular secular terms. Multiplying by $e^{-\mathrm{i}\omega_x t}$, the solvability conditions become

$$D_2 A_\rho = -\frac{i}{2\omega_r}\left[\mathrm{K}_{1200}\lvert A_\rho\rvert^2 + \mathrm{K}_{0111}\lvert A_\theta\rvert^2\right]A_\rho, \tag{2.41}$$

$$D_2 A_\theta = -\frac{i}{2\omega_\theta}\left[\Lambda_{1101}\lvert A_\rho\rvert^2 + \Lambda_{0012}\lvert A_\theta\rvert^2\right]A_\theta. \tag{2.42}$$

A particular solution of equation (2.40) is given by linear combination of cubic terms constructed from $\widehat{A}_{\pm\rho}$ and $\widehat{A}_{\pm\theta}$

$$x_3 = \sum_{|\alpha|=3} Q_\alpha^{(3,x)}\widehat{A}_{-\rho}^{\alpha_1}\widehat{A}_\rho^{\alpha_2}\widehat{A}_{-\theta}^{\alpha_3}\widehat{A}_\theta^{\alpha_4}, \tag{2.43}$$

$\omega_\theta : \omega_r$	**Secular terms**
Outside resonance	$2\mathrm{i}\omega_r D_3\widehat{A}_\rho$ $2\mathrm{i}\omega_\theta D_3\widehat{A}_\theta$
$1:4$	$2\mathrm{i}\omega_r D_3\widehat{A}_\rho,\ \mathrm{K}_{0004}\widehat{A}_\theta^4$ $2\mathrm{i}\omega_\theta D_3\widehat{A}_\theta,\ \Lambda_{0103}\widehat{A}_\rho\widehat{A}_\theta^3$
$2:3$	$2\mathrm{i}\omega_r D_3\widehat{A}_\rho,\ \mathrm{K}_{0130}\widehat{A}_\rho\widehat{A}_{-\theta}^3$ $2\mathrm{i}\omega_\theta D_3\widehat{A}_\theta,\ \Lambda_{0220}\widehat{A}_\rho^2\widehat{A}_{-\theta}^2$
$3:2$	$2\mathrm{i}\omega_r D_3\widehat{A}_\rho,\ \mathrm{K}_{2002}\widehat{A}_{-\rho}^2\widehat{A}_\theta^2$ $2\mathrm{i}\omega_\theta D_3\widehat{A}_\theta,\ \Lambda_{0310}\widehat{A}_\rho^3\widehat{A}_{-\theta}$
$4:1$	$2\mathrm{i}\omega_r D_3\widehat{A}_\rho,\ \mathrm{K}_{0301}\widehat{A}_\rho^3\widehat{A}_\theta$ $2\mathrm{i}\omega_\theta D_3\widehat{A}_\theta,\ \Lambda_{0400}A_\rho^4$

Table 2.3: Possible resonances in the fourth order of approximation.

with real coefficients $Q_\alpha^{(3,x)}$.

2.3.4 Fourth order

The terms proportional to ϵ^4 in the expanded left-hand side of the equations (2.28) and (2.29) are

$$\left[\ddot{\delta x} + \omega_x^2 x\right]_4 = (D_0^2 + \omega_x^2)x_3 + 2D_3D_0x_1 + 2D_0D_2x_2. \tag{2.44}$$

The operator D_0D_2 acts on x_2 given by equation (2.37). The result is given by solvability conditions (2.41), (2.42) and can be written in the form

$$2D_0D_2x_2 = \omega_x^2 \sum_{|\alpha|=4} J_\alpha^{(x)} \widehat{A}_{-\rho}^{\alpha_1}\widehat{A}_\rho^{\alpha_2}\widehat{A}_{-\theta}^{\alpha_3}\widehat{A}_\theta^{\alpha_4}, \tag{2.45}$$

where constants $J_\alpha^{(x)}$ are real because both D_0 and D_2 produce one imaginary unit. The right-hand side is expanded similarly. Finally, we arrive at the expanded governing equation in the form

$$(D_0^2 + \omega_x^2)x_4 = -2\mathrm{i}\omega_x D_3\widehat{A}_x + 2\mathrm{i}\omega_x D_3\widehat{A}_{-x} + \sum_{|\alpha|=4} C_\alpha^{(x)} \widehat{A}_{-\rho}^{\alpha_1}\widehat{A}_\rho^{\alpha_2}\widehat{A}_{-\theta}^{\alpha_3}\widehat{A}_\theta^{\alpha_4}, \tag{2.46}$$

with real constants $C_\alpha^{(x)}$. On the right-hand side there is only one regular secular term $-2\mathrm{i}\omega_x D_3\widehat{A}_x$ independently of ω_r and ω_θ, the sum contains only resonant terms. These terms and solvability conditions are listed in the table 2.3.

2.3.5 Secular terms

A simplicity of multiple scales and algorithmic nature of this method allowed us to predict a general form of secular conditions in a general conservative system with two degrees of

freedom. The conditions arise from elimination of terms that are secular in fastest variable T_0. These terms are eliminated because otherwise the expansions of solutions become nonuniform. In the expansion few secular terms appear regularly, independently of the actual ratio of system eigenfrequencies. Such terms are referred to as regular secular terms. In addition, if eigenfrequencies are close to a fraction of small integers, other nonlinear terms mixing the two oscillations become secular. These terms and the situation when this occurs are referred to as nearly secular terms and the internal resonance, respectively.

One particular feature of an internal resonance k:l is that $k\omega_r$ and $l\omega_\theta$ need not to be infinitesimally close as would be expected from other resonances that are studied by means of linear analysis. Let us consider, for example, an internal resonance $1:2$. The resonance occurs when $\omega_\theta \approx 2\omega_r$. Eliminating secular terms, we obtain solvability conditions (see table 2.1)

$$-2\mathrm{i}\omega_r D_1 \widehat{A}_\rho + \mathrm{K}_{1001}\widehat{A}_{-\rho}\widehat{A}_\theta = 0, \quad -2\mathrm{i}\omega_\theta D_1 \widehat{A}_\theta + \Lambda_{0200}\widehat{A}_\rho^2 = 0. \tag{2.47}$$

The first term in each equation is regular and the second one is resonant. The solvability conditions give us the long term behavior of the amplitudes and phases of oscillations. These are included in the complex amplitudes A_ρ and A_θ. Suppose now that the system departs from the exact ratio by small (first-order) deviation $\omega_\theta = 2\omega_r + \epsilon\sigma$, where σ is *detuning parameter* describing vicinity of the resonance. The terms proportional to $\widehat{A}_{-\rho}\widehat{A}_\theta$ and $\widehat{A}_\rho^2$ remain still secular in the variable T_0 because

$$\widehat{A}_{-r}\widehat{A}_\theta = A_\rho^* A_\theta e^{\mathrm{i}(\omega_\theta-\omega_r)T_0} = A_\rho^* A_\theta e^{\mathrm{i}(\omega_r+\epsilon\sigma)T_0} = A_\rho^* A_\theta e^{\mathrm{i}\sigma T_1} e^{\mathrm{i}\omega_r T_0} \tag{2.48}$$

Analogical situation occur in the θ-equation in the case of the secular term $\widehat{A}_\rho^2$.

Chapter 3

Epicyclic resonances

3.1 The nonlinearities in governing equations

In this chapter we study nonlinear oscillations and internal resonances of epicyclic oscillators governed by equations (1.41) and (1.42). It represents one particular example of a general conservative system of two degrees of freedom described by equations (2.28) and (2.29) that has been studied in section 2.3. The nonlinear functions on the right-hand sides take the form

$$f_\rho(\delta\rho,\delta\theta,\delta\dot\rho,\delta\dot\theta) = (1+\delta\rho)\delta\dot\theta - \left[\frac{1}{1+\delta\rho}\frac{\partial\mathcal{U}}{\partial r} - \omega_r^2\delta\rho\right], \tag{3.1}$$

$$f_\theta(\delta\rho,\delta\theta,\delta\dot\rho,\delta\dot\theta) = 2\frac{\delta\dot\rho\delta\dot\theta}{1+\delta\rho} - \left[\frac{1}{(1+\delta\rho)^2}\frac{\partial\mathcal{U}}{\partial\theta} - \omega_\theta^2\delta\theta\right]. \tag{3.2}$$

The derivatives of the effective potential are evaluated at the actual position of particles. Note also that linear terms in expanded potential derivatives gives epicyclic frequencies, therefore, the first nonzero terms in expansion of the square brackets are quadratic.

We expand the effective potential derivatives into the Taylor series about a circular orbit, for which $\delta\rho = \delta\theta \equiv 0$. For simpler notation, we denote derivatives of the potential at the circular orbits as

$$u_{ij} \equiv \left(\frac{\partial^{i+j}\mathcal{U}}{\partial r^i \partial\theta^j}\right)_{[r_0,\pi/2]}. \tag{3.3}$$

We consider only the case of the potentials symmetric with respect to the equatorial plane. This implies condition $u_{i(2k+1)} = 0$, where $k \in \mathcal{N}$.

The Taylor expansion of functions f_ρ and f_θ up to the fourth order provides many nonlinear terms,

$$\begin{aligned} f_\rho &= -\tfrac{1}{2}r_0u_{30}\,\delta\rho^2 + \delta\dot\theta^2 - \frac{u_{12}}{2r_0}\,\delta\theta^2 - \tfrac{1}{6}r_0^2u_{40}\,\delta\rho^3 + \delta\rho\,\delta\dot\theta^2 + \tfrac{1}{2}u_{22}\,\delta\rho\,\delta\theta^2 \\ &\quad -\tfrac{1}{24}r_0^3u_{50}\,\delta\rho^4 - \tfrac{1}{4}r_0u_{30}\,\delta\rho^2\,\delta\theta^2 - \frac{u_{14}}{24r_0}\,\delta\theta^4, \end{aligned} \tag{3.4}$$

$$\begin{aligned} f_\theta &= \left(2\omega_\theta^2 - \frac{u_{12}}{r_0}\right)\delta\rho\,\delta\theta - 2\delta\dot\rho\,\delta\dot\theta - \left(\tfrac{1}{2}u_{22} + 3\omega_\theta^2 - \frac{2u_{12}}{r_0}\right)\delta\rho^2\delta\theta + 2\,\delta\rho\,\delta\dot\rho\,\delta\dot\theta, \\ &\quad -2\,\delta\rho^2\delta\dot\rho\,\delta\dot\theta + \left(4\omega_\theta^2 + u_{22} - \frac{3u_{12}}{r_0} - \frac{1}{6}r_0u_{32}\right)\delta\rho^3\delta\theta \\ &\quad + \left(\frac{u_{04}}{3r_0^2} - \frac{u_{14}}{6r_0}\right)\delta\rho\,\delta\theta^3. \end{aligned} \tag{3.5}$$

3.2 The multiple-scales expansion

We introduce small perturbation parameter ϵ expressing the strength of the oscillations. Hence, we assume that $\delta\rho \sim \delta\theta \sim \epsilon$. We seek the solutions of nonlinear governing equations in the form (2.30). We should also substitute expansions (2.13) and (2.14) of the time derivatives. This involves simple but considerably lengthy algebra. We used *Mathematica* for this purpose. Here we briefly summarize several results important for further discussion. We closely follow the general calculations of section 2.3. We compare coefficients of same powers of ϵ on both sides of expanded governing equations. We obtain equations for functions $\rho_i(T_j)$ and $\theta_i(T_j)$ that can be solved successively – lower order solutions appear on the right-hand sides of higher order equations as in a general case discussed in section 2.3. In each order of approximation we rearrange the equations for radial and vertical oscillations to "canonical" forms,

$$(D_0^2 + \omega_r^2)\rho_n = \sum_{i+j+k+l=n} \mathrm{K}_{ijkl} \widehat{A}^i_{-\rho} \widehat{A}^j_{\rho}\, \widehat{A}^k_{-\theta} \widehat{A}^l_{\theta}, \tag{3.6}$$

$$(D_0^2 + \omega_\theta^2)\theta_n = \sum_{i+j+k+l=n} \Lambda_{ijkl} \widehat{A}^i_{-\rho} \widehat{A}^j_{\rho}\, \widehat{A}^k_{-\theta} \widehat{A}^l_{\theta}, \tag{3.7}$$

where n is the order of approximation. This way we identify constants K_{ijkl} and Λ_{ijkl}.

3.2.1 Possible resonances

The studied gravitational potential is symmetric with respect to the equatorial plane. Therefore, the Taylor expansions (3.4) and (3.5) do not contain terms that arise from odd derivatives of the effective potential with respect to θ. Contrary to the general case, the right hand sides of equations (3.6) and (3.7) do not contain all the terms and the system shows only few resonances. The only resonances that appear in the system with such additional symmetry are

$$1:2, \quad 1:1, \quad 3:2 \quad \text{and} \quad 1:4, \tag{3.8}$$

The first three were already identified by Rebusco (2004). where the numbers refer to ratio $\omega_\theta : \omega_r$. The remaining resonances do not appear because corresponding coefficients K_{ijkl} and Λ_{ijkl} vanish.

3.2.2 Solvability conditions

1:2 resonance. The solvability conditions take the form (compare with table 2.1)

$$D_1 \widehat{A}_\rho = -\frac{i}{2\omega_r} \mathrm{K}_{0002} \widehat{A}^2_\theta, \tag{3.9}$$

$$D_1 \widehat{A}_\theta = -\frac{i}{2\omega_\theta} \Lambda_{0110} \widehat{A}_\rho\, \widehat{A}_{-\theta}, . \tag{3.10}$$

The coefficients of the resonant terms are given by

$$\mathrm{K}_{0002} = -\omega_\theta^2 - \frac{u_{12}}{2r_0}, \quad \Lambda_{0110} = -2\omega_\theta^2 - \frac{u_{12}}{r_0}. \tag{3.11}$$

Clearly, the coefficients of resonant terms satisfy $2\mathrm{K}_{0002} = \Lambda_{0110}$. We find similar relations also in the cases of other resonances. The reason for this relation will be apparent in the next section.

1:1 resonance. When the system is far from the 1:2 resonance, the solvability conditions of the first order $D_1\widehat{A}_\rho = D_1\widehat{A}_\theta = 0$ imply that the complex amplitudes $\widehat{A}_\rho$ and $\widehat{A}_\theta$ depend only on the second time-scale T_2. The 1:1 resonance is the only one epicyclic resonance of the system with reflection symmetry in the third order of approximation. Dependence on T_2 implies slower behavior. The solvability conditions are (see Table 2.1)

$$D_2\widehat{A}_\rho = -\frac{\mathrm{i}}{2\omega_r}\left[\mathrm{K}_{1200}\,|A_\rho|^2\,\widehat{A}_\rho + \mathrm{K}_{0111}\,|A_\theta|^2\,\widehat{A}_\rho + \mathrm{K}_{1002}\widehat{A}_{-\rho}\,\widehat{A}_\theta^2\right], \tag{3.12}$$

$$D_2\widehat{A}_\theta = -\frac{\mathrm{i}}{2\omega_\theta}\left[\Lambda_{1101}\,|A_\rho|^2\,\widehat{A}_\theta + \Lambda_{0012}\,|A_\theta|^2\,\widehat{A}_\theta + \Lambda_{0210}\widehat{A}_\rho^2\widehat{A}_{-\theta}\right] \tag{3.13}$$

and the coefficients of the secular terms are given by

$$\mathrm{K}_{1200} = r_0^2\left(\frac{5\,u_{30}^2}{6\,\omega_\theta} - \tfrac{1}{2}u_{40}\right), \tag{3.14}$$

$$\mathrm{K}_{0111} = \tfrac{1}{3}\left(-10\,\omega_\theta^2 + 2\frac{u_{12}^2}{r_0^2\omega_\theta^2} - 3\,u_{22} - 6\,r_0u_{30} + u_{12}\left[\frac{8}{r_0} + \frac{3\,u_{30}}{\omega_\theta^2}\right]\right), \tag{3.15}$$

$$\mathrm{K}_{1002} = \tfrac{1}{6}\left(-6\,\omega_\theta^2 + \frac{6\,u_{12}^2}{r_0^2\omega_\theta^2} - 3\,u_{22} - 2\,r_0u_{30} - \frac{u_{12}\,u_{30}}{\omega_\theta^2}\right), \tag{3.16}$$

$$\Lambda_{0012} = -\frac{u_{04}}{2r_0^2} - \frac{7\,u_{12}}{6\,r_0} + \frac{5\,u_{12}^2}{6\,r_0^2\omega_\theta^2} + \tfrac{10}{3}\omega_\theta^2, \tag{3.17}$$

$$\Lambda_{0210} = \mathrm{K}_{1002}, \tag{3.18}$$

$$\Lambda_{1101} = \mathrm{K}_{0111}. \tag{3.19}$$

In evaluation we use the fact that $\omega_r \approx \omega_\theta$.

3:2 resonance. when $|\omega_\theta - \omega_r| \gg \epsilon$, the elimination of regular secular terms in the third order gives (compare with Table 2.2)

$$D_2\widehat{A}_\rho = -\frac{\mathrm{i}}{2\omega_r}\left[\mathrm{K}_{1200}\,|A_\rho|^2\,\widehat{A}_\rho + \mathrm{K}_{0111}\,|A_\theta|^2\,\widehat{A}_\rho\right], \tag{3.20}$$

$$D_2\widehat{A}_\theta = -\frac{\mathrm{i}}{2\omega_\theta}\left[\Lambda_{1101}\,|A_\rho|^2\,\widehat{A}_\theta + \Lambda_{0012}\,|A_\theta|^2\,\widehat{A}_\theta\right]. \tag{3.21}$$

with the coefficients given as

$$\mathrm{K}_{1200} = r_0^2\left(\frac{15\,u_{30}^2}{8\,\omega_\theta} - \tfrac{1}{2}u_{40}\right), \tag{3.22}$$

$$\mathrm{K}_{0111} = \tfrac{1}{4}\left(-15\,\omega_\theta^2 + \frac{9\,u_{12}}{4\,r_0^2\omega_\theta^2} - 4\,u_{22} - 18\,r_0u_{30} + 9\,u_{12}\left[\frac{1}{r_0} + \frac{u_{30}}{\omega_\theta^2}\right]\right), \tag{3.23}$$

$$\Lambda_{0012} = -\frac{u_{04}}{2r_0^2} + \frac{135}{64}\,\frac{u_{12}^2}{r_0^2\omega_\theta^2} - \frac{153}{16}\,\frac{u_{12}}{r_0} + \frac{135}{16}\,\omega_\theta^2, \tag{3.24}$$

$$\Lambda_{1101} = \mathrm{K}_{0111}, \tag{3.25}$$

where we used the fact that $3\omega_r \approx 2\omega_\theta$.

The elimination of the resonant terms in the forth order gives the solvability condition of the form (compare with table 2.3)

$$D_3\widehat{A}_\rho = -\frac{\mathrm{i}}{2\omega_r}\,\mathrm{K}_{2002}\widehat{A}_{-\rho}^2\widehat{A}_\theta^2, \quad D_3\widehat{A}_\theta = -\frac{\mathrm{i}}{2\omega_\theta}\,\Lambda_{0310}\widehat{A}_\rho^3\widehat{A}_{-\theta}, \tag{3.26}$$

where the resonant coefficients are given by

$$\begin{aligned}
\mathrm{K}_{2002} &= -\tfrac{15}{16}\,\omega_\theta^2 + \tfrac{27}{32}\,\frac{u_{12}}{r_0} + \tfrac{135}{64}\,\frac{u_{12}^2}{r_0^2\omega_\theta^2} - \tfrac{243}{128}\,\frac{u_{12}^3}{r_0^3\omega_\theta^4} - \tfrac{9}{8}\,u_{22} + \tfrac{27}{16}\,\frac{u_{12}\,u_{22}}{r_0\omega_\theta^2} \\
&\quad -\tfrac{27}{16}\,r_0 u_{30} + \tfrac{81}{64}\,\frac{u_{12}^2\,u_{30}}{r_0\omega_\theta^4} - \tfrac{9}{16}\,\frac{r_0 u_{22}\,u_{30}}{\omega_\theta^2} - \tfrac{81}{256}\,\frac{r_0^2 u_{30^2}}{\omega_\theta^2} \\
&\quad -\tfrac{81}{512}\,\frac{r_0 u_{12}\,u_{30}^2}{\omega_\theta^4} - \tfrac{1}{4}\,r_0 u_{30} - \tfrac{9}{64}\,r_0^2 u_{40} - \tfrac{9}{128}\,\frac{r_0 u_{12}\,u_{40}}{\omega_\theta^2} \qquad (3.27) \\
\Lambda_{0310} &= \tfrac{2}{3}\mathrm{K}_{2002} \qquad (3.28)
\end{aligned}$$

3.2.3 Spherically-symmetric gravitational potential

Let us consider the case when the gravitational potential is function of r only, $\Phi(r,\theta) \equiv \Phi(r)$. The trajectories of the orbiting particles are strictly planar and the epicyclic resonances do not appear. This fact can be recovered also in our calculations. The coefficients in the solvability conditions are

$$\mathrm{K}_{0111} = \Lambda_{1101} = -4\,r_0\Phi_0^{(3)} + 36\,\frac{\Phi_0'}{r_0}, \qquad (3.29)$$

$$\mathrm{K}_{1200} = \tfrac{1}{2}\left(r_0\Phi_0^{(4)} + 40\,\Phi_0^{(3)}\right) + \tfrac{5}{6}r_0^3\,\frac{\Phi^{(3)}}{\Phi_0'} + 90\,\frac{\Phi_0'}{r_0}, \qquad (3.30)$$

$$\Lambda_{0012} = 12\,\frac{\Phi'}{r_0} \qquad (3.31)$$

$$\mathrm{K}_{1002} = \Lambda_{0210} = 0 \qquad (3.32)$$

in the case of 1:1 epicyclic resonance and

$$K_{0111} = \Lambda_{1101} = -9\,r_0\Phi_0^{(3)} + 96\,\frac{\Phi_0'}{r_0}, \qquad (3.33)$$

$$K_{1200} = \tfrac{1}{2}\left(r_0\Phi_0^{(4)} + 90\,\Phi_0^{(3)}\right) + \tfrac{15}{8}r_0^3\,\frac{\Phi^{(3)}}{\Phi_0'} + 240\,\frac{\Phi_0'}{r_0}, \qquad (3.34)$$

$$\Lambda_{0012} = 32\,\frac{\Phi_0'}{r_0} \qquad (3.35)$$

$$\mathrm{K}_{2002} = \Lambda_{0310} = 0 \qquad (3.36)$$

in the case of 3:2 epicyclic resonance. All resonant terms vanishes. Hence, there are *no* epicyclic resonances in the strictly spherically symmetric gravitational potential. In the next sections we consider fully general case of the axisymmetric gravitational field.

3.3 The 1:2 resonance

In this section, we study properties of the epicyclic motion when internal resonance 1:2 between vertical and radial epicyclic modes occurs. Through the section we suppose that the eigenfrequencies are nearly commersuable, i.e. $\omega_r \approx 2\omega_\theta$. This resonance appears in the second order, where only quadratic terms of the expansion contributes. The quadratic nonlinearity is sufficient to wake up this resonance. We note that this resonance appears in the fourth order again. However, the fourth order would provide only negligible corrections to the results of second order alone. Hence, we consider only two time scales, the fast one

T_0 (that is identical with the physical time t) and the slow one T_1. Our discussion is similar to that of Nayfeh & Mook (1979) in the case of the system with quadratic nonlinearity.

The solvability conditions are given by equations (3.9) and (3.10). From equation (3.11) we observe that coefficients K_{0002} and Λ_{0110} satisfy

$$\Lambda_{0110} = 2\mathrm{K}_{0002} \equiv \omega_\theta^2 \beta. \tag{3.37}$$

By substituting expressions for $\widehat{A}_{\pm\rho}$ and $\widehat{A}_{\pm\theta}$ and deviding equations by the term $e^{\mathrm{i}\omega_r T_0}$ and $e^{\mathrm{i}\omega_\theta T_0}$, respectively we obtain differential equations that describes long-term behavior of complex amplitudes $A_\rho(T_1)$ and $A_\theta(T_1)$,

$$D_1 A_\rho = -\tfrac{1}{8}\mathrm{i}\beta\omega_\theta\, A_\theta^2 e^{-\mathrm{i}(\omega_r - 2\omega_\theta)T_0} = -\tfrac{1}{8}\mathrm{i}\beta\omega_\theta\, A_\theta^2\; e^{-\mathrm{i}\tilde{\sigma}\omega_\theta T_1} \tag{3.38}$$

$$D_1 A_\rho = -\tfrac{1}{2}\mathrm{i}\beta\omega_\theta\, A_\rho A_\theta^\star e^{\mathrm{i}(\omega_r - 2\omega_\theta)T_0} = -\tfrac{1}{2}\mathrm{i}\beta\omega_\theta\, A_\rho A_\theta^\star\; e^{\mathrm{i}\tilde{\sigma}\omega_\theta T_1}, \tag{3.39}$$

where we introduced *detuning parameter* by

$$\sigma \equiv 1 - \frac{2\omega_\theta}{\omega_r}, \quad \sigma = \epsilon\tilde{\sigma}. \tag{3.40}$$

We assume that $\sigma = \mathcal{O}(\epsilon)$ and $\tilde{\sigma} = \mathcal{O}(1)$.

The complex amplitudes can be rewritten in polar forms, $A_\rho = \frac{1}{2}\tilde{a}_\rho e^{i\phi_\rho}$ and $A_\theta = \frac{1}{2}\tilde{a}_\theta e^{i\phi_\theta}$. Again, the symbol $\tilde{x}$ refers to the fact that $\tilde{x} = \mathcal{O}(1)$. The actual amplitudes of oscillations are given as $a_\rho = \epsilon\tilde{a}_\rho$ and $a_\theta = \epsilon\tilde{a}_\theta$, respectively.

Separating real and imaginary parts of the equations we get four differential equations

$$\dot{a}_r = \tfrac{1}{16}\beta\omega_\theta\, a_\theta^2 \sin\gamma, \tag{3.41}$$

$$\dot{a}_\theta = -\tfrac{1}{4}\beta\omega_\theta\, a_\rho a_\theta \sin\gamma, \tag{3.42}$$

$$\dot{\phi}_\rho = -\tfrac{1}{16}\beta\omega_\theta \frac{a_\theta^2}{a_\rho} \cos\gamma, \tag{3.43}$$

$$\dot{\phi}_\theta = -\tfrac{1}{4}\beta\omega_\theta\, a_\rho \cos\gamma, \tag{3.44}$$

where $\gamma(t) \equiv -\sigma\omega_\theta t - \phi_\rho + 2\phi_\theta$ is called phase function. Its time derivative follows from equations (3.43) and (3.44),

$$\dot{\gamma} = -\sigma\omega_\theta - \frac{\beta\omega_\theta}{2a_\rho}\left(a_\rho^2 - \tfrac{1}{8}a_\theta^2\right)\cos\gamma. \tag{3.45}$$

Equations (3.41) and (3.42) together with equation (3.45) governs the long-term behavior of amplitudes and phases of oscillations. They are nonlinear first-order differential equations for variables $a_\rho(t)$, $a_\theta(t)$ and $\gamma(t)$. However, the number of dynamical equations that must be solved can be further reduced if we introduce the integrals of motion.

3.3.1 Integrals of motion

Equations (3.41) and (3.42) imply the relation

$$\frac{\mathrm{d}}{\mathrm{d}t}\left(a_\rho^2 + \tfrac{1}{4}a_\theta^2\right) = 0, \tag{3.46}$$

and thus we introduce

$$\mathcal{E} \equiv a_\rho^2 + \tfrac{1}{4}a_\theta^2 = \mathrm{const}. \tag{3.47}$$

The constant $\mathcal{E}$ is obviously connected with the *energy* of epicyclic oscillations. One can verify using equation (1.20) that $\delta E = r\omega_r^2 \mathcal{E}$ (here r is the radius of the circular orbit of the same angular momentum).

To satisfy equation (3.47) manifestly, we introduce following parameterization of the amplitudes

$$a_\rho^2 = \xi^2 \mathcal{E}, \quad a_\theta^2 = 4(1-\xi^2)\mathcal{E}. \tag{3.48}$$

This way the two equations (3.41) and (3.42) are replaced by a single equation for $\xi(t)$ and the system of evolution equation becomes

$$\dot{\xi} = \tfrac{1}{4}\beta\omega_\theta \left(1-\xi^2\right) \mathcal{E}^{1/2} \sin\gamma, \tag{3.49}$$

$$\xi\dot{\gamma} = -\sigma\omega_\theta\xi + \tfrac{1}{4}\beta\omega_\theta \left(1-3\xi^2\right) \mathcal{E}^{1/2} \cos\gamma. \tag{3.50}$$

The second integral of motion is found in the following way. Relation $\mathrm{d}\gamma/\mathrm{d}\xi = \dot{\gamma}/\dot{\xi}$ implies that

$$\xi\left(\dot{\xi}\mathrm{d}\gamma - \dot{\gamma}\mathrm{d}\xi\right) = 0. \tag{3.51}$$

By substituting from equations (3.49) and (3.50), we get

$$\tfrac{1}{4}\beta\xi(1-\xi^2)\mathcal{E}^{1/2}\mathrm{d}\gamma + \sigma\xi\mathrm{d}\xi - \tfrac{1}{4}\beta(1-3\xi^2)\cos\gamma\mathrm{d}\xi = 0 \tag{3.52}$$

that can be integrated to the form

$$\mathrm{d}\left[\bar{\sigma}\xi^2 - \xi(1-\xi^2)\cos\gamma\right] = 0, \tag{3.53}$$

where $\bar{\sigma} \equiv 2\sigma/\beta\mathcal{E}^{1/2}$. This equation implies existence of another integral of motion,

$$\mathcal{F} \equiv \bar{\sigma}\xi^2 - \xi(1-\xi^2)\cos\gamma. \tag{3.54}$$

3.3.2 Stationary solutions and phase-plane topologies

The solutions of equations (3.49) and (3.50) correspond to trajectories in the (γ,ξ)-plane. This plane is also referred to as the *phase plane*. The stationary solutions are critical points of dynamical equations (3.49) and (3.50). They corresponds to oscillations with constant amplitudes and phase difference given by phase function γ. Setting $\dot{\xi} = \dot{\gamma} = 0$ we get algebraic equations that determines position of critical points in the (ξ,γ)-plane,

$$(1-\xi^2)\sin\gamma = 0, \quad 2\bar{\sigma}\xi + (1-3\xi^2)\cos\gamma = 0. \tag{3.55}$$

Obviously, the former equation is satisfied only if $\gamma = k\pi$. In that case $\cos\gamma = \pm 1$ and the latter equation implies

$$3\xi^2 \mp 2\bar{\sigma}\xi - 1 = 0. \tag{3.56}$$

The sign refers to that of $\cos\gamma$. The positive solutions are

$$\xi_{0,\pi} = \tfrac{2}{6}\left(\pm\bar{\sigma}^2 + \sqrt{\bar{\sigma}+3}\right), \tag{3.57}$$

where ξ_0 or ξ_π is a ξ-coordinate of the critical point for $\gamma = 0$ or π, respectively. The next condition is $\xi < 1$ that further limit the range of detuning parameter $\bar{\sigma}$. Imposing it on solutions (3.57) we find

$$0 < \xi_0 < 1, \quad \text{when} \quad \bar{\sigma} > -1, \tag{3.58}$$

$$0 < \xi_\pi < 0, \quad \text{when} \quad \bar{\sigma} < +1. \tag{3.59}$$

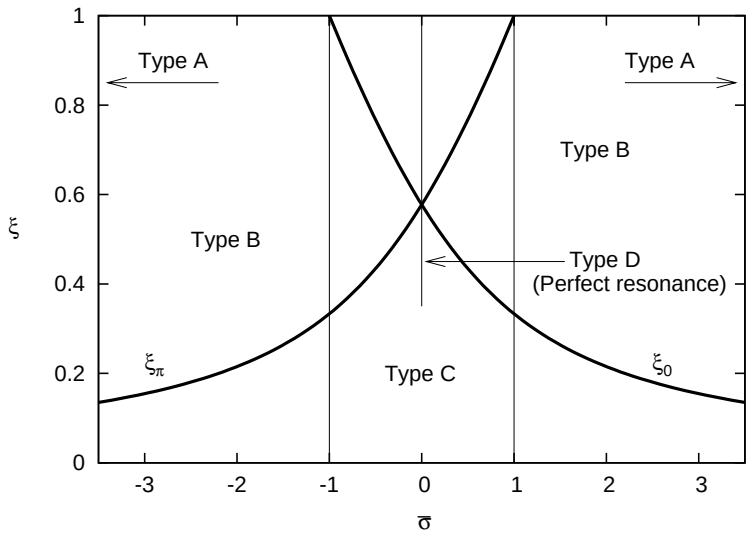

Figure 3.1: The position of the stationary points ξ_0 and ξ_π in dependence on the detuning parameter $\bar{\sigma}$ and the classification of possible phase-plane topologies according to number and position of critical points. Figure shows regions with three different topology types: B, C and D. The phase-plane of the type A corresponds to the limit $|\bar{\sigma}| \to \infty$.

Positions of critical points are shown in Figure 3.1. According to the number of critical points in the (γ, ξ)-plane we can distinguish several types of topologies. The phase plane of type A does not contain any critical point. In the case of the 1:2 resonance this correspond to the limit case $|\bar{\sigma}| \to \infty$. For $\bar{\sigma}$ the absolute value of which is in the range $1 \leq |\bar{\sigma}| < \infty$, the phase-plane topology is of type B. The corresponding phase planes contain one critical point at $\gamma = 0$ (for $\bar{\sigma}$ positive) or $\gamma = \pi$ (for $\bar{\sigma}$ negative). The phase-plane has topology of type C with two critical points at $\gamma = 0$ and $\gamma = \pi$ if $0 < |\bar{\sigma}| < 1$. The last type D corresponds to the perfect resonance occurring when $\bar{\sigma} = 0$.

Nature of critical points can be inferred from the eigenvalues of the linearized system of dynamical equations. The eigenvalues λ are solutions of equation

$$\left(\frac{\partial \dot{\xi}}{\partial \xi} - \lambda\right)\left(\frac{\partial \dot{\gamma}}{\partial \gamma} - \lambda\right) - \frac{\partial \dot{\xi}}{\partial \gamma}\frac{\partial \dot{\gamma}}{\partial \xi} = 0, \tag{3.60}$$

where the partial derivatives are evaluated in the critical point. Because $\sin\gamma = 0$ there, the derivatives $\partial\dot{\xi}/\partial\xi$ and $\partial\dot{\gamma}/\partial\gamma$ vanishes. The remainder leads to equation that is same for both cases, $\gamma = 0$ and $\gamma = \pi$,

$$\lambda^2 = -\frac{\mathcal{E}\beta^2\omega_\theta^2}{16}\,\frac{(1-\xi^2)(1+3\xi^2)}{\xi^2}. \tag{3.61}$$

The right-hand side is always negative for all ξ of interest implying that critical points are always *centers*.

The oscillations of the epicyclic oscillator considered here is described by three variables. These are the amplitudes a_ρ and a_θ of the radial and vertical epicyclic oscillations and the phase function γ, that relates phases of oscillations. In the last sections we find two integral of motion $\mathcal{E}$ and $\mathcal{F}$. Therefore, dynamics of the system is given by single

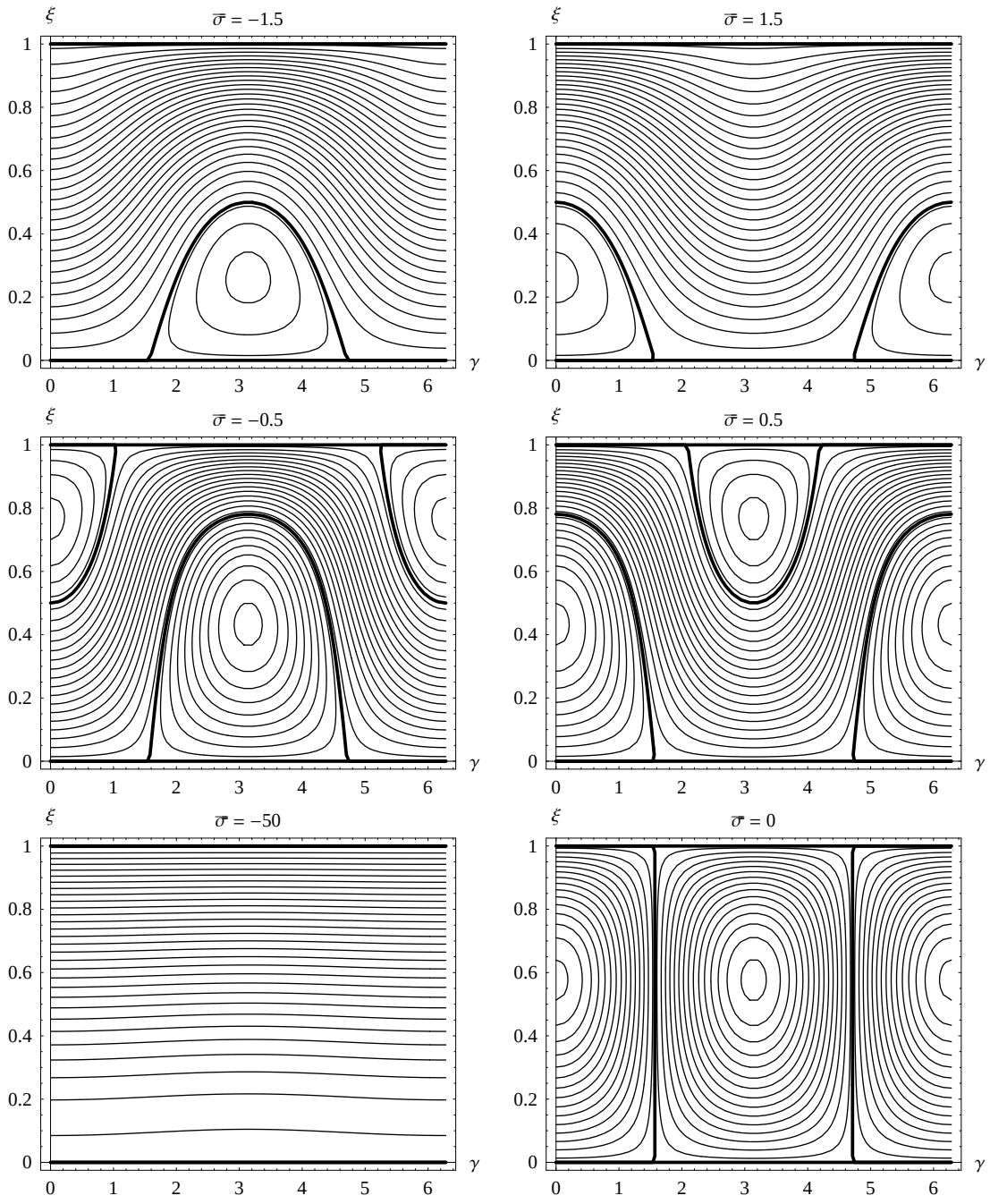

Figure 3.2: The four possible topologies of the (γ, ξ) plane for different values of detuning parameter. Top: the phase-plane of type B for $\bar{\sigma} = -1.5$ (left panel) and 1.5 (the right panel). Middle: topology of type C for $\bar{\sigma} = -0.5$ and 0.5. Bottom left: phase-plane of type A (for $\bar{\sigma} = -50$). Bottom right: the case of perfect resonance ($\bar{\sigma} = 0$) corresponds to the type D.

equation of motion, that determines time behavior of function $\xi(t)$. Later on, we derive this equation. For present moment, we ignore time dependence by considering projections of solutions into the (γ, ξ)-plane.

For a fixed energy $\mathcal{E}$ of oscillations, the system follows curves of constant $\mathcal{F}$. Then the projections of solutions into the (γ, ξ)-plane are given by equation

$$\mathcal{F}(\gamma, \xi) = \text{const.} \tag{3.62}$$

The possible topologies of the (γ, ξ)-plane in dependence on detuning parameter $\bar{\sigma}$ are shown in Figure 3.2. The variable ξ expresses the fraction of the total energy of epicyclic oscillations contained by the radial mode. In all resonant topologies (except that of type A) ξ is a subject to periodic variations. This clearly reflects the periodic exchange of the energy between the two modes of oscillations.

3.3.3 Time behavior

The equation describing time behavior of the system can be found as follows. The square of equation (3.49) gives

$$\frac{16}{\mathcal{E}\beta^2\omega_\theta^2}\dot{\xi}^2 = \left(1-\xi^2\right)^2 (1-\cos^2\gamma). \tag{3.63}$$

Isolating $\cos\gamma$ from equation (3.54), we get $\cos\gamma = (\bar{\sigma}\xi^2 - \mathcal{F})/[\xi(1-\xi)]$. Further substitution gives

$$\frac{4}{\mathcal{E}\beta^2\omega_\theta^2}\dot{u}^2 = u(1-u)^2 - (\bar{\sigma}u + \mathcal{F})^2, \tag{3.64}$$

where we introduced function $u(t) = \xi^2(t)$. The right-hand side can be regarded as a difference of two functions, $F^2(u) - G^2(u)$, where $F(u) \equiv (1-u)u^{1/2}$ and $G(u) \equiv \bar{\sigma}u - \mathcal{F}$. is a linear functions. The reality of $\dot{u}$ requires $F^2(u) > G^2$. This gives us range of allowed values of u. Functions $\pm F(u)$ and $G(u)$ are plotted in Figure 3.3. Functions $\pm F(u)$ forms a closed convex curve and functions $G(u)$ are always linear. Therefore, there are maximally two turning points u_1 and u_2 where $F(u) = \pm F_2(u)$ and hence the time derivative $\dot{u}$ vanishes. As time goes, $u(t)$ oscillates between u_1 and u_2 and the energy flows from one mode of oscillations to other one.

The time period of the energy exchange is given by integral

$$T = \frac{2}{\beta\omega_\theta\mathcal{E}^{1/2}}\int_{u_1}^{u_2}\frac{\mathrm{d}u}{\sqrt{u(1-u)^2 - (\bar{\sigma}u - \mathcal{F})^2}}. \tag{3.65}$$

The square-root in the denominator of the integrant is a cubic function in variable u, hence it is possible to express the integral in terms of Jacobi elliptic integrals. Another possibility is that function $G(u)$ only touch one of the functions $\pm F(u)$. This situation corresponds to a stationary point. It follows that the integral (3.65) diverges in that case.

3.4 The 1:1 resonance

Discussion of the system behavior in the case of 1:1 epicyclic resonance will be similar to that of the 1:2 resonance in many respects. In that case, the fact that solvability conditions depend on the single parameter β allowed us to make a complete and fully

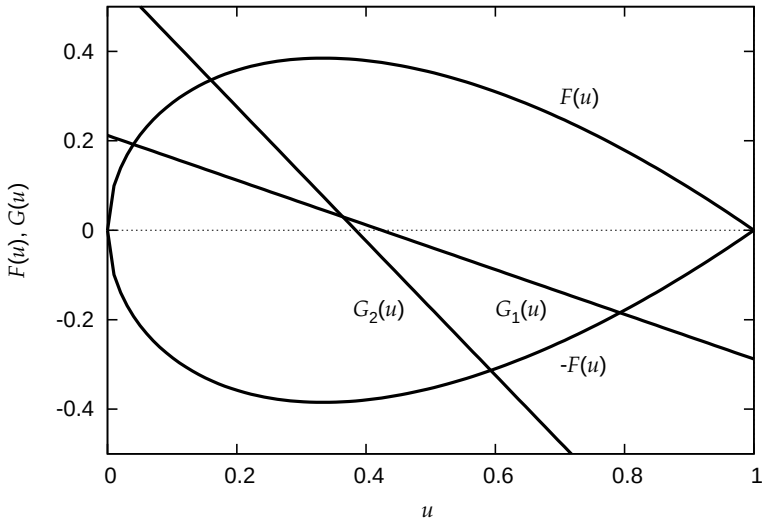

Figure 3.3: Functions $\pm F(u)$ and $G(u)$ that appear on the right-hand side of equation of motion (3.64). The functions $F(u)$ and $-F(u)$ delimites closed convex area and $G(u)$ is a linear function. Hence, there are generally two points where the function G crosses one of the functions $\pm F(u)$. These correspond to the turning points where $\dot{u}$ vanishes. For reference, function $G(u)$ is plotted for two different values of $\bar{\sigma}$ and $\mathcal{F}$: $G_1(u)$ correspond to the trajectory passing point $[0, 0.2]$ in the (γ, ξ)-plane with $\bar{\sigma} = -0.5$ and $G_2(u)$ is for a trajectory going through point $[0, 0.4]$ in the (γ, ξ)-plane with $\bar{\sigma} = -1.5$.

general discussion of all possible topologies of the (γ, ξ)-plane. In the case of the 1:1 resonance the situation are a bit more complicated and similar discussion will be done only for the particular example of resonant orbits in the gravitational field of a Newtonian star and a massive disk.

The solvability conditions for 1:1 resonance have been derived in section 3.1. They are given by equations (3.12) and (3.13). By substituting of $\widehat{A}_{\pm\rho}$ and $\widehat{A}_{\pm\theta}$ and deviding the terms $e^{\mathrm{i}\omega_r T_0}$ and $e^{\mathrm{i}\omega_\theta T_0}$ in equations (3.12) and (3.13), respectively, we get the equations for complex amplitudes in the form

$$2\mathrm{i}\omega_r D_2 A_\rho = \mathrm{K}_{1200} |A_\rho|^2 A_\rho + \mathrm{K}_{0111} |A_\theta|^2 A_\theta + \mathrm{K}_{1002} A_\rho^\star A_\theta^2 e^{-2\mathrm{i}\sigma\omega_\theta T_0}, \quad (3.66)$$

$$2\mathrm{i}\omega_\theta D_2 A_\theta = \Lambda_{1101} |A_\rho|^2 A_\rho + \Lambda_{0012} |A_\theta|^2 A_\theta + \Lambda_{0210} A_\rho^2 A_\theta^\star e^{2\mathrm{i}\sigma\omega_\theta T_0}, \quad (3.67)$$

where we introduced the detuning parameter as

$$\sigma \equiv \frac{\omega_r}{\omega_\theta} - 1, \quad \sigma = \tilde{\sigma}\epsilon^2 \quad (3.68)$$

and we assume $\tilde{\sigma} = \mathcal{O}(1)$. The 1:1 resonance allowes much smaller range of detuning parameter than the resonance 1:2 that was easier to tune.

Expressing complex amplitudes in the polar forms, $A_\rho = \frac{1}{2}\tilde{a}_\rho e^{i\phi_\rho}$ and $A_\theta = \frac{1}{2}\tilde{a}_\theta e^{i\phi_\theta}$, and separating the real and imaginary parts we get

$$D_2 \tilde{a}_\rho = \frac{\mathrm{K}_{1002}}{8\omega_r} \tilde{a}_\rho \tilde{a}_\theta^2 \sin 2\gamma, \quad (3.69)$$

$$D_2\tilde{a}_\theta = -\frac{\Lambda_{0210}}{8\omega_\theta}\,\tilde{a}_\rho^2\tilde{a}_\theta \sin 2\gamma, \tag{3.70}$$

$$D_2\phi_\rho = -\frac{\mathrm{K}_{1200}}{8\omega_r}\,\tilde{a}_\rho^2 - \frac{K_{0111}}{8\omega_\rho}\,\tilde{a}_\theta^2 - \frac{\mathrm{K}_{1002}}{8\omega_r}\,\tilde{a}_\theta^2 \cos 2\gamma, \tag{3.71}$$

$$D_2\phi_\theta = -\frac{\Lambda_{1101}}{8\omega_\theta}\,\tilde{a}_\rho^2 - \frac{\Lambda_{0012}}{8\omega_\theta}\,\tilde{a}_\theta^2 - \frac{\Lambda_{0210}}{8\omega_\theta}\,\tilde{a}_\rho^2 \cos 2\gamma, \tag{3.72}$$

where we introduced the phase function $\gamma \equiv -\sigma\omega_\theta - \phi_\rho - \phi_\theta$. The two amplitudes and the phase function are three variables characterizing oscillations of the system. Introducing the physical time t, the differential equations describing their evolution reads

$$\dot{a}_\rho = \omega_\theta\beta a_\rho a_\theta^2 \sin 2\gamma, \tag{3.73}$$

$$\dot{a}_\theta = -\omega_\theta\beta a_\rho^2 a_\theta \sin 2\gamma, \tag{3.74}$$

$$\dot{\gamma} = \omega_\theta\left[-\sigma + \mu_r a_\rho^2 + \mu_\theta a_\theta^2 + \beta\left(a_\theta^2 - a_\rho^2\right)\cos 2\gamma\right], \tag{3.75}$$

where the dimensionless parameters β, μ_r and μ_θ are introduced by

$$\beta \equiv \frac{\mathrm{K}_{1002}}{8\omega_\theta} = \frac{\Lambda_{0210}}{8\omega_\theta}, \quad \mu_r \equiv \frac{\mathrm{K}_{1200} - \Lambda_{1101}}{8\omega_\theta}, \quad \mu_\theta \equiv \frac{\mathrm{K}_{0111} - \Lambda_{0012}}{8\omega_\theta}. \tag{3.76}$$

3.4.1 Integrals of motion

As in the case of the 1:2 resonance, there are two integrals of motion. Also the way how to find them is very similar. Multiplying equation (3.73) by a_ρ and equation (3.73) by a_θ and integrating, we find that the sum

$$\mathcal{E} \equiv a_\rho^2 + a_\theta^2 \tag{3.77}$$

is conserved during oscillations. The constant $\mathcal{E}$ is proportional to the energy of epicyclic oscillations as it follows from equation (1.20) and it will be referred to as *energy*.

Next, we introduce a parameterization of the amplitudes by function $\xi(t)$ using relations

$$a_\rho^2 = \xi^2\mathcal{E}, \quad a_\theta^2 = (1-\xi^2)\mathcal{E}. \tag{3.78}$$

With the aid of the energy conservation the equations (3.73)–(3.75) are reduced to the two differential equations

$$\dot{\xi} = \omega_\theta\beta\mathcal{E}\xi\left(1-\xi^2\right)\sin 2\gamma \tag{3.79}$$

$$\dot{\gamma} = -\omega_\theta\sigma + \omega_\theta\mathcal{E}\left[\mu_r\xi^2 + \mu_\theta\left(1-\xi^2\right) + \beta\left(1-2\xi^2\right)\cos 2\gamma\right] \tag{3.80}$$

The other integral of motion can be found in the exactly same way as in the case of 1:2 resonance. By substituting equations (3.79) and (3.80) into the relation

$$\dot{\gamma}\xi\mathrm{d}\xi - \xi\dot{\xi}\mathrm{d}\gamma = 0 \tag{3.81}$$

and after soma algebra, we get

$$\mathrm{d}\left[-\bar{\sigma}\xi^2 + \tfrac{1}{2}\mu_r\xi^4 + \tfrac{1}{2}\mu_\theta\xi^2\left(2-\xi^2\right) + \beta\xi^2\left(1-\xi^2\right)\cos 2\gamma\right] = 0, \tag{3.82}$$

where $\bar{\sigma} \equiv \sigma/\mathcal{E}$. Hence, the quantity

$$\mathcal{F} \equiv \xi^2\left[\bar{\sigma} + \tfrac{1}{2}\mu_r\xi^2 + \tfrac{1}{2}\mu_\theta\left(2-\xi^2\right) + \beta\left(1-\xi^2\right)\cos 2\gamma\right] \tag{3.83}$$

is another integral of motion.

3.4.2 Stationary solutions and phase-plane topologies

Stationary points are given by condition $\dot{\gamma} = \dot{\xi} = 0$. From equation (3.79), we deduce that these point appears at $\gamma = k\pi/2$, where k is an integer. This is remarkable difference from the case of 1:2 resonance: the phase plane is periodic in γ-direction with period π, contrary to the 2π-periodicity of the phase plane in the case of the 1:2 resonance. Substituting the $\cos\gamma = \pm 1$ into equation (3.80) we get a quadratic equation for ξ with solutions (the upper and lower sign refers to the odd and even values of k, respectively)

$$\xi^2 = \frac{\bar{\sigma} - \mu_\theta \mp \beta}{\mu_r - \mu_\theta \mp 2\beta}. \tag{3.84}$$

In further discussion we separate two cases according to the signum of the denominator $D \equiv \mu_r - \mu_\theta \mp 2\beta > 0$. If $D > 0$ we find that corresponding critical points exists for $\bar{\sigma}$ in the range

$$\mu_\theta \pm \beta < \bar{\sigma} < \mu_r \mp \beta. \tag{3.85}$$

On the other hand, for $D < 0$ the critical points appear only if $\bar{\sigma}$ satisfies

$$\mu_r \mp \beta < \bar{\sigma} < \mu_\theta \pm \beta. \tag{3.86}$$

Next, we linearize equations (3.79) and (3.80) in the vicinity of critical points. The toology of the (γ, ξ) plane can be deduced from the eigenvalues λ of the linearized system. These are roots of a characteristic polynomial

$$\left(\frac{\partial\dot{\xi}}{\partial\xi} - \lambda\right)\left(\frac{\partial\dot{\gamma}}{\partial\gamma} - \lambda\right) - \frac{\partial\dot{\xi}}{\partial\gamma}\frac{\partial\dot{\gamma}}{\partial\xi} = 0. \tag{3.87}$$

The partial derivatives are evaluated at critical points. As in the case of the 1:2 resonance, we find that $\partial\dot{\xi}/\partial\xi = \partial\dot{\gamma}\partial\gamma = 0$ because they are proportional to $\sin 2\gamma$ that vanishes for $\gamma = k\pi/2$. The remaining two derivatives gives

$$\frac{\partial\xi}{\partial\gamma} = \pm 2\omega_\theta\beta\mathcal{E}\xi\left(1 - \xi^2\right), \quad \frac{\partial\gamma}{\partial\xi} = 2\omega_\theta\mathcal{E}\xi D. \tag{3.88}$$

Hence, equation (3.87) takes the form

$$\lambda^2 = \pm 4\beta\omega_\theta^2\mathcal{E}^2\xi^2\left(1 - \xi^2\right)D. \tag{3.89}$$

The (γ, ξ)-plane contain critical points of both types, centers and saddles. If $D > 0$ critical points at $\gamma = k\pi$ are saddles and that at $\gamma = (2k+1)\pi/2$ between them are centers. In the opposite case $D < 0$, the situation is exactly opposite: centers are at $\gamma = (2k+1)\pi/2$ and saddles at $\gamma = k\pi$. Particular examples of phase planes are given in the next section.

3.4.3 1:1 epicyclic resonance close to a massive ring

Let us illustrate the above-given theory on the practical example of orbits in gravitational field of the Newtonian star surrounded by the massive ring. In the case considered here, the ratio of masses of the ring and the star is set to the value $\mu = 0.1$.

The epicyclic frequencies were already calculated in section 1.2.3. Using these results we determine detuning parameter according to equation (3.68). Using equations (3.14)–(3.19) we find the parameters μ_r, μ_θ and β. These are shown in Figure 3.4 as functions

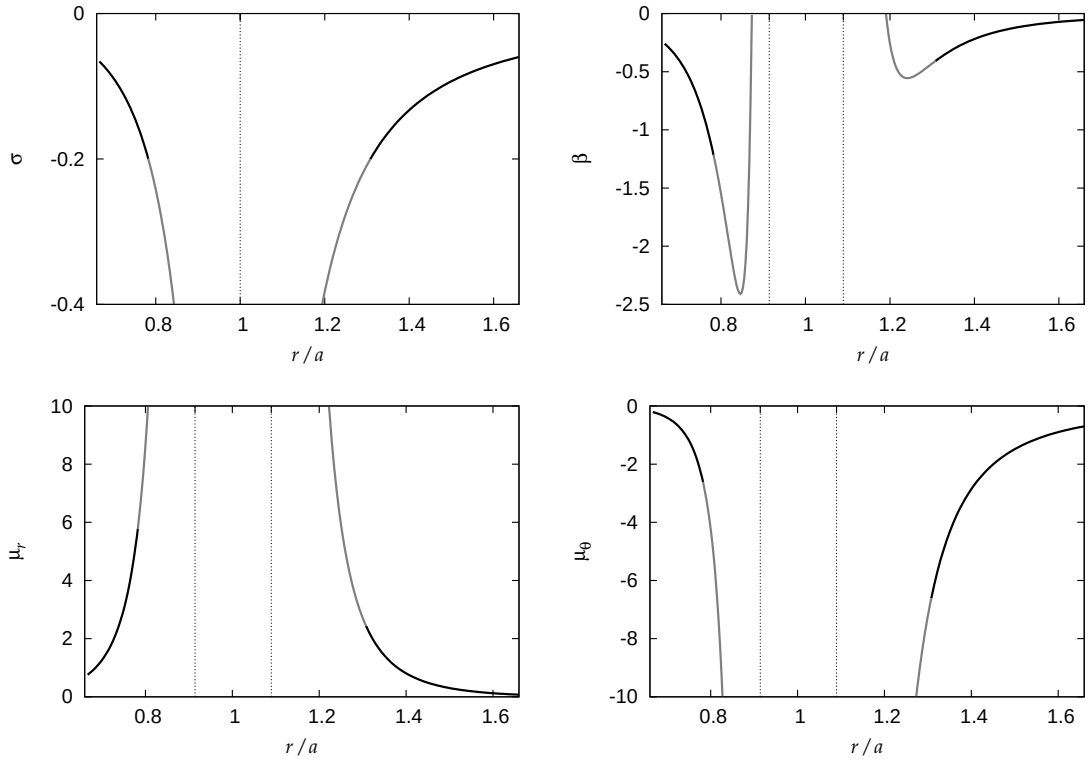

Figure 3.4: Detuning parameter σ (left), parameters μ_r, μ_θ (middle) and parameter β (right) as functions of radial coordinate for the 1:1 epicyclic resonance in the gravitational field of a Newtonian star surrounded by a massive ring. The ratio of masses is $\mu = 0.1$ and the ring is at the radius $r = a$. The branches on curves where our theory is relevant are denoted by thick black line.

of the radial coordinate. The perturbation approach used here is limited by requirement on the amplitudes of oscillations, $a_\rho \sim a_\theta \sim \epsilon \ll 1$. That means that both, the energy and the detuning parameter must satisfy $\mathcal{E} \sim \sigma \sim \epsilon^2 \ll 1$. In figures the thick black line denotes regions where $\sigma < 0.2$.

For a given radius r, equation (3.86) gives us the range of energies for which the (γ, ξ)-plane contains critical points. Applying this condition we found that three different topologies of (γ, ξ)-plane occurs. These are referred to as types A, B, C. While the phase-planes of the type A do not contain any critical point, the critical points of both the saddle and central topology appear in phase-planes of type C. Finally, B is a "transient" type that contains only critical points with central topology. The top panel of Figure 3.5 shows regions of different phase-plane topology in the $(r, \mathcal{E})$ plane. Clearly the phase planes of a type A occurs for epicyclic oscillations of small energy at all radii. This is because the epicyclic frequencies are quite different from each other and thus the oscillations with small energy are almost uncoupled. On the other hand, with higher energy of oscillations, the frequency of oscillations are shifted toward the exact 1:1 ratio by nonlinear effects (amplitude-frequency interaction) and the two oscillation modes become coupled much strongly.

Particular examples of the phase plane topology at different radii and for different

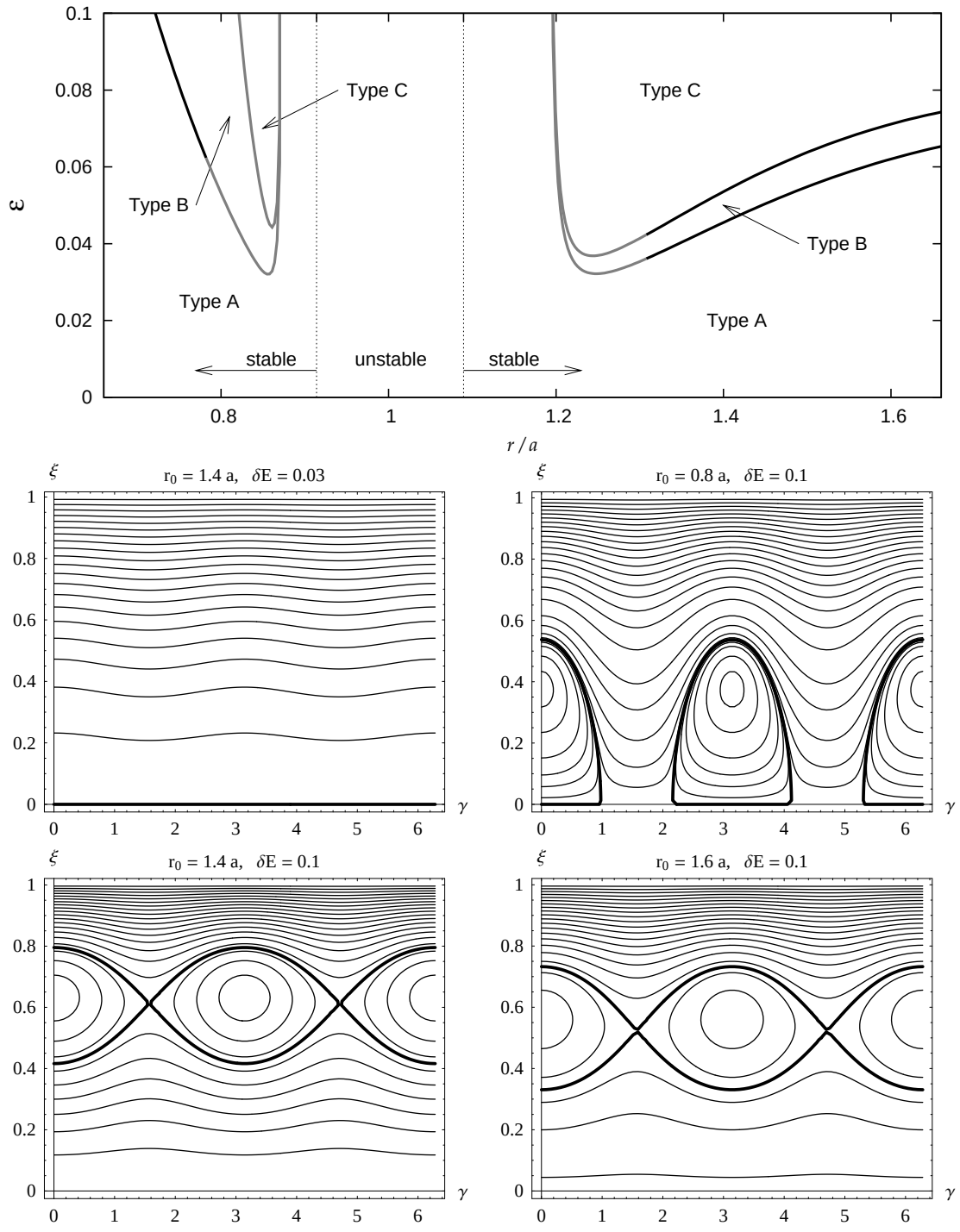

Figure 3.5: The 1:1 epicyclic resonance in gravitational field of a Newtonian star and massive ring. The ring is at radius $r = a$ and this distance also provides a natural length-scale of the problem. The ratio of masses is $\mu = 0.1$. The top panel shows regions of different phase-plane topology in the $(r, \mathcal{E})$-plane. We distinguish three types (A,B,C) of the topology. The middle-left panel shows a phase plane of type A that does not contain critical points. An example of the type-B topology is given in the middle-right panel. Finally, the bottom row shows two phase-planes of the type-C topology.

energies of oscillations are shown in the middle and bottom panels of Figure 3.5

3.5 The 3:2 resonance

Finally, we consider 3:2 epicyclic resonance. The solvability conditions involves that of both the third and the fourth orders. Hence the complex amplitudes A_ρ and A_θ are functions of both time scales T_3 and T_4. Also, the detuning parameter should be introduced as

$$\sigma \equiv 3\,\frac{\omega_r}{\omega_\theta} - 2 = \epsilon^2\tilde{\sigma}_2 + \epsilon^3\tilde{\sigma}_3. \tag{3.90}$$

The solvability conditions takes the form

$$2\mathrm{i}\omega_r D_3 A_\rho = \mathrm{K}_{2002}(A_\rho^\star)^2 A_\theta^2\; e^{\mathrm{i}(\tilde{\sigma}_2 T_2 + \tilde{\sigma}_3 T_3)}, \tag{3.91}$$

$$2\mathrm{i}\omega_\theta D_3 A_\theta = \Lambda_{0310} A_\rho^3 A_\theta^\star\; e^{\mathrm{i}(\tilde{\sigma}_2 T_2 + \tilde{\sigma}_3 T_3)}, \tag{3.92}$$

$$2\mathrm{i}\omega_r D_2 A_\rho = \left[\mathrm{K}_{1200}\left|A_\rho\right|^2 + \mathrm{K}_{0111}\left|A_\theta\right|^2\right] A_\rho, \tag{3.93}$$

$$2\mathrm{i}\omega_\theta D_2 A_\theta = \left[\Lambda_{1101}\left|A_\rho\right|^2 + \Lambda_{0012}\left|A_\theta\right|^2\right] A_\theta. \tag{3.94}$$

By substituting polar form of complex amplitudes A_ρ and A_θ and separating real and imaginary parts of the equations we get eight equations governing long-term behavior of phases and amplitudes.

$$D_2\tilde{a}_\rho = 0, \tag{3.95}$$

$$D_2\tilde{a}_\theta = 0, \tag{3.96}$$

$$D_3\tilde{a}_\rho = \frac{\mathrm{K}_{2002}}{16\omega_r}\tilde{a}_\rho^2\tilde{a}_\theta^2\sin\gamma, \tag{3.97}$$

$$D_3\tilde{a}_\theta = -\frac{\Lambda_{0310}}{16\omega_\theta}\tilde{a}_\rho^3\tilde{a}_\theta\sin\gamma, \tag{3.98}$$

$$D_2\phi_\rho = -\frac{1}{8\omega_r}\left[\mathrm{K}_{1200}\tilde{a}_\rho^2 + \mathrm{K}_{0111}\tilde{a}_\theta^2\right], \tag{3.99}$$

$$D_2\phi_\theta = -\frac{1}{8\omega_\theta}\left[\Lambda_{1101}\tilde{a}_\rho^2 + \Lambda_{0012}\tilde{a}_\theta^2\right], \tag{3.100}$$

$$D_3\phi_\rho = -\frac{\mathrm{K}_{2002}}{16\omega_r}\,\tilde{a}_\rho\tilde{a}\theta^2\cos\gamma, \tag{3.101}$$

$$D_3\phi_\theta = -\frac{\Lambda_{0310}}{16\omega_\theta}\,\tilde{a}_\rho^3\cos\gamma, \tag{3.102}$$

where the phase function was introduces as $\gamma(T_2, T_3) \equiv -\sigma_2 T_2 - \sigma_3 T_3 - 3\phi_\rho + 2\phi_\theta$. The amplitudes $\tilde{a}_\rho$ and $\tilde{a}_\theta$ of oscillations change slowly, because they depend only on the third time-scale T_3. Phases ϕ_r and ϕ_θ of oscillations are modified on both time scales T_2 and T_3. The equations of the second and third order can be further merged introducing the single physical time t. Time derivatives are then given by $\mathrm{d}/\mathrm{d}t = \epsilon^2 D_2 + \epsilon^3 D_3$. Oscillations of the system are determined by both amplitudes and by the phase functions. They are governed by equations

$$\dot{a}_r = \tfrac{1}{24}\beta\omega_r a_r^2 a_\theta^2\sin\gamma, \tag{3.103}$$

$$\dot{a}_\theta = -\tfrac{1}{16}\beta\omega_\theta a_r^3 a_\theta\sin\gamma, \tag{3.104}$$

$$\dot{\gamma} = -\sigma\omega_\theta + \frac{\omega_\theta}{4}\left[\mu_r a_r^2 + \mu_\theta a_\theta^2 + \frac{a_r}{2}\left(\alpha a_\theta^2 - \beta a_r^2\right)\cos\gamma\right], \tag{3.105}$$

where we introduced μ_r, μ_θ and β by equations

$$\Lambda_{0310} = \tfrac{2}{3}\mathrm{K}_{2002} = \beta\omega_\theta^2, \quad \mathrm{K}_{1200} - \Lambda_{1101} = \omega_r^2\mu_r, \quad \mathrm{K}_{0111} - \Lambda_{0012} = \omega_\theta^2\mu_\theta. \tag{3.106}$$

3.5.1 Integrals of motion

Equations (3.103) and (3.104) imply that the following quantity is conserved,

$$\mathcal{E} = a_\rho^2 + \tfrac{9}{4}a_\theta^2 = \text{const.} \tag{3.107}$$

where constant $\mathcal{E}$ is proportional to the total energy in epicyclic oscillations δE.

The equations (3.103) and (3.104) can be replaced by single equation when following parameterization is introduced

$$a_\rho^2 = \xi^2\mathcal{E}, \quad a_\theta^2 = \tfrac{4}{9}\left(1-\xi^2\right)\mathcal{E}. \tag{3.108}$$

Then, the oscillations are governed by two equations for $\xi(t)$ and $\gamma(t)$,

$$\dot{\xi} = \tfrac{1}{16}\beta\omega_\theta\xi^2\left(1-\xi^2\right)\mathcal{E}^{3/2}\sin\gamma, \tag{3.109}$$

$$\dot{\gamma} = -\sigma\omega_\theta + \tfrac{1}{4}\omega_\theta\mathcal{E}\left[\mu_r\xi^2 + \tfrac{4}{9}\mu_\theta\left(1-\xi^2\right) + \tfrac{1}{4}\beta\xi\left(3-5\xi^2\right)\mathcal{E}^{1/2}\cos\gamma\right]. \tag{3.110}$$

The second integral of motion can be found in the exactly same way as in the case of 1:2 and 1:1 resonances. We obtain

$$\mathcal{F} \equiv 8\left(1-\xi^2\right)\sigma + \mathcal{E}\left[\mu_r\xi^4 - \tfrac{4}{9}\mu_\theta\left(1-\xi^2\right)^2\right] + \beta\mathcal{E}^{3/2}\xi^3\left(1-\xi^2\right)\cos\,\gamma. \tag{3.111}$$

3.5.2 Stationary points and phase-plane topology

Stationary points are given by condition $\dot{\xi} = \dot{\gamma} = 0$. According to equation (3.109) the γ-coordinate of these points satisfy $\sin\gamma = 0$ and therefore $\gamma = k\pi$ with k of integer value. Substituting $\dot{\gamma} = 0$ and $\cos\gamma = \pm 1$ into equation (3.110), we get

$$-4\sigma + \left[\mu_r\xi^2 + \tfrac{4}{9}\mu_\theta(1-\xi^2)\right]\mathcal{E} \pm \beta\xi\left(3-5\xi^2\right)\mathcal{E}^{3/2} = 0 \tag{3.112}$$

that is a cubic equation, the solution of which gives us ξ-coordinate of a stationary point. Equation (3.112) calls for a numerical solution. However, in the case of small oscillations for which $\mathcal{E} \ll 1$, its solution can be roughly approximated kepping only terms that are linear in $\mathcal{E}$. Then the problem is reduced to solution of a simple quadratic equation. We obtain

$$\xi^2 = \frac{9\bar{\sigma} - \mu_\theta}{\frac{9}{4}\mu_r - \mu_\theta}, \tag{3.113}$$

where we defined $\bar{\sigma} \equiv \sigma/\mathcal{E}$. The first correction to this solution is of order of $\mathcal{E}^{1/2}$. Deviation between ξ-coordinates of stationary points at odd and even multiples of π is of the same order.

Depending on the sign of the denominator $D \equiv \frac{9}{4}\mu_r - \mu_\theta$, the solution (3.113) lies in the allowed range if $\frac{1}{4}\mu_r < \bar{\sigma} < \frac{1}{9}\mu_\theta$ or $\frac{1}{9}\mu_\theta < \bar{\sigma} < \frac{1}{4}\mu_r$ in the case of D negative or positive, respectively. This can be expressed in terms of energy $\mathcal{E}$: for a given detuning parameter σ stationary points appear in the (γ, ξ) plane if energy of oscillations $\mathcal{E}$ satisfies

$$9\,\frac{\sigma}{\mu_\theta} < \mathcal{E} < 4\,\frac{\sigma}{\mu_r} \quad \text{or} \quad 4\,\frac{\sigma}{\mu_r} < \mathcal{E} < 9\,\frac{\sigma}{\mu_\theta} \tag{3.114}$$

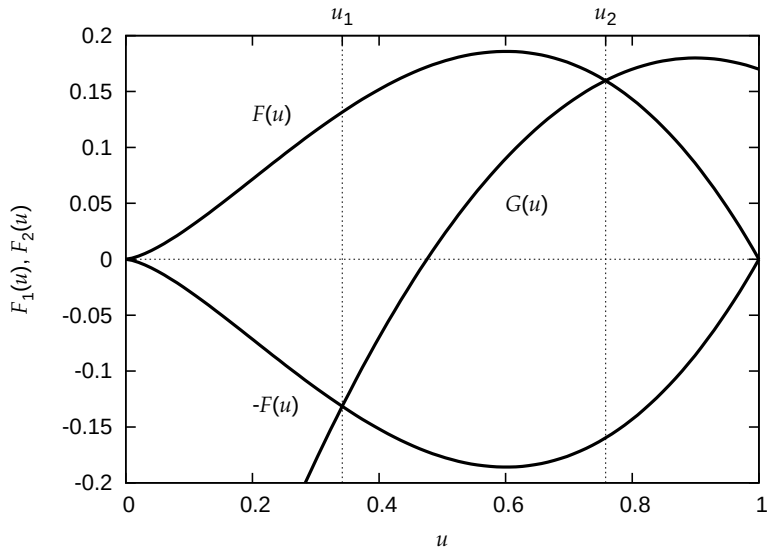

Figure 3.6: The functions $\pm F(u) = \pm(1-u)u^{3/2}$ and the quadratic function $G(u)$ which second powers are first and second terms on the right-hand side of equation (3.118). The behavior of the system corresponds to u in the interval $[u_1, u_2]$ (denoted by the two dotted vertical lines) where the condition $|F(u)| \geq |G(u)|$ is satisfied.

when D is positive or negative, respectively.

Examination of phase-plane topology in a vicinity of critical points leads to equation

$$\left(\frac{\partial\dot{\xi}}{\partial\xi} - \lambda\right)\left(\frac{\partial\dot{\gamma}}{\partial\gamma} - \lambda\right) - \frac{\partial\dot{\xi}}{\partial\gamma}\frac{\partial\dot{\gamma}}{\partial\xi} = 0. \tag{3.115}$$

for eigenvalues λ of the system of linearized equations (3.109) and ((3.110). Evaluating partial derivatives in a critical point and keeping only the terms of lowest order in $\mathcal{E}^{3/2}$, we obtain

$$\lambda = \mp\tfrac{1}{72}\omega_\theta^2\xi^2\left(1-\xi^2\right)D\mathcal{E}^{5/2}. \tag{3.116}$$

Hence the situation is exactly same as in the case of the 1:1 resonance: critical points of central topology alternate that of saddle topology. An example of a phase-plane of epicyclic oscillations in a particular gravitational field will be presented in the next chapter.

3.5.3 Time dependence

The equation describing an evolution of $\xi(t)$ can be derived as follows. Square of equation (3.109) gives

$$\dot{\xi}^2 = \tfrac{1}{16^2}\beta^2\omega_\theta^2\xi^4\left(1-\xi^2\right)^2\mathcal{E}^3\left(1-\cos^2\gamma\right), \tag{3.117}$$

Then, isolating $\cos\gamma$ from equation (3.111) and substituting into equation (3.117) we find the equation in the form

$$\mathcal{K}\dot{u}^2 = F^2(u) - G^2(u), \tag{3.118}$$

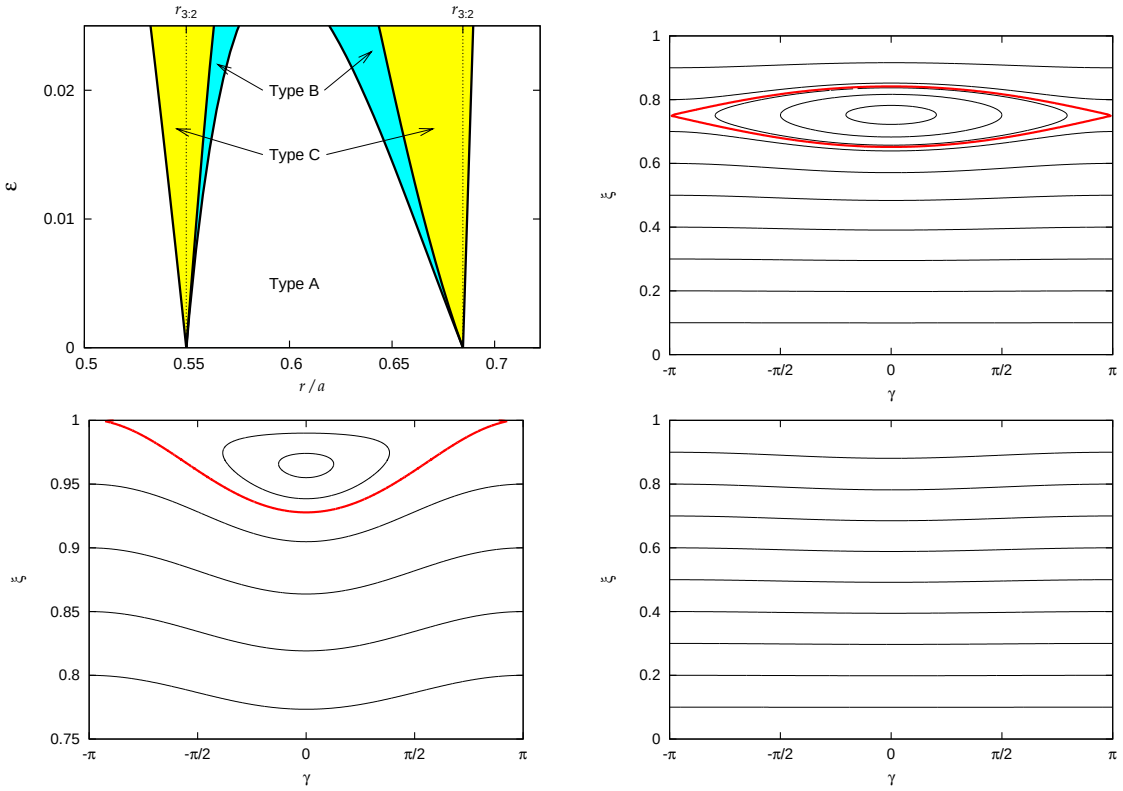

Figure 3.7: The 3:2 inner epicyclic resonances in the gravitational field of a pseudo-Newtonian star and a massive ring. The ratio of masses is $\mu = 0.1$. The top-left panel shows regions of different phase-plane topology in the $(r, \mathcal{E})$-plane. According to number of critical points we distinguish three types (A,B,C) of the phase-plane topology. The top-right panel shows phase plane of type C that contain two critical points (for $-\pi \leq \gamma < \pi$). The bottom-left panel captures the phase-plane of type B that contains only one critical point at $\gamma = 0$. The bottom-right panel shows the situation far from the resonance radii. In that case the phase-plane has A-type topology. The parameters of the phase-planes are: $r = 0.6a$, $\mathcal{E} = 0.02$ (type A), $r = 0.647a$, $\mathcal{E} = 0.02$ (type B) and $r = 0.55a$, $\mathcal{E} = 0.05$ (type C).

where we introduced new variable $u(t) \equiv \xi^2$ and the constant $\mathcal{K}$ and functions $F(u)$ and $G(u)$ are define as

$$\mathcal{K} \equiv \frac{1}{\mathcal{E}^{3/2}} \left(\frac{8}{\omega_\theta \beta} \right)^2, \tag{3.119}$$

$$F(u) \equiv u^{3/2}(1-u) \tag{3.120}$$

$$G(u) \equiv \frac{1}{\beta \mathcal{E}^{3/2}} \left[\mathcal{F} - 8\sigma(1-u) - \mu_r \mathcal{E} u^2 + \tfrac{4}{9} \mu_\theta \mathcal{E} (1-u)^2 \right]. \tag{3.121}$$

The motion is allowed only for $\dot{u}^2$ positive, the condition $\pm F(u) = G(u)$ gives us the two limit values u_1 and u_2, between which u oscillates. The functions $\pm F(u)$ and $G(u)$ are plotted together in Figure 3.6. Obviously, the equation of motion describes flow of energy between the radial and vertical mode of epicyclic oscillations.

The period of the energy exchange can be find by integration of the equation (3.118)

$$T = \frac{16}{\beta\omega_\theta} E^{-3/2} \int_{u_1}^{u_2} \frac{du}{\sqrt{F^2(u) - G^2(u)}}. \tag{3.122}$$

The integral on the right-hand side can be estimated in the following way. Since $P_5 \equiv F^2(u) - G^2(u)$ is a polynomial of the fifth order in u having two roots u_1 and u_2 in the interval $[0, 1]$, we can write it as $-(u - u_1)(u - u_2)P_3(u)$, where $P_3(u)$ is a polynomial of the third order positive in the interval $[0, 1]$. Using the mean-value theorem we get

$$\int_{u_1}^{u_2} \frac{du}{\sqrt{-(u - u_1)(u - u_2)P_3(u)}} = \frac{1}{p} \int_{u_1}^{u_2} \frac{du}{\sqrt{-(u - u_1)(u - u_2)}} = \frac{\pi}{p}, \tag{3.123}$$

where $p > 0$ is a value of P_3 for some u in the interval $[u_1, u_2]$. Since $P_5 \sim F^2 \sim 0.01$ and $(u_2 - u_1)^2 \sim 0.01$ typically, the values of $P_3(u)$ are of order of unity, and therefore $p \sim 1$. The period of the energy exchange can be roughly approximated by

$$T \sim \frac{16\pi}{\beta\omega_\theta} E^{-3/2}. \tag{3.124}$$

However, near stationary points $(u_2 - u_1)^2$ approaches to zero and the period of energy exchange becomes much longer.

3.5.4 The 3:2 epicyclic resonance close to a massive ring

Again, we illustrate our results on the simple case. The gravitational field is generated by a pseudo-Newtonian star and a massive ring. We chose the ratio of masses $\mu = 0.1$ and the radius of the disk $a = 9R_S$, where R_S is Schwarzschild radius of the star. The epicyclic frequencies have been studied in section 1.2.3. The resonant condition $\omega_\theta/\omega_r = 3/2$ is satisfied on three different radii, two of them lie between the star and the ring and one behind the ring. The resonances at first two radii will be referred to as the *inner* epicyclic resonance and the third one as the *outer*. Here, we consider only the inner resonances.

Using the epicyclic frequencies we calculated the detuning parameter σ and the parameters μ_r, μ_θ and β as functions of r. For a fixed radius inequalities (3.114) give us the possible range of the energy of oscillations for which the phase-planes contains critical points. The result is shown in Figure 3.7. The regions of different phase-plane topologies in the $(r, \mathcal{E})$-plane are shown in the top-left panel. We employ the same classification of phase planes as in the case of the 1:1 resonance. The other panels show examples of phase planes for different values of the radius r and the energy $\mathcal{E}$.

Chapter 4

A model for QPO sources

In Chapter 3 we discussed properties of nonlinear epicyclic resonance in the orbital motion of a test particle. In that case the coupling was provided by non-spherical gravitational potential. We suppose that similar phenomenon may occur also in the accretion flow. In fact, accretion flow surrounding neutron stars and galactic black holes may exhibit global epicyclic motion too. Several authors studied oscillations of the fluid in the vicinity of compact objects under different simplifications. For example, Blaes (1985) gives all possible modes (e.g. eigenfrequencies and eigenfunctions) of slender-torus oscillations. In this approach the size of the stationary torus is small enough that pressure and density can be approximated by a quadratic function in the whole torus. Blaes (1985) considered the Newtonian gravitational field. Recently, Kluźniak & Abramowicz (2002) reconsidered the problem in general relativity and pointed to the existence of particular modes when the torus moves rigidly in vertical and horizontal direction across its equilibrium position in the equatorial plane (see also Abramowicz et al. 2005a for more detailed calculations). The eigenfrequencies of these modes are equal to the vertical and radial epicyclic frequencies, ω_θ and ω_r. Similar results are valid also for radial oscillations. The presence of rigid modes in torus oscillations has been found also in recent numerical simulations (e.g. Lee et al. 2004;Rubio-Herrera & Lee 2005). We expect that the resulting X-ray signal is affected by global oscillations of the accretion flow more strongly than by internal modes. A possible modulation mechanism will be described in Section 4.4.

The global modes of the torus oscillations may be coupled. However, in this case the coupling is rather due to the pressure of the fluid (Abramowicz et al. 2005a). The exact prescription of the coupling calls for the *nonlinear* theory of torus oscillations. However some, rather qualitatively, results can be derived without specification of the coupling by use of arguments based on the general approach described in Chapters 2 and 3.

For our purpose it is sufficient to assume that the torus epicyclic oscillations are governed by very general governing equations

$$\ddot{\delta\rho} + \omega_r^2\,\delta\rho = \omega_r^2\, f_\rho(\delta\rho, \delta\theta, \dot{\delta\rho}, \dot{\delta\theta}), \tag{4.1}$$

$$\ddot{\delta\theta} + \omega_\theta^2\,\delta\theta = \omega_\theta^2\, f_\theta(\delta\rho, \delta\theta, \dot{\delta\rho}, \dot{\delta\theta}), \tag{4.2}$$

where $\delta\rho$ and $\delta\theta$ are radial and vertical epicyclic deviations (note that they are functions of time only because of axisymmetry and global character of the modes). The only requirement posed on general functions f_ρ and f_θ is that the two equations 4.1 and 4.2 are invariant with respect to reflection of time, i.e., the Taylor expansion of functions f_ρ and f_θ does not contain odd powers of the time derivatives of $\delta\rho$ and $\delta\theta$.

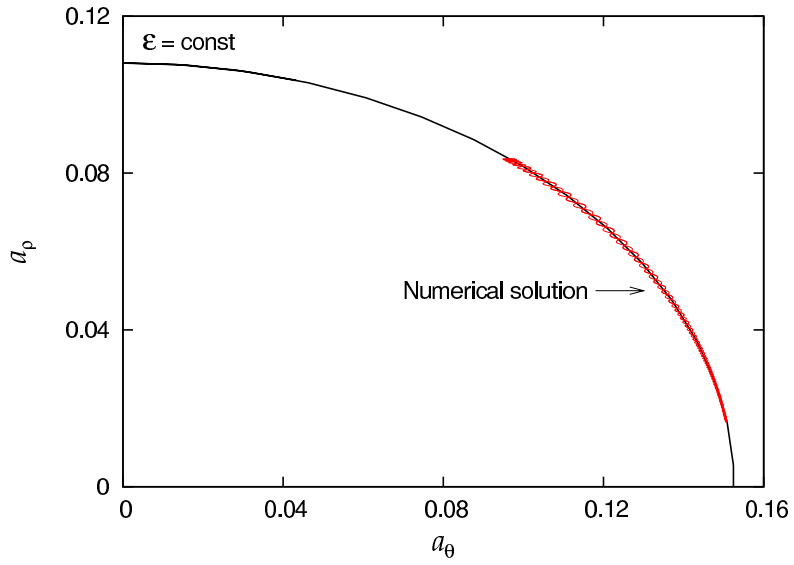

Figure 4.1: Comparison between an analytical constraint (4.7) and the corresponding numerical solution of the system studied by Abramowicz et al. (2003). Each point corresponds to the amplitudes of the oscillations at a particular time. On the other hand, from the discussion of equation (4.7) we know that these points must lie on an ellipse, whose shape is determined by the multiple-scales method.

As it was shown in chapter 2, the multiple-scales expansion carried out for the system described by very general equations in the vicinity of the $\omega_\theta : \omega_r \approx 3 : 2$ internal resonance leads to the solvability conditions for the amplitudes and phases of oscillations of the form

$$\dot{a}_\rho = \frac{\alpha\omega_r}{16}\, a_\rho^2\, a_\theta^2\, \sin\gamma, \tag{4.3}$$

$$\dot{a}_\theta = -\frac{\beta\omega_\theta}{16}\, a_\rho^3\, a_\theta\, \sin\gamma, \tag{4.4}$$

$$\dot{\phi}_\rho = -\frac{\omega_r}{2}\left[\kappa_r\, a_\rho^2 + \kappa_\theta\, a_\theta^2\right] - \frac{\alpha\omega_r}{16}\, a_\rho\, a_\theta^2\, \cos\gamma, \tag{4.5}$$

$$\dot{\phi}_\theta = -\frac{\omega_\theta}{2}\left[\lambda_r\, a_\rho^2 + \lambda_\theta\, a_\theta^2\right] - \frac{\beta\omega_\theta}{16} a_\rho^3\, \cos\gamma, \tag{4.6}$$

where $\gamma \equiv 2\phi_\theta - 3\phi_\rho - \sigma t$ and $\sigma = 3\omega_r - 2\omega_\theta$ are the phase function and the detuning parameter, and α, β, κ_r, κ_θ, λ_r and λ_θ are now real dimensionless constants depending on the coupling of the radial and vertical epicyclic modes. As it was shown in Chapter 3 the equations (4.3) and (4.4) imply that the total energy of these oscillations

$$\mathcal{E} = a_\rho^2 + \frac{\alpha\omega_r}{\beta\omega_\theta}\, a_\theta^2 \tag{4.7}$$

is conserved. Therefore, we can parameterize the amplitudes by single variable $\xi(t) = a_\rho/\mathcal{E}^{1/2}$. In order to verify accuracy of our work, we checked that the numerical solution of a special form (Abramowicz et al. 2003) of the system of equations (4.1)–(4.2) does indeed closely follow the ellipse of equation. (4.7). This is shown in Figure 4.1. Therefore we can be confident that the above-described analytical method gives credible results.

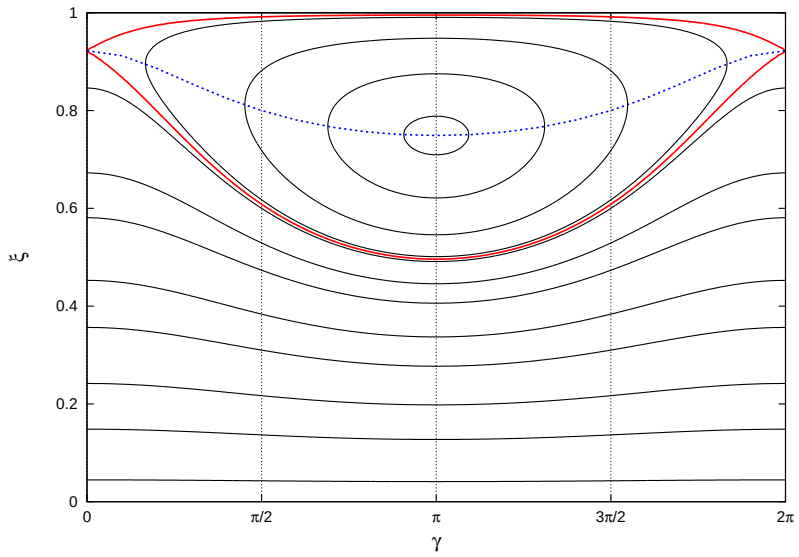

Figure 4.2: Example of the (γ, ξ) for the system close to the 3:2 resonance. It corresponds to the type C according to the classification introduced in Chapter 3. The epicyclic oscillations are coupled by nonlinear functions f_ρ and f_θ [see equation (4.1) and (4.2)]. These functions give us values of the constants α, β, κ_r, κ_θ. λ_r and λ_θ. The solid red line is separatrix dividing the librating and circulating trajectories The blue dotted line connects points where $\dot{\gamma} = 0$.The example is for values $\alpha = \beta = \kappa_r = \lambda_\theta = 1$, $\kappa_\theta = \lambda_\theta = 2$, $\mathcal{E} = 0.1$ and $\sigma = -0.165$.

4.1 Frequencies of resonant oscillations

Equations (4.5) and (4.6) give the shift of actual (observed) frequencies of oscillations ω_r^* and ω_θ^* with respect to the eigenfrequencies ω_r and ω_θ,

$$\omega_r^* = \omega_r + \dot{\phi}_r, \quad \omega_\theta^* = \omega_\theta + \dot{\phi}_\theta. \tag{4.8}$$

Equations (4.8) together with equations (4.5) and (4.6) imply important relation between observed frequencies and the phase function

$$2\omega_\theta^* - 3\omega_r^* = 2\omega_\theta - 3\omega_r + (2\dot{\phi}_\theta - 3\dot{\phi}_r) = -\sigma + (2\dot{\phi}_\theta - 3\dot{\phi}_r) = \dot{\gamma}. \tag{4.9}$$

Hence, the observed frequencies are in exact 3:2 ratio if (and only if) the time-derivative of the phase function vanishes. Trivial implication of this relation is that the frequencies of stationary resonant oscillations with constant amplitudes are in exact 3:2 ratio even if the eigenfrequencies depart from it. This is very interesting and very general feature of nonlinear internal resonance. Moreover, in the case of nonstationary oscillations equation (4.9) discriminates between librating and circulating trajectories in the (γ, ξ)-plane (see Figure 4.2). Because circulating trajectories orbits in full range of γ (here $-\pi \leq \gamma < \pi$), they do not contain any turning point, where $\dot{\gamma} = 0$. It follows from equation (4.9) that the ratio of the observed frequencies of the oscillations are always above or below 3/2 if the evolution of the system follows circulating trajectories. (Whether above or below depends on properties of the system through the constants α, β, κ_r, κ_θ, λ_r and λ_θ). On the other hand, there are two points on the librating trajectories, where $\dot{\gamma} = 0$. Hence, the ratio of observed frequencies from a system that follows librating trajectory oscillates about 3:2.

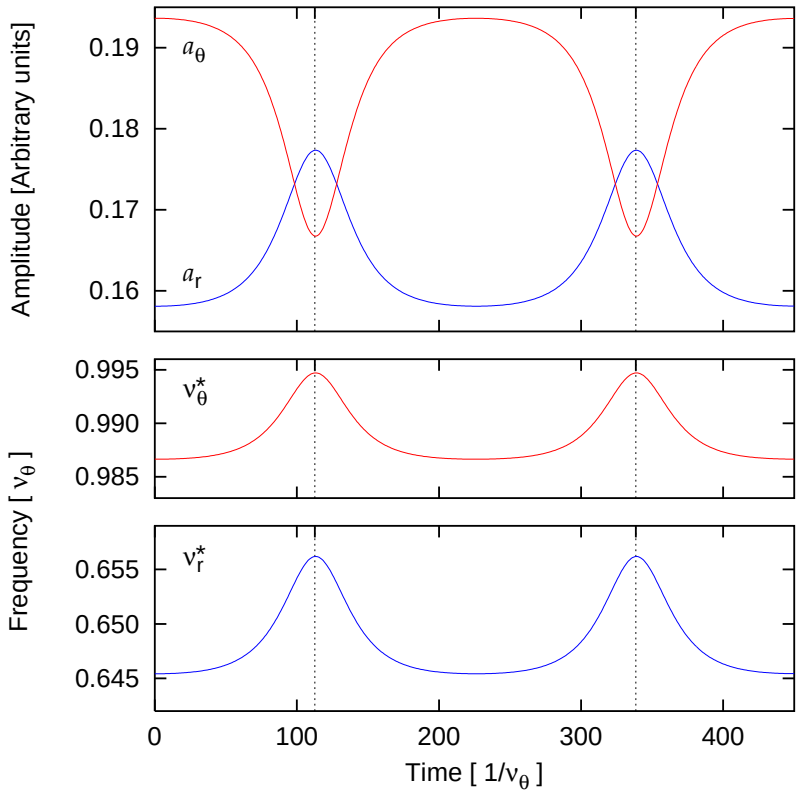

Figure 4.3: Time evolution of amplitudes (top panel) and the epicyclic frequencies (vertical in the middle, radial at bottom) of high-frequency QPOs. The two epicyclic modes are interpreted as radial/vertical oscillations of the accreting fluid. The variation of the oscillation amplitudes is *not* arbitrary in the adopted resonance model: instead, a relation between the amplitudes and frequencies is naturally predicted.

4.2 Low-frequency modulation of high-frequency QPOs

The general solution of equations (4.3)–(4.6) corresponds to the periodic exchange of energy between the two oscillators. The amplitudes and frequencies of oscillations fluctuate, maintaining the energy conservation. The approximation (3.124) for the period of energy exchange is valid also in the case of general coupling,

$$T \sim \frac{16\pi}{\beta\omega_\theta}\,\mathcal{E}^{-3/2}. \tag{4.10}$$

We note, however, that its validity ceases for trajectories in the vicinity of the stationary points where period becomes much greater.

It is evident from equations (4.3), (4.4), (4.7), and (4.10), that the amplitudes and frequencies of high-frequency QPOs are modulated at the frequency $\nu_3 \equiv 1/T$, which is related to the amplitudes of the original high-frequency QPOs. In the general discussion with unspecified coupling, our model has six free parameters. These corresponds to (a combination of) the lowest order expansion coefficients in the Taylor series of the functions f_ρ and f_θ in equations (4.1) and (4.2). Hence, we cannot predict unique behavior. However, it is remarkable that a modulation of frequencies and amplitudes follows naturally from

the assumptions made. Because the oscillators are non-linear, their frequency varies with amplitude. Because the two oscillators are coupled in a system with constant energy, the amplitudes of the oscillators are anticorrelated. Because the two oscillators are in resonance, their frequencies are correlated.

It is not lost on us that similar correlations — discussed by Yu et al. (2001) — hold also on long timescales. For example, van der Klis et al. (1997) show that as the kHz frequencies increase, the ratio of power in the upper to lower kHz QPOs decreases (up to a point). Our Figure 4.3 demonstrates this to be the case also here. We note that in previous work, a particular relation was found to hold between the two frequencies of the system, in agreement with that observed in long-term variations of the twin kHz QPO frequencies in Sco X-1 (Abramowicz et al. 2003; Rebusco 2004). Here, we consider variations on shorter timescales.

4.3 High and low frequency QPOs in Sco X-1

Except the kHz QPOs also low frequency (below about 50 Hz) QPOs are exhibited by LMXBs. They are observed with variety amplitudes and coherence and their properties are often correlated with the spectral state of the source (van der Klis 2000). Here we examine the possibility of connection between kHz QPOs and so called Normal-Branch oscillations (NBOs) observed from Z-sources along the normal track in the color-color digram (Swank 2004). Recently, Yu et al. (2001) find that the both kHz QPOs and the ratio of lower to upper kHz QPO amplitude are anticorrelated to variations in the X-ray flux on the time-scale of normal-branch oscillations in the source Sco X-1.

As we mentioned above [see equation (4.10)], the timescale of modulation in our model is directly related to energy $\mathcal{E}$, We identify the corrected frequencies of our model, i.e., $\nu_r^* = 2\pi\omega_r^*$ and $\nu_\theta^* = 2\pi\omega_\theta^*$, with the twin kHz QPO frequencies $\nu_{\rm lower}$ and $\nu_{\rm upper}$, respectively. We adjusted the energy $\mathcal{E}$ to obtain a modulation at the NBO frequency of Sco X-1, $\nu_3 \approx 6\,{\rm Hz}$.

Figure 4.3 (top panel) exhibits the time variation of the "radial" and "vertical" amplitudes of oscillations. In the lower panels we show the correlation between the two kHz frequencies found in our solution. By the assumption of nearly 3:2 resonance, the two frequencies of actual oscillations satisfy relation $\nu^*_{\rm upper} \approx 1.5\nu^*_{\rm lower}$. Notice a perfect correlation between the variation of the lower amplitude and the variation of the upper frequency $\nu^*_{\rm upper}$. This we interpret as the same correlation that was found by Yu et al. (2001); compare their Figure 2. The magnitude of frequency variation agrees to within a factor of 3 with the data: it is 20 Hz for $\nu_{\rm upper} = 1.1\,{\rm kHz}$ in the data, and about 7 parts in 1000 in our calculation.

We have found that a non-linear resonance in a system simulating an accretion disk, invoked previously to explain the appearance of two frequencies in approximately 3:2 ratio in black-hole and neutron-star X-ray data, results in a periodic time variation of the frequencies.

The Fourier transform of the frequency-modulated and amplitude-modulated periodic signal would result in several sidebands, in practice leading to an increase in width of the (noisy) signal. If the observed radiation flux were modulated with the squared modulus of the amplitudes a_ρ and a_θ, its Fourier transform would exhibit a (weak) component at low frequency of the modulation apparent in Figure 4.3, in addition to the high-frequency signal with its sidebands. In this exploratory work, we are not attempting to model the full power spectrum of QPO sources and, as yet, we have made no attempt to translate the

amplitudes of motion in the model into modulations of the X-ray flux. Strictly speaking, our toy-model gives a coherent signal rather than a QPO, and no details of the excitation or damping were modelled.

It has been suggested that the high-frequency QPOs vary on a timescale of seconds in some sources, notably in Sco X-1 (Yu et al. 2001) and in the black hole candidate XTE J1550-564 (Yu et al. 2002). The low-frequency modulation occurs at ≈ 6 Hz in both sources. In the above described calculation we were able to reproduce this variation for Sco X-1, including the anti-correlation between the amplitude of the lower peak and the frequency of the upper one. A similar approach is possible also in case of XTE J1550-564, although the black hole candidates typically exhibit lower frequencies compared to those in neutron stars, and particularly to those in Sco X-1. This means that if the 6 Hz QPO seen by Yu et al. (2002) corresponds to the modulation discussed in our model, then the ratio $\nu_{\rm lower}/\nu_3$ has to be set differently (about 30 in XTE 1550-564 with $\nu_{\rm lower} = 184$ Hz). And this in turn implies $\mathcal{E}$ is different in both systems.

If the correspondence of our results with the observed modulation of kHz QPO properties on the 6 Hz NBO timescale is not accidental, for the first time we would have a physical explanation for the presence of the rather low frequency QPO in what is otherwise a domain of rapid variability. The larger point is that non-linear resonance (most likely between modes of oscillation possible only in strong gravity) holds promise for explaining not only the highest frequencies observed in accreting neutron stars and black holes, but also the mysterious phenomenology of low frequency features in the power density spectrum, without invoking additional mechanisms.

4.4 A possible mechanism for X-ray modulation

In the case of the neutron-stars sources, the modulation of the X-ray radiation may originate in the modulation of the local accretion rate (Kluźniak & Abramowicz 2004).

In LMXBs that are not pulsars, the magnetic field of the neutron star is sufficiently weak, allowing the accretion disk to extend down to ISCO. The strongest X-ray radiation then originates in the boundary layer, where accreted material hits the star surface. Depending on the star radius $R_\star$, the amount of energy released in the boundary layer exceeds that radiated by the whole disk. It gives about 69% of the total luminosity if $R_\star = 3R_{\rm S}$, or even 86% if $R_\star = 1.5R_{\rm S}$.

In this context, Paczyński (1987) pointed out that a variability of X-ray luminosity of accreting neutron stars may be governed by physical properties of the accretion flow close to ISCO. In Einstein gravity, the inner edge of the pressure supported thick accretion disks is slightly below ISCO (Abramowicz 1985). The material is accreted from the disk through a narrow potential nozzle onto the neutron star. Obviously, if the innermost part of the disk is not stationary but is a subject to some oscillations then the fine structure of the flow at the inner disk edge is significantly changed. This strongly affects the accretion rate through the nozzle and the resulting X-ray luminosity of the boundary layer. This scenario is in agreement with the recent observations of Gilfanov et al. (2003) and more recently Revnivtsev & Gilfanov (2005) that strongly point to the fact that neutron-star QPOs are modulated in the boundary layer.

In sections 4.4.1 and 4.4.2 we briefly summarize equations important for the disk structure close to the ISCO and reproduce the calculations of the accretion rate through the inner edge of the stationary disk. Then in section 4.4.3 we calculate the accretion rate

from the disk that is subject to nonstationary axisymmetric perturbations. We derive a simple formula for the accretion rate modulation of a vertically oscillating disk.

4.4.1 Disk structure close to ISCO

We consider an axisymmetric thick disk made of a perfect fluid surrounding a neutron star of mass M. The dynamics of the fluid is governed by Euler equation, poloidal component of which takes the form

$$\frac{\partial \boldsymbol{v}}{\partial t} + \boldsymbol{v} \cdot \nabla\ \boldsymbol{v} - \frac{\ell^2}{r^2}\boldsymbol{e}_r + \frac{\nabla p}{\rho} - \nabla\Phi = 0, \tag{4.11}$$

where the bold-face letters refer to the poloidal part of the vectors, $\boldsymbol{a} \equiv (a^r, a^z)$, Φ is a gravitational potential, r denotes radial coordinate (we employ the cylindrical coordinates $\{r, \phi, z\}$, with the origin coinciding with the center of the star) and p, ρ and ℓ are the pressure, density and the angular momentum of the orbiting flow respectively (in general all dependent on r and z). The azimuthal component of the Euler equation gives conservation of angular momentum,

$$\frac{\partial \ell}{\partial t} + \boldsymbol{v} \cdot \nabla \ell = 0. \tag{4.12}$$

We assume that the angular momentum is constant in the whole volume of the disk, $\ell(r, z) = \ell_0$, and that the fluid obeys the polytropic equation of state, $P = K\rho^{1+1/n}$, where K and n are polytropic constant and polytropic index, respectively. In addition, we assume that the poloidal velocity $\boldsymbol{v} = (v^r, v^z)$ can be derived from the potential χ. Hence, equation (4.12) is satisfied automatically and equation (4.11) can be further integrated to Bernoulli equation,

$$\frac{\partial \chi}{\partial t} + \frac{v^2}{2} + h + \mathcal{U} = \text{const} \equiv \mathcal{U}_{\rm S}. \tag{4.13}$$

Here we introduced the poloidal-velocity potential by $\boldsymbol{v} = \nabla\chi$, the enthalpy of the fluid $h \equiv \int_0^p \mathrm{d}p/\rho = nK\rho^{1/n}$ and the effective potential $\mathcal{U} = \Phi(r, z) + \ell_0^2/2r^2$.

As a model of a strong gravitational field of the star, we use the pseudo-Newtonian potential $\Phi(r) = -GM/(R - R_{\rm S})$, where $R \equiv \sqrt{r^2 + z^2}$ and $R_{\rm S}$ is Schwarzschild radius. It was introduced by Paczyński & Wiita (1980) and allows us to model general relativistic effects using Newtonian calculations with remarkable simplicity. Particularly, it gives a correct position of the marginally stable orbit at $r = r_{\rm ISCO} = 3R_{\rm S}$ and well reproduces the Keplerian angular momentum of test particles orbiting the star, $\ell_{\rm K} = \sqrt{GMr^3}/(r - R_{\rm S})$. The angular momentum is not a monotonic function of r, as it is in Newtonian gravity ($R_{\rm S} \to 0$). Instead, it has a minimum at the marginally stable orbit.

The structure of the stationary disk is shown in Figure 4.4. The inner edge is at radius $r = r_{\rm in}$, where the angular momentum of the flow equals the Keplerian value, $\ell_0 = \ell(r_{\rm in})$. The Lagrange point is at coordinates $[r_{\rm in}, 0]$. The equipotential surface corresponding to the value $\mathcal{U}_{\rm R}$ that crosses itself at the Lagrange point is called Roche lobe. The equilibrium configuration exists only if the surface of the torus is inside the Roche lobe, e.g. when $\mathcal{U}_{\rm s} \leq \mathcal{U}_{\rm R}$. (Boyer 1965; Abramowicz et al. 1978)

Otherwise, the dynamical equilibrium is impossible and the overflowed matter will be accreted through the potential nozzle onto the star.

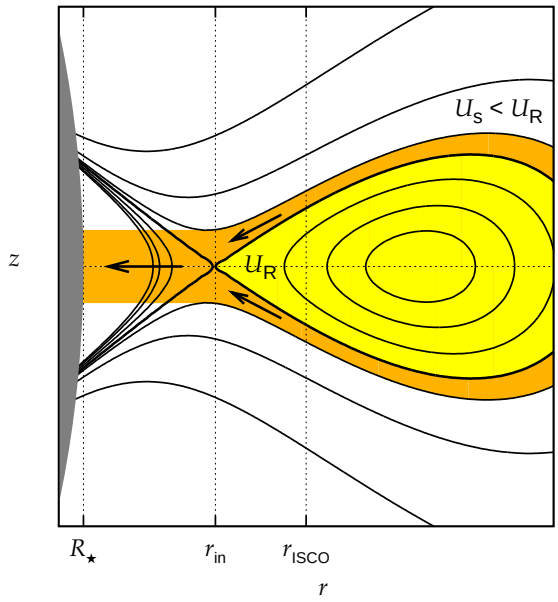

Figure 4.4: Accretion from a thick stationary accretion disk. The position of the disk inner edge and the shape of the equipotentials are determined by the distribution of the fluid angular momentum. Here we consider the simplest case of the constant distribution, $\ell(r,z) = \ell_0$. The plot shows projections of the equipotential surfaces to the poloidal plane (solid lines) and the distribution of the fluid (shaded region). The matter that overflows the Roche lobe (the equipotential surface that crosses itself) is accreted onto the neutron star.

4.4.2 Stationary flow

The stationary accretion rate for Roche overflow was first calculated by Kozłowski et al. (1978), who used Einstein's theory. Here we closely follow the Newtonian calculations of Abramowicz (1985). We consider a small overflow, so that all quantities can be expanded to the second order in the vicinity of the Lagrange point L. Particularly, the vertical profile of enthalpy can be expressed as

$$h(r_{\rm in}, z) \;=\; h^\star - \frac{1}{2}\kappa^2 z^2, \qquad \kappa^2 \equiv -\left(\frac{\partial^2 h}{\partial z^2}\right)_L , \tag{4.14}$$

where $h^\star \equiv h(r_{\rm in}, 0)$ denotes a maximal value of the enthalpy on the cylinder $r = r_{\rm in}$. The linear order does not contribute because the flow is symmetric with respect to the equatorial plane. The thickness of the inner edge is $H = \sqrt{2h^\star}/\kappa$. Close to $r = r_{\rm in}$ the accretion flow becomes transonic. After Abramowicz (1985), we assume that the radial velocity of the flow equals to the local sound speed and that the vertical component of the velocity is negligible compared to the radial one. This significantly simplifies the solution because it allows us to express the poloidal velocity using the enthalpy,

$$\boldsymbol{v} \;=\; \sqrt{\frac{h}{n}}\,\boldsymbol{e}_r. \tag{4.15}$$

The local mass flux through the nozzle is $\dot{m} = \rho v^r = \rho c_{\rm s} = h^{n+1/2}/K^n(1+n)^n n^{1/2}$ and the integration over the cylinder $r = r_{\rm in}$ gives the total mass flux in therms of the

central enthalpy $h^\star$

$$\begin{aligned}\dot{M} &= \int_0^{2\pi} r_1 \,\mathrm{d}\phi \int_{-H}^{H} \dot{m}\mathrm{d}z \\ &= (2\pi)^{3/2} \frac{r_{\rm in}}{n^{1/2}} \left[\frac{1}{K(n+1)}\right]^n \frac{\Gamma(n+3/2)}{\Gamma(n+2)} \frac{(h^\star)^{n+1}}{\kappa},\end{aligned} \tag{4.16}$$

where $\Gamma(x)$ is the Euler gamma function.

In the Bernoulli equation (4.13) we keep the term $v^2/2$ and neglect only the time derivative because of stationarity of the flow. We obtain

$$\frac{v^2}{2} + h + \mathcal{U} = \left(1 + \frac{1}{2n}\right) h + \mathcal{U} = \mathcal{U}_{\rm S}. \tag{4.17}$$

The parameter κ that determines the shape of the enthalpy profile can be expressed using a derivative of the effective potential. That introduces the vertical epicyclic frequency ω_z to the problem. From equation (4.17) we obtain

$$\kappa^2 = \left(\frac{n}{n+1/2}\right)\omega_z^2, \qquad \omega_z = \left(\frac{\partial^2 \mathcal{U}}{\partial z^2}\right)_L. \tag{4.18}$$

By substituting the equations (4.17) and (4.18) and introducing $\Delta\mathcal{U} \equiv \mathcal{U}_0 - \mathcal{U}_{\rm S}$ we finally recover the result obtained by Abramowicz (1985),

$$\dot{M} = A(n) \frac{r_{\rm in}}{\omega_z} \Delta\mathcal{U}^{n+1}, \tag{4.19}$$

$$A(n) \equiv (2\pi)^{3/2} \left[\frac{1}{K(n+1)}\right]^n \left[\frac{1}{n+1/2}\right]^{n+1/2} \frac{\Gamma(n+3/2)}{\Gamma(n+2)}. \tag{4.20}$$

4.4.3 A perturbed flow

Now, we suppose that the disk is disturbed and oscillates. In that case, the accretion flow will not be stationary anymore and in order to described the flow we must use the Bernoulli equation (4.13) in the full form. The presence of the "non-stationary" term $\partial\chi/\partial t$ breaks however the correspondence between the enthalpy and the effective potential. The equipotential surfaces and the surfaces of constant enthalpy will not coincide anymore. If the oscillations are a small perturbation, we can expand the Bernoulli equation in the vicinity of the stationary flow considered above.

We suppose that the velocity potential can be expressed as

$$\chi(\boldsymbol{r}, t) = \chi_{(0)}(\boldsymbol{r}) + \epsilon\chi_{(1)}(\boldsymbol{r}, t), \tag{4.21}$$

where the subscript "(0)" refers to the stationary flow and the dimensionless parameter ϵ characterizes strength of the perturbation. We assume $\epsilon \ll 1$. Then, using the definition $\boldsymbol{v}(\boldsymbol{r}, t) = \nabla\chi(\boldsymbol{r}, t)$ we find

$$\begin{aligned}v^2 &= v_{(0)}^2 + 2\epsilon \boldsymbol{v}_{(0)} \cdot \boldsymbol{v}_{(1)} + \epsilon^2 v_{(1)}^2 \\ &= c_{\rm s}^2 + 2\epsilon c_{\rm s} \frac{\partial\chi_{(1)}}{\partial r} + \epsilon^2 \left[\left(\frac{\partial\chi_{(1)}}{\partial r}\right)^2 + \left(\frac{\partial\chi_{(1)}}{\partial z}\right)^2\right].\end{aligned} \tag{4.22}$$

The perturbation affects also the enthalpy. The new value can be approximated by an expansion via the parameter ϵ

$$h = h_{(0)} + \epsilon h_{(1)} + \epsilon^2 h_{(2)} + \mathcal{O}(\epsilon^3). \tag{4.23}$$

By substituting into the Bernoulli equation (4.13) and equating coefficients of same powers of ϵ, we get

$$h_{(1)} = -\frac{\partial \chi_{(1)}}{\partial t} - \left(\frac{\bar{h}}{n}\right)^{1/2} \frac{\partial \chi_{(1)}}{\partial r}, \tag{4.24}$$

$$h_{(2)} = -\frac{1}{2}\left[\left(\frac{\partial \chi_{(1)}}{\partial r}\right)^2 + \left(\frac{\partial \chi_{(1)}}{\partial z}\right)^2\right]. \tag{4.25}$$

This way all thermodynamic quantities are expressed using the poloidal-velocity potential.

In the following, we model vertical disk oscillations by a simple ansatz for the poloidal-velocity potential.

$$\chi_{(1)} = z v_z \cos \omega t, \tag{4.26}$$

where ω is the frequency of the oscillations. As we show elsewhere (Abramowicz et al. 2005a) this is one of the possible modes that may be present in a slender-torus oscillations. Calculating the velocity perturbation, we find

$$\boldsymbol{v}_{(1)} = v_z \boldsymbol{e}_z \cos \omega t\,. \tag{4.27}$$

Hence, $\epsilon v_z = \text{const}$ can be interpreted as the amplitude of the vertical velocity. Equations (4.24) and (4.25) give

$$h_{(1)} = z v_z \omega \sin \omega t, \quad h_{(2)} = -\frac{1}{2} v_z^2 \cos^2 \omega t. \tag{4.28}$$

The vertical profile of the enthalpy at $r = r_{\rm in}$ reads

$$h(r_{\rm in}, z, t) = h^\star - \kappa^2 z^2 + \epsilon z v_z \omega \sin \omega t - \tfrac{1}{2}\epsilon^2 v_z^2 \cos^2 \omega t + \mathcal{O}(\epsilon^3) \tag{4.29}$$

that is quadratic in the variable z. The position of the enthalpy maximum on the cylinder $r = r_{\rm in}$ is shifted from $z = 0$ to height $\delta z(t)$ given as

$$\delta z(t) = \delta Z \sin \omega t, \quad \delta Z = \epsilon \frac{\omega v_z}{\kappa^2}. \tag{4.30}$$

We can interpret δZ as the amplitude of the oscillations. Also the value of enthalpy in the maximum differs from the stationary case by

$$\delta h^\star \equiv h(r_{\rm in}, \delta z) - h^\star \frac{1}{2}\kappa^2 \left[\delta z^2 - \frac{\kappa^2}{\omega^2}(\delta Z^2 - \delta z^2)\right] + \mathcal{O}(\epsilon^3). \tag{4.31}$$

According to equation (4.16) the actual accretion rate depends on the maximal enthalpy as $\dot{M} \propto (h^\star)^{n+1}$. This relation can be applied also in the case of vertical oscillations because the z-dependence of enthalpy on the cylinder $r = r_{\rm in}$ remains quadratic also in this case and the oscillations do not contribute to the radial velocity of accreted matter. Hence, using equations (4.14), (4.18) and (4.31) and assuming that the frequency

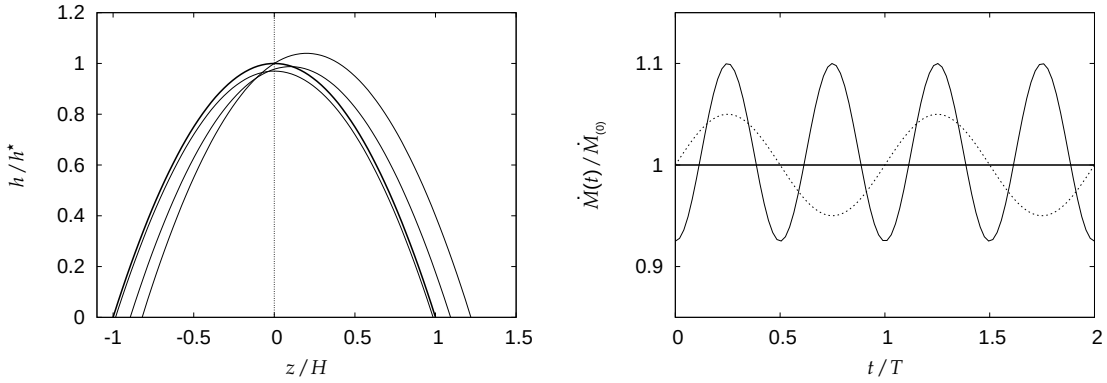

Figure 4.5: Left: The vertical profiles of the enthalpy $h(r_{\rm in}, z)$ on the cylinder $r = r_{\rm in}$ during vertical disk oscillations (thin lines). The amplitude of oscillations is $\delta Z = 0.2H$ and we chose the polytropic index of the fluid $n = 1.5$. The figure captures profiles with the enthalpy maxima at $\delta z = 0, 0.1H$ and $0.2H$. The enthalpy profile for the unperturbed stationary disk is also shown (thick line). Right: The modulated accretion rate from the oscillating disk (thin solid line). The accretion rate for the stationary disk is plotted by thick line. Time is rescaled by the period of oscillations. For reference we plot also the phase of disk oscillations (dotted line) The accretion rate is modulated with twice the frequency of oscillations.

of oscillations equals to the local vertical epicyclic frequency, $\omega = \omega_z$, we arrive at our final result

$$\frac{\delta\dot{M}}{\dot{M}_{(0)}} = (n+1)\frac{\delta h^\star}{h^\star}\frac{2-p}{2-2p}\left[(1+p)\frac{\delta z^2}{H^2} - p\frac{\delta Z^2}{H^2}\right], \tag{4.32}$$

where $\delta M \equiv \dot{M} - \dot{M}_{(0)}$ and $p \equiv n/(n+1/2)$.

Figure 4.5 shows the result. The enthalpy profiles $h(r_{\rm in}, z)$ are shown for several values of δz in the left panel. The amplitude of oscillations is $\delta Z/H = 0.3$. The right panel shows the modulation of the accretion rate from the oscillating disk. The time is rescaled by the oscillation period, $T = 2\pi/\omega_z$. Finally, the time-averaged accretion rate is given by

$$\frac{\langle\delta\dot{M}\rangle}{\dot{M}_{(0)}} = \tfrac{1}{4}(2-p)\frac{\delta Z^2}{H^2} \tag{4.33}$$

that is positive for reasonable values of n.

In this note we studied the accretion rate from a non-stationary pressure supported accretion disk that undergoes the vertical axisymmetric oscillations. The oscillations were modelled by a simple ansatz for the perturbation of poloidal-velocity field. We believe, however, that several features would be present also in more sophisticated (perhaps numerical) solutions: (1) the first correction to the stationary accretion rate is of the quadratic order in both the actual perturbation δz and the amplitude δZ. This is probably because of the symmetry of the stationary flow with respect to the equatorial plane. Hence, the frequency of the modulation must be twice the oscillation frequency. (2) The accretion rate is maximal when the disk reaches the maximal amplitude $\delta z = \delta Z$. (3) The averaged accretion rate from the periodically perturbed flow is greater than the that of the stationary flow.

Summary and further prospects

In the first part of this work we studied the mechanism of epicyclic resonances in the orbital motion in a general axisymmetric gravitational field. For this purpose we adopted the method of multiple scales, sometimes used in different fields of nonlinear physics. The resonance occurs at radii where the epicyclic frequencies are in a ratio of small integers. In particular, we discussed properties of the 1:2, 1:1 and 3:2 resonances in a very general manner (Chapter 3). In the same chapter we also demonstrated that this mechanism does not operate in spherically symmetric gravitational fields, because all resonant terms vanishes in those cases. Instead, the radial and vertical epicyclic modes have to be coupled by an additional nonlinear force. We assumed the Newtonian (or the pseudo-Newtonian) model of the central gravitational field with additional gravitational field of a ring as an example. We remind that, while the 1:1 epicyclic resonance likely operates in the vicinity of Newtonian objects where the two epicyclic frequencies are very close, the 3:2 resonance is more prominent in vicinity of very compact relativistic objects (in this work modeled in terms of pseudo-Newtonian potential).

In our scenario, amplitudes and phases of the oscillations are mutually connected and they follow trajectories in the phase plane with distinct topologies. Our approach also allows to find regions of different phase-plane topology in the $(r, \mathcal{E})$-plane. We note a remarkable similarity of our phase-planes with results of Kozai (1962) who studied resonances in orbit averaged gravitational potentials as well. In some sense these two analyses may be complementary: Our approach is restricted to small eccentricities and inclinations of orbits however it allows large perturbations of spherical gravitational field (it works also in the gravitational field that are highly non-spherical).

The assumption of small epicyclic oscillations is valid in the case of accretion flows. Assuming that the radial and vertical modes are coupled we found that both oscillation frequencies are periodically modulated. We found that this third frequency is inversely proportional to the energy of oscillations. In this context, we pointed to possible connection between the high-frequency and low-frequency QPOs in Sco X-1. Dependending on the phase plane topology and on the initial conditions the ratio of the observed frequencies fluctuates about 3:2 ratio (in the case of librating trajectories) or about a slightly different value (in the case of circulating trajectories).

Finally we remind that we assumed that the nonlinear coupling of the two modes conserves the total energy of epicyclic oscillations. As a next step one intend answer what is the source of the energy.

Part II

Polarization from inverse Compton scattering in relativistic outflows

Introduction

The presence of a dense radiation field is one of the key factors limiting the pre-acceleration of relativistic jets and outflows the innermost regions of active galactic nuclei (AGN) and galactic X-ray binaries often referred as microquasars. The Lorentz factors of the bulk motion $\Gamma \sim 10$ observed in AGN and relatively smaller values $\Gamma \sim 3$ observed in the galactic microquasars well agree with models of radiation drag suggested by many authors (e.g. Abramowicz et al. 1990; Phinney 1982; O'Dell 1981). The interaction of the jet with surrounding radiation as an acceleration mechanism to relativistic speeds has been originally proposed by O'Dell (1981). This issue has been further reconsidered by Phinney (1982) who has shown that the net effect is deceleration rather then acceleration due to the extended distribution of photon fields from an accretion disk. It has been pointed out that if the jet originates in the vicinity of the central black hole it must pass through dense radiation fields from the central region and be subject to the radiative deceleration through the inverse Compton scattering (Sikora et al. 1996a,b). We note that there is an evidence that jet is formed at the distance between 30–100 Schwarzschild radii from the central black hole in the galaxy M87 (Junor et al. 1999). The effects of strong gravity are significant in this region

In many models the Compton scattering is replaced by the Thomson scattering – its classical (non-quantum) analog – for which the cross-section formula does not depend on the energy of incident photons in the electron rest frame, which allows simple analytical calculations. However several authors calculated effects of radiation drag in full Klein-Nishina regime (Luo & Protheroe 1999; Renaud & Henri 1998; Keane et al. 2001). The approximation of the scattering in the Thomson regime seems quite accurate in case of AGN jets where the incident radiation field in the innermost regions is dominated by optical and UV, however it ceases in case of microquasars where the radiation fields are dominated by X-rays. It has been suggested that this difference leads to substantially smaller terminal speed of microquasar jets (Renaud & Henri 1998).

The Compton drag has an important impact on the radiation field. Photons scattered by fast moving electrons are beamed to substantially higher energies reaching X-ray in case of AGNs and γ-ray in case of microquasars. The most of them emerge in the cone with the opening angle proportional to $1/\Gamma^2$ along the bulk motion of the jet. It follows that the Compton up-scattered radiation is an important component of radiation of blazars whose jets are observed almost along the axis of symmetry (Urry & Padovani 1995). The inverse Compton scattering of ambient seed photons by fast moving electrons has been recognized as a prospective source of large degree of linear polarization in different classes of objects. This mechanism likely contributes to polarization of originally unpolarized soft radiation up-scattered in blazar jets (Begelman & Sikora 1987), fast winds from accretion discs (Beloborodov 1998) and in gamma-ray bursts (see Shaviv & Dar 1995a,b; Lazzati et al. 2004; Levinson & Eichler 2004). Optical polarization of $\sim 5\%$ was reported in a

microquasar LS 5039 (Combi et al. 2004), but X-ray polarimetry is still a challenge on technological side, where it requires new generation polarimeters in the focal plane of large area optics (e.g. Costa et al. 2001). It has been noticed that the potential role of polarization is rather important because it can provide additional information with respect to traditional spectroscopy and help to discriminate between different geometries and physical states of sources where accretion processes are accompanied by a rapid ejection. The polarization vector is parallel transported along light rays in strong gravitational fields (Misner, et al. 1973). Therefore, the polarimetry of scattered radiation provides a useful probe into the physics of jets (jet geometry, distribution of particle energies, acceleration mechanism) as well as into the strong gravitational field of the central compact object.

In this part we study linear polarization due to scattering on electron electron clouds. We take into account the radiation drag and the gravitational pull exerted on them in the system consisting of a black hole and thin accretion disk. In Chapter 5 the Stokes paramater describing polarization of radiation are introduced according to standard text books of Rybicky & Lightman (1979), Chandrasekhar (1960) and Sobolev (1963). We calculate the polarization arising from the Thomson scattering on a electron cloud at rest. We show that the Stokes parameters can be expressed using the stress-energy tensor of the incident radiation field. In Chapter 6 we carry out the Lorentz boost and this way we calculate the polarization from Thomson scattering on moving clouds. We show that the in dependence on the cloud velocity resulting linear polarization can be parallel or perpendicular to the projection of cloud velocity onto the observing plane. We also consider scattering on hot clouds with an additional random velocity of the electrons. In that case we show that the electron random motion has depolarizating influence on the scattered radiation. In Chapter 7 the theory is illustrated with the astrophysically relevant example of radiation driven electron clouds in the accreting black hole system. We assume that the spacetime is described by Schwarzschild metric. The cloud motion is included in a self-consistent manner: the clouds move under combined influence of gravitational and radiation fields. The source of radiation field is a standard thin accretion disk and the photons follow rays, which are bent by the black hole gravity. A conceptually similar are the Monte-Carlo simulations of Melia & Königl (1989) who studied simultaneously radiative deceleration of jets and spectral properties of the scattered radiation. However their calculations do not include neither polarization of scattered photons nor general relativistic effects.

We restrict the cloud motion to the axis of symmetry and show possible trajectories in the distance–velocity plane for both, cold and hot clouds. Finally we give several examples of polarization and intensity light curves. These include also contributions of higher order images by photons that encircle the black hole. The detailed calculations of the light rays are presented in the two appendices.

Chapter 5

Polarization and Stokes parameters

5.1 Stokes parameters

First, let us consider a plane monochromatic electromagnetic wave. The time behavior of electric field can be written as $\vec{E}(t,\vec{r}) = \Re[E_0 e^{i(\vec{k}\cdot\vec{r}-\omega t)}]\vec{n}$, where E_0 is a complex amplitude, $\Re$ denotes real part, ω is a wave angular frequency and the unit vector $\vec{n}$ is perpendicular to the wave-vector $\vec{k}$. These two vectors define the polarization plane. The most general plane wave is obtained by a superposition of two waves polarized in perpendicular directions $\vec{e}_X$ and $\vec{e}_Y$

$$\vec{E}(t,0) = \Re\left[(E_{0X}\vec{e}_X + E_{0Y}\vec{e}_Y)\, e^{-i\omega t}\right] = \Re\left[\vec{E}_0 e^{-i\omega t}\right] , \tag{5.1}$$

where we assumed that the waves propagates in the z-direction and we evaluated the electric field at the origin. The vectors $\{\vec{e}_X, \vec{e}_Y, \vec{e}_Z\}$ form the *polarization basis*. The complex amplitudes E_{0x} and E_{0y} can be expressed as $E_{0x} = \mathcal{E}_x e^{i\phi_x}$ and $E_{0y} = \mathcal{E}_y e^{i\phi_y}$ respectively, where all quantities on the right-hand sides are real – $\mathcal{E}_i$ and ϕ_i denote "initial" amplitudes and phases respectively ($i = x, y$). Hence, the equation (5.1) can be rewritten as

$$\vec{E}(t) = \vec{e}_X \mathcal{E}_X \cos(\omega t - \phi_X) + \vec{e}_Y \mathcal{E}_Y \cos(\omega t - \phi_Y). \tag{5.2}$$

Obviously, the end-point of the vector $\vec{E}(t)$ moves along a closed curve in the (X, Y) plane with a period $T = 2\pi/\omega$. In fact this curve is a rotated ellipse as it is apparent from the following procedure: denote $\{X', Y'\}$ the reference which axes coincide with the principal axes of the ellipse traced by the vector $\vec{E}(t)$. This frame is rotated with respect to the frame $\{X, Y\}$ by an angle χ. If the curve is an ellipse, then the components E'_X and E'_Y of the vector $\vec{E}(t)$ in the rotated frame must satisfy equations

$$E'_X = \mathcal{E}\cos\beta\cos\left[\omega(t-t_0)\right] , \quad E'_Y = \mathcal{E}\sin\beta\sin\left[\omega(t-t_0)\right] , \tag{5.3}$$

where β is the circularity parameter of the ellipse, $\beta = \pi/4$ correspond to the circle of a radius $\mathcal{E}$, $\beta = 0$ occurs when the ellipse collapses to a line. Applying the rotation through the angle $-\chi$, we express equation (5.3) in the frame $\{X, Y\}$ using

$$\begin{pmatrix} E_X \\ E_Y \end{pmatrix} = \begin{pmatrix} \cos\chi & -\sin\chi \\ \sin\chi & \cos\chi \end{pmatrix} \begin{pmatrix} E'_X \\ E'_Y \end{pmatrix} . \tag{5.4}$$

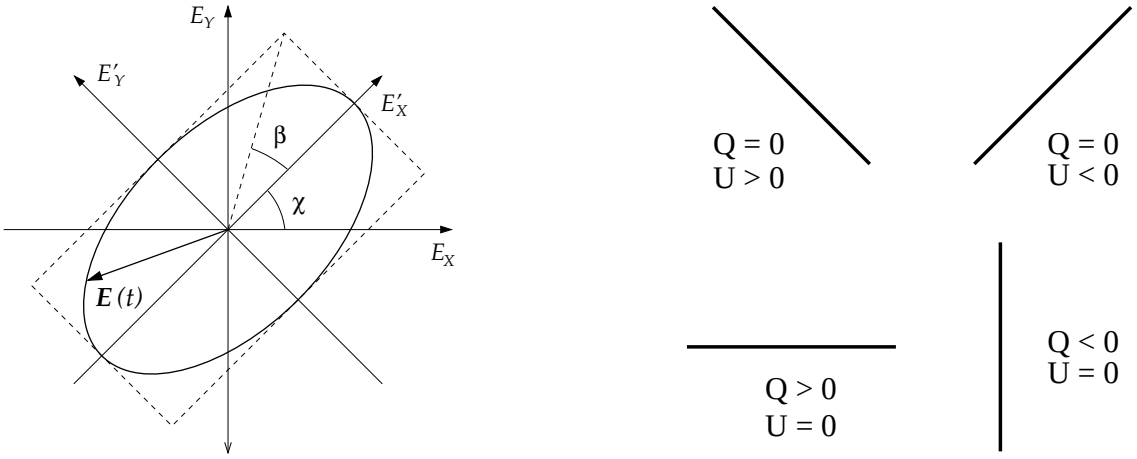

Figure 5.1: Left: The polarization ellipse. Right: Linear-polarization states described by combinations of Stokes Q and U-parameters in the singular cases when one of the Stokes parameter equals zero. The orientation of the polarization plane is deduced directly from the equations (5.8) and (5.7).

Expanding the the right-hand side and comparing E_X and E_Y with components of the vector $\vec{E}(t)$ in equation (5.2), we obtain parameters $\mathcal{E}$, β and χ expressed using $\mathcal{E}_X$, $\mathcal{E}_Y$ ϕ_X and ϕ_Y. A convenient way is to express them using the Stokes parameters that are defined as:

$$I \equiv \mathcal{E}_X^2 + \mathcal{E}_Y^2 = \mathcal{E}^2, \tag{5.5}$$
$$Q \equiv \mathcal{E}_X^2 - \mathcal{E}_Y^2 = \mathcal{E}^2 \cos 2\beta \, \cos 2\chi, \tag{5.6}$$
$$U \equiv 2\mathcal{E}_X \mathcal{E}_Y \cos(\phi_Y - \phi_X) = \mathcal{E}^2 \cos 2\beta \, \sin 2\beta, \tag{5.7}$$
$$V \equiv 2\mathcal{E}_X \mathcal{E}_Y \sin(\phi_Y - \phi_X) = \mathcal{E}^2 \sin 2\beta \tag{5.8}$$

The parameter I is clearly the intensity of the radiation field since it is equal to the amount of energy carried by the wave per time unit. Also other Stokes parameters have clear geometric meaning: V is a circularity parameter, because it is proportional to $\sin 2\beta$. The wave is circularly or linearly polarized when $V = I$ or $V = 0$ respectively. Two other Stokes parameters are connected with the polarization angle χ (the angle of a rotation of the polarization ellipse). Dividing the equations (5.8) and (5.7), we find that

$$\tan 2\chi = \frac{U}{Q}. \tag{5.9}$$

The orientation of a polarization plane (assuming linear polarization) for the singular cases when one of the Stokes Q and U-parameters is zero are shown in the right panel of Figure 5.1.

Let us consider a counter-clockwise rotation in the (X, Y)-plane about the Z-axis through an angle φ by which the polarization basis $\{\vec{e}_X, \vec{e}_Y, \vec{e}_Z\}$ becomes a new one, $\{\vec{e}'_X, \vec{e}'_Y, \vec{e}'_Z\}$. Obviously, the intensity I and the circulation V are invariants, because they do not depend on the angle χ (see the equations (5.6) and (5.8)). The transformation of the two remaining parameters can be found substituting $\chi \to \chi - \varphi$ in the equations (5.7)

and (5.8). Hence, we obtain

$$\begin{pmatrix} Q' \\ U' \end{pmatrix} = \begin{pmatrix} \cos 2\varphi & \sin 2\varphi \\ -\sin 2\varphi & \cos 2\varphi \end{pmatrix} \begin{pmatrix} Q \\ U \end{pmatrix}. \tag{5.10}$$

It follows that also the sum $Q^2 + U^2$ is invariant.

Finally it can be easily shown that only three parameters are needed to describe polarization state of the completely polarized radiation: e.g. the polarization angle χ, the circularity of the polarization ellipse β and the intensity I. The four Stokes parameters are not independent, they satisfy the relation

$$I^2 = Q^2 + U^2 + V^2, \tag{5.11}$$

that easily follows from the equations (5.6)–(5.8).

So far, we have concerned only on the monochromatic waves. But in practice, even in the case of approximately monochromatic light the amplitudes and the phases must be regarded as a liable to incessant variations. These irregular changes may occurs millions of times a second (however, for a completely polarized wave these changes are such that the ratio of the amplitudes in two perpendicular directions and the phase difference should remain absolute constants) Measurements of electromagnetic waves that takes place on much longer time-scales therefore often invokes averaging over time and bandpass. Hence, for a quasi-monochromatic radiation, we define the Stokes parameters by averaging

$$I \equiv \left\langle \mathcal{E}_X^2 + \mathcal{E}_Y^2 \right\rangle = \langle \mathcal{E}^2 \rangle, \tag{5.12}$$

$$Q \equiv \left\langle \mathcal{E}_X^2 - \mathcal{E}_Y^2 \right\rangle = I \cos 2\beta \, \cos 2\chi, \tag{5.13}$$

$$U \equiv 2 \langle \mathcal{E}_X \mathcal{E}_Y \rangle \cos(\phi_Y - \phi_X) = I \cos 2\beta \, \sin 2\beta, \tag{5.14}$$

$$V \equiv 2 \langle \mathcal{E}_X \mathcal{E}_Y \rangle \sin(\phi_Y - \phi_X) = I \sin 2\beta \tag{5.15}$$

Constancy of the amplitude ratio and the phase difference assures that the shape and the orientation of the polarization ellipse is constant through all variations. The equations (5.9) and (5.10) remain valid also in this case.

All four Stokes parameters are independent in the case of a quasi-monochromatic wave. However, they satisfy the relation that is generalization of equation (5.11) and follows from the Schwarz inequality for mean values (Rybicky & Lightman 1979)

$$I^2 \geq Q^2 + U^2 + V^2. \tag{5.16}$$

The proof can be found in standard textbooks (e.g. Chandrasekhar 1960 or Rybicky & Lightman 1979). The relation (5.16) allows to define the degree of polarization or the polarization magnitude of the light as

$$\Pi \equiv \frac{\sqrt{Q^2 + U^2 + V^2}}{I}. \tag{5.17}$$

We have $\Pi = 1$ for a *completely polarized* light and $\Pi = 0$ for an *unpolarized* or a *natural* light for which $U = Q = V = 0$.

A very important property of the Stokes parameters is their additivity for a combination of incoherent streams of radiation. Consider a ray that is mixture of several

independent streams of elliptically polarized light. The total Stokes parameters of the mixture are given as

$$I = \sum_j I^{(j)}, \quad Q = \sum_j Q^{(j)}, \quad U = \sum_j U^{(j)}, \quad V = \sum_j V^{(j)}, \tag{5.18}$$

where $I^{(j)}$, $Q^{(j)}$, $U^{(j)}$ and $V^{(j)}$ are Stokes parameters of the streams. The words "incoherent" and "independent" mean that the component streams that form the mixture have no permanent phase relations between themselves. We do not expect the light from astronomical sources to be completely polarized because it generally comes from different parts of the source with different intensity and polarization angle.

The additivity of the Stokes parameters has several important consequences. Firstly, any partially polarized beam of radiation can be regarded as a mixture of the natural and completely polarized beams. Let (I, Q, U, V) be the Stokes parameters of the beam, then the Stokes parameters of the natural and completely polarized beams are $(I - \sqrt{Q^2 + U^2 + V^2}, 0, 0, 0)$ and $(\sqrt{Q^2 + U^2 + V^2}, Q, U, V)$ respectively. Secondly, the completely unpolarized beam of radiation with the intensity I can be regarded as a superposition of two completely linearly polarized beams in two perpendicular directions. Consider a polarization basis $\{\vec{e}_X, \vec{e}_Y, \vec{e}_Z\}$. The Stokes parameters of that two components are $(I/2, I/2, 0, 0)$ and $(I/2, -I/2, 0, 0)$.

5.2 Thomson scattering

Let us consider the plane monochromatic electromagnetic wave propagating in the direction of a basis vector $\vec{e}_X$. The scatterer is a free electron located in the origin of the basis $\{\vec{e}_X, \vec{e}_Y, \vec{e}_Z\}$, we assume that the observer is situated along the vector $\vec{e}_Z$. The physics behind the Thomson scattering is very simple; The wave interacts with the electron and causes its oscillations in the direction of the electric vector $\vec{E}(t)$. Observed is then a scattered radiation is a dipole radiation due to electron oscillations. Let the wave be completely polarized in the y-direction. Then, according to the dipole formula, the electron will radiate with the intensity proportional to $\sin^2\psi$, where ψ is the angle between the direction of polarization of the incident wave and the direction of observation ($\psi = \pi/2$ in our case). The "scattered" radiation is completely polarized in the y-direction. On the other hand, if the incident wave is polarized in the z-direction then the wave causes electron oscillations in the direction of observation and according to the dipole formula (now $\psi = 0$) and no radiation is emitted toward the observer.

The Thomson scattering is an important source of polarized radiation. If the incident radiation of the intensity I is unpolarized, then it can be imagined as a mixture of two components of the same intensity $I/2$ completely polarized in the direction X and Y respectively. However, only the the component polarized in the X-direction contributes to the signal radiated into the Y-direction and the observer receive radiation completely polarized in the direction Y.

The above-given considerations can be easily formalized and further generalized. Let us consider the scattering of the incident unpolarized beam of radiation on the small optically thin electron cloud. For present we do not consider individual motion of electrons, hence, we can assume that the electrons are at rest with respect to the observer. The electron density in the cloud is n_e and the volume of the cloud is V. The direction of the incident radiation beam $\vec{n}_\mathrm{i}$ and the direction of observation $\vec{e}_Z$ make an angle ω. The

angle ω and the plane which contains the directions of the incident and the scattered light will be referred to as the scattering angle and the scattering plane respectively. The other vectors of the polarization basis $\vec{e}_X$ and $\vec{e}_Y$ are chosen in the scattering plane and perpendicularly to it respectively. The incident beam is regarded as a mixture of two perpendicularly polarized components of the same intensity $I_\mathrm{i}/2$ labeled as a and b. The a-component is completely polarized in the scattering plane and the b-component is polarized perpendicularly to it (e.g. b is polarized in the direction of the vector $\vec{e}_Y$). Thomson differential cross-section for a completely polarized incident radiation can be expressed according to the dipole formula

$$\left(\frac{\mathrm{d}\sigma}{\mathrm{d}\Omega}\right)_\mathrm{pol} = r_\mathrm{e}^2 \sin^2\psi, \quad r_\mathrm{e} \equiv \frac{e^2}{mc^2} = \sqrt{\frac{3\sigma_\mathrm{T}}{8\pi}}, \tag{5.19}$$

where r_e is the electron classical radius and σ is the Thomson total cross-section as will be shown below. The components a and b are scattered with angles $\psi_a = \omega$ and $\psi_b = \pi/2$ independently on the scattering angle ω. Hence for the intensities of the scattered components on the cloud we get

$$I_a = \tfrac{1}{2} n r_\mathrm{e}^2 R I_\mathrm{i} \sin^2\psi_a = A I_\mathrm{i} \cos^2\omega, \tag{5.20}$$

$$I_b = \tfrac{1}{2} n r_\mathrm{e}^2 R I_\mathrm{i} \sin^2\psi_b = A I_\mathrm{i}, \tag{5.21}$$

where R is the size of the cloud, $A \equiv 3\tau/16\pi$ and $\tau \equiv n_\mathrm{e}\sigma_\mathrm{T}R$ is the Thomson optical depth of the cloud. As the scattered radiation (if any) is always completely polarized in the direction of the original radiation, the Stokes parameters Q_a and Q_b with respect to the observer polarization basis $\{\vec{e}_X, \vec{e}_Y, \vec{e}_Z\}$ can be written as $Q_a = -I_a$ and $Q_b = I_b$ because the a and b components of the incident radiation was polarized in the directions $\vec{e}_X$ and $\vec{e}_Y$ respectively. The other parameters are zero. Due to the additivity of the Stokes parameters (5.18), the resulting polarization is given as

$$I = A(1+\cos^2\omega) I_\mathrm{i}, \quad Q = -A I_\mathrm{i} \sin^2\omega, \quad U = 0, \quad V = 0. \tag{5.22}$$

From this we recover the well-know result that the polarization magnitude from the single scattering of a single beam of radiation is

$$\Pi = \frac{|Q|}{I} = \frac{\sin^2\omega}{1+\cos^2\omega}. \tag{5.23}$$

Let us consider now a more general case where the scattering plane is not aligned with the basis vector $\vec{e_X}$. Then the Q and U parameters given by equation (5.22) are valid in the basis $\{\vec{e}'_X, \vec{e}'_Y, \vec{e}'_Z\}$ that arises from the observer polarization basis $\{\vec{e}_X, \vec{e}_Y, \vec{e}_Z\}$ by a rotation about the vector $\vec{e}_Z$ so that the scattering plane and the vector $\vec{e}'_X$ become aligned. Let us denote the angle of the rotation η and the Stokes parameters with respect to the rotated polarization basis Q' and U'. The parameters Q' and U' are given by the equation (5.22) and the angle η is measured from the vector $\vec{e}_X$ to the rotated vector $\vec{e}'_X$. Using the transformation rule (5.10), we find that

$$Q = Q' \cos 2\eta, \quad U = Q' \sin 2\eta. \tag{5.24}$$

Hence, the nonzero stokes parameters from the single scattering of the incident unpolarized radiation beam of the intensity I_i are given as

$$I = A I_\mathrm{i}(1+\cos^2\omega), \quad Q = -A I_\mathrm{i} \cos 2\eta \, \sin^2\omega, \quad U = -A I_\mathrm{i} \sin 2\eta \, \sin^2\omega \tag{5.25}$$

The scattering takes place in the plane that forms an angle η with the vector $\vec{e}_X$. Angles η and ω can be expressed using direction cosines, which are defined here as components of the direction vector $\vec{n}_\mathrm{i}$ of the incident radiation beam,

$$n_\mathrm{i}^X = \cos\eta\,\sin\omega, \quad n_\mathrm{i}^Y = \sin\eta\,\sin\omega, \quad n_\mathrm{i}^Z = \cos\omega. \tag{5.26}$$

We obtain

$$I = A\left(1 + n_\mathrm{i}^Z n_\mathrm{i}^Z\right) I_\mathrm{i} \quad Q = A\left(n_\mathrm{i}^Y n_\mathrm{i}^Y - n_\mathrm{i}^X n_\mathrm{i}^X\right) I_\mathrm{i}, \quad U = -2A\, n_\mathrm{i}^X n_\mathrm{i}^Y I_\mathrm{i}. \tag{5.27}$$

even for one particular source The form of the Stokes parameters in equation (5.27) is useful, as it allows us to formally integrate partial contributions over incident directions in a general radiation field. Let the radiation field is described by the frequency-integrated intensity $I(\vec{n})$. Then the Stokes parameters from the Thomson scattering is given by the integration over the direction of incident radiation $\vec{n}_\mathrm{i}$. This way we find

$$I = A\left(\varepsilon + \wp^{ZZ}\right), \tag{5.28}$$

$$Q = A\left(\wp^{YY} - \wp^{XX}\right), \tag{5.29}$$

$$U = -2A\wp^{XY}, \tag{5.30}$$

for the total Stokes parameters of scattered light. Where

$$\varepsilon \equiv \int_{4\pi} I_\mathrm{i}(\vec{n}_\mathrm{i})\,\mathrm{d}\Omega, \quad \wp^{ij} \equiv \int_{4\pi} n_\mathrm{i}^i n_\mathrm{i}^j I_\mathrm{i}(\vec{n}_\mathrm{i})\,\mathrm{d}\Omega \tag{5.31}$$

are the radiation energy density and the radiation pressure tensor of the incident radiation field.

The relationship between the Stokes parameters of the scattered radiation and the moments of incident radiation intensity given by equations can be found in Sobolev (1963). It represents a starting point of the presented work. It was derived under the assumption that the scatterer is at rest with respect to the observer polarization basis. In the next chapter we further generalize it to the case of a general motion by means of the special relativity. This approach also allows us to give an analogical expressions in the situations when the scatterer contains warm electrons with their own individual motion.

Chapter 6

Scattering on moving clouds

Incident photons of ambient unpolarized radiation become highly polarized when scattered by relativistically moving electrons. The total polarization is obtained by integrating over all directions of incident photons and all scattering electrons in the observation volume. In this section we generalize our considerations to the case of the on-axis motion of a scatterer in an axially symmetric radiation field with an arbitrary velocity. The both cases when the scatterer is a cold electron cloud and when it is a cloud with random electron velocities are considered. The simplicity of derived equations between frequency-integrated quantities allows us to include the effects arising from the geometry of an incident radiation field without any approximation.

We denote spatial three-vectors by an arrow and the corresponding four-vectors by boldface letters. Hereafter we will simply use four-vector notation. For example, indices of four-vectors with respect to a local-frame basis are manipulated by flat-spacetime metric $\eta_{\alpha\beta} = \mathrm{diag}(-1, 1, 1, 1)$. We also use the geometrical units where $G = c = 1$ for simplicity. However, we will keep c and G in several cases where dimensions of the quantities are important.

6.1 Polarization and laboratory reference frames

Let us consider a simple case when the incident radiation field is axially symmetric in the laboratory frame (LF) $(\boldsymbol{e}_t, \boldsymbol{e}_x, \boldsymbol{e}_y, \boldsymbol{e}_z)$ and the scattering medium is a swarm of electrons, which can be assigned a unique velocity. We orient the vector $\boldsymbol{e}_z$ along the symmetry axis, two other spatial vectors $\boldsymbol{e}_x$ and $\boldsymbol{e}_y$ lie in a plane containing the electron velocity and are perpendicular to $\boldsymbol{e}_z$. Further, we assume that the electrons are moving along the symmetry axis with four-velocity $\boldsymbol{u} = u^t \boldsymbol{e}_t + u^z \boldsymbol{e}_z$ with components $u^t = \gamma$ and $u^z = \gamma\beta$ (γ is Lorentz factor, β is velocity in LF divided by the speed of light). Later on we carry out a Lorentz boost to co-moving frame (CF) of the scatterer, $(\bar{\boldsymbol{e}}_t, \bar{\boldsymbol{e}}_x, \bar{\boldsymbol{e}}_y, \bar{\boldsymbol{e}}_z)$, which is equipped with time-like four-vector $\bar{\boldsymbol{e}}_t = \boldsymbol{u}$ and three space-like four-vectors $\bar{\boldsymbol{e}}_x = \boldsymbol{e}_x$, $\bar{\boldsymbol{e}}_y \equiv \boldsymbol{e}_y$. Spatial part of $\bar{\boldsymbol{e}}_z$ is oriented in the direction of relative velocity of both frames.

In order to describe propagation of scattered photons, we define four-vectors $\boldsymbol{n} \equiv \boldsymbol{p}/p^t$ (with respect to LF) and $\bar{\boldsymbol{n}} \equiv \boldsymbol{p}/\bar{p}^t$ (with respect to CF), where $\boldsymbol{p}$ is the photon four-momentum (a null four-vector). Due to the axial symmetry we can assume $n^y = \bar{n}^y = 0$.

In addition to the above-defined reference frames LF and CF, we introduce two 'polarization' frames that are spacetime generalizations of the polarization basis introduced in the previous section: the laboratory polarization frame (LPF) with basis $(\boldsymbol{e}_t, \boldsymbol{e}_X, \boldsymbol{e}_Y, \boldsymbol{e}_Z)$,

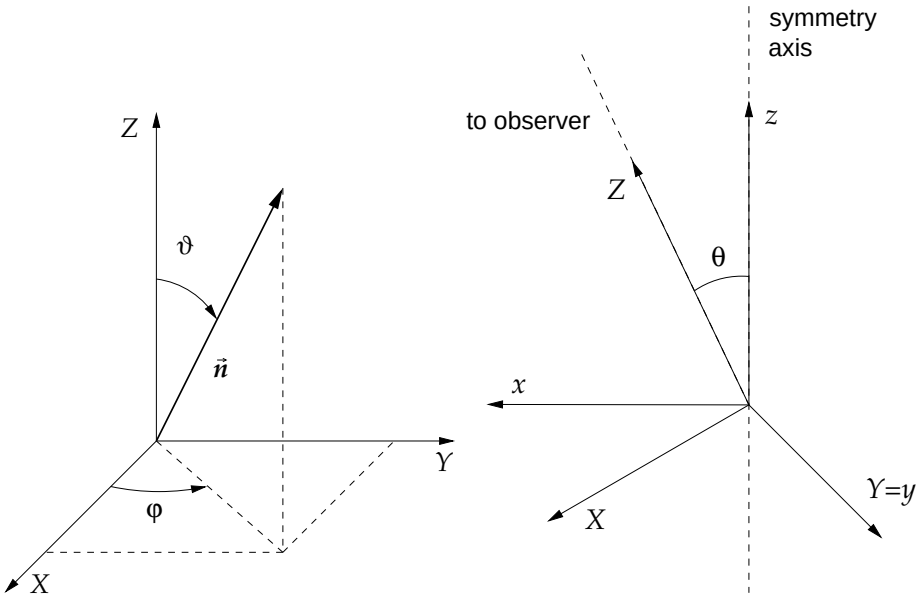

Figure 6.1: Definition of angles and the polarization basis. Left: co-moving polarization frame (CPF) The direction to the observer is along the $\bar{Z}$-axis. The direction of the incident photon $\vec{n}_\mathrm{i}$ is described by the angles φ and ϑ. Right: The laboratory frame (LF) and the laboratory polarization frame (LPF). The direction toward the observer is along the Z-axis. The axis of symmetry is identical with the z-axis. The two frames are transformed by rotation about the y-axis through the angle θ. The definitions of co-moving frames CF and CPF are analogical.

and the co-moving polarization frame (CPF) with the basis $(\bar{\boldsymbol{e}}_t, \bar{\boldsymbol{e}}_X, \bar{\boldsymbol{e}}_Y, \bar{\boldsymbol{e}}_Z)$. LPF is defined in such a way that $\boldsymbol{e}_Z$ is the three-space projection of the propagation four-vector $\boldsymbol{n}$, $\boldsymbol{e}_X$ lies in the $(\boldsymbol{e}_x, \boldsymbol{e}_z)$-plane, and $\boldsymbol{e}_Y$ is identical with the LF tetrad vector $\boldsymbol{e}_y$. CPF is defined analogically and denoted by bars over variables. Note that because of the condition $n^y = \bar{n}^y = 0$ the y-axes are the same in all reference frames. Our definition of the reference frames is apparent from Figure 6.1.

6.2 Stokes parameters of the scattered radiation

We start by calculating the polarization of the scattered radiation in CPF. For this purpose we use the equations (5.28)–(5.30). The radiation energy density ε and the radiation pressure tensor $\wp^{ij}$ find their relativistic analogs in the stress-energy tensor defined as

$$\bar{T}^{\mu\nu} \equiv \int_{4\pi} \bar{n}_\mathrm{i}^\mu \bar{n}_\mathrm{i}^\nu \bar{I}_\mathrm{i}(\bar{\boldsymbol{n}}_\mathrm{i})\,\mathrm{d}\Omega, \tag{6.1}$$

where $\bar{\boldsymbol{n}}_\mathrm{i}$ is the propagation vector of the incident radiation and $\bar{I}_\mathrm{i}(\bar{\boldsymbol{n}})$ is its frequency-integrated intensity. In CPF we have

$$\bar{T}^{tt} = \bar{\varepsilon}, \quad \bar{T}^{ij} = \bar{\wp}^{ij}. \tag{6.2}$$

Hence with aid of this equation the equations (5.28)–(5.30) become

$$\bar{I} = A\left(\bar{T}^{tt} + \bar{T}^{ZZ}\right), \tag{6.3}$$

$$\bar{Q} = A\left(\bar{T}^{YY} - \bar{T}^{XX}\right), \tag{6.4}$$

$$\bar{U} = -2A\bar{T}^{XY}, \tag{6.5}$$

We remind, that the incident radiation field was assumed axially symmetric in the CF, therefore the only nonzero components in this frame are $\bar{T}^{tt}$, $\bar{T}^{tz}$, $\bar{T}^{zz}$, T^{xx}, T^{yy}. These are further constrained by symmetry, $T^{xx} = T^{yy} = (T^{tt} - T^{zz})/2$, and related to the components in CPF by rotation about $\bar{y}$-axis by angle $\bar{\vartheta}$:

$$\bar{T}^{ZZ} = \bar{T}^{xx}\sin^2\bar{\vartheta} + \bar{T}^{zz}\cos^2\bar{\vartheta}, \tag{6.6}$$

$$\bar{T}^{XX} = \bar{T}^{xx}\cos^2\bar{\vartheta} + \bar{T}^{zz}\sin^2\bar{\vartheta}, \tag{6.7}$$

$$\bar{T}^{YY} = \bar{T}^{yy}, \tag{6.8}$$

$$\bar{T}^{XY} = 0 \tag{6.9}$$

By substituting into the equations (6.3)–(6.5) we find that

$$\bar{I} = \tfrac{1}{2}A\left[\left(3\bar{T}^{tt} - \bar{T}^{zz}\right) - \left(\bar{T}^{tt} - 3\bar{T}^{zz}\right)\cos^2\bar{\vartheta}\right], \tag{6.10}$$

$$\bar{Q} = \tfrac{1}{2}A\left(\bar{T}^{tt} - 3\bar{T}^{zz}\right)\sin^2\bar{\vartheta}. \tag{6.11}$$

Due to the axial symmetry the remaining Stokes parameter $\bar{U}$ vanishes. The Stokes parameters are related to CPF. As a consequence the scattered radiation is partially polarized either in the $(\bar{x}, \bar{z})$-plane or perpendicularly to it (see equation (5.9) and the following discussion). The former and the latter case will be referred as *longitudinal* or *transversal polarization*, respectively.

The degree of polarization can be calculated directly from the definition (5.17)

$$\Pi(\bar{\theta}) = \frac{|\bar{Q}|}{\bar{I}} = \frac{|\Pi_{\mathrm{m}}|\sin^2\bar{\vartheta}}{1 - \Pi_{\mathrm{m}}\cos^2\bar{\vartheta}}, \quad \Pi_{\mathrm{m}} \equiv \frac{\bar{T}^{tt} - 3\bar{T}^{zz}}{3\bar{T}^{tt} - \bar{T}^{zz}}. \tag{6.12}$$

The meaning of the quantity Π_{m} is evident: the absolute value $|\Pi_{\mathrm{m}}|$ is the maximum degree of polarization of the scattered light observed under the suitable angle and the sign of Π_{m} determines the sign of $\bar{Q}$-parameter. The radiation scattered along the z-axis, for which $\bar{\vartheta} = 0$, is completely unpolarized. As $\bar{\vartheta}$ grows the polarization degree increases to its maximal magnitude $|\Pi_{\mathrm{m}}|$, which occurs for $\bar{\vartheta} = \pi/2$. This states a well-known fact that the polarization is maximal for the radiation scattered perpendicularly to axis of symmetry in the CF.

In order to determine the polarization magnitude as seen by an observer in LF we carry out the Lorentz boost. Non-zero coefficients of Lorentz transformation are $\Lambda^t_t = \Lambda^z_z = \gamma$, $\Lambda^t_z = \Lambda^z_t = -\gamma\beta$ and $\Lambda^x_x = \Lambda^y_y = 1$. The angle of observation $\bar{\vartheta}$ is transformed according to:

$$\sin\bar{\vartheta} = \mathcal{D}\sin\vartheta, \quad \cos\bar{\vartheta} = \mathcal{D}(\cos\vartheta - \beta), \tag{6.13}$$

where $\mathcal{D} \equiv \gamma^{-1}(1 - \beta\cos\theta)^{-1}$ is Doppler factor (c.f. Rybicky & Lightman 1979). All Stokes parameters are transformed from the CPF to PF in the same way as the radiation intensity because the boost retains the four-vector $\boldsymbol{e}_y$ unchanged (Cocke & Holm 1972). Therefore we find

$$I = \mathcal{D}^4\bar{I} \quad \text{and} \quad Q = \mathcal{D}^4\bar{Q}. \tag{6.14}$$

It follows that the polarization magnitude Π_{m} is Lorenz invariant. Performing the Lorentz transformation (6.14) and expressing all quantities in LF we find explicit formulae for the

Stokes parameters of the scattered radiation,

$$Q = \tfrac{1}{2} A \mathcal{D}^6 \gamma^2 \left[(1-3\beta^2) T^{tt} + 4\beta T^{tz} - (3-\beta^2) T^{zz} \right] \sin^2 \vartheta, \tag{6.15}$$

$$I = A \mathcal{D}^4 \gamma^2 \left[(1+\beta^2) \left(T^{tt} + T^{zz} \right) - 4\beta T^{tz} \right] + Q. \tag{6.16}$$

6.3 Change of the polarization direction

The aim of this section is to connect, in a self-consistent manner, the properties of particle motion through the ambient radiation field with Stokes parameters of scattered light. In order to prepare for this discussion it is useful to introduce two critical velocities of the particle motion.

Firstly, of particular interest is the velocity at which the polarization of scattered radiation vanishes (Beloborodov 1998). The condition for velocity follows from the requirement

$$\bar{T}^{tt} - 3\bar{T}^{zz} = 0. \tag{6.17}$$

Performing the Lorentz boost to LF we obtain

$$\left(1-3\beta^2\right) T^{tt} + 4\beta T^{tz} + \left(\beta^2 - 3\right) T^{zz} = 0. \tag{6.18}$$

This is a quadratic equation for β, which has two roots,

$$\beta_{1,2} = a \pm \sqrt{a^2 + b}\,, \tag{6.19}$$

where

$$a \equiv \frac{2T^{tz}}{3T^{tt} - T^{zz}}\,, \quad b \equiv \frac{T^{tt} - 3T^{zz}}{3T^{tt} - T^{zz}}\,. \tag{6.20}$$

Clearly, equation (6.17) can be satisfied independently of the direction of observation. For $\beta \to \beta_{1,2}$ the polarization changes from longitudinal to transversal.

Next, we introduce the saturation velocity β_0 (Sikora & Wilson 1981). As was shown by various authors under different approximations about the particle cross-section and the form of gravitational field (see e.g. Abramowicz et al. 1990; Vokrouhlický & Karas 1991; Melia & Königl 1989; Fukue & Hachiya 1999; Keane et al. 2001), the saturation velocity plays an important role in the dynamics of relativistic jets: particles moving at velocity smaller/greater than the saturation velocity gain/lose their momentum at the expense of the radiation field. In absence of other acceleration mechanisms and neglecting inertia of particles, the effect of radiation pressure eventually leads to $\beta \to \beta_0$ as terminal speed of the particle motion.

The saturation velocity is determined by the requirement of the vanishing radiation flux in CF, i.e.

$$\bar{T}^{tz} = 0. \tag{6.21}$$

This gives another quadratic equation,

$$\left(1+\beta^2\right) T^{tz} - \beta \left(T^{tt} + T^{zz} \right) = 0, \tag{6.22}$$

with the solution

$$\beta_0 = \frac{1 - \sqrt{1-\sigma^2}}{\sigma}\,, \tag{6.23}$$

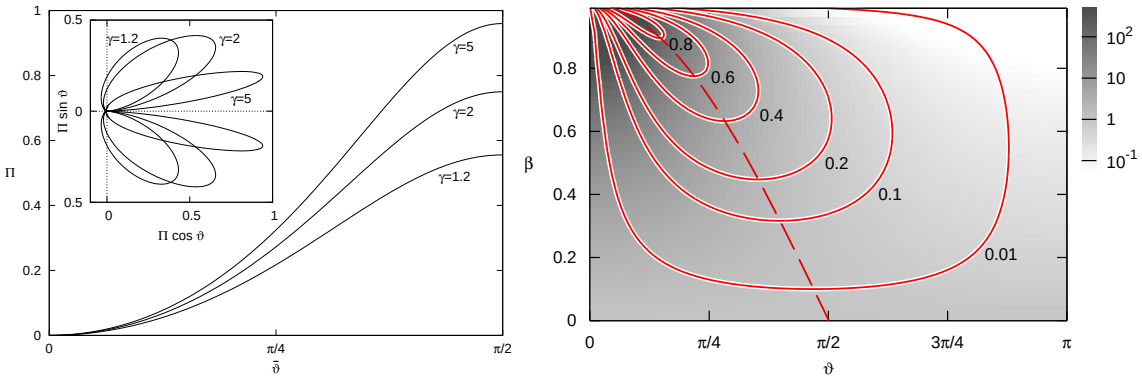

Figure 6.2: Left: the magnitude of transversal polarization $\Pi(\bar{\vartheta};\gamma)$ due to up-scattering by a relativistic electron as a function of the observing angle in the local co-moving frame. The case of locally isotropic ambient radiation field is shown for three different values of Lorentz factor γ. In the inset the emission diagram shows the corresponding lab-frame polarization. The lobes become gradually flattened toward the front direction of motion as γ increases. Right: Contours of $\Pi(\vartheta,\beta) = \text{const}$ are shown superposed on the density plot of $I(\vartheta,\beta)$. Levels of shading give the intensity (in arbitrary units) and illustrate the progressive beaming towards $\vartheta = 0$ direction in the ultra-relativistic limit. On the other hand, given a value of β, the polarization degree $\Pi(\vartheta;\beta)$ as function of ϑ reaches maximum at a non-zero angle, always off axis (dashed line). This corresponds to a well-known fact that polarization is maximum for the radiation scattered perpendicularly to axis of symmetry in the CF.

where $\sigma \equiv 2T^{tz}/(T^{tt}+T^{tz})$. We ignore the second solution, as it has no physical meaning.

Let us illustrate the theory proposed above by two examples. We first assume the incident radiation field to be purely isotropic in the laboratory frame, i.e.

$$T^{\alpha\beta} = \text{diag}\left(\varepsilon, \tfrac{1}{3}\varepsilon, \tfrac{1}{3}\varepsilon, \tfrac{1}{3}\varepsilon\right), \tag{6.24}$$

with $\varepsilon \equiv T^{tt}$ being energy density of radiation. Evaluating the stress-energy tensor in CF we find $\Pi_{\rm m} = -\beta^2$. Substituting into the equation (6.12) we obtain polarization degree

$$\Pi(\bar{\vartheta},\beta) = \frac{\beta^2 \sin^2\bar{\vartheta}}{1+\beta^2\cos^2\bar{\vartheta}}\ . \tag{6.25}$$

Lorentz transformation to LF gives

$$\Pi(\vartheta,\beta) = \frac{\beta^2\sin^2\vartheta}{(2\gamma^2-1)\left(1-\beta\cos\vartheta\right)^2 - \beta^2\sin^2\vartheta}\ . \tag{6.26}$$

Since $\Pi_{\rm m} \le 0$, the scattered radiation is polarized transversely. The critical velocities are $\beta_0 = \beta_1 = \beta_2 = 0$ in this case.

Figure 6.2 shows the dependence of Π on the observing angle according to equation (6.25). It can be seen (in the left panel) that the resulting curves closely resemble the numerical result of Lazzati et al. (2004; cp. their Figure 1) who employ specific (frequency-dependent) quantities. In particular, the curves are identical for $\gamma \gg 1$ and they approach the ultra-relativistic limit $\Pi = (1-\cos^2\bar{\vartheta})/(1+\cos^2\bar{\vartheta})$ of Shaviv & Dar (1995a). This limit corresponds to the case of a head-on collision, when all photons are

impinging at incident angles $\bar{\vartheta}_{\rm i} \to \pi$ because of aberration in CF (this result can be also directly obtained from equation (5.23) in the limit $\omega \to \pi$).

For moderate Lorentz factors there is some difference between our profile of $\Pi(\bar{\vartheta})$ and the corresponding numerical values plotted in Lazzati et al. (2004). For example, checking the $\gamma = 2$ curve, we notice that relative difference amounts to roughly 13%. This apparent discrepancy is explained by realizing that our eq. (6.25) has been derived in terms of frequency integrated quantities (which are magnified by a factor of $\mathcal{D}^4$ by the transformation from CF to LF, as mention above). On the other hand, Lazzati et al. employ specific quantities. We can reproduce their values if we limit the frequency range to some finite interval $\langle \nu_{\rm min}, \nu_{\rm max} \rangle$ in our calculation, although then we lose some photons – those which are up-scattered to frequency higher than $\mathcal{D}_+ \nu_{\rm max}$ or, vice-versa, down-scattered to frequency lower than $\mathcal{D}_- \nu_{\rm min}$, where $\mathcal{D}_\pm \equiv (1 \pm \beta)^{1/2}(1 \mp \beta)^{-1/2}$. In order to demonstrate clearly the relationship between both approaches, let us also consider, for a moment, the case of frequency dependent specific intensity $I_{{\rm i}\nu}$ of incident light. We restrict the range in such a way that non-zero $I_{{\rm i}\nu} = {\rm const}$ is for $\nu_{\rm min} \le \nu \le \nu_{\rm max}$, otherwise $I_{{\rm i}\nu} = 0$. We calculated numerically the corresponding frequency-dependent Stokes parameters and polarization Π_ν of scattered radiation. It was shown that the scattered intensity is non-zero in the mentioned range $\mathcal{D}_- \nu_{\rm min} \le \nu \le \mathcal{D}_+ \nu_{\rm max}$. We also find that Π_ν is constant and identical with Lazzati et al. profile for $\mathcal{D}_+ \nu_{\rm min} \le \nu \le \mathcal{D}_- \nu_{\rm max}$. Within this range the directional distribution of the incident radiation in the electron CF is not affected by existence of two cut-off frequencies $\nu_{\rm min}$ and $\nu_{\rm max}$. However, outside this range the polarization depends on frequency. The resulting polarization degree comes out greater than the value shown by Lazzati et al. in the entire interval $\langle \mathcal{D}_- \nu_{\rm max}, \mathcal{D}_+ \nu_{\rm max} \rangle$. In the end, by integrating the polarization over frequency we recover exactly the value predicted by equation (6.25).

Next, we consider the simplest case of an anisotropic incident radiation field. The radiation field is axially symmetric with respect to the direction of the particle motion. We assume that the intensity of incident radiation is nonzero in the cone of the opening angle α and it is zero everywhere else. Finally we explore effects of a mixture of both, the isotropic and the anisotropic component. The stress-energy tensor of the anisotropic component can be calculated according to definition (6.1). We obtain

$$T^{tt}_{\rm a} = 2\pi I \left(1 - \cos\alpha\right), \tag{6.27}$$

$$T^{tz}_{\rm a} = \pi I \sin^2\alpha, \tag{6.28}$$

$$T^{zz}_{\rm a} = \tfrac{2}{3}\pi I \left(1 - \cos^3\alpha\right). \tag{6.29}$$

There are two other nonzero components, $T^{xx}_{\rm a} = T^{yy}_{\rm a}$, which can be evaluated from the condition $T^\sigma_{{\rm a}\sigma} = 0$. The stress-energy tensor of the mixture of the isotropic and anisotropic components is given by the a sum of the stress tensors of the two components.

We first calculate the polarization for a given velocity β of the scatterer. The incident radiation field is parameterized by the angle α. Figure 6.4 shows the effect of vanishing and changing polarization which occurs at particular values of $\beta(\alpha)$. The Left panel shows the case of purely anisotropic radiation field and the Right one shows shows the case of the mixture of both components. The intensity of the isotropic component is smaller than that of the anisotropic by a factor 10^{-3}. Clearly, the isotropic component is important only at small values of the angle α, for which the energy density of both components are comparable. Note also, that the polarization of the scattered radiation is transversal when the scatterer is accelerated or decelerated by the radiation field and it is longitudinal when the velocity of the scatterer is saturated by the radiation field.

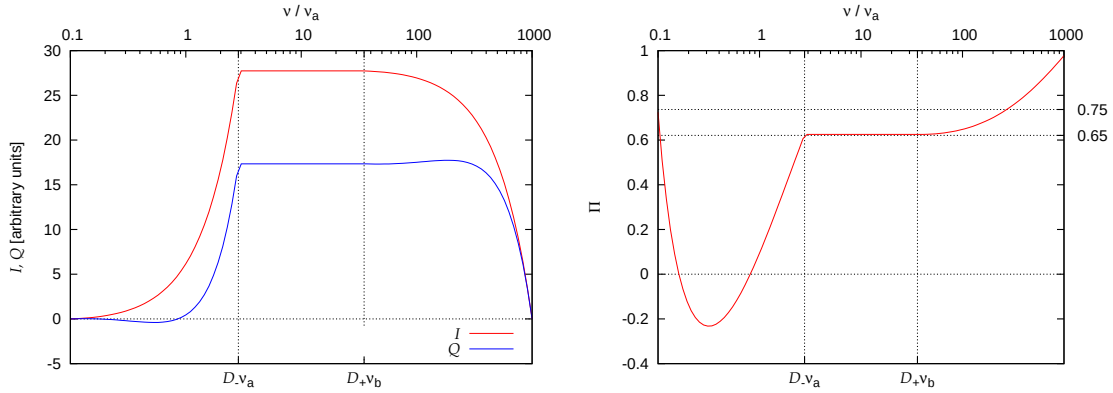

Figure 6.3: Numerically calculated specific (frequency dependent) quantities of Thomson-scattered radiation on the electron moving in the isotropic incident radiation field. The specific intensity of the incident radiation is $I_{\mathrm{i}\nu} = \mathrm{const}$ for $\nu_{\min} \le \nu \le \nu_{\max}$, otherwise $I_{\mathrm{i}\nu} = 0$. The left panel shows the frequency dependences of the Stokes parameters I_ν and Q_ν, the right panel shows the specific polarization Π_ν. Clearly, scattered radiation do not depend on the frequency in the frequency range $\mathcal{D}_+\nu_{\min} \le \nu \le \mathcal{D}_-\nu_{\max}$ where the angular distribution of the incident intensity in the electron co-moving frame is not affected by cut-offs at $\nu_{\min}$ and $\nu_{\max}$. The polarization magnitude is equal to the value 0.65 of Lazzati et al. (2004) in this frequency range. However integrating the polarization over the whole range we obtain value 0.75 given by the equation (6.25).

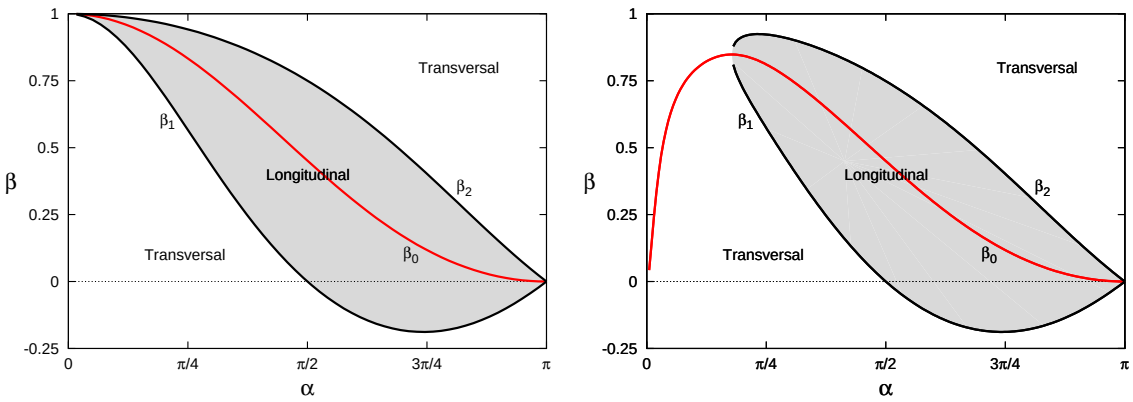

Figure 6.4: Left: The case of incident radiation originating from an isotropic source of angular radius α; see equations (6.27)–(6.29). Two branches of critical velocity are shown, $\beta_1(\alpha)$ and $\beta_2(\alpha)$, at which the total polarization of scattered light vanishes independent of the observing direction. The saturation curve $\beta_0(\alpha)$ is also plotted assuming that the radiation drag dominates the particle dynamics. Right: the same as on the left but for a mixture of two components of the incident radiation, i.e. the ambient isotropic ($\alpha = \pi$) source plus (non-isotropic) contribution of radiation from the source. The intensity of the isotropic component is smaller than that of the anisotropic one by the factor $\lambda_{\mathrm{i}} = 0.001$. In both panels, the regions of longitudinal and transversal polarization are distinguished by shading.

Despite of its simplicity, this model gives interesting consequences. Consider the case when the source of incident radiation field is a compact relativistic star. The star of radius $R_\star$ appears to the static observer (i.e. the particle) located at radial coordinate r as a bright disc of angular radius α, where

$$\sin\alpha(r) = \frac{\tilde{R}}{r}\,\frac{\xi(r)^{1/2}}{\xi(\tilde{R})^{1/2}} \tag{6.30}$$

and $\tilde{R} \equiv \max\{\frac{3}{2}R_{\rm S}, R_\star\}$ (Synge 1967), where $R_{\rm S} \equiv 2GMc^{-2} \doteq 1.5\times10^5 (M/M_\odot)$cm is the Schwarzschild radius and M is the mass of the star. $R_{\rm S}$ is the Schwarzschild gravitational radius. Due to the light bending the solid angle subtended by a compact star on the sky is larger than the Euclidean (flat space) estimate. The stellar radiation field provide physical realization of the anisotropic component of radiation field with the intensity

$$I(r) = \frac{\xi(R_\star)^2}{\xi(r)^2} I_\star(R_\star), \tag{6.31}$$

where $\xi(r)$ is the redshift function (see Appendix A for its definition) and we neglect effects of a limb darkening for simplicity. Both, the angular radius of the star α and the intensity of the radiation field are functions of radial distance r, which together with velocity β of the scatterer are considered as the only independent variables in the problem.

In addition, there are two possibilities for the origin of the other, isotropic component of the radiation field. This component can be produced either independently on the stellar radiation (i.e. the case of background radiation) or its origin could be connected with the stellar radiation (i.e. the case of scattered or reprocessed radiation – perhaps by clumps accreted onto the star). The both contributions are linked to each other and their energy density decreases at identical rate with the distance in that case. In the former case, we set the redshifted *intensity* of the isotropic component to be a fixed ratio λ_I of the stellar intensity, on the other hand we set the radiation *energy density* of the isotropic component to be a fixed ratio λ_ε of the stelar radiation energy density in the latter case.

Polarization is non-zero provided that particle velocity is not equal to $\beta_{1,2}(r)$ and, indeed, Π can reach large values. This is shown in Figure 6.5, where we plot the extremal value of polarization degree $\Pi_{\rm m}(\beta,\zeta)$ in the plane of particle velocity β versus radial distance r and where we assume constant ratio of the redshifted intensities of the stellar and background radiation field. We use a dimensionless parameter $\zeta \equiv 1 - R_\star/r$. Each panel captures the whole range of radii from $r = R_\star$ ($\zeta = 0$) to $r \to \infty$ ($\zeta = 1$). $\Pi_{\rm m}(\beta,\zeta)$ is equal to the extreme value of the polarization degree measured along a suitably chosen observing angle ϑ. The curve of zero polarization is also plotted: notice that this is independent of ϑ, as discussed above. In this figure the primary unpolarized light was assumed to be a mixture of stellar and ambient contributions (the latter component was assumed to be distributed isotropically in the lab frame). The saturation curve $\beta_0(\zeta)$ is also shown. It is worth noticing that, for some values of the model parameters, $\beta_0(\zeta)$ crosses the contour of $\Pi = 0$ twice. Therefore, a hypothetical particle which moves or oscillates along the saturation curve would exhibit polarization that sweeps its direction by 90 degrees.

In the case of the fixed ratio of energy densities of the two components, we again constructed graphs of $\Pi_{\rm m}(\beta,\zeta)$ and found a similar structure of contours at small radii as those shown in Fig. 6.5, including the double-valued function $\beta_{1,2}(\zeta)$. However, the saturation velocity $\beta_0(\zeta)$ does not fall to zero at $r \to \infty$ and, instead, it generally reaches

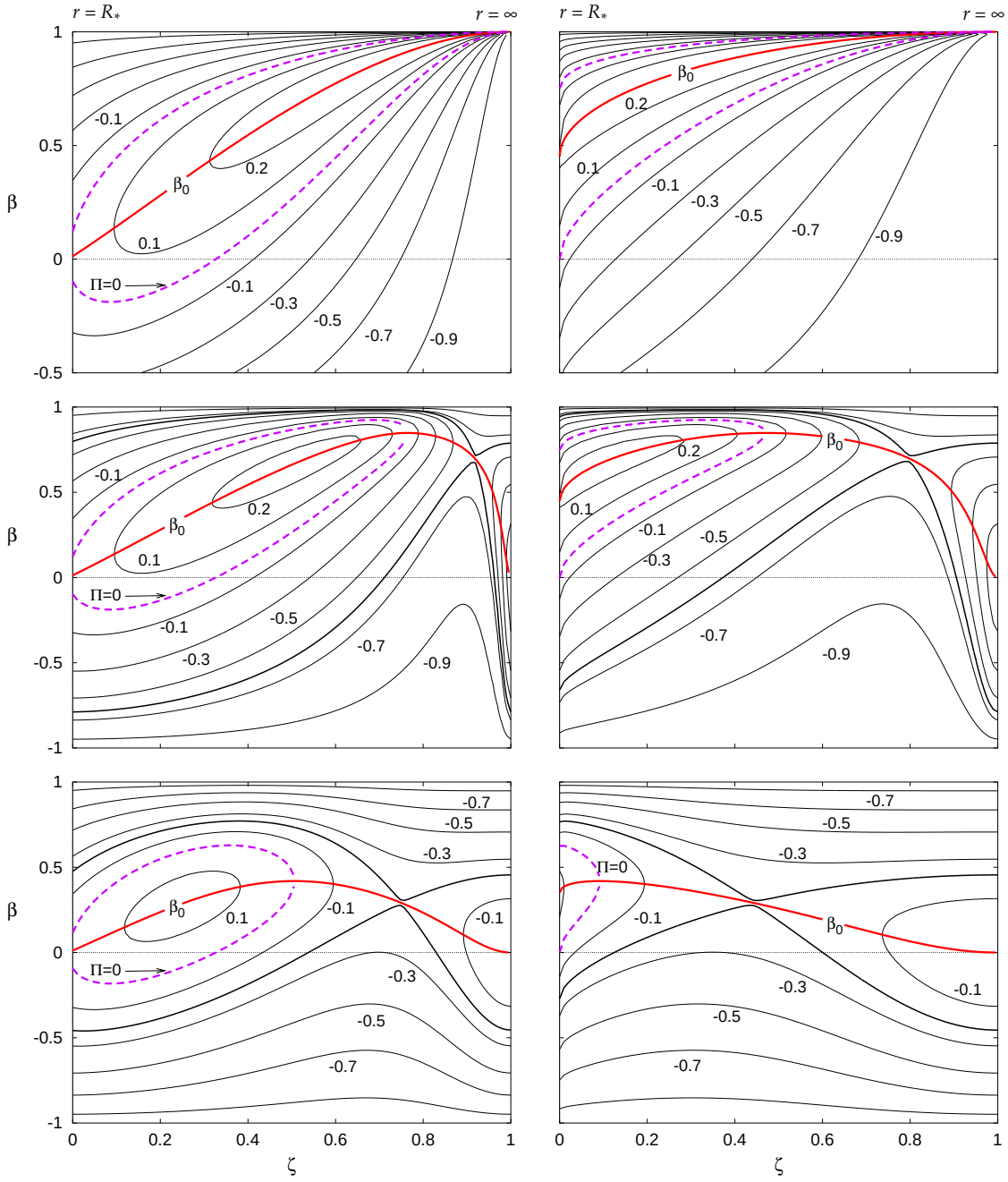

Figure 6.5: Contour graphs of extremal values of the polarization magnitude $\Pi_{\rm m}(\beta,\zeta)$ of photons Thomson-scattered on an electron, moving with a given velocity β through a mixture of stellar and ambient diffuse light. The three rows correspond to progressively increasing luminosity of the star: (i) $\lambda_{\rm i}=0$ (top); (ii) $\lambda_{\rm i}=0.001$ (middle); and (iii) $\lambda_{\rm i}=0.1$ (bottom). The left column is for a highly compact star with $R_\star=1.01R_{\rm S}$, while the right column is for $R_\star=10^3R_{\rm S}$. Hence, the light-bending effects are significant on the left and negligible on the right. The curve of zero polarization $\Pi=0$ is plotted with a dashed line. Generally, if the star is sufficiently compact then the curve of zero polarization becomes double-valued with respect to velocity, with two branches corresponding to solutions $\beta_{1,2}(\zeta)$ in the previous figure. A separatrix is a particular contour which distinguishes regions of different topology in the graph. The saturation curve $\beta_0(\zeta)$ is also plotted.

substantially higher values that depend on the λ_ε. Moreover, the saddle point (where the curve of constant maximal polarization self-crosses) is shifted to higher r and eventually vanishes, which is seen in Figure 6.5.

Polarization of the scattered light obviously depends on the electron motion and in our model it can be calculated together with radiation and gravitational acceleration in a very simple way, since both, electron dynamics in the ambient radiation field and the polarization properties of the scattered radiation can be easily found from the stress energy tensor of the incident radiation. Simultaneous examination of the particle dynamics together with the polarization of the scattered radiation in the radiation field of the relativistic star is a matter of the paper of Horák & Karas (2005b).

6.4 Polarization from hot electron clouds

So far, we ignored inner structure of the scatterer. We considered a cloud composed of cold electrons uniformly moving with bulk velocity. The next natural step is to include s more realistic case of the isotropic distribution of directions of electron individual motion as considered by many authors studying the radiative acceleration processes (Sikora et al. 1996a,b; Renaud & Henri 1998) or inverse Compton scattering on the relativistic electrons (Begelman & Sikora 1987).

Hence, the aim of this section is to average the equations (6.3)–(6.5) over the isotropic electron distribution. We assume that the electron distribution function $n(\vec{\beta}_\mathrm{e})$ does not depend on the direction of the individual electron velocity $\vec{\beta}_\mathrm{e}$ in a cloud co-moving frame (hereafter CCF), $n(\vec{\beta}_\mathrm{e}) = n_\mathrm{e} f(\gamma_\mathrm{e})$, where $\gamma_\mathrm{e} \equiv (1-\beta_\mathrm{e}^2)^{-1/2}$. For a given direction of observation, the total Stokes parameters are found by the following procedure: (i) For an electron that moves with velocity

$$\vec{\beta}_\mathrm{e} = \beta_\mathrm{e}(\sin\theta_\mathrm{e}\cos\phi_\mathrm{e}, \sin\theta_\mathrm{e}\sin\phi_\mathrm{e}, \cos\theta_\mathrm{e}), \tag{6.32}$$

we find a Lorentz transform $\Lambda^\alpha_\beta(\phi_\mathrm{e}, \theta_\mathrm{e})$ according to which the radiation stress-energy tensor $T^{\mu\nu}$ is transformed from CCF to the electron co-moving frame (hereafter ECF). (ii) The local Stokes parameters I_e, Q_e, U_e, are evaluated using the stress-energy with aid of the equations (6.3)–(6.5), respectively. Then (iii) the Stokes parameters are transformed back to the CCF. Finally (iv), the Stokes parameters are averaged over directions of electron velocity β_e - i.e. over the angles θ_e and ϕ_e.

6.4.1 The Lorentz transform

First, let us consider the case of zero azimuthal angle ϕ_e. The orthonormal polarization tetrads $\{\boldsymbol{e}_{(t)}, \boldsymbol{e}_{(X)}, \boldsymbol{e}_{(Y)}, \boldsymbol{e}_{(Z)}\}$ and $\{\tilde{\boldsymbol{e}}_{(t)}, \tilde{\boldsymbol{e}}_{(X)}, \tilde{\boldsymbol{e}}_{(Y)}, \tilde{\boldsymbol{e}}_{(Z)}\}$ of the CCF and ECF[1] can be invariantly expressed using the three four-vectors given in the spacetime: the electron four-velocity $\boldsymbol{u}_\mathrm{e}$, the bulk four-velocity $\boldsymbol{u}$ of the electron cloud and the photon four-momentum $\boldsymbol{p}$, of the scattered radiation. The time-like basis four-vectors $\boldsymbol{e}_{(t)}$ and $\tilde{\boldsymbol{e}}_{(t)}$ are identical with the four-velocities $\boldsymbol{u}$ and $\boldsymbol{u}_\mathrm{e}$ respectively.

Let us introduce the four-vectors $\boldsymbol{e}_{(Z)}$ and $\tilde{\boldsymbol{e}}_{(Z)}$ as normalized projections of the photon four-momentum $\boldsymbol{p}$ onto the three-space perpendicular to $\boldsymbol{u}$ and $\boldsymbol{u}_\mathrm{e}$, respectively. The projections can be found using the projection tensors $h^{\alpha\beta}$ and $h^{\alpha\beta}_\mathrm{e}$ defined as

$$h^{\alpha\beta} \equiv g^{\alpha\beta} + u^\alpha u^\beta, \quad h^{\alpha\beta}_\mathrm{e} \equiv g^{\alpha\beta} + u^\alpha_\mathrm{e} u^\beta_\mathrm{e}, \tag{6.33}$$

[1] Note that these two frames have the same time-like four-vectors.

in the space-time with signature +2. The projections give

$$e^{\alpha}_{(Z)} \equiv u^{\alpha} - \frac{p^{\alpha}}{\nu}, \quad \tilde{e}^{\alpha}_{(Z)} \equiv u^{\alpha}_{\rm e} - \frac{p^{\alpha}}{\tilde{\nu}}, \tag{6.34}$$

where $\nu = -u^{\alpha}p_{\alpha}$ and $\tilde{\nu} = -u^{\alpha}_{\rm e}p_{\alpha}$ are frequencies of the scattered photon measured in the CCF and ECF respectively. The spatial parts of the four-vectors $\boldsymbol{e}_{(Z)}$ and $\tilde{\boldsymbol{e}}_{(Z)}$ point along the direction of photon propagation in each reference frame.

The third basis four-vectors $\boldsymbol{e}_{(X)}$ and $\tilde{\boldsymbol{e}}_{(X)}$ can be chosen as normalized projections of the other four-velocity, $\boldsymbol{u}_{\rm e}$ and $\boldsymbol{u}$ (respectively), onto the two-space perpendicular to the two already defined four-vectors of the tetrads. The projector onto the two-space perpendicular to $\boldsymbol{e}_{(t)}$ and $\boldsymbol{e}_{(Z)}$

$$P^{\alpha\beta} \equiv g^{\alpha\beta} + u^{\alpha}u^{\beta} - e^{\alpha}_{(Z)}e^{\beta}_{(Z)}. \tag{6.35}$$

The projection gives

$$e^{\alpha}_{(X)} = C\left[\tilde{u}^{\alpha} - \frac{1}{\mathcal{D}_{\rm e}}u^{\alpha} + \frac{1-\mathcal{D}_{\rm e}\gamma_{\rm e}}{\mathcal{D}_{\rm e}}\frac{p^{\alpha}}{\nu}\right], \tag{6.36}$$

where $\mathcal{D}_{\rm e}$ and $\gamma_{\rm e}$ are respectively Doppler and Lorentz factors of the electron that can be invariantly defined as

$$\mathcal{D}_{\rm e} \equiv \frac{\nu}{\tilde{\nu}} = \frac{p_{\alpha}u^{\alpha}}{p_{\alpha}u^{\alpha}_{\rm e}}, \quad \gamma_{\rm e} \equiv -u_{\alpha}u^{\alpha}_{\rm e} \tag{6.37}$$

and C is a normalization constant given by

$$C = \frac{\mathcal{D}_{\rm e}}{\sqrt{2\mathcal{D}_{\rm e}\gamma_{\rm e} - \mathcal{D}^2_{\rm e} - 1}}. \tag{6.38}$$

Analogical considerations lead to the expression for $\tilde{\boldsymbol{e}}_{(X)}$

$$e^{\alpha}_{(X)} = C\left[\tilde{u}^{\alpha} - \frac{1}{\mathcal{D}_{\rm e}}u^{\alpha} + (\mathcal{D}_{\rm e} - \gamma_{\rm e})\frac{p^{\alpha}}{\nu}\right]. \tag{6.39}$$

The three-vectors of relative velocities of the electron with respect to the CCF and vice-versa are $\beta^i_{\rm e} \equiv u^{(i)} - u^{(i)}_{\rm e}/\gamma$ and $\tilde{\beta}^i \equiv u^{(i)}_{\rm e} - u^{(i)}/\gamma$ respectively. They both lie in the $X-Z$ plane of both systems. This result is consistent with our initial assumption that $\phi_{\rm e} = 0$. Note also, that there is a simple relation between the four-vectors $\boldsymbol{e}_{(X)}$ and $\tilde{\boldsymbol{e}}_{(X)}$:

$$e^{\alpha}_{(X)} - \tilde{e}^{\alpha}_{(X)} = -\frac{1}{C}\frac{p^{\alpha}}{\nu} \tag{6.40}$$

Finally, the last four-vectors in the tetrads, $e^{\alpha}_{(Y)}$ and $\tilde{e}^{\alpha}_{(Y)}$ are perpendicular to that already defined. Because all of them were introduced as linear combinations of the four-velocities $\boldsymbol{u}_{\rm e}$, $\boldsymbol{u}$ and the photon four-momentum $\boldsymbol{p}$, the both four-vectors, $e^{\alpha}_{(Y)}$ and $\tilde{e}^{\alpha}_{(Y)}$ are perpendicular to them and therefore we can set

$$e^{\alpha}_{(Y)} \equiv \tilde{e}^{\alpha}_{(Y)}. \tag{6.41}$$

Having constructed orthonormal tetrads, we can proceed to the Lorentz transform, that is treated as a coordinate transform from CCF to ECF

$$\Lambda_{\mu\nu}(0,\theta_{\rm e}) \equiv g_{\rho\sigma}\tilde{e}^{\rho}_{(\mu)}e^{\sigma}_{(\nu)}. \tag{6.42}$$

When evaluating the transformation coefficients we use the products between the four-vectors $\boldsymbol{u}_{\rm e}$, $\boldsymbol{u}$ and $\boldsymbol{p}$ given by equation (6.37) and well-known normalization conditions for photon four-momentum and four-velocities of particles.

After a considerable algebra we find

$$\Lambda^{\alpha}_{\beta}(0,\theta_{\rm e}) = \begin{pmatrix} \gamma_{\rm e} & -\frac{1}{C} & 0 & \frac{1}{\mathcal{D}_{\rm e}} - \gamma_{\rm e} \\ -\frac{\mathcal{D}_{\rm e}}{C} & 1 & 0 & \frac{\mathcal{D}_{\rm e}}{C} \\ 0 & 0 & 1 & 0 \\ \gamma_{\rm e} - \mathcal{D}_{\rm e} & -\frac{1}{C} & 0 & \frac{1}{\mathcal{D}_{\rm e}} + \mathcal{D}_{\rm e} - \gamma_{\rm e} \end{pmatrix}. \tag{6.43}$$

Let us express the Doppler factor as $\mathcal{D}_{\rm e} = \gamma_{\rm e}^{-1}(1 - \beta_{\rm e}\cos\theta_{\rm e})^{-1}$ Then we find that $C = 1/(\gamma_{\rm e}\beta_{\rm e}\sin\theta_{\rm e})$ and the Lorentz transform takes the form

$$\Lambda^{\alpha}_{\beta}(0,\theta_{\rm e}) = \begin{pmatrix} \gamma_{\rm e} & -\gamma_{\rm e}\beta_{\rm e}\sin\theta_{\rm e} & 0 & -\gamma_{\rm e}\beta_{\rm e}\cos\theta_{\rm e} \\ -k & 1 & 0 & k \\ 0 & 0 & 1 & 0 \\ l & -\gamma_{\rm e}\beta_{\rm e}\sin\theta_{\rm e} & 0 & m \end{pmatrix}. \tag{6.44}$$

where for simplicity we defined

$$k = \gamma\mathcal{D}_{\rm e}\beta_{\rm e}\sin\theta_{\rm e}, \quad l = \gamma_{\rm e}^2\beta_{\rm e}\mathcal{D}_{\rm e}(\beta_{\rm e} - \cos\theta_{\rm e}), \quad m = \mathcal{D}_{\rm e} - \gamma_{\rm e}\beta_{\rm e}\cos\theta_{\rm e}. \tag{6.45}$$

The more general case when the projection of the electron velocity to the (X, Y) plane and the X-axis make nonzero angle $\phi_{\rm e}$ is realized by a composition of the Lorentz transform (6.44) with the rotation about Z-axis through the angle $\phi_{\rm e}$. The components of the stress-energy tensor are first transformed by the rotation matrix

$$R_Z(\phi_{\rm e}) = \begin{pmatrix} 1 & 0 & 0 & 0 \\ 0 & \cos\phi_{\rm e} & \sin\phi_{\rm e} & 0 \\ 0 & -\sin\phi_{\rm e} & \cos\phi_{\rm e} & 0 \\ 0 & 0 & 0 & 1 \end{pmatrix} \tag{6.46}$$

and then tranformed by the Lorentz transform (6.44). Finally, the total Lorentz transform (that includes the rotation) is given by

$$\Lambda^{\alpha}_{\beta}(\phi_{\rm e},\theta_{\rm e}) = \begin{pmatrix} \gamma_{\rm e} & -\gamma_{\rm e}\beta_{\rm e}\sin\theta_{\rm e}\cos\phi_{\rm e} & -\gamma_{\rm e}\beta_{\rm e}\sin\theta_{\rm e}\sin\phi_{\rm e} & -\gamma_{\rm e}\beta_{\rm e}\cos\theta_{\rm e} \\ -k & \cos\phi_{\rm e} & \sin\phi_{\rm e} & k \\ 0 & -\sin\phi_{\rm e} & \cos\phi_{\rm e} & 0 \\ l & -\gamma_{\rm e}\beta_{\rm e}\sin\theta_{\rm e}\cos\phi_{\rm e} & -\gamma_{\rm e}\beta_{\rm e}\sin\theta_{\rm e}\sin\phi_{\rm e} & m \end{pmatrix}. \tag{6.47}$$

Let use derive the backward Lorentz transform for the Stokes parameters of the scattered radiation in this subsection. The calculations are done for a completely polarized radiation only, but the results are valid also for the partially polarized radiation because the degree of polarization is Lorentz invariant. (Cocke & Holm 1972).

Transformation rules of the Stokes parameters will be derived from the transformation properties of the electromagnetic tensor $F^{\mu\nu}$. Consider monochromatic plane wave in vacuum described by an electromagnetic four-potential

$$A^{\mu} = A^{\mu}_0 \exp(ik^{\sigma}_0 x_{\sigma}), \tag{6.48}$$

where A^{μ}_0 is a constant amplitude of the wave and k^{μ}_0 is a wave four-vector. This potential satisfies the wave equation $\nabla^2 A^{\mu} = 0$ and Lorentz calibration condition $\nabla_{\sigma} A^{\sigma} = 0$ when

k_0^μ is a null four-vector perpendicular to the amplitude A_0^μ. In units where $G = c = h = 1$ the wave-four-vector is simply related to the photon four-momentum by $k_0^\mu = 2\pi p_0^\mu$.

The electric field $\mathcal{E}$ measured in a particular reference frame can be derived from the antisymmetric tensor $F^{\mu\nu} \equiv \nabla^\mu A^\nu - \nabla^\nu A^\mu$. For the plane monochromatic wave it has a form

$$F^{\mu\nu} = iF_0^{\mu\nu} \exp(ik_0^\sigma x_\sigma), \tag{6.49}$$

where the amplitude $F_0^{\mu\nu}$ is given as

$$F_0^{\mu\nu} = k_0^\mu A_0^\nu - k_0^\nu A_0^\mu. \tag{6.50}$$

Consider a particular reference frame (e.g. CCF). The frequency and the propagation three-vector of the wave are given by the tetrad components of the photon four-momentum $\boldsymbol{p_0}$

$$\nu_0 = -p_0^{(t)}, \quad n_0^i \equiv \frac{p_0^{(i)}}{p_0^{(t)}} = \delta_Z^i. \tag{6.51}$$

The frequency is projection of the wave four-vector on to observer four-velocity, two other independent components of give us the unit three-vector n_0^i along the wave propagation.

The electric field measured by the observer is $E^i = F^{(t)(i)} = u_{(\rho)}F^{(\rho)(i)}$. The energy density carried by the electric field is proportional to the square of magnitude of the electric intensity

$$|E|^2 = E^i E_i^* = g_{\alpha\beta}F_0^{\alpha\rho}F_0^{\beta\sigma *}u_\rho u_\sigma = (u_\rho k_0^\rho)^2 A_{0\alpha}A_0^{\alpha *} = (2\pi\nu_0)^2|A_0|^2, \tag{6.52}$$

where the stars denotes complex conjugation.

Since the magnetic component of the wave carries the same amount of energy as the electric one, the radiation intensity can be expressed as

$$I_\nu(n^i) = 4\pi^2\epsilon_0\nu_0^2|A_0|^2\delta(\nu - \nu_0)\delta(n^i - n_0^i), \tag{6.53}$$

where ϵ_0 is a vacuum permittivity. We added two delta-functions on the right-hand side because radiation intensity is expressed per unit frequency and solid angle and the plane monochromatic wave has sharp frequency and direction of propagation. Using equations (6.51) we can express them as a single delta-function in the photon four-momentum $\boldsymbol{p}_0$

$$\delta(\nu - \nu_0)\delta(n^i - n_0^i) = \nu\delta(p^\alpha - p_0^\alpha). \tag{6.54}$$

Finally, substituting it into equation (6.53) we find

$$\frac{I_\nu(n^i)}{\nu^3} = 4\pi^2\epsilon_0|A_0|^2\delta(p^\alpha - p_0^\alpha) \equiv \text{invariant}, \tag{6.55}$$

because the term on the right-hand side does not depend on choice of the particular reference frame.

The two other nonzero Stokes parameter Q and U of the linearly polarized wave depend on the polarization basis. Consider first the case $\phi_e = 0$. The polarization bases in both reference frames are introduced by the equations (6.34), (6.36), (6.39) and (6.41), The X and Y-components of the amplitudes of the electric intensity measured in CCF are

$$E_0^a = e_\alpha^{(t)}e_\beta^{(a)}F_0^{\alpha\beta} = -u_\alpha k_0^\alpha e_\beta^{(a)}A_0^\beta + u_\alpha A_0^\alpha e_\beta^{(a)}k_0^\beta = 2\pi\nu_0 A_0^{(a)}, \tag{6.56}$$

where $a = X, Y$. The second term vanishes because $\boldsymbol{e}_{(a)}$ are perpendicular to the wave vector. Similarly, an observer in ECF measures

$$\tilde{E}_0^a = 2\pi\tilde{\nu}_0 \tilde{A}_0^{(a)} = 2\pi\tilde{\nu}_0 A_0^{(a)}. \tag{6.57}$$

The last equality is valid because $\boldsymbol{e}^{(a)}$ equals to $\tilde{\boldsymbol{e}}^{(a)}$ (for $a = Y$) or they differs by multiple of the wave vector (for $a = X$ – see equation (6.40)), which gives zero in the scalar product $k_{0\alpha}A_0^\alpha = 0$ from the Lorentz calibration condition.

Hence in both reference frames, the two Stokes parameters can be expressed as

$$\frac{Q_\nu}{\nu^3} = \frac{\tilde{Q}_{\tilde{\nu}}}{\tilde{\nu}^3} = 4\pi^2 \left[\left| A_0^{(X)} \right|^2 - \left| A_0^{(Y)} \right|^2 \right] \delta(p^\alpha - p_0^\alpha), \tag{6.58}$$

$$\frac{U_\nu}{\nu^3} = \frac{\tilde{U}_{\tilde{\nu}}}{\tilde{\nu}^3} = 8\pi^2 \Re \left[A_0^{(X)} A_0^{(Y)*} \right] \delta(p^\alpha - p_0^\alpha), \tag{6.59}$$

where the delta-functions were expressed in the invariant way using the equation (6.54).

Finally, three frequency-integrated Stokes parameters characterizing linear polarization are transformed between ECF and CCF according to

$$I = \mathcal{D}_{\rm e}^4 \tilde{I}, \quad Q = \mathcal{D}_{\rm e}^4 \tilde{Q}, \quad U = \mathcal{D}_{\rm e}^4 \tilde{U}, \tag{6.60}$$

The transformation (6.60) is valid if (and only if) the Y-axis of CCF is aligned with the Y-axis of ECF, e.g. when $\phi_{\rm e} = 0$. The more general case of the nonzero angle $\phi_{\rm e}$ is treated by composition of the transformations (6.60) with the rotation through the angle $-\phi_{\rm e}$.[2] The transformations of the Stokes parameters under the rotation are given by equation (5.10). Therefore, in fully general case we find

$$I = \mathcal{D}_{\rm e}^4 \tilde{I}, \quad Q = \mathcal{D}_{\rm e}^4 \left(\tilde{Q} \cos 2\phi_{\rm e} - \tilde{U} \sin 2\phi_{\rm e} \right), \quad U = \mathcal{D}_{\rm e}^4 \left(\tilde{Q} \sin 2\phi_{\rm e} + \tilde{U} \cos 2\phi_{\rm e} \right), \tag{6.61}$$

The equations (6.61) are valid if the source *as a whole* moves with respect to the observer. In our case, however the source is rather *stationary* and at rest in a sense that it contains warm electrons with fast individual motions in random direction, however a direction of an electron motion is frequently changed so that the photons are essentially radiated from the constant place. In a former case the transformation contains also a contribution of the aberration effect. The Stokes parameters are expressed per time of observation $\mathrm{d}t$ in CCF and per time of emission $\mathrm{d}\tilde{t}$ in ECF. These two time intervals are related by $\mathrm{d}\tilde{t} = \gamma \mathrm{d}t$ if the source is stationary as a whole and radiates essentially from the same point or by $\mathrm{d}\tilde{t} = \gamma(1 - \beta\cos\theta)\mathrm{d}t$ if the source is in a bulk motion and its distance from the observer is changing as $ct(1 - \beta\cos\theta)$. For this reason one should complete the Lorentz transform by an extra factor $(1 - \beta\cos\theta_{\rm e}) = 1/(\gamma\mathcal{D}_{\rm e})$ (see also Begelman & Sikora 1987,Blumenthal & Gould 1970 and Rybicky & Lightman 1979 sec. 4.8). We obtain

$$I = \frac{\mathcal{D}_{\rm e}^3}{\gamma_{\rm e}} \tilde{I}, \quad Q = \frac{\mathcal{D}_{\rm e}^3}{\gamma_{\rm e}} \left(\tilde{Q} \cos 2\phi_{\rm e} - \tilde{U} \sin 2\phi_{\rm e} \right), \quad U = \frac{\mathcal{D}_{\rm e}^3}{\gamma_{\rm e}} \left(\tilde{Q} \sin 2\phi_{\rm e} + \tilde{U} \cos 2\phi_{\rm e} \right). \tag{6.62}$$

The transformations are derived for the plane monochromatic completely polarized wave, however it can be easily shown (Cocke & Holm 1972) that our results remain valid also for a general radiation field with partial polarization. It also follows from equation (6.62), that the degree of polarization of a linearly polarized wave $\Pi = (Q^2 + V^2)^{1/2}/I$ is invariant under Lorentz transformations.

[2] We consider the *backward* transformation of the Stokes parameters from ECF to CF contrary to the transformation of the four-vectors considered before.

6.4.2 The Stokes parameters of the scattered radiation

The Stokes parameters of the scattered radiation with respect to the co-moving frame of an electron swarm with an uniform velocity are given by the equations (6.3)–(6.5). The components of the stress-energy tensor of an incident radiation in the ECF are

$$\tilde{T}^{\alpha\beta} \equiv \Lambda^{\alpha}_{\rho}(\phi_{\rm e},\theta_{\rm e})\Lambda^{\beta}_{\sigma}(\phi_{\rm e},\theta_{\rm e})T^{\rho\sigma}, \tag{6.63}$$

where $\Lambda^{\beta}_{\sigma}(\phi_{\rm e},\theta_{\rm e})$ are coefficients of the Lorentz transform given by equation (6.47) (from this point we use a shorter notation without arguments) and $T^{\rho\sigma}$ are components of the radiation stress-energy tensor in CCF.

Let us denote $\delta\tilde{I}_{\rm e}$, $\delta\tilde{Q}_{\rm e}$ and $\delta\tilde{U}_{\rm e}$ contributions to the total Stokes parameters of the scattered radiation from electrons with Lorentz factor $\gamma_{\rm e}$ and direction of velocity given by angles $\phi_e l$ and $\theta_{\rm e}$. After substitution into the equations (6.3)–(6.5), we find

$$\delta\tilde{I}_{\rm e} = Af(\gamma_{\rm e})\left(\Lambda^{t}_{\rho}\Lambda^{t}_{\sigma}+\Lambda^{Z}_{\rho}\Lambda^{Z}_{\sigma}\right)T^{\rho\sigma}, \tag{6.64}$$

$$\delta\tilde{Q}_{\rm e} = Af(\gamma_{\rm e})\left(\Lambda^{Y}_{\rho}\Lambda^{Y}_{\sigma}-\Lambda^{X}_{\rho}\Lambda^{X}_{\sigma}\right)T^{\rho\sigma}, \tag{6.65}$$

$$\delta\tilde{U}_{\rm e} = -Af(\gamma_{\rm e})\left(\Lambda^{X}_{\rho}\Lambda^{Y}_{\sigma}+\Lambda^{Y}_{\rho}\Lambda^{X}_{\sigma}\right)T^{\rho\sigma}. \tag{6.66}$$

Transforming the Stokes parameters according to equation (6.62) we obtain

$$\delta X_{\rm e} = Af(\gamma_{\rm e})\,\Xi^{(X)}_{\rho\sigma}\,T^{\rho\sigma} \tag{6.67}$$

where $X = I, Q, U$ stands for any Stokes parameter and we defined

$$\Xi^{(I)}_{\rho\sigma} \equiv \frac{\mathcal{D}^3_{\rm e}}{\gamma_{\rm e}}\left(\Lambda^{t}_{\rho}\Lambda^{t}_{\sigma}+\Lambda^{Z}_{\rho}\Lambda^{Z}_{\sigma}\right), \tag{6.68}$$

$$\Xi^{(Q)}_{\rho\sigma} \equiv \frac{\mathcal{D}^3_{\rm e}}{\gamma_{\rm e}}\left[\left(\Lambda^{Y}_{\rho}\Lambda^{Y}_{\sigma}-\Lambda^{X}_{\rho}\Lambda^{X}_{\sigma}\right)\cos 2\phi_{\rm e}-\left(\Lambda^{X}_{\rho}\Lambda^{Y}_{\sigma}+\Lambda^{Y}_{\rho}\Lambda^{X}_{\sigma}\right)\sin 2\phi_{\rm e}\right], \tag{6.69}$$

$$\Xi^{(U)}_{\rho\sigma} \equiv \frac{\mathcal{D}^3_{\rm e}}{\gamma_{\rm e}}\left[\left(\Lambda^{X}_{\rho}\Lambda^{Y}_{\sigma}-\Lambda^{Y}_{\rho}\Lambda^{X}_{\sigma}\right)\sin 2\phi_{\rm e}+\left(\Lambda^{Y}_{\rho}\Lambda^{Y}_{\sigma}+\Lambda^{X}_{\rho}\Lambda^{X}_{\sigma}\right)\cos 2\phi_{\rm e}\right] \tag{6.70}$$

6.4.3 Integration over the electron distributions

The intensity of the total radiation scattered by the electron cloud is given by integration over the electron distribution in CCF. The total intensity given by the integral

$$X = \int_{\gamma_{\rm e}}\int_{4\pi}\delta X_{\rm e}{\rm d}\Omega\,{\rm d}\gamma_{\rm e} = AT^{\rho\sigma}\int_{\gamma_{\rm e}}\int_{4\pi}f(\gamma_{\rm e})\,\Xi^{(X)}_{\rho\sigma}\,{\rm d}\Omega\,{\rm d}\gamma_{\rm e} \tag{6.71}$$

Performing the integration over the full solid angle in the case of intensity $X = I$, we obtain

$$\int_{\gamma_{\rm e}}\int_{4\pi}f(\gamma_{\rm e})\,\Xi^{(I)}_{\rho\sigma}\,{\rm d}\Omega\,{\rm d}\gamma_{\rm e} = \begin{pmatrix} 1+\mathcal{A} & 0 & 0 & -\mathcal{A} \\ 0 & \mathcal{B} & 0 & 0 \\ 0 & 0 & \mathcal{B} & 0 \\ -\mathcal{A} & 0 & 0 & 1+\mathcal{A}-2\mathcal{B} \end{pmatrix}, \tag{6.72}$$

where we defined

$$\mathcal{A} \equiv \left\langle \tfrac{4}{3}\gamma^2_{\rm e}\beta^2_{\rm e}\right\rangle, \quad \mathcal{B} \equiv 1-\left\langle\frac{\ln[\gamma_{\rm e}(1+\beta_{\rm e})]}{\beta_{\rm e}\gamma^2_{\rm e}}\right\rangle, \tag{6.73}$$

where $\langle\, x \,\rangle \equiv \int x\, f(\gamma_\mathrm{e})\mathrm{d}\gamma_\mathrm{e}$ denotes averaging over the electron Lorentz factor. According to the equation (6.72) the total intensity can be expressed as

$$I = A\left[(1+\mathcal{A})\left(T^{tt}+T^{ZZ}\right)+\mathcal{B}\left(T^{tt}-3T^{ZZ}\right)-2\mathcal{A}T^{tZ}\right]. \tag{6.74}$$

Performing the integration over the solid angle in the case of the two remaining Stokes parameters we find

$$\int_{\gamma_\mathrm{e}}\int_{4\pi} f(\gamma_\mathrm{e})\,\Xi^{(Q)}_{\rho\sigma}\,\mathrm{d}\Omega\,\mathrm{d}\gamma_\mathrm{e} = \begin{pmatrix} 0 & 0 & 0 & 0\\ 0 & -1 & 0 & 0\\ 0 & 0 & 1 & 0\\ 0 & 0 & 0 & 0 \end{pmatrix}, \tag{6.75}$$

$$\int_{\gamma_\mathrm{e}}\int_{4\pi} f(\gamma_\mathrm{e})\,\Xi^{(U)}_{\rho\sigma}\,\mathrm{d}\Omega\,\mathrm{d}\gamma_\mathrm{e} = \begin{pmatrix} 0 & 0 & 0 & 0\\ 0 & 0 & 1 & 0\\ 0 & 1 & 0 & 0\\ 0 & 0 & 0 & 0 \end{pmatrix}. \tag{6.76}$$

Hence, the Stokes Q and U parameters are the same as if the cloud is composed of cold electrons,

$$Q = A\left(\bar{T}^{YY}-\bar{T}^{XX}\right), \tag{6.77}$$

$$U = -2A\bar{T}^{XY}. \tag{6.78}$$

The equations (6.74), (6.77) and (6.78) are analogous to the equations (6.3)–(6.5). Hence, the discussion of the polarization properties of the radiation scattered by cold cloud carried in section 6.3 is valid also in the case of warm cloud.

6.4.4 The monoenergetic electron distribution

The monoenergetic electron distribution is a rather simple example. However it keeps essential property of the problem: the random direction of electron motion in the blob comoving frame. For its simplicity, it can be a useful probe to more complicated physics.

Let the electron distribution function in the blob comoving frame be $n_\mathrm{e}(\gamma_\mathrm{e}) = n_\mathrm{e}\delta(\gamma_\mathrm{e}-\bar{\gamma}_\mathrm{e})$, where n_e is electron number density and $\bar{\gamma}_\mathrm{e}$ is mean random Lorentz factor of electrons. The expressions for u and v are then

$$u = \tfrac{4}{3}(\bar{\gamma}_\mathrm{e}^2-1), \quad v = 1-\frac{\ln\left[\bar{\gamma}_\mathrm{e}+\sqrt{\bar{\gamma}_\mathrm{e}^2-1}\right]}{\bar{\gamma}_\mathrm{e}\sqrt{\bar{\gamma}_\mathrm{e}^2-1}}. \tag{6.79}$$

Consider a narrow beam of radiation that propagates in the direction $\vec{n}$ in the blob comoving frame. This three-vector and the direction towards the observer $\vec{e}_Z$ make an angle ϑ. Therefore, the integrated intensity of the incident radiation is by $I_\mathrm{i}(\vec{k}) = I_0\delta(\vec{k}-\vec{n})$. Due to the symmetry of the problem, we can restrict our discussion to the plane determined by vectors $\vec{k}$ and $\vec{n}$. Without loss of any generality we can set $n^Y = 0$. Then two other components are $n^X = \sin\vartheta$ and $n^Z = \cos\vartheta$. The stress-energy tensor of the incident radiation can be found by integration over the full solid angle.

$$T^{tt} = \varepsilon, \quad T^{tZ} = \varepsilon n^Z, \quad T^{ZZ} = \varepsilon n^Z n^Z, \quad T^{XX} = \varepsilon n^X n^X, \tag{6.80}$$

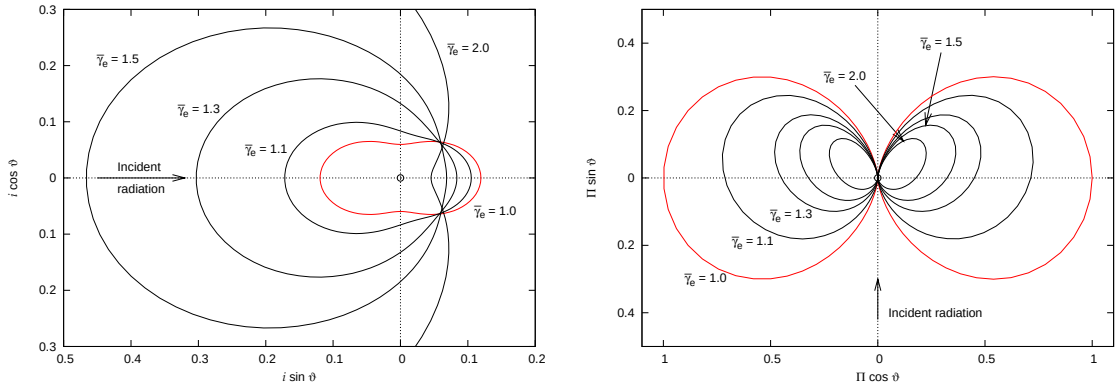

Figure 6.6: Left: the normalized scattered intensity $i \equiv I/(\tau I_0)$ as a function of the scattering angle ϑ between the direction n of the scattering radiation and the direction of observation. The scatterer is the electron cloud. Different curves are for different values of the electron Lorentz factor measured in the blob reference frame. The case of cold electron corresponds to $\bar{\gamma}_e = 1$. Right: the magnitude of transversal polarization Π as a function of the scattering angle for several values of the electron Lorentz factor. The depolarization effect of the electron motions and the shift of the angle of maximal polarization are apparent.

where $\varepsilon = I_0/c$ is the energy density of the radiation field. Substituting it into equation (6.74) we find the intensity of scattered radiation in the form

$$\frac{I}{\tau I_0} = \frac{3}{16\pi}\left[(1+u-3v)\cos^2\vartheta - 2u\cos\vartheta + (1+u+v)\right]. \tag{6.81}$$

If the scatterer contains cold electrons, then both, u and v are zero and the angular dependence of the scattered intensity reduces to $I \propto 1+\cos^2\vartheta$, the same dependence as for Thomson scattering on a single electron. The scattering on the cold electrons is symmetric with respect to the plane perpendicular to the direction of the incident radiation beam. On the other hand, in case of ultrarelativistic electrons with $\bar{\gamma}_e \gg 1$ we have $u \approx 4/3\bar{\gamma}_e^2$ and $v \approx 1$ and equation (6.81) gives the angular dependence $I \propto \bar{\gamma}_e^2(1-\cos\vartheta)^2$ which is highly asymmetric. The most of the radiation is scattered in the backward direction. This fact has an important consequence regarding the dynamics of the Thomson scattering. The scattered radiation transport momentum from the electrons in backward direction and therefore the incident radiation has stronger impact on the dynamics the scatterer if it contains hot electrons. This effect is called Compton rocket and it was firstly studied by O'Dell (1981) and than reconsidered by Phinney (1982). The left panel of Figure 6.6 shows the angular dependences of the scattered intensity for different values of $\bar{\gamma}_e$.

As it was shown in the previous section, the remaining Stokes parameters are not affected by electron motions. Therefore, we get the same result for the parameter Q as in the case of blob containing cold electrons,

$$\frac{Q}{\tau I_0} = -\frac{3}{16\pi}\sin^2\vartheta. \tag{6.82}$$

Since it is negative for any value of ϑ, the polarization of scattered radiation is always perpendicular to the plane of incident and scattered beams. The polarization magnitude

is given by the ratio $|Q|/I$, because other stokes parameters are zero in the considered configuration. We find

$$\Pi = \frac{1-\cos^2\vartheta}{(1+u-3v)\cos^2\vartheta - 2u\cos\vartheta + (1+u+v)}. \tag{6.83}$$

The angular dependence of the polarization magnitude is shown in the right panel of Figure 6.6. In the case of cold electrons, equation (6.83) is identical with the well known expression for polarization of radiation scattered on the single electron, $\Pi = (1-\cos^2\vartheta)/(1+\cos^2\vartheta)$ giving the maximal value of unity for completely polarized radiation, when $\vartheta_{\rm m,cold} = \pi/2$. On the other hand, if the scatterer contains "warm" electrons with relativistic energies, the polarization of scattered radiation is reduced by a factor $\sim \bar{\gamma}_{\rm e}^{-2}$. The maximal polarization occurs closer to the direction of incident radiation, because of the the asymmetric profile $I(\vartheta)$ of the scattered intensity. Simple algebra gives the angle $\vartheta_{\rm m}$ of maximal polarization

$$\cos\vartheta_{\rm m} = \frac{1}{u}\left[1+u-v-\sqrt{(1-v)(1+2u-v)}\right]. \tag{6.84}$$

With aid of equations (6.79), one can check that $\vartheta_{\rm m} \to \pi/2$ when $\bar{\gamma}_{\rm e} \to 1$. On the other hand, $\vartheta_{\rm m}$ approaches zero in the case of highly relativistic electrons with $\bar{\gamma}_{\rm e} \gg 1$. However, polarization is strongly reduced in that case.

Chapter 7

Radiatively driven clouds above an accretion disk

We consider radiation field and electron clouds near a static spherically symmetric black hole surrounded by an accretion disk.

7.1 Gravitational field

Let us consider the gravitational field to be described by the Schwarzschild space-time (we neglect the disk contribution to the gravitational field). The metric expressed in spherical coordinates $\{t, r, \theta, \phi\}$ is (i.e. Chandrasekhar 1992)

$$\mathrm{d}s^2 = -\xi \mathrm{d}t^2 + \xi^{-1}\mathrm{d}r^2 + r^2(\mathrm{d}\theta^2 + \sin^2\theta \mathrm{d}\phi^2), \tag{7.1}$$

where $\xi(r) \equiv 1 - R_\mathrm{S}/r$ is the redshift function in terms of gravitational Schwarzschild radius R_S (see Appendix A for the definition of the redshift function).

We adopt the Schwarzschild metric for simplicity: it allows us to complete the calculation of the particle motion in radiation and gravitational fields, and the resulting polarization in a self-consistent manner. The approach is however sufficiently general and it can be applied also in other situations. In this work we assume $M = \mathrm{const}$.

The adopted spherical coordinates are non-singular everywhere above horizon, $r = R_\mathrm{S}$, and the space-time is asymptotically flat far from the black hole, i.e. for $r \to \infty$. Hence the metric (7.1) is suitable for our purposes and it entirely describes the gravitational field of a non-rotating and electrically neutral black hole above its horizon.

We assume that the accretion disk lies in the equatorial plane $\theta = \pi/2$. In addition we restrict the motion of the cloud to the disk axis, which is given by $\theta = 0$. The radial coordinate along this axis (the height above the disk) will be referred to as z (i.e. when we use the letter z instead of the letter r, we implicitly assume the condition $\theta = 0$)

Each point of the spacetime is equipped by a local orthonormal tetrad with respect to which four-vectors and four-tensors will be expressed. At points that don't lie on the symmetry axis we use the tertad $(\boldsymbol{e}^{(t)}, \boldsymbol{e}^{(r)}, \boldsymbol{e}^{(\theta)}, \boldsymbol{e}^{(\phi)})$, with non-vanishing components

$$e_t^{(t)} = -\xi^{1/2}, \quad e_r^{(r)} = \xi^{-1/2}, \quad e_\theta^{(\theta)} = r, \quad e_\alpha^{(\phi)} = r\sin\theta. \tag{7.2}$$

On the other hand, points on the symmetry axis are equipped with "cartesian" tetrad $(\boldsymbol{e}^{(t)}, \boldsymbol{e}^{(x)}, \boldsymbol{e}^{(y)}, \boldsymbol{e}^{(z)})$ with non-vanishing components

$$e_t^{(t)} = -\xi^{1/2}, \quad e_z^{(z)} = \xi^{-1/2}, \quad e_x^{(x)} = e_y^{(y)} = r \tag{7.3}$$

Tetrad components of four-vectors are denoted with bracketed indices and are raised and lowered using the Minkowski metric tensor $\eta_{\alpha\beta}$.

7.2 Disk radiation field

In order to find the disk radiation field, we first determine the radial profile of its surface temperature. For this purpose, we adopt the standard Shakura & Sunyaev (1973) disk model where the accretion disk is assumed to be optically thick and geometrically thin. The disk effective temperature $T_{\rm d}$ is given by an equilibrium between viscous heating and radiative cooling

$$\sigma_{\rm SB} T_{\rm d}(r)^4 = \frac{3GM\dot{M}}{8\pi r^3}\left(1-\sqrt{\frac{r_{\rm in}}{r}}\right), \tag{7.4}$$

where $\sigma_{\rm SB}$ is Stephan-Boltzmann constant, $\dot{M}$ is the accretion rate and $r_{\rm in}$ is the inner disk radius.

Assuming that at a given radius the disk is a blackbody radiator, the surface specific intensity measured in the reference frame that co-rotates with the disk is given by the Planck function $I_{\rm d}(\nu, r) = B_\nu(T_{\rm eff})$. The frequency-integrated surface intensity is then

$$I_{\rm d}(r) = \int_\nu B_\nu[T_{\rm d}(r)]{\rm d}\nu = \frac{1}{\pi}\sigma_{\rm SB} T_{\rm d}^4. \tag{7.5}$$

Using this equation and equation (7.4) we find

$$I_{\rm d}(r) = \frac{3GM\dot{M}}{8\pi^2 r^3}\left(1-\sqrt{\frac{r_{\rm in}}{r}}\right). \tag{7.6}$$

Now, let us introduce the normalization of disk luminosity by the Eddington parameter

$$\Lambda \equiv \frac{L}{L_{\rm Edd}} = \frac{\sigma_{\rm T}\dot{M}}{8\pi m_{\rm p} c r_{\rm in}}, \tag{7.7}$$

where $L = GM\dot{M}/2r_{\rm in}$ is the disk luminosity and $L_{\rm Edd} = 4\pi cGMm/\sigma_{\rm T}$ is the Eddington luminosity of the central object (m denotes the mass of the particle providing inertia of accelerated medium in this work we assume $m = m_{\rm e}$). Hence, we can express the intensity $I_{\rm d}$ as

$$I_{\rm d}(r) = \frac{mc^3}{\sigma_{\rm T} R_{\rm S}}\Lambda I_{\rm d\star}, \quad I_{\rm d\star} = \frac{6r_{\rm in}}{r^3}\left(1-\sqrt{\frac{r_{\rm in}}{r}}\right), \tag{7.8}$$

where $I_{\rm d\star}$ is the normalized disk intensity. It depends only on the relative spatial variations of the surface intensity and not on its absolute value. This approach allows us to easily discuss effects of radiation field strength.

Particles move in the accretion disk along a circular orbit in the equatorial plane. A four-velocity of a particle can be expressed as $u^\mu_{\rm d} = (u^t_{\rm d}, 0, 0, u^\phi_{\rm d})$, where

$$u^t_{\rm d} = \frac{{\rm d}t}{{\rm d}s}, \quad u^\phi_{\rm d} = \frac{{\rm d}\phi}{{\rm d}s} = \frac{{\rm d}t}{{\rm d}s}\frac{{\rm d}\phi}{{\rm d}t} = u^t_{\rm d}\omega_{\rm d}. \tag{7.9}$$

The velocity components $u^t_{\rm d}$ and $u^\phi_{\rm d}$ are not independent because the four-velocity is normalized by the condition $g_{\alpha\beta}u^\alpha_{\rm d}u^\beta_{\rm d} = -1$. Hence, the circular orbit is completely

determined by the angular orbital frequency $\omega_{\rm d}$ measured by a distant observer. The radial component of the geodesic equation leads to equation

$$\Gamma^r_{tt} + \omega^2_{\rm d}\Gamma^r_{\phi\phi} = 0, \tag{7.10}$$

with the solution

$$\omega^2_{\rm d} = -\frac{g_{tt,r}}{g_{\phi\phi,r}} = \frac{R_{\rm S}}{2r^3}. \tag{7.11}$$

The normalization condition for the four-velocity $u^\alpha_{\rm d}$ implies

$$u^t_{\rm d} = \left(1 - \frac{3R_{\rm S}}{2r_{\rm d}}\right)^{-1/2}. \tag{7.12}$$

Light rays are null geodesics. Denoting the photon four-momentum as p^α, following quantities are conserved along a particular ray: the photon energy E, the photon angular momentum L and the redshifted intensity $\tilde{I}$ given (respectively) by

$$E \equiv -p_t = \text{const}, \quad L \equiv p_\phi = \text{const}, \quad \tilde{I} \equiv \frac{I}{(p_\alpha u^\alpha)^4} = \text{const}, \tag{7.13}$$

where I is the intensity measured by an observer with four-velocity u^α.

Let us consider a particular light ray. The four-velocity of the stationary observer located on the axis at the height z can be expressed as $u^\alpha_{\rm o} = \xi^{-1/2}(z)\delta^\alpha_t$. In the local reference frame of the observer we introduce local orthonormal tetrad according to the definition (7.3). Then we can define photon propagation four-vector $n^{(i)}$ with spacetime components $n^{(\alpha)} \equiv p^{(\alpha)}/p^{(t)}$. Note, that its spatial components satisfy the relation $n^{(i)}n_{(i)} = 1$ and, therefore, they can be expressed using directional cosines

$$n^{(x)} = \cos\varphi\sin\vartheta, \quad n^{(y)} = \sin\varphi\sin\vartheta, \quad n^{(z)} = \cos\vartheta, \tag{7.14}$$

The intensity $I_{\rm d}(r_{\rm d})$ emitted by the disk at the radius $r_{\rm d}$ measured in the co-rotating reference frame and the intensity $I(\vartheta, z)$ received by the stationary observer on the axis at height z are related by

$$I(\vartheta, z) = \frac{(p^\alpha u_\alpha)^4_{\rm o}}{(p^\alpha u_\alpha)^4_{\rm d}}\, I_{\rm d}, \tag{7.15}$$

where the subscripts "o" or "d" denotes evaluation of the bracket in the observer or disk co-rotating reference frame respectively. Using the expressions (7.13) and noting that $L = 0$ for rays that goes through the axis, we find

$$(p^\alpha u_\alpha)_{\rm o} = -E\xi^{-1/2}(z), \quad (p^\alpha u_\alpha)_{\rm d} = -E\left(1 - \frac{3R_{\rm S}}{2r_{\rm d}}\right)^{-1/2}. \tag{7.16}$$

The intensity of radiation intercepted by the observer is

$$I(\vartheta, z) = \frac{1}{\xi^2(z)}\left(1 - \frac{3R_{\rm S}}{2r_{\rm d}}\right)^2 I_{\rm d}(r_{\rm d}). \tag{7.17}$$

The tetrad components of the stress-energy tensor as measured by the observer can be calculated according to definition

$$T^{(\alpha)(\beta)}(z) = \int_{4\pi} I(\vartheta, z) n^{(\alpha)} n^{(\beta)} {\rm d}\Omega, \tag{7.18}$$

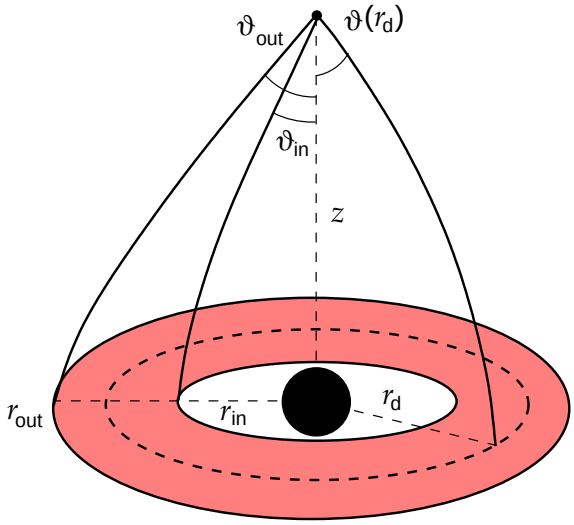

Figure 7.1: Geometry of the disk radiation field. The angle of observation ϑ is given by the radial coordinate in the disk $r_{\rm d}$ and the height z above the disk.

where $\mathrm{d}\Omega = \sin\vartheta \mathrm{d}\vartheta\mathrm{d}\varphi$ is element of solid angle. Due to the axial symmetry of the problem, the intensity does not depend on the angle φ and only three components of the stress-energy tensor are independent,

$$T^{(t)(t)} = 2\pi \int_{-1}^{1} I(\mu, z)\mathrm{d}\mu, \quad T^{(t)(z)} = 2\pi \int_{-1}^{1} I(\mu, z)\mu\mathrm{d}\mu, \quad T^{(z)(z)} = 2\pi \int_{-1}^{1} I(\mu, z)\mu^2\mathrm{d}\mu, \tag{7.19}$$

where we introduced an usual substitution in the viewing angle $\mu \equiv \cos\vartheta$ and performed the trivial integration over the angle φ. The two other non-vanishing components, $T^{(x)(x)} = T^{(y)(y)}$ can be found from condition $T^{(t)(t)} = T^{(x)(x)} + T^{(y)(y)} + T^{(z)(z)}$.

The cosine of the viewing angle μ is connected with the radius of the emission $r_{\rm d}$ and with the height z of the observer above the disk. The relation is given by the shape of the light ray (see Figure 7.1). In the absence of the gravitational field, light rays are straight lines and the relation between ϑ, $r_{\rm d}$ and z becomes a simple trigonometric formula. However, if the light rays are bent by gravity an integration of the geodesic equation is necessary. In presented calculations we traced the photon-path in backward direction – from observer position to the disk. We numerically integrated the geodesic equation (A.9) with the initial conditions chosen according to equation (A.13) that relates the angle ϑ with the impact parameter of the ray. Finally, we found the viewing angle ϑ as a function of the radius $r_{\rm d}$ of the emission point and the observer position z.

Once the function $\mu(r_{\rm d}, z)$ is specified, we can replace the integration over the viewing angle by the integration over the disk radius. We find

$$T^{(\alpha)(\beta)} = \frac{mc^3}{\sigma_{\rm T} R_{\rm S}} \Lambda T_\star^{(\alpha)(\beta)}, \tag{7.20}$$

where we introduced the normalized stress-tensor $T_\star^{(\alpha)(\beta)}$ components given by integrals

$$T_\star^{(t)(t)} = \frac{2\pi}{\xi^2(z)} \int_{r_{\rm in}}^{r_{\rm out}} \left(1 - \frac{3R_{\rm S}}{2r_{\rm d}}\right)^2 I_{\rm d\star}(r_{\rm d}) \frac{\partial\mu}{\partial r_{\rm d}} \mathrm{d}r_{\rm d}, \tag{7.21}$$

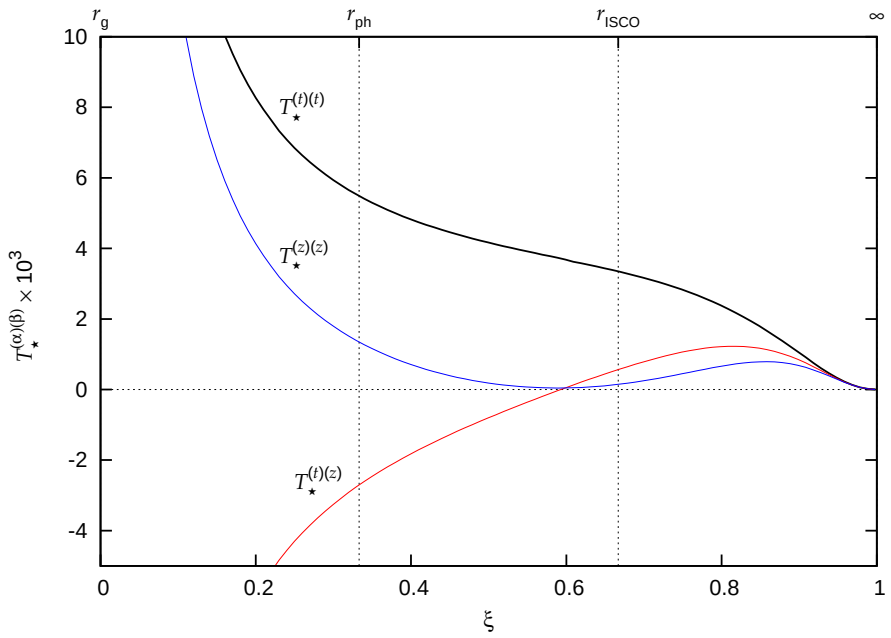

Figure 7.2: Normalized components of the radiation stress-energy tensor on the symmetry axis as calculated using the equations (7.21)–(7.23). The source of radiation is a standard Shakura & Sunyaev (1973) accretion disk surrounding Schwarzschild black hole. The inner disk radius corresponds to the innermost stable circular orbit, $r_{\rm in} = 3R_{\rm S}$ and the outer disk radius is at $r_{\rm out} = 10^3 R_{\rm S}$. We show the dependence on the $\xi \equiv 1 - R_{\rm S}/z$, because it captures the whole range of the z-axis and enlarges the area where effects of strong gravity are important. The locations of the photon-sphere and the radius of the innermost stable circular orbit are also shown. The dimensional values of the stress-energy tensor can be calculated using equation (7.20).

$$T_\star^{(t)(z)} = \frac{2\pi}{\xi^2(z)} \int_{r_{\rm in}}^{r_{\rm out}} \left(1 - \frac{3R_{\rm S}}{2r_{\rm d}}\right)^2 I_{{\rm d}\star}(r_{\rm d})\, \mu(r_{\rm d}, z)\, \frac{\partial \mu}{\partial r_{\rm d}}\, {\rm d}r_{\rm d}, \tag{7.22}$$

$$T_\star^{(z)(z)} = \frac{2\pi}{\xi^2(z)} \int_{r_{\rm in}}^{r_{\rm out}} \left(1 - \frac{3R_{\rm S}}{2r_{\rm d}}\right)^2 I_{{\rm d}\star}(r_{\rm d})\, \mu^2(r_{\rm d}, z)\, \frac{\partial \mu}{\partial r_{\rm d}}\, {\rm d}r_{\rm d}. \tag{7.23}$$

The normalized components of the stress-energy tensor calculated according to equations (7.21)–(7.23) are shown in the Figure 7.2. We assume that the position of the disk inner radius is determined predominantly by general-relativistic effects and therefore it coincides with the radius of the innermost stable circular orbit, $r_{\rm in} = r_{\rm ISCO} = 3R_{\rm S}$. We chose the value $r_{\rm out} = 10^3 R_{\rm S}$ for the outer radius of the disk. Although the disk model chosen here is rather specific, the resulting radiation field shown in Figure 7.2 reflects several important features that are general and can be expected in the radiation of other different and probably more relevant disk models.

- The stress-energy tensor vanishes as $z \to \infty$ ($\xi \to 1$) because the angular size of the disk as observed by distant observers decreases to zero.

- The tz-component measured by a stationary observer changes its sign for a certain value of z. Far from the disk it must be positive because the disk behaves like a

point source at large distances. On the other hand, since the disk is located outside the photon-sphere corresponding to the radius $r = r_{\rm ph}$, a stationary observer located inside receives only photons falling into the black hole. Therefore the $T^{(t)(z)}$ must be negative in this region and the change of the sign must occur above the photon-sphere.

- All three components diverge as $z \to R_{\rm S}$ ($\xi \to 0$). In fact, there are two effects acting against each other: the gravitational bending of light-rays reduces a solid angle that the disk occupy on the observer's local sky by factor $\propto \xi(z)$. On the other hand, the gravitational redshift increases the radiation intensity by factor $\propto \xi^{-2}(z)$. Close to the horizon the accretion disk appears as a point-like source giving the energy density $\propto \xi^{-1}(z)$.

7.3 Dynamics of electron clouds

In this section we consider a dynamics of an electron cloud under combined influence of the radiation and gravitational fields described in previous sections. We assume that the cloud motion is restricted to the z axis. Let us denote V the volume of the cloud measured in its co-moving frame and $n_{\rm e}$ density of the electrons in the cloud. We further assume that the electrons have random directions of velocity in the cloud co-moving frame. Later on we restrict ourselves to the mono-energetic electron distribution, that allows easy calculations, however the governing equations will be derived in full generality.

Let u^α be the cloud four-velocity. Then the cloud four-momentum is given as $p^\alpha = m_{\rm e} n_{\rm e} \bar{\gamma}_{\rm e} u^\alpha V$, where $\bar{\gamma}_{\rm e}$ is the mean Lorentz factor of the electron (i.e. mean energy of the electron in units of electron rest energy $m_{\rm e}c^2$) in the cloud co-moving frame. The equation of motion reads

$$F^\alpha = \frac{{\rm D}p^\alpha}{{\rm D}s} = m_{\rm e} n_{\rm e} V \left(u^\alpha \frac{{\rm d}\bar{\gamma}_{\rm e}}{{\rm d}s} + \bar{\gamma}_{\rm e} a^\alpha \right), \tag{7.24}$$

where ${\rm D}/{\rm D}s$ denotes covariant derivative with respect to the proper time s and a^α is the cloud four-acceleration. A total four-force acting on the cloud F^α affects both, the cloud "microphysics" – the distribution of the electron energies – as well as the dynamics of the cloud as a whole (the first and the second term in the bracket respectively).

In the curved spacetime, the four-acceleration a^α is given by

$$a^\alpha \equiv \frac{{\rm D}u^\alpha}{{\rm D}s} = \frac{{\rm d}u^\alpha}{{\rm d}s} + \Gamma^\alpha_{\mu\nu} u^\mu u^\nu. \tag{7.25}$$

The nonzero components of the four-velocity take simple form when evaluated in the local orthonormal tetrad of a stationary observer. In that case, we found $u^{(t)} = \gamma$ and $u^{(z)} = \gamma\beta$, where γ and β are Lorentz factor and three-velocity of the cloud measured by the observer. Then the nonzero components of the four-velocity measured by the distant observer can be expressed as

$$u^t = \gamma \xi^{-1/2}, \quad u^r = \gamma\beta\xi^{1/2}. \tag{7.26}$$

Substituting them into equation (7.25) we find

$$a^t = \frac{\gamma^2\beta}{\xi} \left(\xi^{1/2} \frac{{\rm d}\beta}{{\rm d}s} + \frac{R_{\rm S}}{2z^2} \right), \quad a^z = \gamma^2 \left(\gamma \xi^{1/2} \frac{{\rm d}\beta}{{\rm d}s} + \frac{R_{\rm S}}{2z^2} \right). \tag{7.27}$$

and when these expressions are further substituted to the equation of motion (7.24) we obtain

$$\frac{F^{(t)}}{m_\mathrm{e} n_\mathrm{e} \bar{\gamma}_\mathrm{e} V} = \frac{\gamma}{\bar{\gamma}_\mathrm{e}} \frac{\mathrm{d}\bar{\gamma}_\mathrm{e}}{\mathrm{d}s} + \gamma^3 \beta \frac{\mathrm{d}\beta}{\mathrm{d}s} + \frac{\gamma^2 \beta}{\xi^{1/2}} \frac{R_\mathrm{S}}{2z^2}, \tag{7.28}$$

$$\frac{F^{(z)}}{m_\mathrm{e} n_\mathrm{e} \bar{\gamma}_\mathrm{e} V} = \frac{\gamma\beta}{\bar{\gamma}_\mathrm{e}} \frac{\mathrm{d}\bar{\gamma}_\mathrm{e}}{\mathrm{d}s} + \gamma^3 \frac{\mathrm{d}\beta}{\mathrm{d}s} + \frac{\gamma^2}{\xi^{1/2}} \frac{R_\mathrm{S}}{2z^2}. \tag{7.29}$$

Finally, after some algebra, the dynamic equations take the form

$$\frac{\mathrm{d}\bar{\gamma}_\mathrm{e}}{\mathrm{d}s} = \frac{F^{(t)} - \beta F^{(z)}}{m_\mathrm{e} n_\mathrm{e} V}, \tag{7.30}$$

$$\gamma \frac{\mathrm{d}\beta}{\mathrm{d}s} = \frac{F^{(z)} - \beta F^{(t)}}{m_\mathrm{e} n_\mathrm{e} V} - \frac{R_\mathrm{S}}{2z^2 \xi^{1/2}}. \tag{7.31}$$

Equation (7.30) expresses the change of the mean electron energy of the cloud when external force is applied. Clearly, the electron energies remain unchanged if the gravitational field acts on the cloud only. The equation (7.31) describes the dynamics of the cloud as a whole. We note that the equations (7.30) and (7.30) were derived with an implicit assumption that the particle distribution remains isotropic. Neglecting the electron individual motion the equation (7.31) becomes identical with equation (3.12)[1] of Abramowicz et al. (1990).

The electrons in the cloud interact with the radiation field via Thomson scattering. Let us consider first scattering on a single electron. Coherence of scattering and front-to-back symmetry of the corresponding differential-cross-section formula implies that the radiation field that interacts with electron lose all its momentum and keep all its energy as measured in the electron rest frame. Therefore, the rate of four-momentum that electron gains in its rest frame can be expressed as $\mathrm{d}\tilde{p}_\mathrm{e}{}^t/\mathrm{d}s_\mathrm{e} = 0$ and $\mathrm{d}\tilde{p}^i_\mathrm{e}/\mathrm{d}s_\mathrm{e} = \sigma_\mathrm{T} \tilde{T}^{ti}$, where s_e is the electron proper time the tildes denotes evaluation in the electron rest frame. These expression can be invariantly expressed using the electron four-velocity u^α_e as

$$\frac{\mathrm{d}p^\alpha_\mathrm{e}}{\mathrm{d}s_\mathrm{e}} = -\sigma_\mathrm{T} \left(T^{\alpha\rho} u_{\mathrm{e}\rho} + T^{\rho\sigma} u_{\mathrm{e}\rho} u_{\mathrm{e}\sigma} u^\alpha_\mathrm{e} \right). \tag{7.32}$$

(Phinney 1982, see) Let the electron four-velocity in the cloud rest frame be

$$u^\alpha_\mathrm{e} = (\gamma_\mathrm{e},\ \gamma_\mathrm{e}\beta_\mathrm{e} \cos\varphi_\mathrm{e} \vartheta_\mathrm{e},\ \gamma_\mathrm{e}\beta_\mathrm{e} \sin\varphi_\mathrm{e} \sin\vartheta_\mathrm{e},\ \gamma_\mathrm{e}\beta_\mathrm{e} \cos\vartheta_\mathrm{e}), \tag{7.33}$$

where φ_e and ϑ_e are directional angles of the electron three-velocity. Total rate of the four-momentum transfered to the whole cloud from the radiation field can be found by integration over the isotropic electron distribution, e.g. averaging equation (7.32) over angles φ_e and ϑ_e and over the electron Lorentz factor γ_e. We find (compare with equations (4) and (5) of Phinney (1982) and equations (5) and (6) of Cheng & Odell (1981))

$$\langle \tilde{f}^{(t)} \rangle = -\sigma_\mathrm{T} \mathcal{A} \tilde{T}^{(t)(t)}, \quad \langle \tilde{f}^{(i)} \rangle = \sigma_\mathrm{T} \mathcal{C} T^{(t)(i)}, \quad \mathcal{C} \equiv 1 + \tfrac{2}{3} \langle \gamma_\mathrm{e}^2 \beta_\mathrm{e}^2 \rangle, \tag{7.34}$$

where tilde refers to quantities measured in the cloud co-moving frame and $\mathcal{A}$ was previously introduced in equation (6.73). Covariant expression of the equations (7.34) can be found in the following way. Denote u^α the cloud four-velocity. Then $\tilde{u}^{(\alpha)} = \delta^\alpha_t$ in the cloud

[1] with substituted expression (3.11)

co-moving frame and components of the radiation stress-energy tensor can be invariantly expressed as $\tilde{T}^{(t)(i)} = -\tilde{u}_\sigma \tilde{T}^{(\sigma)(i)}$ and $\tilde{T}^{(t)(t)} = u_\rho u_\sigma T^{(\rho)(\sigma)}$. The covariant expression can be looked for in the form

$$\langle f^\alpha \rangle = -\sigma_{\rm T} \mathcal{C} u_\sigma T^{\sigma\alpha} + K u^\alpha. \tag{7.35}$$

where K is an undetermined constant. Evaluating the time component of equation (7.35) in the cloud co-moving frame and comparing it with equation (7.34), we find that

$$\langle \tilde{f}^{(t)} \rangle = \sigma_{\rm T} \mathcal{C} \tilde{T}^{(t)(t)} + K = -\sigma_{\rm T} \mathcal{A} \tilde{T}^{(t)(t)}, \tag{7.36}$$

from which we conclude that $K = -\sigma_{\rm T}(\mathcal{A}+\mathcal{C}) T^{\rho\sigma} u_\rho u_\sigma$. Therefore, the equations (7.34) take a form

$$\langle f^\alpha \rangle = -\sigma_{\rm T} \left[\mathcal{C} T^{\alpha\beta} u_\beta - (\mathcal{A}+\mathcal{C}) T^{\rho\sigma} u_\rho u_\sigma u^\alpha \right], \tag{7.37}$$

that is manifestly covariant.

Total four-force acting on the cloud can be found by multiplying the mean force acting on a single electron by the total number of electrons in the cloud

$$F^\alpha = n_{\rm e} V \langle f^\alpha \rangle = -\sigma_{\rm T} n_{\rm e} V \left[\mathcal{C} T^{\alpha\beta} u_\beta - (\mathcal{A}+\mathcal{C}) T^{\rho\sigma} u_\rho u_\sigma u^\alpha \right] \tag{7.38}$$

Evaluating the equation in the local orthonormal tetrad of a stationary observer on the symmetry axis, we find

$$F^{(t)} - \beta F^{(t)} = \sigma_{\rm T} n_{\rm e} \gamma V \mathcal{A} \left[T^{(t)(t)} - 2\beta T^{(t)(z)}, + \beta^2 T^{(z)(z)} \right], \tag{7.39}$$

$$F^{(z)} - \beta F^{(t)} = \sigma_{\rm T} n_{\rm e} \gamma V \mathcal{C} \left[(1+\beta^2) T^{(t)(z)} - \left(T^{(t)(t)} + T^{(z)(z)} \right) \beta \right], \tag{7.40}$$

By substitution equations (7.39) and (7.40) into the equations of motion (7.30) and (7.31), we find

$$\frac{{\rm d}\bar{\gamma}_{\rm e}}{{\rm d}s} = -\gamma \mathcal{A} \frac{\sigma_{\rm T}}{m_{\rm e}} \left[T^{(t)(t)} - 2\beta T^{(t)(z)} + \beta^2 T^{(z)(z)} \right], \tag{7.41}$$

$$\frac{{\rm d}\beta}{{\rm d}s} = \mathcal{C} \frac{\sigma_{\rm T}}{m_{\rm e}\bar{\gamma}_{\rm e}} \left[(1+\beta^2) T^{(t)(z)} - \left(T^{(t)(t)} + T^{(z)(z)} \right) \beta \right] - \frac{R_{\rm S}}{2\gamma z^2 \xi^{1/2}}. \tag{7.42}$$

Finally, introducing the dimensionless normalized components of the radiation stress-energy tensor according to equation (7.20) we arrive at the result

$$\frac{{\rm d}\bar{\gamma}_{\rm e}}{{\rm d}s} = -\gamma \mathcal{A} \Lambda \left[T_\star^{(t)(t)} - 2\beta T_\star^{(t)(z)} + \beta^2 T_\star^{(z)(z)} \right], \tag{7.43}$$

$$\frac{{\rm d}\beta}{{\rm d}s} = \frac{1}{\bar{\gamma}_{\rm e}} \mathcal{C} \Lambda \left[(1+\beta^2) T_\star^{(t)(z)} - \left(T_\star^{(t)(t)} + T_\star^{(z)(z)} \right) \beta \right] - \frac{R_{\rm S}}{2\gamma z^2 \xi^{1/2}}, \tag{7.44}$$

where we assume that the proper time s is expressed in convenient units $R_{\rm S}/c = 2GM/c^3$. The equations (7.43) and (7.44) should be completed by

$$\frac{{\rm d}t}{{\rm d}s} = \gamma \xi^{-1/2} R_{\rm S}, \tag{7.45}$$

$$\frac{{\rm d}r}{{\rm d}s} = \gamma \beta \xi^{1/2} R_{\rm S}. \tag{7.46}$$

Let us make few comments about equations (7.43) and (7.44): (i) The first one describes the evolution of the electron distribution in the cloud co-moving frame. Note, that the

right-hand side of this equation is *always* negative for *any* radiation field because the terms in the square bracket are proportional to the radiation energy density measured in the cloud co-moving frame. Therefore the averaged electron Lorentz factor $\bar{\gamma}_{\rm e}$ will be decreasing function of the proper time and the electrons will cool. We note, however, that a qualitatively different behavior is obtained by including the pressure of the electron gas that has been neglected for simplicity (Phinney 1982).

Except the Compton cooling there can be other important processes that influence the electron distribution: synchrotron losses, injection of highly energetic particles, etc. For an extensive discussion we refer the reader to the papers of Sikora et al. (1996a,b). These processes can be easily taken into account by adding another terms to right-hand side of equation (7.43). This approach, however considerably enlarges a number of free parameters of the model.

The dynamics of the cloud as a whole is governed by equation (7.44). The right-hand side contains contributions of both, the radiation (first term) and the gravitational (the second term) field. The relative importance of them is expressed by the Eddington parameter Λ. The gravitational field always accelerates the cloud toward the black hole. On the other hand, the effect of radiation field depends on the cloud height z above the accretion disk, on the mean Lorentz factor $\bar{\gamma}_{\rm e}$ of electrons in the cloud co-moving reference frame and also on the cloud velocity β because of the relativistic aberration.

In the case of cold clouds ($\mathcal{A}=0$, $\mathcal{C}=1$) an appropriate tool in discussion of particle dynamics is the saturation velocity introduced by many authors (see e.g. Sikora & Wilson 1981; Abramowicz et al. 1990; Vokrouhlický & Karas 1991; Melia & Königl 1989; Keane et al. 2001).

First, let us consider the limit $\Lambda \to \infty$. In this case we neglect the contribution of the gravity on the right-hand side of the equation (7.44). The condition $\mathrm{d}\beta/\mathrm{d}s = 0$ gives a quadratic equation with the solution

$$\beta_{\rm sat}(z;\infty) \equiv \beta_0 = \sigma - \sqrt{\sigma^2 - 1}\,, \quad \sigma \equiv \frac{T_\star^{(t)(t)} + T_\star^{(t)(z)}}{2T_\star^{(t)(z)}}\,, \tag{7.47}$$

that is the equilibrium velocity given by equation (6.23).

Now, consider the case of general Λ. We denote $\mathcal{F}(z,\beta,\Lambda)$ the right-hand side of equation (7.44). It is not difficult to show that for a given z, $\mathcal{F}$ is a monotonic function of $\beta \in [-1,1]$ even for fully general radiation field: condition $\partial\mathcal{F}/\partial\beta = 0$ leads to the cubic equation

$$\beta^3 - 3\beta + 2\sigma = 0, \tag{7.48}$$

the solution $\beta = \beta_0^{1/3} + \beta_0^{-1/3}$ of which lies always outside the range $[-1,1]$. Hence, for a given height z above the disk the sign of $\partial\mathcal{F}/\partial\beta$ is fixed independently on β. The monotony of the right-hand side implies that the equation (7.44) can be expressed as

$$\frac{\mathrm{d}\beta}{\mathrm{d}s} = -\left[\beta - \beta_{\rm sat}(z)\right]\mathcal{H}(z,\beta,\Lambda), \tag{7.49}$$

where $\mathcal{H}(z,\beta,\Lambda)$ is a positive function and $\beta_{\rm sat}(z)$ is the saturation velocity. Therefore, the electron cloud is accelerated and decelerated when $\beta > \beta_{\rm sat}$ and $\beta < \beta_{\rm sat}$, respectively.

For the cold clouds the equations (7.44)–(7.46) allow a finite set of topologically different solutions. These can be classified into different categories (Vokrouhlický & Karas 1991; see also Abramowicz et al. 1990 and Keane et al. 2001) according to the behavior of the saturation velocity in (ξ,β)-plane.

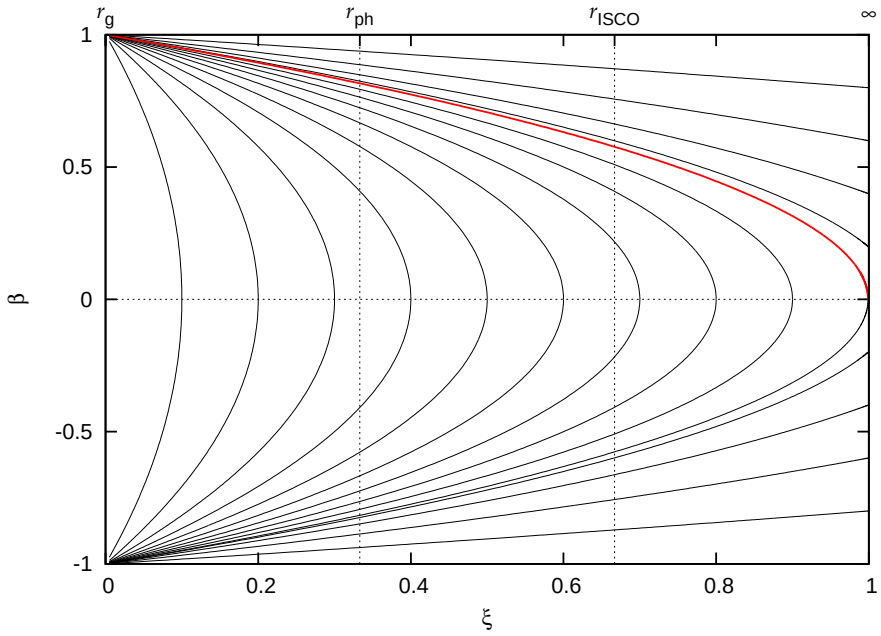

Figure 7.3: Possible trajectories of a cold ($\bar{\gamma}_e \equiv 1$) electron cloud for $\Lambda = 0$ where the radiation field is dynamically unimportant. Trajectories are given by equation (7.50). The red curve separates the trajectories that reach infinity from those falling to the black hole.

As shown by Abramowicz et al. (1990), the situation $\Lambda = 0$ corresponds to the saturation velocity $\beta_{\rm sat}(z) = -1$. The motion of the cloud is determined by gravity only, while the radiation field is dynamically unimportant. The trajectories $\beta(\xi)$ of a cloud are well-known trajectories of freely-falling particles that can be analytically expressed as

$$\beta(\xi) = \pm\sqrt{1 - \xi(1-\beta_\infty)}\,, \quad \beta(\xi) = \pm\sqrt{1 - \frac{\xi}{\xi_{\rm m}}}\,. \tag{7.50}$$

The first equation correspond to escaping (the positive sign) and freely-falling (the negative sign) trajectories which velocity at infinity ($\xi = 1$) is β_∞. The second one describes trajectories of particels initial velocity of which is not high enough to escape from the black-hole gravitational field. Such trajectories contain turning point at $\xi = \xi_{\rm m}$. The positive and negative sign is for approaching and receiving part of a trajectory, respectively. It follows, that cloud escapes from gravitational field only if its initial velocity and ξ-coordinate satisfy condition $\beta_0 > \sqrt{1-\xi_0}$. Possible trajectories in the case of $\Lambda = 0$ are shown in Figure 7.3.

When the normalized disk luminosity Λ is nonzero, it is practically impossible to find an analytic solution and we must carry out a numerical integration of equations (7.44)-(7.46). We used a standard Runge-Kutta integrator with an adaptive step (Press 2002). Figure 7.4. captures possible trajectories of the cold electron cloud in the case when the normalized disk luminosity reaches its critical value $\Lambda = \Lambda_{\rm crit}$. The saturation velocity vanishes as z goes to infinity ($\xi \to 1$) in this case. The only qualitative difference from the case $\Lambda = 0$ involves only infalling trajectories with velocity at infinity β_∞ smaller than $\beta_{\rm sat}(\infty)$. Particles moving along these trajectories are first decelerated until they reach the saturation velocity. Following acceleration toward the black is stronger than in the

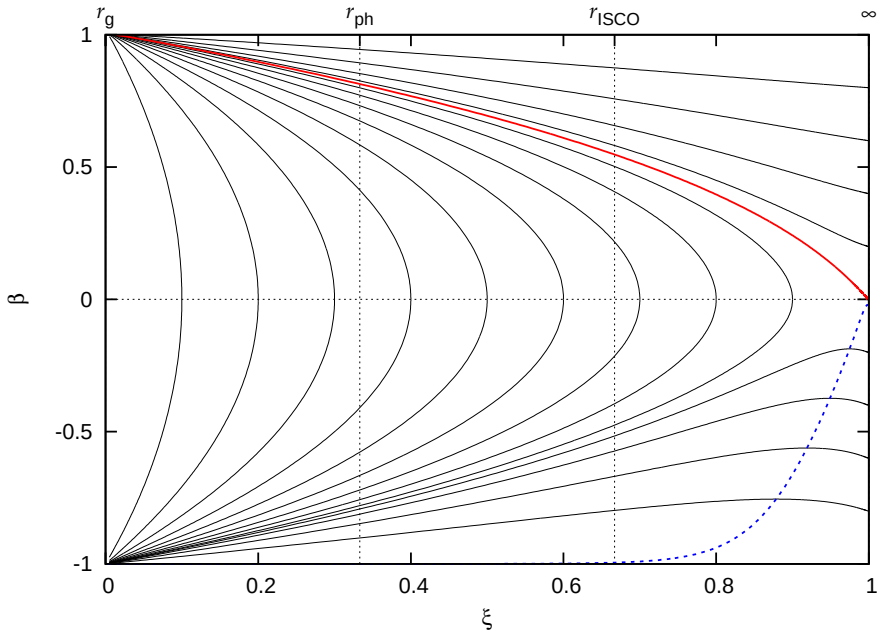

Figure 7.4: The same as in Figure 7.3, but for the radiation field with the normalized luminosity $\Lambda = \Lambda_{\rm crit}$. The red solid line separates region of trajectories that escapes to infinity. The blue dotted line corresponds to the saturation velocity $\beta_{\rm sat}(\xi)$ that vanishes in infinity for the critical value of the Λ-parameter. Trajectories are slightly distorted with respect to the $\beta = 0$ line by the weak influence of gravity. Only the infalling particles are significantly affected.

case $\Lambda = 0$ due to the contribution of radiation field.

Different topology of the phase plane occur, when $\Lambda > \Lambda_{\rm crit}$. There is an equilibrium point $z = z_{\rm eq}$ where the saturation velocity $\beta_{\rm sat}(z)$ changes its sign. The same behavior was reported by Abramowicz et al. (1990) in the case of the radiation field of a bright star. However, there is an important difference: while the saturation velocity changes its sign from positive to negative as ξ grows in their case, the change is from negative to positive in our case. This remarkably changes the topology of trajectories in the (ξ, β) plane: the equilibrium point $[\xi_{\rm eq}, 0]$ is of the *saddle* type in the case of the disk radiation field contrary to the case of the stellar radiation field where the equilibrium point is of the *nodal* type. The two examples are given in figures 7.5 and 7.6. They show situation, when $\Lambda = 10$ and $\Lambda = 100$, respectively.

So far, our discussion involved trajectories of cold clouds with $\bar{\gamma}_{\rm e} \equiv 1$. How the electron random motion affects the motion of whole cloud? First, we assume that the electron distribution is constant in time e.g. that there is an additional mechanism injecting energetic particles i.e. $\mathrm{d}\bar{\gamma}_{\rm e}/\mathrm{d}s = 0$. Then, exploring equation (7.44), we find that the equation takes the same form as in the case the of the cold cloud ($\mathcal{C} = \bar{\gamma}_{\rm e} = 1$) if the normalized luminosity is rescalled as

$$\Lambda \rightarrow \Lambda' \equiv \frac{\mathcal{C}}{\bar{\gamma}_{\rm e}}\Lambda. \tag{7.51}$$

Warm clouds will move identically as the cold ones in the radiation field luminosity of which is greater by factor $\mathcal{C}/\bar{\gamma}_{\rm e}$. Hence, the motion of the warm cloud, which electrons

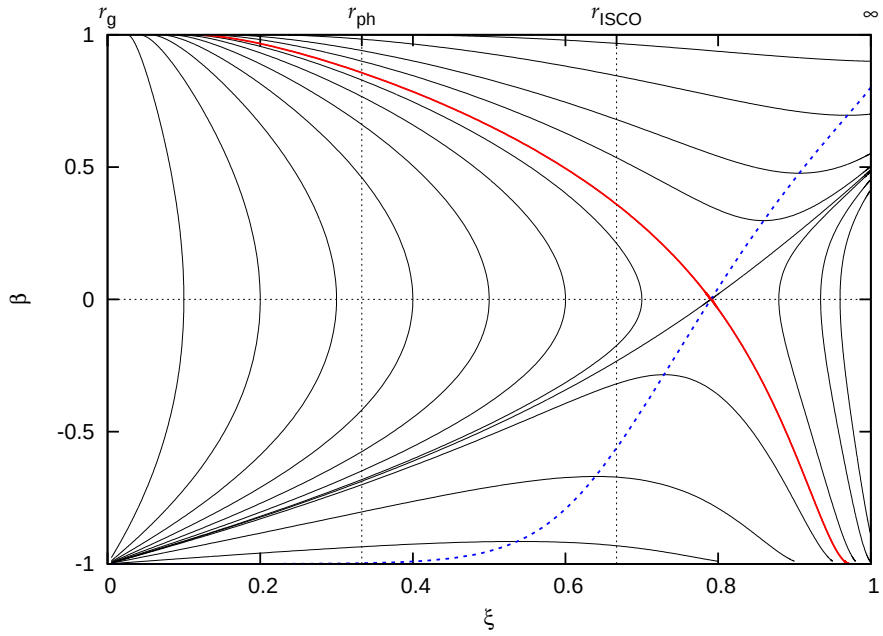

Figure 7.5: The same as in the figure 7.3, but for the radiation field with the normalized luminosity $\Lambda = 10$. The critical point of the saddle topology appears at a place where the saturation velocity (blue dotted line) crosses the $\beta = 0$ line. Again, the thick red curve refers to the separation of trajectories that reach the infinity.

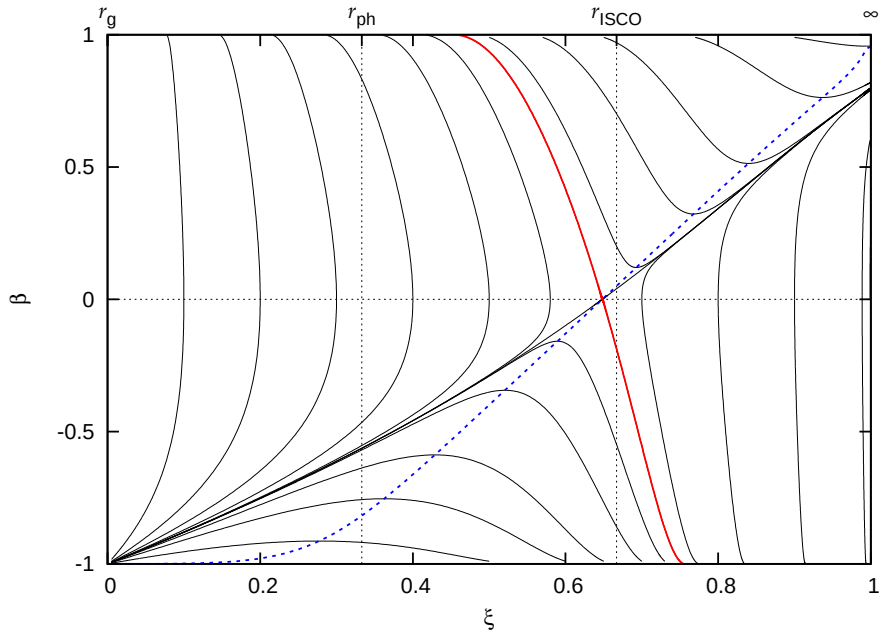

Figure 7.6: The same as in the figure 7.3, but for the radiation field with the normalized luminosity $\Lambda = 100$. The velocity of the cloud quickly adhere to the saturation curve $\beta_{\rm sat}(\xi)$ provided that the dynamics is governed predominantly by the radiation field. Then the motion follows the curve adjacent to but slightly different from the saturation velocity.

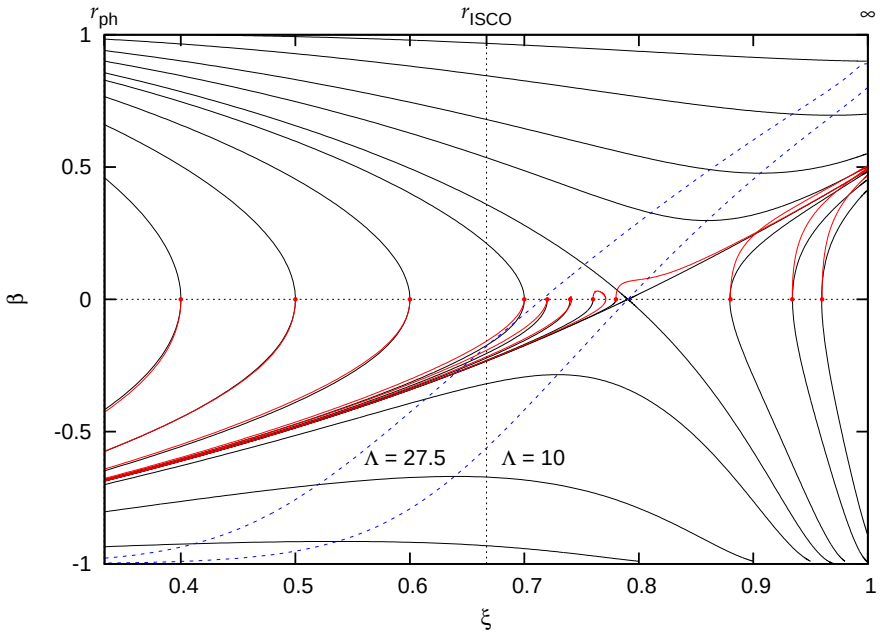

Figure 7.7: Trajectories of a warm electron cloud (red curves). Possible trajectories of a cold cloud are also shown for reference (black curves). The initial conditions for the trajectories are chosen such that they corresponds to some trajectory of the cold cloud. The initial electron Lorentz factor is $(\bar{\gamma}_e)_0 = 4$ and the normalized luminosity of the disk radiation field is $\Lambda = 10$.

cool according to equation (7.43) is identical with the motion of a cold cloud composed in the radiation field which luminosity decreases with time. This approach allows us to qualitatively understand behavior of trajectories in Figure 7.7. The initial conditions for the trajectories of warm cloud are chosen in the way that they corresponds to some trajectory of the cold cloud in the "background" of the figure. The initial mean Lorentz factor is $(\bar{\gamma}_e)_0 = 4$ and the normalized luminosity of the disk radiation field is $\Lambda = 10$. Therefore, at the beginning the cloud will feel a radiation field of a luminosity $\Lambda' = (11/4)\Lambda = 27.5$. Corresponding saturation velocity is also shown in the figure. Clearly, the most affected are the trajectories starting at large distances where the radiation field is not strong enough to the electrons in the cloud. On the other hand, trajectories that start in the close vicinity of the black holes are similar to that of the cold clouds because the electrons become cold immediately. An interesting behavior show the trajectories that start between the two critical points. The clouds following these trajectories are first accelerated toward positive velocities, however, as they are cooled, the acceleration effect of the radiation field is reduced and the gravity becomes important. The cloud is eventually decelerated and attracted by the gravitational field toward the black hole.

7.4 Polarization along cloud trajectories

Different categories of particle motion provide a natural framework also for the discussion of the resulting polarization. By coupling the equations of particle motion with the polarization equations of Chapter 6 we obtain the Stokes parameters of the scattered light along

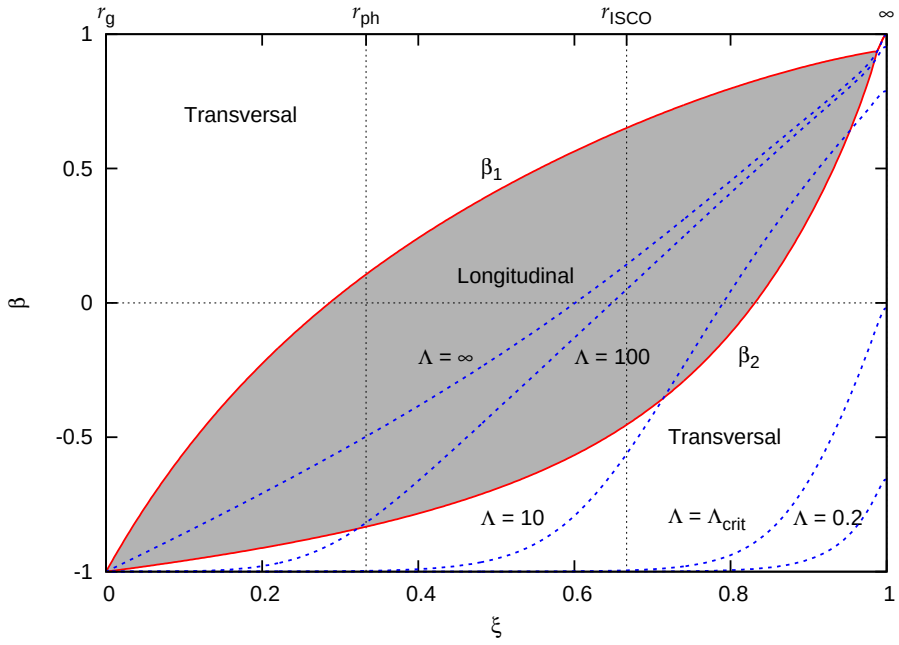

Figure 7.8: Three critical velocities of a cloud motion. The two curves $\beta_1(\xi)$ and $\beta_2(\xi)$ are velocities at which the polarization of the scattered radiation changes its orientation from the longitudinal to the transversal and vice versa (the region of a longitudinal polarization is dashed). The saturation velocities important for the cloud dynamics are also shown for several values of the normalized luminosity Λ.

each particle trajectory. As we showed in the Chapter 6 the relativistic aberration effect strongly affects observed polarization of the Thomson scattered radiation. In a general axisymmetric radiation field there are two velocities, β_1 and β_2, where the polarization changes sign and the orientation of the polarization vector changes from transversal to longitudinal and vice versa. We also showed that these changes are independent of the angle of observation. The two velocities can be immediately calculated from the three independent components of the stress-energy tensor according to equation (6.19). Critical velocities β_1 and β_2 depend only on ratios of the tensor components. Hence, the change of polarization effect is given by the geometry of the radiation field and it is independent of the total luminosity (e.g. it does not depend on Λ-factor). However the dynamics of the clouds is very sensitive to it.

Figure 7.8 shows velocities that are essential in our model. The two curves $\beta_1(\xi)$ and $\beta_2(\xi)$ delimit the region of the longitudinal polarization form the region of the transversal polarization. We also show the saturation velocities $\beta_{\rm sat}(\xi, \Lambda)$ for various values of the normalized luminosity. At high Λ the saturation velocity crosses the region of the longitudinal polarization. The trajectories of the cloud are strongly attracted toward the saturation curve in that case. Hence, we expected that the early change of the polarization sign is a frequent phenomenon in the observed polarization along these trajectories. On the other hand, at low luminosity the saturation velocity lies in the region of the transversal polarization. The trajectories, however are not attracted to the saturation curves so intensively.

Local polarization radiated by the cloud along the three selected trajectories is shown in

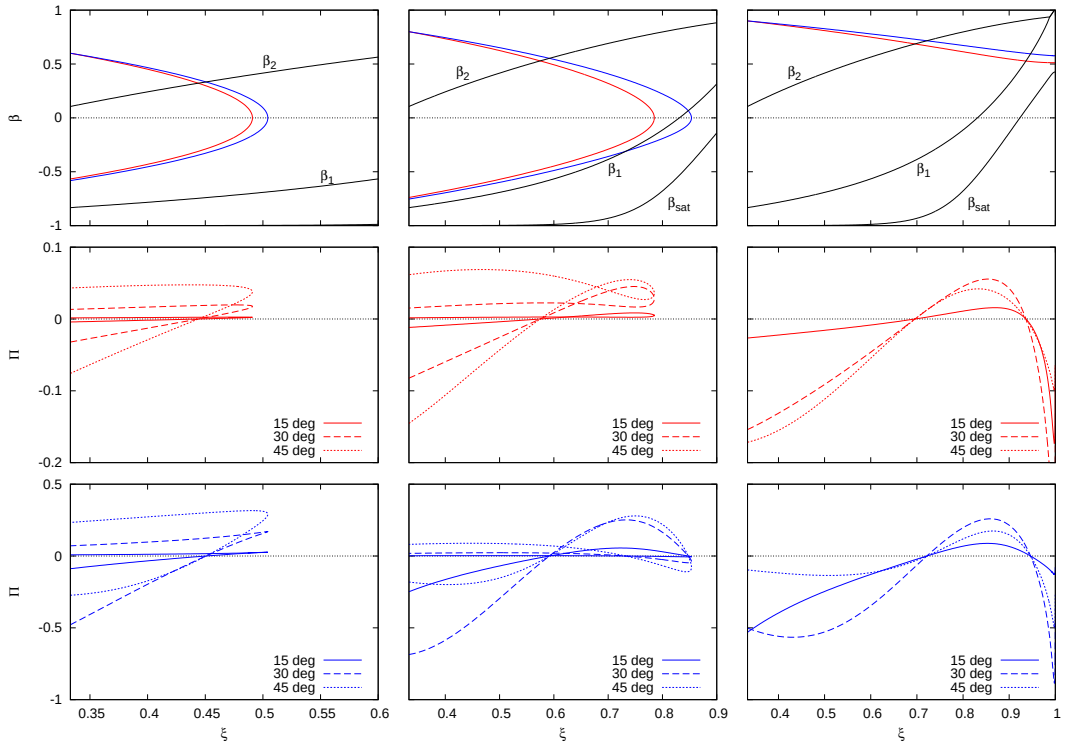

Figure 7.9: The local polarization along three different cloud trajectories. Top row: the velocity of a cold (the blue curve) and warm (the red curve) electron cloud. The initial electron Lorentz factor of the warm cloud is $\bar{\gamma}_{e0} = 3$. Each trajectory starts from the photon-sphere $z = 1.5\ R_S$ and it proceeds towards infinity. Three cases are shown for different values of the initial velocity: $\beta_0 = 0.6$ (left panel), $\beta_0 = 0.8$ (middle panel) and $\beta_0 = 0.9$ (right panel). Middle row: the polarization magnitude $\Pi(\xi)$ along the trajectory of the warm cloud corresponding to the above-given solutions. All curves have a common zero point where they cross each other. The sign of Π distinguishes the case of transversal polarization from the longitudinal one. The polarization is shown for three different inclinations: $i = 15$ (solid line), 30 (dashed line) and 45 deg (dotted line). Bottom row: the same as in the middle row but for the cold cloud.

Figure 7.9. We calculated polarization of the light scattered into three different directions. The luminosity of the incident radiation field is rather moderate, $\Lambda = 2$. The top panels show the trajectory of initially cold ($\bar{\gamma}_e = 1$) and warm ($\bar{\gamma}_e = 3$) cloud. The initial radius corresponds to the photon-sphere in all cases and the initial velocity is $\beta = 0.6$ (left panels), 0.8 (middle panels) and 0.9 (right panels) and is the same for both trajectories. In the middle and the bottom panels we show a local polarization radiated at angles $\vartheta = 15$, 45 and 90 deg. The middle panels shows polarization from the warm cloud an the bottom panel that from the cold cloud. The local polarization is calculated from the Stokes parameters given by the equations (6.16) and (6.16) or (6.74) and (6.77). Clearly, the change of the polarization angle occurs independently of the angle of observation. Note also that the radiation scattered by a hot cloud is strongly depolarized by an electron chaotic motion (the maximal value of the polarization magnitude is reduced by a factor ~ 5).

On the other hand, figure 7.10 shows the trajectory of the cloud in an intensive incident radiation field with $\Lambda = 100$. The initial conditions are $\xi_0 = 0.55$ ($z = 2.22\ R_{\rm S}$) and $\beta_0 = 0.99$. The cloud is first strongly decelerated to the saturation velocity and further accelerated to the terminal velocity $\beta_\infty \sim 0.8$. The mean Lorentz factor was initially set to the value ($\bar{\gamma}_{\rm e0} = 3$. The top-left panel shows the trajectory of the cloud in the (ξ, β)-plane. The trajectory of a cold cloud is also shown for comparison. The radiation cooling of electrons is shown in the top-right panel where the dependence of the electron mean Lorentz factor on the ξ-coordinate is shown. Clearly, the cloud becomes cold already in the initial deceleration phase and that is why the following acceleration is same as in the case of the cold cloud. This is apparent in the bottom two panels showing the polarization: starting from $\xi = 0.6$, the polarization curves become practically identical.

7.5 Intensity and polarization light curves

The self-consistency of the model allows us to calculate a temporal evolution of the intensity and the polarization of a scattered radiation as seen by an observer in infinity. The observed signal will be affected by both the special and general relativistic effects. An example of the first one are aberration and beaming effects that must be present because the source (an electron cloud) moves with a velocity comparable to the speed of light. A prominent example of the general relativistic effects are gravitation redshift and contribution of a higher-order images in the observed radiation. Hence identifying these effects could help in determination of the parameters of the central black hole.

The light curves presented in this section were calculated using the approximation of a source at low inclination that is introduced in the appendix B. We also refer the reader there for the expressions of local emission angles and time delays along direct and retro-lensed rays.

The geometry considered in calculations is shown in Figure B.1. Clouds move along the direction that makes an angle i with the line of sight. We consider contribution of three images to the observed radiation: one direct image and two retro-lensed images whose rays make a single round about the black hole (by the angle $\Phi = 2\pi \pm i$; corresponding images are referred to as + and −). The observed polarization and intensity for a cloud moving with velocity β at hight z above the accretion disk can be computed as follows. Let $I(z, \vartheta)_{\rm loc}$ and $\Pi(z, \vartheta)_{\rm loc}$ be a local intensity and polarization of a scattered radiation measured measured at the point of emission by a local stationary observer. The local emission angle ϑ is given by equation (B.8) for the direct ray and by the equation (B.30) for the retro-rays. Both, the polarization magnitude and the direction of polarization vector is conserved along rays in the Schwarzschild spacetime. Hence $\Pi_{\rm obs} = \Pi_{\rm loc}$. The intensity measured by the distant observer at rest is equal to the redshifted intensity, $I_{\rm obs} = \tilde{I} = \xi^2(z) I(z)$. The source occupies on the observer's sky small solid angle $\Delta\Omega_{\rm d}$ when projected by direct rays and $\Delta\Omega_\pm$ when projected by retro-rays. At low inclination $\Delta\Omega_{\rm d}$ approaches the value $\Delta\Omega_0$ in the flat spacetime in the absence of the gravitational field. However, $\Delta\Omega_\pm$ could be considerably different from it due to strong lensing effect that provides gravitational (de)magnification. For this purpose we multiply the intensity of the retro-lensed images by gravitational gain factor $\mathcal{M}_\pm(i, z)$ introduced by equation (B.35). Hence, the resulting intensity from the retro-lensed images has a meaning of the intensity per a direct-image solid angle $\Delta\Omega_{\rm d}$. Finally we consider mutual time delays between different images. The solution of the equations of motion (7.43)–(7.46) provides the cloud trajectory $z(t)$ as a function of the coordinate time t that coalesces with the

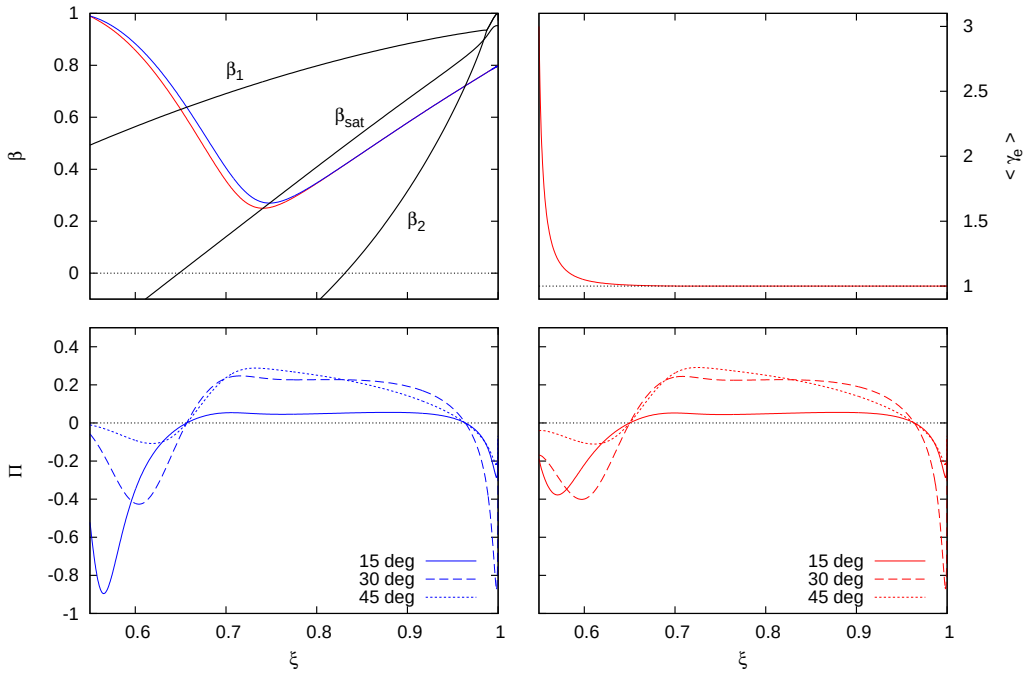

Figure 7.10: The local polarization along trajectory of the strongly decelerated clouds by an intensive radiation field. As in Figure 7.9 we show the trajectories of both, cold and warm clouds. The initial conditions are $\xi = 0.55$ and $\beta 0 = 0.99$. The initial electron Lorentz factor in the warm cloud is $\bar{\gamma}_{e0} = 3$. Top-left: The trajectories of the clouds (the notation is the same as in Figure 7.9). Top-right the radiative cooling of electrons of the warm cloud. Bottom-left and Bottom-right: the polarization of the radiation scattered by the cold and warm cloud respectively.

proper time of the distant static observer. The photon traveling time along direct rays is given by the equation (B.6) and by equation (B.29) for retro-rays.

We can distinguish three cases depending on the normalized luminosity of the incident radiation field: (i) the case of a dynamically unimportant radiation field with $\Lambda \ll 1$, (ii) the case $\Lambda \sim 1$ and (iii) the case $\Lambda \gg 1$, where the dynamic of a scatterer is strongly affected by the radiation field. The intensity light-curves are shown with a normalization by the initial intensity from direct image. This allows to compare relative importance of retro-lensed images in the result radiation as well as the temporal evolution of the intensity and polarization, however it complicates comparison of intensity between different light-curves. For this purpose, we remind that the exact value of the observed intensity can be recovered from equation (6.16) if the scatterer is a cold cloud or using the equations (6.74) and Lorentz transforms (6.14). Above given if the the scatterer contains hot electrons. However, for a raw comparisons the following scaling-law is sufficient if the electron Lorentz factor is not much greater than unity

$$I_{\rm obs} \propto \xi^2 \gamma^2 \mathcal{D}^4 \Lambda \varepsilon_\star \,. \tag{7.52}$$

Here $\varepsilon_\star$ is a normalized energy density of the incident radiation field (e.g. the tt-component of the normalized stress energy tensor). The time is given in the light crossing time, that is a natural unit in the system. The time span of the plots can be therefore rescaled

according to

$$t \simeq 1.5\,\frac{R_{\rm S}}{c} = 1.5\times 10^{-4}\frac{M}{10M_{\odot}} \quad [\rm sec], \tag{7.53}$$

i.e. proportionally to the central mass.

7.5.1 Dynamically unimportant radiation field ($\Lambda \ll 1$)

The solution of the equations of motion (7.43)–(7.46) is given analytically by the equation (7.50). The mean electron Lorentz factor $\bar{\gamma}_{\rm e}$ is constant. There is no difference between trajectories of cold and warm clouds. Figures 7.11 and 7.12 shows a temporal evolution of the observed polarization and intensity for three values of inclination $i = 1, 5$ and 30 deg. The scatterer is cold electron cloud moving along the trajectory with $\beta_{\infty} = 0$. The initial conditions are $\xi_0 = 0.5$ and $\xi_0 = 0.95$ in the case of inward and outward motion respectively.

In the case of the inward motion the observed intensity first slightly increases and then sharply decreases. The increase is connected with the increasing energy density of the incident radiation field (see Figure 7.2) the decrease is because of the gravitational redshift and relativistic beaming effect, since the cloud gradually reaches relativistic velocities. The same effects act together in the retro-lensed image, because the source is moving in the direction of observation in that case. The large intensity of retro-lensed images is also contributed by the gravitation lensing maximum of which occurs at $z = 2.36\ R_{\rm S}$ (see Figure B.4). However this effect strongly reduces the retro-lensed intensity as the source approach the photon-sphere. The time delay between the two retro-lensed images and different intensities becomes apparent at higher inclinations (middle and bottom panels of Figure 7.11). The polarization light-curves show change from the transversal to the longitudinal orientation. The same effect can be seen in the retro-lensed polarization with some time delay. With increasing inclination polarization of the direct image increases, however, the polarization of retro-lensed images practically remains the same. The reason is that the while the local emission angle for the direct ray increases, the emission angle of the retro-lensed rays is always close to the viewing angle of the photon-sphere. Finally, the duration of the direct light curve is approximately two-times greater than the duration of the retro-lensed curves because of the aberration effect.

The light curves corresponding to the outward motion (7.12) show gradual decrease of the observed intensity in both direct and retro-lensed images. The reason is a decrease of the energy density of the incident radiation field along the trajectory and the gravitational deceleration of the cloud that reduces the relativistic beaming effect. In the case of the retro-lensed images the intensity is reduced mainly by the decrease of the gain-factor. The retro-lensed intensity is negligible compared to the direct one even under a favorable conditions of very low inclination $i = 1$ deg. The polarization light curves show two changes of the polarization orientation: from the transversal to the longitudinal and then back to the transversal.

7.5.2 Incident radiation field of a moderate luminosity ($\Lambda = 2$)

Figures 7.13 and 7.14 show the observed intensity and polarization light curves from the cold and warm clouds moving in the radiative field of a moderate normalized luminosity $\Lambda = 2$. The initial conditions are $z_0 = r_{\rm ph}$ ($\xi_0 = 0.33$) and $\beta_0 = 0.8$. The initial electron Lorentz factor of the warm cloud is $\bar{\gamma}_{\rm e0} = 3$. The trajectories have two parts: the cloud

initially moves towards infinity, then in turns back and falls into the black hole. This is easily seen in the shape of the intensity light curve from the direct image. The start is similar to the intensity curves in Figure 7.12 (fast drop in the intensity). The cloud is decelerated from the initial relativistic velocity and the radiation from it is de-beamed. Then the intensity is nearly saturated for some time as the cloud passes through the turning point. The following phase is similar to the light curves in Figure 7.11. The cloud is accelerated by gravity toward the black hole. The onset in the retro-lensed light curves is different in the initial stage from that in Figure 7.12 because the cloud motion starts on the photon-sphere where the gain-factor vanishes. Note also that the initial drop in the observed intensity is greater in the case of the warm cloud. The reason is in the the radiative cooling of electrons: beaming by single electrons in the cloud initially remarkably contributes to the observed intensity.

The polarization light curve from the cold cloud demonstrates rich phenomenology. The observed polarization changes its orientation three-times as it passes through different regions in the (ξ, β)-plane. The polarization changes find their counterparts in the light curves by the retro-lensed images. In the case of the warm cloud, the polarization is initially smaller by a factor of ≈ 10 than that from the cold cloud. However, as the electrons cool down, it takes similar values. The "saddle" in the double-peak shape of the light curves appears when the cloud velocity approaches to the critical velocity $\beta_1(\xi)$.

7.5.3 Super-critical radiation field ($\Lambda = 100$)

Finally, we consider the case of fast ejection in a very intensive radiation field. We note that this configuration produces the most energetic radiation and therefore it could be easy to observe. However, for $\gamma \gg 1$ the scattered photons are boosted in the direction of motion and therefore most of the photons are radiated only to a narrow range of inclinations. Only few photons are scattered backwards, and therefore the direct image greatly dominates the signal received by an observer. The temporal behavior of the observed intensity and polarization is shown in Figure 7.15 (the case of a cold cloud) and in Figure 7.16 (for the case of an initially warm cloud). The initial electron Lorentz factor of the warm cloud is $\bar{\gamma}_{\rm e0} = 3$. We show only the most intensive part of the light curves. We assume that the cloud has been pre-accelerated to large initial speed $\beta_0 = 0.999$ (the corresponding Lorentz factor is $\gamma_0 \doteq 32$. at the radius $z_0 = 2.22\ R_{\rm S}$. The light curves capture the subsequent phase of gravitational and radiative deceleration. The scattered light contributes significantly to the total signal only for a short initial phase (peaks occur in the intensity curves).The local maxima of the observed intensity and polarization can be understood in terms of a relativistic beaming effect: most of radiation from the cloud is emitted in a cone with the opening angle $\sim 1/\gamma$ about the direction of motion. For small inclinations ($i \leq 1/\gamma_0$ deg) the observer was initially located outside this cone but, as time proceeds, the electron cloud decelerates, the cone opens and the observer receives more radiation. The maximum observed polarization occurs with a certain delay (proportional to M) after the peak of radiation flux. This is because of the not perfect correlation between the angles of maximal scattered intensity and polarization shown for a very simple case of the isotropic incident radiation in Figure 6.2. Subsequent decay of the signal is connected with a diminishing scattering power of the cloud and the overall dilution of the radiation field. We selected large initial velocity in this example, otherwise the effects of aberration and the Doppler boosting would be less prominent, time-scales longer and the effect of lagged maxima of the intensity and polarization would dissappear.

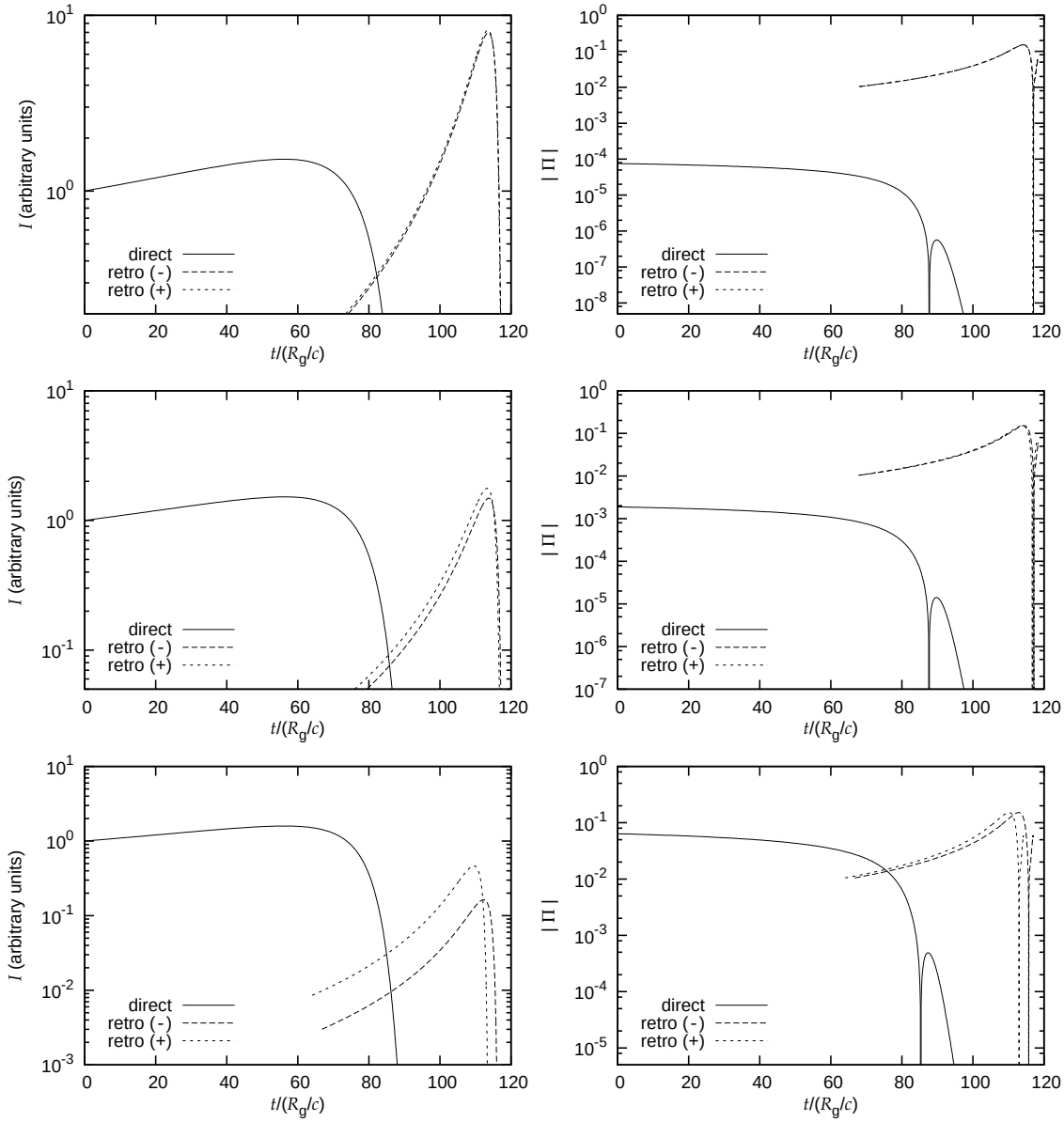

Figure 7.11: Temporal evolution of the observed intensity (left) and polarization (right) of the radiation scattered on the freely-falling cold electron cloud. (the cloud is moving towards the black hole). The initial electron mean Lorentz factor is $\bar{\gamma}_{\rm e} = 3$. Top row: Observed intensity and polarization for the inclination $i = 1$ deg of the cloud motion with respect to the line of sight. The contributions of the retro-lensed images + and – are also shown. Middle and bottom rows: the same for the inclinations $i = 5$ deg and $i = 30$ deg respectively.

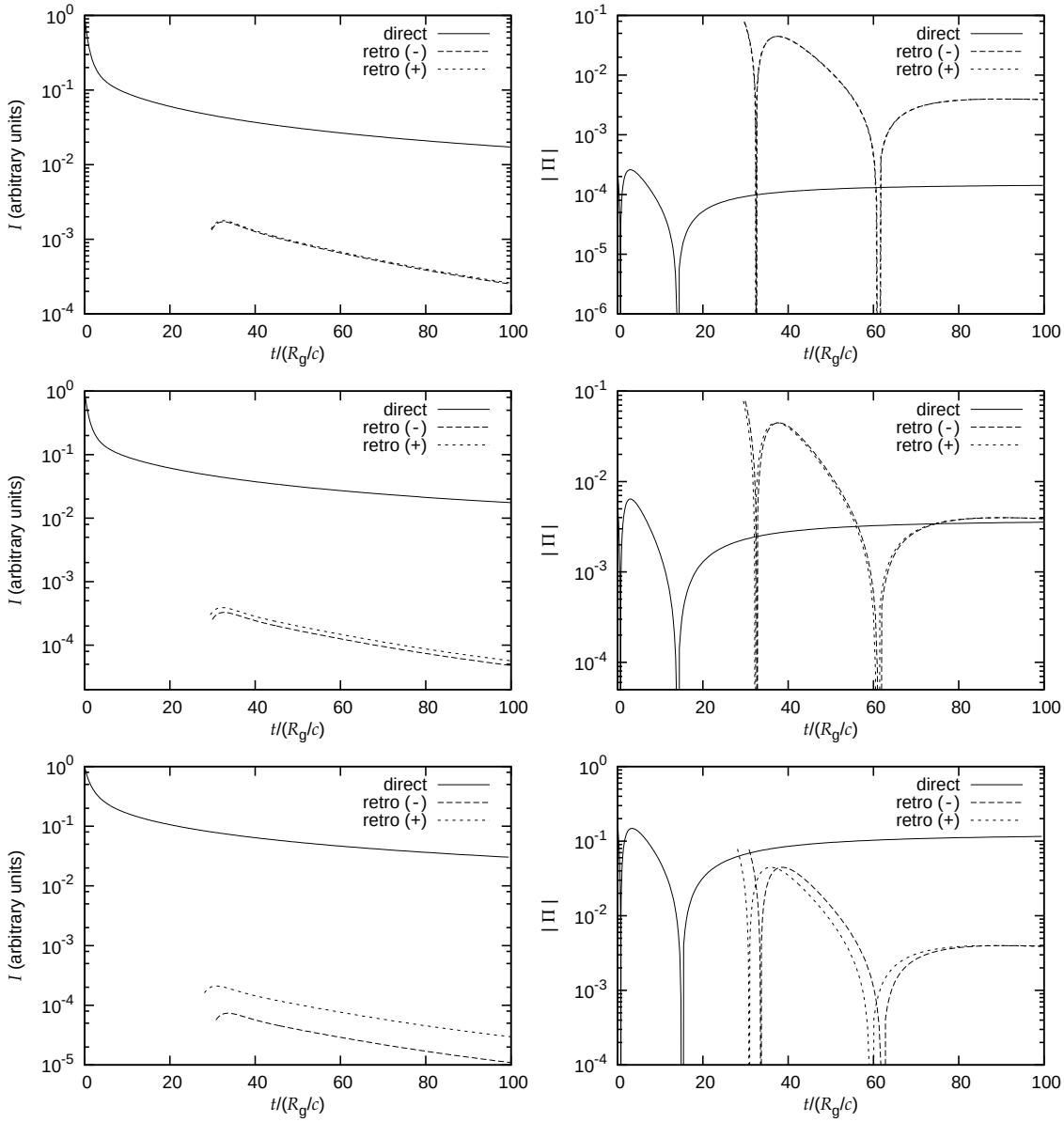

Figure 7.12: The same as in Figure 7.11 but for the outward motion. The contribution of the retro-lensed images to the total intensity is negligible even in a favorable condition of very low inclination. The polarization curves show two changes of the polarization orientation from the transversal to longitudinal and then back to the transversal.

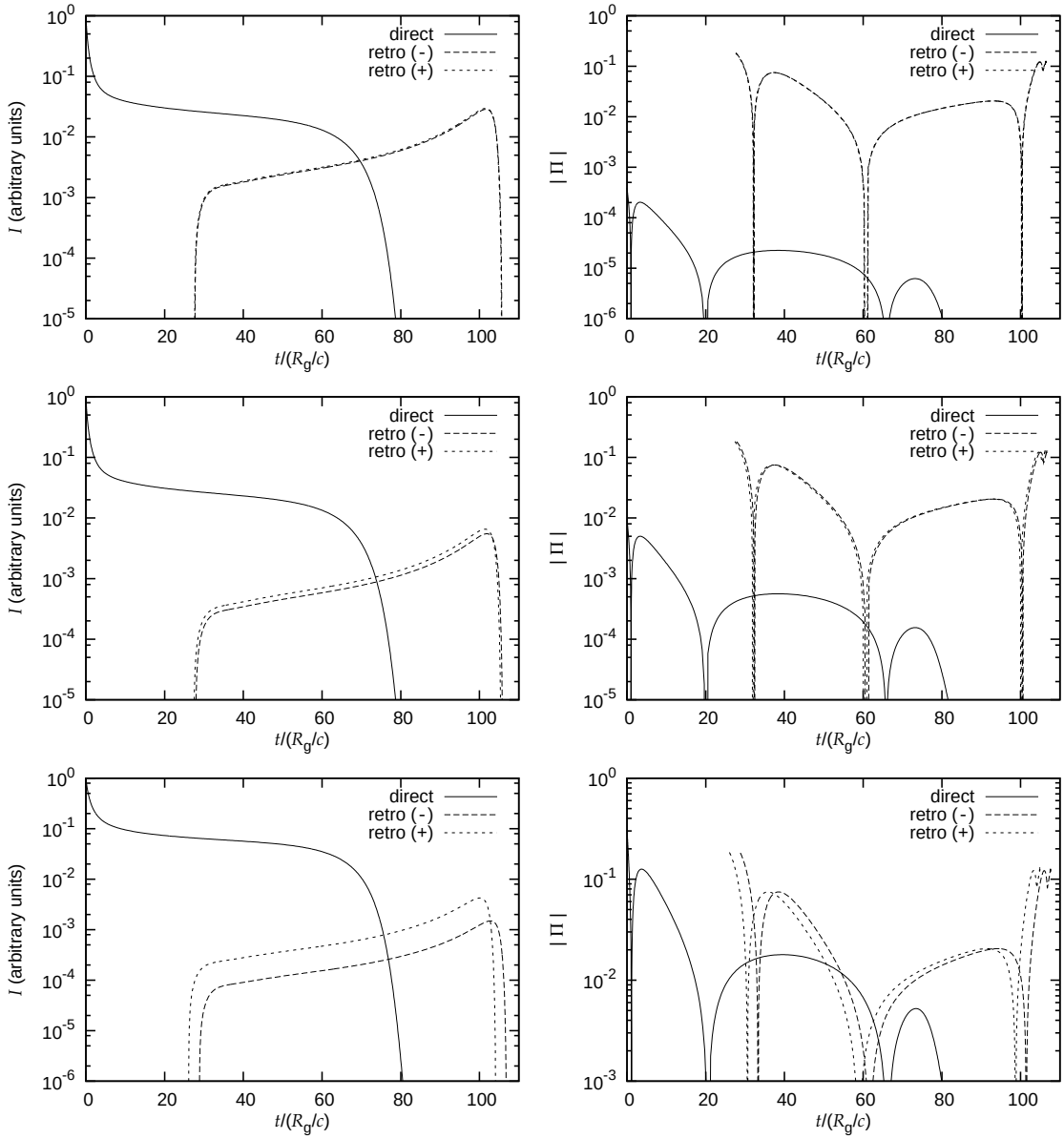

Figure 7.13: The case of a moderately luminous incident radiation field $\Lambda = 2$. The intensity and polarization light curves are for inclinations $i = 1$ (top panels), 5 (middle panels) and 30 deg (bottom panels). The scatterer is a cold electron cloud whose motion starts with the initial condition $z_0 = r_{\rm ph}$ and $\beta_0 = 0.8$. The meaning of symbols is the same as in Figure 7.11.

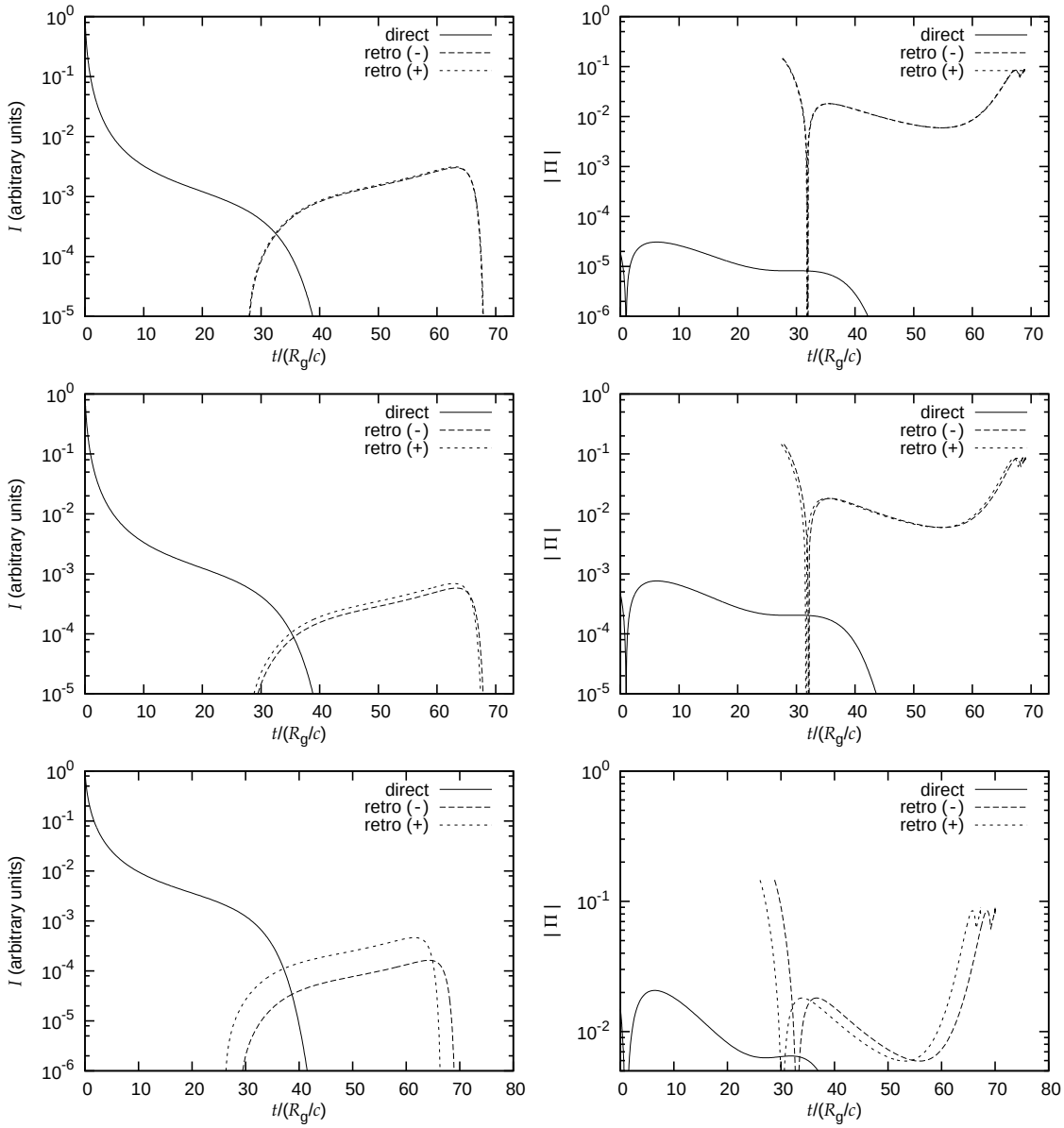

Figure 7.14: The same as in Figure 7.13 but for initially warm cloud with the initial electron Lorentz factor $\bar{\gamma}_{\rm e0} = 3$.

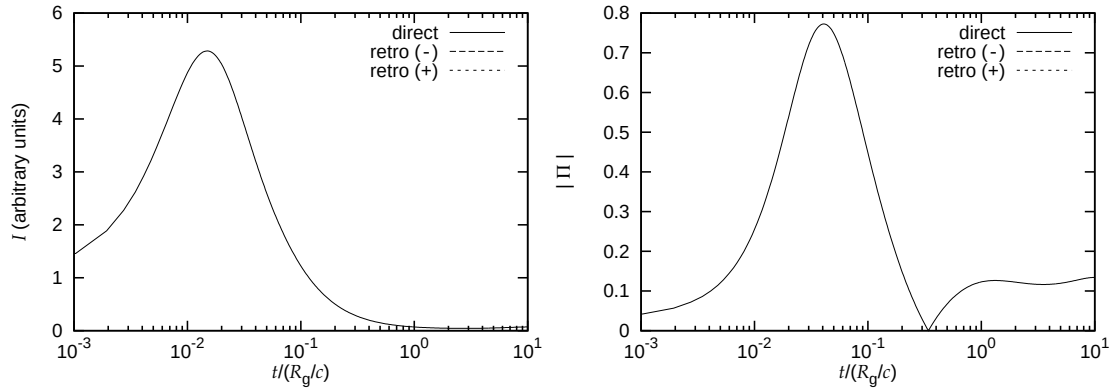

Figure 7.15: The observed intensity (left) and polarization (right) light curve from the cold electron cloud. Cloud is strongly decelerated by the intensive external radiation field with $\Lambda = 100$. The inclination of the cloud motion to the line of sight is $i = 30$ deg. The initial condition for the cloud motion is $\beta_0 = 0.999$ and $z_0 = 2.22\ R_{\rm S}$. Notice the time lag between the intensity and polarization maxima. The polarization light curve clearly shows the change of the polarization orientation.

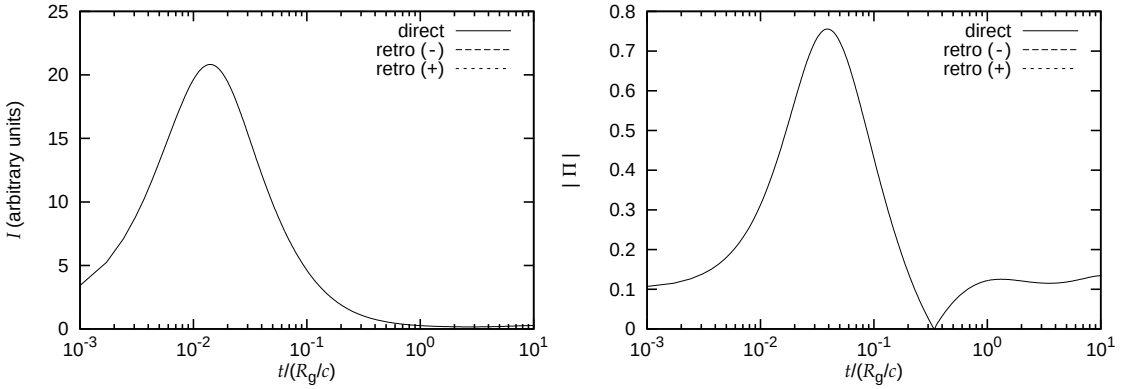

Figure 7.16: The same as in Figure 7.15 but for the warm electron cloud. The initial electron Lorentz factor is $\bar{\gamma}_{\rm e0} = 3$.

Summary and further prospects

The aim of this work was to study dynamics of relativistic jets and the polarization properties of Compton-scattered radiation arising in strong gravity in the vicinity of a black hole. Especially, we paid attention to the geometry of the ambient radiation field interacting with a stream of electrons and to general relativistic effects (e.g. light-bending of light rays, gravitational redshift and rotation of the polarization vector) but we neglect the magnetic field.

Dynamics of a cloud and properties of the scattered radiation were studied simultaneously, in a self-consistent manner: the particles in the cloud move under combined influence of the radiation force arising from the Compton scattering and the gravity of the central black hole. The trajectories of the cloud were used for calculations of integrated intensity and polarization of scattered radiation. We note that this approach considerably restricts the number of free parameters of the model and allows to discuss temporal properties of the scattered radiation. The intensity and polarization light-curves were studied in details in section 7.5.

We have found analytical expressions for three non-zero Stokes parameters I, Q, U of radiation arising from the Compton scattering on a cold electron cloud. The incident radiation field is specified by stress-energy tensor and the Compton scattering is treated in the Thomson approximation. Then, we considered one of the natural configurations: The source of incident radiation was assumed a standard Shakura & Sunyaev (1973) accretion disk surrounding a Schwarzschild black-hole that provides a gravitational field. Another configuration, where the source of both radiation and gravitational fields is a compact relativistic star was discussed elsewhere (Horák & Karas 2005b). The incident photons follow null geodesics from the disk to an electron cloud. Their paths were calculated numerically by integrating geodesic equation.

The geometry of the radiation field determines the saturation velocity $\beta_0(r)$, at which the dynamical effect of the radiation on the cloud changes from acceleration ($\beta < \beta_0(r)$) to deceleration ($\beta > \beta_0(r)$), and two other critical velocities, $\beta_1(r)$ and $\beta_2(r)$ important for the polarization properties of the scattered radiation. When the electron cloud reaches one of these velocities, the polarization of scattered radiation is zero, independently of the direction of observation. Moreover, the polarization changes its direction when the velocity of the electrons β goes across β_1 or β_2. When $\beta_1 < \beta < \beta_2$ the polarization of the scattered radiation is longitudinal (the polarization vector is in the plane determined by direction of the electron motion and direction of observation – the polarization vector is parallel to the projection of the electron velocity onto the polarization plane) otherwise the polarization is transversal (the polarization vector is perpendicular to that plane).

The above results suggest that the polarization properties of the Compton-scattered radiation are sensitive to the geometry of the ambient radiation and – through relativistic aberration – to the velocity of the scattering medium. Regarding this point, the further

improvements follow four logical directions:

1. *Geometry of the ambient radiation field.* We intend to proceed to more realistic geometry of the ambient radiation field relevant in the sources where Compton scattering plays an important role. The prominent set-up is a system with a rotating black hole surrounded by a slim accretion disk.

2. *Frequency resolution.* So far we determine the polarization properties in terms of frequency-integrated quantities. However, our discussion can be rewritten for specific (per energy bin) quantities. The spectral properties of the scattered radiation are very sensitive to the micro-physics of the jet (including a particle distribution and a magnetic field) which is matter of the next point. We note that present results remains valid also for specific quantities if the power-law spectrum with the spectral index $s = 1$ is considered.

3. *Jet structure and "micro-physics".* In presented work we assume that the electron distribution in the cooled cloud is kept isotropic by some additional processes, however, we ignore the influence of this process to the energy of electrons (we consider only Compton cooling). The next step is to include detailed description of other processes (i.e. synchrotron cooling) that affect the particle distribution as considered by many authors studying the radiative acceleration mechanism.

4. *Radiative transfer.* There is a growing evidence that relativistic jets are optically thick at the initial stage. The finite optical depth of the scattering material requires simultaneous solving of the radiative transfer equation. Recently we have shown that the Compton drag of the continuous jet of finite optical depth naturally leads to the creation of the transverse velocity profile (Horák 2002). The fastest material forming the jet "spine" moves along the axis and slower boundary layer.

Appendix A

Light rays in Schwarzschild spacetime

The geometry of a spacetime surrounding static or slowly rotating black holes and relativistic stars is described by the Schwarzschild line element

$$\mathrm{d}s^2 = -\xi(r)\mathrm{d}t^2 + \frac{1}{\xi(r)}\mathrm{d}r^2 + r^2(\mathrm{d}\theta^2 + \sin^2\theta\mathrm{d}\phi), \tag{A.1}$$

expressed using the spherical coordinates (t, r, θ, ϕ), where $\xi(r) \equiv 1 - R_\mathrm{S}/r$ is a redshift function. It approaches to one when $r \to \infty$ providing that t is time measured by distant and static observers and it diverges when $r \to R_\mathrm{S}$ where the event horizon is located. Because the Schwarzschild spacetime is static and axially symmetric (i.e. the metric coefficients in equation (A.1) does not depend explicitly on time t and azimuthal coordinate ϕ), there are two Killing vectors, $\eta^\alpha \equiv \delta^\alpha_t$ and $\zeta^\alpha \equiv \delta^\alpha_\phi$ along which the geometry does not change.

Photons and freely falling particles follow geodesic lines. Because of spherical symmetry these geodesics are planar. The plane of the ray is determined by the initial particle four-momentum and the center of the star (the photon path remain planar because of the reflection symmetry of the spacetime with respect to that plane). Without loss of any generality we restrict our discussion to the particles moving in the equatorial plane, where $\theta = \pi/2$. In that case, the four-momentum of the particle $p^\alpha \equiv dx^\alpha/ds$ has three nonzero components, p^t, p^ϕ and p^r, where s is an affine parameter. The first two are connected with two integrals of motion,

$$E \equiv -p_\alpha\eta^\alpha = -p_t \quad \text{and} \quad L \equiv p_\alpha\zeta^\alpha = p_\phi \tag{A.2}$$

that follows from the symmetry of the spacetime and are conserved along geodesics The quantities E, L will be referred to as the particle energy and angular momentum respectively.

The third, radial component of the particle four-momentum is not independent because the four-momentum is normalized to zero or to the particle rest mass m in the case of motion of photons or of particles with nonzero rest mass, respectively. The normalization condition reads

$$m = p^\alpha p_\alpha = -\frac{E^2}{\xi} + \frac{(p^r)^2}{\xi} + \frac{L^2}{r^2}. \tag{A.3}$$

Changing the parameterization of the particle trajectory from the affine parameter s to the coordinate ϕ, we can express the radial component of the particle four-momentum

as

$$p^r = \frac{\mathrm{d}r}{\mathrm{d}s} = p^\phi \frac{\mathrm{d}r}{\mathrm{d}\phi} = \frac{L}{r^2}\frac{\mathrm{d}r}{\mathrm{d}\phi} \tag{A.4}$$

By substituting it into equation (A.3) we get

$$\frac{1}{r^2}\left(\frac{\mathrm{d}r}{\mathrm{d}\phi}\right)^2 = r^2\left(\frac{E}{L}\right)^2 - \xi + m\xi\frac{r^2}{L^2}. \tag{A.5}$$

for a particle of non-zero rest mass and

$$\frac{1}{r^2}\left(\frac{dr}{\mathrm{d}\phi}\right)^2 = \frac{r^2}{B^2} - \xi \tag{A.6}$$

for a particle with zero rest-mass. Trajectories of freely falling particles with non-zero rest mass are completely determined by two independent parameters, the energy and angular momentum. On the other hand, only one parameter, the ratio of the energy and the angular momentum, $B \equiv L/E$ is needed to specify trajectory of a particle with zero rest mass. The parameter B has analogical meaning as an impact parameter defined used in the scattering problems of classical physics. Equation (A.6) takes a simple form by the substitution $u \equiv R_\mathrm{S}/r$. Then we get

$$\left(\frac{\mathrm{d}u}{\mathrm{d}\phi}\right)^2 = \frac{1}{b^2} - u^2(1-u), \tag{A.7}$$

where $b \equiv B/R_\mathrm{S}$.

The expression $\mathcal{U} \equiv u^2(1-u)$ in this equation plays a role of the effective potential (Misner, et al. 1973). It reaches its maximal value $\mathcal{U}_\mathrm{max} = 4/27$ at the point $u = 2/3$. The photons with the impact parameter smaller than the critical value $b_\mathrm{c} = 3\sqrt{3}/2$ are captured by the black hole. The photons with impact parameter greater than b_c escape to infinity being deflected. The point of closest approach u_0 (the pericenter) is given by the condition $\mathrm{d}u/\mathrm{d}\phi = 0$ and it is the only real root of the cubic equation

$$u^3 - u^2 + \frac{1}{b^2} = 0, \tag{A.8}$$

that satisfy $0 < u_0 < 2/3$.

The equation (A.7) is a good starting point for further analytic approximations (as will be derived in the appendix B), it fails, however, in numerical calculations because it gives imaginary numbers for $\mathrm{d}u/\mathrm{d}\phi$ for a negative right-hand side. More suitable for the purpose of the numerical integration is equation

$$\frac{\mathrm{d}^2u}{\mathrm{d}\phi^2} + u - u^2 = 0. \tag{A.9}$$

that follows from equation (A.7) if one applies the derivative with respect to ϕ.

Increment of polar angle. Consider two distinct points A and B at radii $r_A = R_\mathrm{S}/u_A$ and $r_B = R_\mathrm{S}/u_B$ connected by the ray with the impact parameter b. Assume that $u_B < u_A$. The total increment of the polar angle Φ_{AB} along the ray is given by integral

$$\Phi_{AB} = |\phi_B - \phi_A| = \int_{u_A}^{u_B} \frac{\mathrm{d}u}{[1/b^2 - u^2(1-u)]^{1/2}}. \tag{A.10}$$

Time delay. Similarly, the photon traveling time or time delay between the points A and B can be expressed as the integral

$$t_{AB} = \int_{u_A}^{u_B} \frac{p^t}{p^\phi}\frac{d\phi}{du}du = \frac{1}{b}\int_{u_A}^{u_B} \frac{\mathrm{d}u}{u^2(1-u)\left[1/b^2 - u^2(1-u)\right]^{1/2}} \tag{A.11}$$

Integrals in equations (A.10) and (A.11) can be expressed using elliptic integrals (Darwin 1959, 1961) or hyper-elliptic integrals (Čadež & Kostić 2005) respectively. In several limit cases, they can be approximated by elementary functions (e.g. Bozza 2002; Bozza & Mancini 2004; Chandrasekhar 1992 and the appendix B of this work).

Local emission angles. We define the local emission angle as the angle between a ray and the radial direction. Consider particular ray passing through a point S. The local emission angle can be deduced from the components of photon four-momentum $p^{(\alpha)}$ with respect to a local orthonormal tetrad $(\boldsymbol{e}^{(t)}, \boldsymbol{e}^{(r)}, \boldsymbol{e}^{(\theta)}, \boldsymbol{e}^{(\phi)})$ of a static observer at the point S. First, let us define a four-vector $n^{(\alpha)} \equiv p^{(\alpha)}/p^{(t)}$. Obviously, $n^{(t)} = 1$ and, since $p^{(\alpha)}$ is a null four-vector, the spatial components satisfy $n^{(i)}n_{(i)} = 1$. It is natural to interpret the four-vector $n^{(\alpha)}$ as the photon propagation vector which spatial components points along the direction of the ray. In the case of equatorial ray these can be written as $n^{(r)} = \cos\vartheta$, $n^{(\phi)} = \sin\vartheta$ and $n^{(\theta)} = 0$. Hence the angle ϑ will be referred to as the local emission angle.

Expressing the photon four-momentum using the dimensionless impact parameter b we found

$$\sin\vartheta = \frac{p^{(\phi)}}{p^{(t)}} = bu\sqrt{1-u} \tag{A.12}$$

In the numerical ray-tracing the initial conditions are often chosen in terms of the local emission angle (we trace the photon emitted in the particular direction in the local reference frame). Therefore, it is useful to express the initial condition for equation (A.9). Let the source is at the radius r. Substituting the impact parameter into the photon four-momentum, we find the propagation vector in the form $n^{(r)} = \cos\vartheta = b(\mathrm{d}u/\mathrm{d}\phi)$ and $n^{(\phi)} = \sin\vartheta = bu\xi$. Therefore, we obtain

$$u_0 = \frac{1}{r}\,, \quad \left(\frac{\mathrm{d}u}{\mathrm{d}\phi}\right)_0 = \frac{1}{r}\,\xi^{1/2}(r)\cot\vartheta\,. \tag{A.13}$$

Appendix B

A source at low inclination

An interesting consequence of the gravitational bending of light-rays is the fact that a source and an observer can be connected by more than one ray. Consider situation in Figure B.1. The direction to the source and direction to the distant observer makes the angle i. Later on, the inclination i will play the role of the independent parameter that many expressions will be expanded according to, therefore we require $i \ll 1$. Practical estimations of accuracy and the strength of this requirement will be given. The observer is located on a sphere of the radius $D \gg 1$. The source is located at the radius r. As distinct from the classical retro-lensing problem, we concern a more general case when the source is everywhere above the photon orbit, $r \geq r_{\rm ph}$. Furtermore, it is assumed that the source is a point-like particle, i.e. its angular radius is small compared to the inclination. Then, in principle, three different rays connects it with the observer: slightly deflected *direct ray* $R_{\rm d}$ and two *retro-rays* $R_{\pm}$ that are highly deflected by black hole gravity and represents purely general-relativistic effect. In principle, there is infinite number of other rays that encircles the black hole more than once. These rays, however, give negligible contributions to the total flux measured by the observer in comparison to the rays $R_{\pm}$ (the contributions of these higher-order rays are smaller by the factor $e^{-2\pi n} \doteq (1.9 \times 10^{-3})^n$, where n is number of revolutions – the order of the ray).

All three rays can be treated analytically as approximations to on the two exact analytical solution which are a radial ray and the light circle at $r_{\rm ph}$. The total increment of the polar angle for the direct ray is $\Phi_{\rm d} = i$. In the next section we show that it is proportional to the ratio of impact parameter and source position B/r. We obtain $B/r = 0$ for the radial rays. Therefore, all quantities we are interested in will be calculated as expansions in that ratio about the value $B/r = 0$ that corresponds to the radial ray. The retro-rays R_+ and R_- have their pericenters very close to the photon orbit at $r_{\rm ph}$. Also their dimensionless impact parameters are very close to the critical value $b_{\rm c} = 3\sqrt{3}/2$. We carry out the expansions in the difference $\beta \equiv b - b_c$ in the section B.2.

B.1 Slightly deflected direct rays

Consider light rays radiated by a source at radius $r = 1/u$ outward the black hole almost radially. The impact parameter of the ray B is small compared to the radial coordinate r along the whole ray. Let us define small parameter $\epsilon \equiv B/r = bu$. Then introducing the substitution $x \equiv \tilde{u}/u$, in the integration variable, the expression for the increment of the

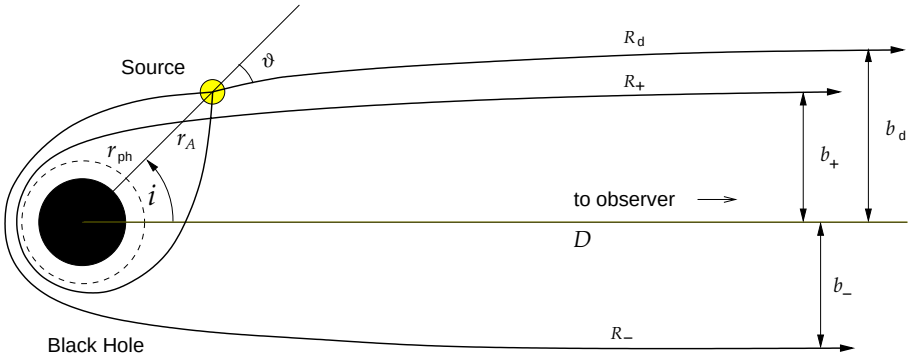

Figure B.1: Source at low inclination.

polar angle (A.10) becomes

$$\Phi_{\rm d} = \epsilon \int_0^1 \frac{dx}{\sqrt{1-\epsilon^2 x^2(1-ux)}}. \tag{B.1}$$

Expanding the integrand to the second order in ϵ we get

$$\Phi_{\rm d} = \epsilon \int_0^1 \left[1 + \tfrac{1}{2}\epsilon^2 x^2(1-ux)\right] dx + \mathcal{O}(\epsilon^5). \tag{B.2}$$

The increment of polar angle $\Phi_{\rm d}$ along the ray equals the inclination i of the source with respect to the observer. Integration over x gives

$$i = \epsilon + \left(\tfrac{1}{6} - \tfrac{1}{8}\,u\right)\epsilon^3 + \mathcal{O}(\epsilon^5). \tag{B.3}$$

In order to express the impact parameter B as a function of the inclination of the source, we invert equation (B.3). This is not difficult for small i. We obtain

$$B = r\left(i - \tfrac{1}{6}\,i^3\right) + \tfrac{1}{8}\,R_{\rm S} i^3 + \mathcal{O}(i^5). \tag{B.4}$$

The term in the bracket is expanded $r\sin i$ up to the third order in i, This term will be present in the expansion carried out for a straight ray. The second term represents the contribution of gravitational light bending. For a given inclination and distance of the source the impact parameter is greater because the gravity bends light rays toward the black hole. This effect is of the third order.

The time delay is given by the integral

$$T_{\rm d} = \int_{u_{\rm o}/u}^1 \frac{dx}{ux^2(1-ux)\sqrt{1-\epsilon^2x^2(1-ux)}} \tag{B.5}$$

We expand the square-root up to the fourth order in ϵ and integrate. Keeping only the terms that are not negligible when $u_{\rm o} \ll 1$, we get

$$T_{\rm d} = T_{\rm rad} + \tfrac{1}{2}b^2u + \tfrac{1}{8}b^4u^3\left(1 - \tfrac{3}{4}u\right), \tag{B.6}$$

where

$$T_{\rm rad} = \frac{1}{u_{\rm o}} - \frac{1}{u} - \ln\frac{(1-u)u_{\rm o}}{u} \tag{B.7}$$

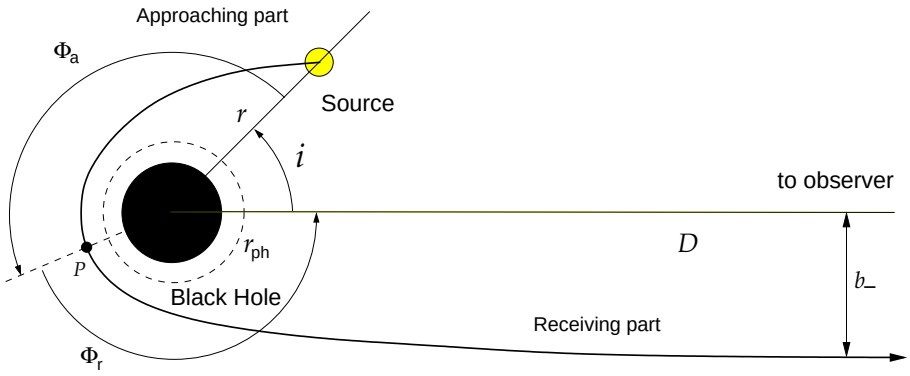

Figure B.2: Highly deflected ray.

is the time delay between radii of source and observer along a radial ray.

The local emission angle can be calculated using the expression (A.12)

$$\sin\vartheta = \sqrt{1-\frac{R_\mathrm{S}}{r}}\left[i-\left(\frac{1}{3}+\frac{R_\mathrm{S}}{4r}\right)\frac{i^3}{2}\right]+\mathcal{O}(i^5) \tag{B.8}$$

B.2 Highly deflected retro-rays

Let us consider the ray in the Figure B.2. The ray is radiated by the source toward the black hole and the radial coordinate first decreases along the ray until it reaches the pericenter, the point of the closest approach behind the hole at radius r_0. At this point the gravitational bending is strongest. Then, the ray proceeds to higher radii until it reaches a distant observer at $r \to \infty$. The pericenter lies very close to the photon-sphere, $r_0 \sim 3/2R_\mathrm{S}$. In order to use single valued functions of r or u respectively, the two parts, approaching (a) and receiving (r) of the ray will be studied separately.

First, let us consider the approaching part of the ray. The cubic function in the square-roots in equations (A.10) and (A.11) can be expressed using its roots. Obviously, the pericenter is one of the roots. Hence we can write

$$\frac{1}{b^2}-u^2(1-u)=(u-u_0)(u-u_1)(u-u_2), \tag{B.9}$$

where $u_0 = R_\mathrm{S}/r_0$ and we suppose the ordering $u_1 < 1 < u_0 \leq 2/3 \leq u_2$. The both equalities are valid in the case of critical orbits. The two other roots u_1 and u_2 can be found equating coefficient of the same powers of u in the equation (B.9). We obtain

$$u_{1,2} = \tfrac{1}{2}\left(1-u_0 \mp \sqrt{1-3u_0^2+2u_0}\right) \tag{B.10}$$

Let us expand the roots u_0, u_1 and u_2 via the difference of u_0 from 2/3. Denoting this difference as $\epsilon/2$ we get

$$u_0 = \tfrac{2}{3}-\tfrac{1}{2}\epsilon, \quad u_1 = -\tfrac{1}{3}+\mathcal{O}(\epsilon^2) \quad \text{and} \quad u_2 = \tfrac{2}{3}+\tfrac{1}{2}\epsilon+\mathcal{O}(\epsilon^2). \tag{B.11}$$

With the aid of these approximations and introducing additional substitution

$$\tau \equiv u_0 - u = \tfrac{2}{3}-u+\tfrac{1}{2}\epsilon, \tag{B.12}$$

equation (B.9) can be rewritten as

$$\frac{1}{b^2} - u^2(1-u) = \tau(\tau+\epsilon)(1-\tau) \tag{B.13}$$

Using the substitution (B.12), the total increment of the polar angle on the approaching part can be expressed as

$$\Phi_{\mathrm{a}} = \int_0^{2/3-u} \frac{d\tau}{\sqrt{\tau(\tau+\epsilon)(1-\tau)}} \tag{B.14}$$

The integral on the right hand side is symmetric elliptic integral of the first kind. Its approximated value in the case when $\epsilon \ll 1$ can be found in the following way (compare with Carlson & Gustafson 1994). Denote the integrand as $f(\tau)$. It can be approximated by the sum $f_{\mathrm{est}}(\tau) = f_{\mathrm{i}}(\tau) + f_{\mathrm{o}}(\tau) - f_{\mathrm{m}}(\tau)$, where $f_{\mathrm{i}}(\tau)$ is an approximation in the inner region where τ can be neglected compared to 1, $f_{\mathrm{o}}(\tau)$ is an approximation in an outer region where ϵ can be neglected compared to τ and f_{m} is approximation in the overlap region where both, ϵ and t can be neglected compared to 1. We have

$$f_{\mathrm{i}}(\tau) = \frac{1}{\sqrt{\tau(\tau+\epsilon)}}, \quad f_{\mathrm{o}}(\tau) = \frac{1}{\tau\sqrt{1-\tau}} \quad \text{and} \quad f_{\mathrm{m}}(\tau) = \frac{1}{\tau} \tag{B.15}$$

Then

$$\Phi_{\mathrm{a}} \approx \int_0^{2/3-u} \left[f_{\mathrm{i}}(\tau) + f_{\mathrm{o}}(\tau) - f_{\mathrm{m}}(\tau)\right] d\tau = -\ln\left[\frac{\epsilon}{16}\frac{\sqrt{3}+\sqrt{3u+1}}{\sqrt{3}-\sqrt{3u+1}}\right] \tag{B.16}$$

The error of this approximation can be estimated by finding upper and lower bounds for difference of integrand and its approximated value, $f(\tau) - f_{\mathrm{est}}(\tau)$. Doing this we found

$$(\text{Error of the approximation}) \sim \epsilon \ln \epsilon. \tag{B.17}$$

The angular increment Φ_{r} along the receiving part of the ray can be calculated in the similar way. By substituting $u = 0$ into equation (B.16) we find that

$$\Phi_{\mathrm{r}} = -\ln\left[\frac{\epsilon}{16}\frac{\sqrt{3}+1}{\sqrt{3}-1}\right] \tag{B.18}$$

The total angular increment Φ along the whole ray is sum of the angular increments of the approaching and the receiving parts

$$\Phi = \Phi_{\mathrm{a}} + \Phi_{\mathrm{r}} = \ln\left[\frac{\epsilon^2}{256}\,\frac{\sqrt{3}+1}{\sqrt{3}-1}\,\frac{\sqrt{3}+\sqrt{3u+1}}{\sqrt{3}-\sqrt{3u+1}}\right] \tag{B.19}$$

The impact parameter of the ray orbits is slightly greater then the critical value $b_{\mathrm{c}} = 3\sqrt{3}/2$. The deviation β can be expressed using ϵ as

$$\beta \equiv b - b_{\mathrm{c}} = \frac{3^4\sqrt{3}}{2^6}\epsilon^2. \tag{B.20}$$

Expressing ϵ using β and substituting into equation (B.19), we find

$$\Phi = \Phi_{\mathrm{a}} + \Phi_{\mathrm{r}} = \ln\left[\frac{4\beta}{6^4\sqrt{3}}\,\frac{\sqrt{3}+1}{\sqrt{3}-1}\,\frac{\sqrt{3}+\sqrt{3u+1}}{\sqrt{3}-\sqrt{3u+1}}\right]. \tag{B.21}$$

The angular increments along the retro-rays $R_\pm$ are connected to the inclination i by the relation $\Phi_\pm = 2\pi \pm i$. Substituting it into equation (B.21) and isolating impact parameter β we get

$$\beta_\pm = \frac{6^4\sqrt{3}}{4}\,\frac{\sqrt{3}-1}{\sqrt{3}+1}\,\frac{\sqrt{3}-\sqrt{3u+1}}{\sqrt{3}+\sqrt{3u+1}}\,e^{-2\pi\mp i}, \tag{B.22}$$

where the upper and lower sign is for the retro-ray R_+ and R_- respectively.

Our calculation of the time delay is similar to that of angular increments in many respects. As in that case we split up the ray into the approaching and receiving parts. Then we express the cubic argument of the square root in the integral (A.11) by its roots. Finally, we express the roots as small deviations from the values corresponding to the critical orbit. The time delay along the approaching part is expressed as

$$T_\mathrm{a} = \int_0^{2/3-u} \frac{d\tau}{(2/3-\tau)^2(\tau+1/3)\sqrt{\tau(\tau+\epsilon)(1-\tau)}} \tag{B.23}$$

Again, we approximate the integrand by the sum $f_\mathrm{est}(\tau) = f_\mathrm{i}(\tau) + f_\mathrm{o}(\tau) - f_\mathrm{m}(\tau)$, where $f_\mathrm{i}(\tau)$, $f_\mathrm{o}(\tau)$ and $f_\mathrm{m}(\tau)$ are approximations in the inner, outer and overlap regions respectively given by

$$f_\mathrm{i} = \frac{27}{4\sqrt{\tau(\tau+\epsilon)}}, \quad f_0 = \frac{1}{(2/3-\tau)^2(\tau+1/3)\tau\sqrt{1-\tau}}, \quad f_\mathrm{m} = \frac{27}{4\tau} \tag{B.24}$$

The approximated integrand can be transformed by substitutions to the rational function and analytically integrated. After considerable algebra we obtain

$$T_\mathrm{a} = \frac{3\sqrt{3}}{2}\,(\Phi_\mathrm{a}-1) + \frac{\sqrt{1+3u}}{u} - \ln\left[\frac{(9-5\sqrt{3})(\sqrt{1+3u}+1+u)}{(9+5\sqrt{3})(\sqrt{1+3u}-1-u)}\right]. \tag{B.25}$$

The time delay for the receiving part of the ray is deduced from this equation by replacement $u \to u_\mathrm{o}$, where $u_\mathrm{o} \equiv R_\mathrm{S}/D$ and D is distance of the black hole and observer. Assuming that u_o is negligible compared to one, we get

$$T_\mathrm{b} = \frac{3\sqrt{3}}{2}\,(\Phi_\mathrm{b}-1) + \frac{1}{u_\mathrm{o}} - \ln\left[\frac{u_\mathrm{o}}{4}\right] - \ln\left[\frac{9-5\sqrt{3}}{9+5\sqrt{3}}\right]. \tag{B.26}$$

Summing the equations (B.25) and (B.26) we get the expression for the time delay along the whole ray

$$T = \frac{3\sqrt{3}}{2}\,\Phi + \frac{1}{u_\mathrm{o}} - \ln\left[\frac{u_\mathrm{o}}{4}\right] + \frac{\sqrt{1+3u}}{u} - \ln\left[\frac{\sqrt{1+3u}+1+u}{\sqrt{1+3u}-1-u}\right] + C, \tag{B.27}$$

where

$$C \equiv \frac{3\sqrt{3}}{2} - 2\ln\left[\frac{9-5\sqrt{3}}{9+5\sqrt{3}}\right] \doteq 10.5 \tag{B.28}$$

Hence, the time delay along the retro-rays R_+ and R_- is given by

$$T = \frac{3\sqrt{3}}{2}\,(2\pi \pm i) + \frac{1}{u_\mathrm{o}} - \ln\left[\frac{u_\mathrm{o}}{4}\right] + \frac{\sqrt{1+3u}}{u} - \ln\left[\frac{\sqrt{1+3u}+1+u}{\sqrt{1+3u}-1-u}\right] + C. \tag{B.29}$$

Finally, the local emission angle for the retro-rays can be approximated by the viewing angle of the photon-sphere. Substituting the critical value of the impact parameter $b_\mathrm{c} = 3\sqrt{3}/2$ into the expression (A.12), we obtain

$$\sin\vartheta = \frac{3\sqrt{3}}{2}\,\frac{R_\mathrm{S}}{r}\,\xi^{1/2}(r)\,. \tag{B.30}$$

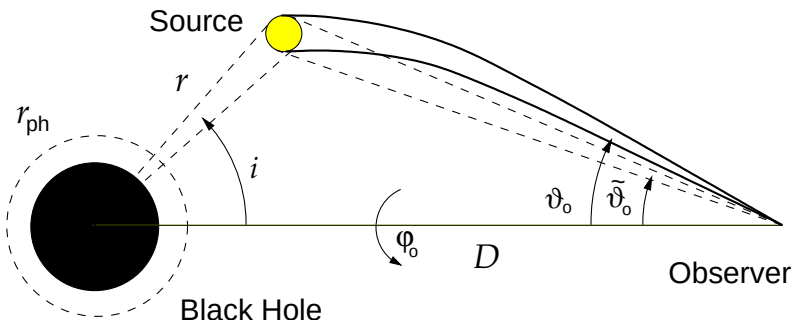

Figure B.3: Solid angles used in calculation of the gravitational gain factor.

B.3 Magnification by gravitational lensing

In previous sections we give approximated expressions for the impact parameter that determines position of the source on a local sky of a distant observer and the time delay connected to the time of receiving of the the photons radiated by the source. It follows that the gravitational bending of light rays could have an important effect on a appearance of the source and therefore amount of the radiation received from it and possibly other physical properties of the source measured by observer (i.e. polarization).

Let us introduce two angles ϑ_o and φ_o that parameterize the apparent position of the source on the observer local sky. (see Figure B.3). The polar angle ϑ_o is connected with the impact parameter b of the incoming rays by the equation (A.12) which far from the hole takes the form

$$\vartheta_o \simeq \sin\vartheta_o = bu_o(1-u_o) \simeq \frac{B}{D}, \tag{B.31}$$

where we used $u_o = R_S/D$ and $b = B/R_S$. The element of the solid angle can be expressed as

$$d\Omega_o = \sin\vartheta_o d\vartheta_o d\varphi_o = \frac{1}{D^2}\, B\, dB\, d\varphi_o. \tag{B.32}$$

In absence of the gravitational field the same solid-angle can be expressed as

$$d\tilde{\Omega}_o = \sin\tilde{\vartheta}_o d\tilde{\vartheta}_o d\varphi_o = \frac{r^2}{D^2}\sin i\, di\, d\varphi_o. \tag{B.33}$$

The magnification or gain factor is defined as the ratio of the elements of the solid angle with and without presence of gravitational field

$$\mathcal{M} \equiv \left|\frac{d\Omega_o}{d\tilde{\Omega}_o}\right| = \frac{1}{r^2}\left|\frac{B}{\sin i\,\frac{di}{dB}}\right| \tag{B.34}$$

The effect of the gravitational magnification is negligible for direct rays where the gain factor is very close to 1 (first correction is proportional to $i^2 R_S/r$). However it is of great importance for retro-rays, where the gravitational lensing substantially magnifies the radiation flux received by distant observer.

The dependences of the impact parameter $B = bR_S$ on the inclination of the source for the retro-rays $R_\pm$ are given by equation (B.22). By substituting into equation (B.34) and noting that $B \sim B_c = 3\sqrt{3}/2$, we get

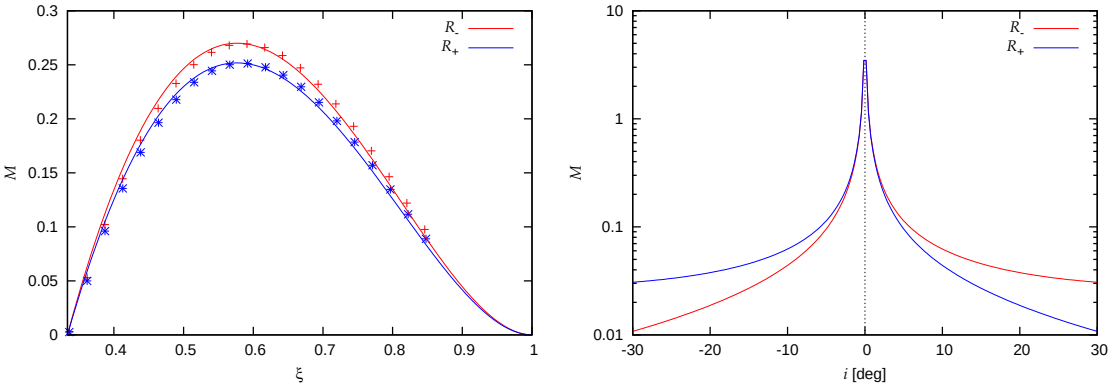

Figure B.4: Left: Gain factors $\mathcal{M}_+$ and $\mathcal{M}_-$ for two retro-rays R_+ and R_- as functions of $\xi = 1 - u$. The photon orbit and infinity correspond to $\xi = 3/2$ and $\xi = 1$ respectively. The inclination of the source is 2 degrees. Points denote result of numerical calculation. The radius of maximal gain is at $r \doteq 2.3622\, R_{\rm S}$. Right: Dependence of the gain-factors $\mathcal{M}_+$ and $\mathcal{M}_-$ on the inclination at the radius of maximal gain.

$$\mathcal{M}_\pm(u,i) = 2 \times 3^6 (2-\sqrt{3})\, u^2\, \frac{\sqrt{3}-\sqrt{1+3u}}{\sqrt{3}+\sqrt{1+3u}}\, \frac{e^{-2\pi\mp i}}{|\sin i|}. \tag{B.35}$$

The gain-factor as a function of radial coordinate $\xi = 1 - u$ and inclination i of the source is shown in Figure B.4. In the case of ξ-dependence we show also the result of numerical calculations. These was obtained by numerical integration of the geodesic equation. The gain factors were found by dividing the small areas delimited by two nearby geodesics. Clearly the ray R_+ that corresponds to the higher polar-angle increment gives smaller magnification then R_-. Exploring the equation we see that the contribution of higher-order retro-rays $T_{n\pm}$ to the resulting image can be neglected, because corresponding gain-factors $\mathcal{M}_{n\pm}$ are smaller then $\mathcal{M}_\pm$ by a factor $e^{-2(n-1)\pi}$. The gain-factor has maximum at the point $\xi = 0.5767$ that corresponds to the radius $r \doteq 2.3622\, R_{\rm S}$.

Bibliography

Part I:

Abramowicz M. A., Jaroszyński M., Sikora M., 1978, A&A, 63, 221

Abramowicz M. A., 1985, PASJ, 37, 727

Abramowicz, M. A., Kluźniak, W., 2001, A&A, 374, L19

Abramowicz M. A., Karas V., Kluźniak W., Lee W. H., Rebusco P., 2003, PASJ, 55, 467

Abramowicz M. A., Blaes O. M., Horák J., Kluźniak W., Rebusco P., 2005, in preparation

Abramowicz M. A., Horák J., Kluźniak W., 2005, in preparation

Binney J., Tremaine S., 1950, Galactic dynamics, Princeton series in astrophysics

Blaes O. M., 1985, MNRAS, 216, 553

Boyer R. H., 1965, Proc. Cambridge Phil. Soc., 61, 527

Bursa M., Abramowicz M. A., Karas V., Kluźniak W., 2004, ApJ

Chandrasekhar S., 1960, Principles of stellar dynamics, Dover

Gilfanov, M., Revnivtsev, M., Molkov, S., 2003, A&A, 410, 217

Horák J., Abramowicz M. A., Karas V., Kluźniak W., 2004, PASJ, 56, 819

Horák J., 2004, Proceedings of RAGtime workshops 4/5, Eds. S. Hledík & Z Stuchlík

Horák, J. Karas, V., 2005a, A&A, submitted

Horák J., 2005a, Astron. Nachr., submitted

Kato S., 2004, PASJ, 56, 905

Kluźniak W., Michelson P., Wagoner R. V., 1990, ApJ, 358, 538

Kluźniak, W., Abramowicz, M. A., 2001, Acta Phys. Pol. B, B32, 3605

Kluźniak W., Abramowicz, M. A., 2002 astro-ph/0203314

Kluźniak W., Abramowicz M. A., Kato S., Lee W. H., Stergioulas N., 2004, ApJ, 603, L89

Kluźniak, W., Abramowicz, M. A., 2004, proceedings of the Amsterdam conference, in press

Kozai Y., 1962, AJ, 67, 579

Kozłowski M., Jaroszynski M., Abramowicz M. A., 1978, A&A, 63, 209

Lai D., 1999, ApJ, 524, 1030

Landau L. D., Lifshitz E. M., 1969, Machanics, Course of Theoretical Physics, Oxford: Pergamon Press, 1969, 2nd ed.

Lee W. H., Abramowicz M. A., Kluźniak W., 2004, ApJ, 603, L93

McClintock J. E, Remillard R. A., 2003, *Compact Stellar X-ray Sources* eds. W.H.G. Lewin and M. van der Klis, Cambridge University Press, astro-ph/0306213

Nayfeh A. H., Mook D. T., 1979, Nonlinear oscillations, Wiley-interscience publication

Paczyński B., Wiita P. J., 1980, A&A, 88, 23

Paczyński B., 1987, Nature, 327, 303
Rebusco P., 2004, PASJ, 56, 553
Revnivtsev M. & Gilfanov M., 2005, astro-ph/0506019
Rezzolla L., Yoshida S., Maccarone T. J., Zanotti O., 2003, MNRAS, 344, L37
Rubio-Herrera E., Lee W. H., 2005, MNRAS, 357, L31
Stella L., Vietri M., 1999, PhRvL, 82, 17
Sunyaev R. A., Shakura N. I., 1986, Sov. Astron. Lett, 12, 117
Swank J., 2004, AIPC, 714, 357
Titarchuk L., 2002, ApJ, 578, L71
van der Klis M., Wijnands R. A. D., Horne K., Chen W., 1997, ApJ, 481, L97
van der Klis M., 2000, ARA&A, 38, 717
Wijnands R., van der Klis M., Homan J., Chakrabarty D., Markwardt C. B., Morgan E. H., 2003, Natur, 424, 44
Yu W., van der Klis M., Jonker P. G., 2001, ApJ, 559, L29
Yu W., van der Klis M., Fender R. P., 2002, miqu.work, 72

Part II:

Abramowicz M. A., Ellis G. F. R., Lanza A., 1990, ApJ, 361, 470
Agol E., Blaes O., 1996, MNRAS, 282, 965
Angel J. R. P., 1969, MNRAS, 158, 219
Bao G., Hadrava P., Wiita P. J., Xiong Y., 1997, ApJ, 487, 142
Begelman M. C., Sikora M., 1987, ApJ, 322, 650
Beloborodov A. M., 1998, ApJ, 496, L105
Blumenthal G. R., Gould R. J., 1970, RvMP, 42, 237
Born M., Wolf E., 1964, Principles of Optics (Pergamon Press, Oxford)
Bower G. C., Falcke H., Wright M. C. H., Backer D. C., 2005, ApJ, 618, L29
Bozza V., 2002, Phys. Rev. D, 66, 103001
Bozza V., Mancini L., 2004, Gen. Rel. Grav., 36, 435
Brown J. C., McLean I. S., 1977, A&A, 57, 141
Čadež A., Kostić U., A&A, submitted (gr-qc/0405037)
Carlson, B. C., Gustafson, 1994, J. L., SIAM Journal on Mathematical Analysis, 25, 288
Chandrasekhar S., 1960, Radiative Transfer (Dover Publ., New York)
Chandrasekhar S., 1992, The Mathematical Theory of Black Holes (Oxford Univ. Press, New York)
Chiaberge M., Celotti A., Capetti A., Ghisellini G., 2000, A&A, 358, 104
Cocke W. J., Holm D. A., 1972, Nature Physical Science, 240, 161
Combi J. A., Cellone S. A., Martí J., Ribó M., Mirabel I. F., Casares J., 2004, A&A, 427, 959
Connors P. A., Stark R. F., Piran T., 1980, ApJ, 235, 224
Costa E., Soffitta P., Bellazzini R., Brez A., Lumb N., Spandre G., 2001, Nature, 411, 662
Cheng A. Y. S., Odell S. L., 1981, ApJ, 251, L49
Darwin C., 1959, Proc. R. Soc. London A 249, 180
Darwin C., 1961, Proc. R. Soc. London A 263, 39

Fukue J., Hachiya M., 1999, PASJ, 51, 185
Ghisellini G., Haardt F., Matt G., 2004, A&A, 413, 535
Ghisellini G., Lazzati D., 1999, MNRAS, 309, L7
Holz D. E., Wheeler J. A., 2002, ApJ, 578, 330
Horák J., Karas V., 2005b, MNRAS, submitted
Horák J., 2002, WDS 02 – Proceedings of contributed Papers, III, 449
Inoue S., Takahara F., 1997, PThPh, 98, 807
Junor W., Biretta J. A., Livio M., 1999, Nature, 401, 891
Keane A. J., Barrett R. K., Simmons J. F. L., 2001, MNRAS, 321, 661
Lazzati D., Rossi E., Ghisellini G., Rees M. J., 2004, MNRAS, 347, L1
Levinson A., Eichler D., 2004, ApJ, 613, 1079
Lightman A. P., Shapiro S. L., 1975, ApJ, 198, L73
Luo Q., Protheroe R. J., 1999, MNRAS, 304, 800
Melia F., Königl A., 1989, ApJ, 340, 162
Misner C. W., Thorne K. S., Wheeler J. A., 1973, Gravitation, W. H. Freedman & co.
O'Dell S. L., 1981, ApJ, 243, L147
Ohanian H. C., 1987, Am. J. Phys., 55, 428
Phinney E. S., 1982, MNRAS, 198, 1109
Pineault S., 1977, MNRAS, 179, 691
Poeckert R., Marlborough J. M., 1976, ApJ, 206, 182
Portsmouth J., Bertschinger E., 2004, astro-ph/0412094
Press W. H., 2002, Numerical recipes in C++: the art of scientific computing
Rees M. J., 1975, MNRAS, 171, 457
Renaud N., Henri G., 1998, MNRAS, 300, 1047
Rybicki G. B., Lightman A. P., 1979, Radiative Processes in Astrophysics (Wiley, New York)
Scaltriti F., Bodo G., Ghisellini G., Gliozzi M., Trussoni E., 1997, A&A, 325, L29
Shakura N. I., Sunyaev R. A., 1973, A&A, 24, 337
Schnittman J. D., Bertschinger E., 2004, ApJ, 606, 1098
Shaviv N. J., Dar A., 1995a, ApJ, 447, 863
Shaviv N. J., Dar A., 1995b, MNRAS, 277, 287
Sikora M., Wilson D. B., 1981, MNRAS, 198, 529
Sikora M., Sol H., Begelman M. C., Madejski G., 1996, A&AS, 120, 579
Sikora M., Sol H., Begelman M. C., Madejski G. M., 1996, MNRAS, 280, 781
Sobolev V. V., 1963, A treatise on radiative transfer, Princeton, N.J., Van Nostrand
Sunyaev R. A., Titarchuk L. G., 1985, A&A, 143, 374
Synge J. L., 1967, MNRAS, 136, 195
Urry C. M., Padovani P., 1995, PASP, 107, 803
Vaidya P. C., 1951, Proc. Indian. Acad. Sci., A33, 264
Viironen K., Poutanen J., 2004, A&A, 426, 985
Virbhadra K. S., Ellis G. F. R., 2000, Phys. Rev. D, 62, 084003
Vokrouhlický D., Karas V., 1991, A&A, 252, 835
Winterberg F., Phillips W. G., 1973, Phys. Rev. D, 8, 3329